

AD-A121 012

APPLIED COMPUTATIONAL TRANSONIC AERODYNAMICS(U)
ADVISORY GROUP FOR AEROSPACE RESEARCH AND DEVELOPMENT
NEUILLY-SUR-SEINE (FRANCE) T L HOLST ET AL. AUG 82
AGARD-AG-286

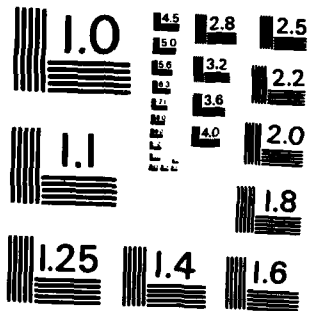
1/2

UNCLASSIFIED

F/G 20/4

NL





MICROCOPY RESOLUTION TEST CHART
NATIONAL BUREAU OF STANDARDS-1963-A

AD A 121012

012



THE MISSION OF AGARD

The mission of AGARD is to bring together the leading personalities of the NATO nations in the fields of science and technology relating to aerospace for the following purposes:

- Exchanging of scientific and technical information;
- Continuously stimulating advances in the aerospace sciences relevant to strengthening the common defence posture;
- Improving the co-operation among member nations in aerospace research and development;
- Providing scientific and technical advice and assistance to the North Atlantic Military Committee in the field of aerospace research and development;
- Rendering scientific and technical assistance, as requested, to other NATO bodies and to member nations in connection with research and development problems in the aerospace field;
- Providing assistance to member nations for the purpose of increasing their scientific and technical potential;
- Recommending effective ways for the member nations to use their research and development capabilities for the common benefit of the NATO community.

The highest authority within AGARD is the National Delegates Board consisting of officially appointed senior representatives from each member nation. The mission of AGARD is carried out through the Panels which are composed of experts appointed by the National Delegates, the Consultant and Exchange Programme and the Aerospace Applications Studies Programme. The results of AGARD work are reported to the member nations and the NATO Authorities through the AGARD series of publications of which this is one.

Participation in AGARD activities is by invitation only and is normally limited to citizens of the NATO nations.

The content of this publication has been reproduced
directly from material supplied by AGARD or the authors.

Published August 1982

Copyright © ACARD 1982
All Rights Reserved

ISBN 92-835-1431-9



*Printed by Technical Editing and Reproduction Ltd
5-11 Mortimer Street, London, W1N 7RH*

FOREWORD

The knowledge about transonic aerodynamics increased considerably during the last fifteen years or so. Around 1970 it became clear that the operational efficiency of military aircraft at transonic speeds could be improved significantly through a better aerodynamic design based on the application of advanced supercritical wings and favourable interference concepts. This was in fact the starting point for the development of transonic computational fluid dynamics, a development that was strongly supported by the increasing need for more effective and fuel efficient aircraft and the rapid progress made in numerical mathematics and computer technology. The Fluid Dynamics Panel of AGARD stimulated the development of transonic computational fluid dynamics by organizing several meetings and symposia on the subject bringing the experts in this area together. In 1980 the Fluid Dynamics Panel concluded that it was highly desirable to describe the state of the art in an Agardograph. The contents of this Agardograph prove that it was indeed the right time for a comprehensive summary on transonic computational fluid dynamics. The review clearly indicates, however, that a large effort is still needed to improve the accuracy of the methods, to decrease the computation costs, to extend their applicability to real configurations, as well as to make them more directly useful for aircraft design. It also shows, however, that there is a strong foundation already available upon which such improvements can be based. It is hoped that this Agardograph will find its way into the hands of many teams working on the aerodynamic design of military aircraft whose success is so much dependent on the application of advanced aerodynamic concepts.

H.YOSHIHARA
B.M.SPEE
Editors
Fluid Dynamics Panel

CONTENTS

	Page
FOREWORD	iii
1. INTRODUCTION AND SUMMARY	1
2. GENERAL THEORY	2
2.1 Governing Equations and Boundary Conditions	2
2.1.1 Inviscid Rotational Flow; Euler's Equations	2
2.1.2 Irrotational, Isentropic Flow; The Full Potential Equation	3
2.1.3 Transonic Small Perturbation Theory	6
2.2 The Representations of Shock Waves	10
2.2.1 Shock Systems on Wings in Transonic Flow; Jump Relations	10
2.2.2 Artificial Viscosity and Asymptotic Shock Layer Structure	11
2.2.3 Conservative Versus Non-Conservative Formulations	11
2.3 Drag	12
2.4 References	14
Figures 2.1-2.8	15
3. EXISTING COMPUTATIONAL TRANSONIC AERODYNAMIC (CTA) METHODS	19
3.1 The Typical Transonic Solution Procedure	19
3.2 Existing CTA Methods (Two Dimensions)	20
3.3 Existing CTA Methods (Three Dimensions)	21
3.3.1 Introduction	21
3.3.2 Specific Code Characteristics	21
3.3.3 Selected Results Obtained with Existing Methods	22
3.3.4 Conservative Versus Nonconservative Formulations	24
3.4 Problems and Limitations with Existing Techniques	24
3.4.1 Introduction	24
3.4.2 TSP Equation Leading Edge Limitation	25
3.4.3 Slow Convergence	25
3.4.4 Viscous Corrections	26
3.4.5 Problems due to the Inadequate Treatment of Geometry	26
3.5 References	27
Figures 3.1-3.30	33
4. VISCOUS INTERACTIONS	43
4.1 Introduction	43
4.2 Planar Viscous Interactions	43
4.2.1 Green's Lag Entrainment Method	44
4.2.2 Inviscid-Viscous Flow Coupling	44
4.2.3 Weak Coupling with Exact Potential Methods	44
4.2.4 Strong Coupling with the Small Disturbance Inviscid Method	45
4.3 Three Dimensional Viscous Interactions	45
4.3.1 Integral Boundary Layer Methods	45
4.3.2 3D Coupling Examples	46
4.4 Concluding Remarks	47
4.5 References	47
Figures 4.1-4.8	48
5. COMPUTATIONAL PROCEDURES IN TRANSONIC AERODYNAMIC DESIGN	52
5.1 Introduction	52
5.2 Indirect Methods	52
5.2.1 Hodograph Methods	52
5.2.2 Fictitious Gas Method	53
5.3 Inverse Methods	54
5.3.1 General	54
5.3.2 Methods Based on Small Perturbation Theory	54
5.3.3 Methods Based on Full Potential Theory	57
5.4 Design by Means of Numerical Optimization	62
5.5 Concluding Remarks	63
5.6 References	64
Figures 5.1-5.20	67

	Page
6. ADVANCED CONCEPTS	76
6.1 Algorithm Development	76
6.1.1 Spatial Discretization Schemes	76
6.1.2 Accelerated Iteration Schemes	79
6.1.2.1 Approximate Factorization Schemes	80
6.1.2.2 Semi-Direct Iteration Schemes	82
6.1.2.3 Multigrid Iteration Schemes	83
6.1.2.4 Extrapolation Techniques	84
6.1.2.5 Methods Tailored to Vector Computers	85
6.2 Grid Generation	86
6.2.1 Analytical Grid Mapping Procedures	87
6.2.2 Numerical Grid Mapping Procedures	87
6.2.3 Geometric Grid Mapping Procedures	89
6.3 References	90
Figures 6.1–6.19	94
7. CONCLUDING REMARKS AND FUTURE PROSPECTS	100
8. ACKNOWLEDGEMENTS	101

1. INTRODUCTION AND SUMMARY

The present AGARDOGRAPH has been written for the applied aerodynamicist engaged in the transonic computational design of combat and airlift aircraft. Its objectives are to review:

- (1) the theoretical fluid dynamic bases on which the computer programs are based;
- (2) the near-decade of computational experience with the established codes;
- (3) selected aspects of treating the viscous interactions;
- (4) computational procedures used in aerodynamic design; and
- (5) advanced concepts presently being developed.

In preparing the AGARDOGRAPH, primary responsibility for each chapter was assigned to one or more authors as follows:

Chapter 2	General theory	Mr. J. Slooff
Chapter 3	Existing CTA methods	Dr. T. Holst / Dr. W. Ballhaus
Chapter 4	Viscous interactions	Dr. H. Yoshihara
Chapter 5	Design procedures	Mr. J. Slooff
Chapter 6	Advanced concepts	Dr. T. Holst / Dr. W. Ballhaus

Each chapter was then reviewed and commented upon by the other authors, with the prime author's viewpoint prevailing in case of diverging opinions.

Note that developments later than 1980, including recently revived interests in solving the Euler equations, are not necessarily covered.

Chapter 2 reviews the formulation of the inviscid transonic boundary value problem. A hierarchy of approximations is considered starting with the Euler formulation followed by the potential approximation and several forms of the small disturbance hypotheses. The physical nature of the approximations at each level is given as a reminder to the numerical aerodynamicist. The necessity of expressing the flow equations in the proper conservation form is stressed to insure the appropriate shock jump conditions. The chapter is concluded by a discussion of the difficult problem of drag determination.

Chapter 3 describes several typical codes presently in wide use summarizing past computational experience with these codes over a wide spectrum of cases and providing user guidelines to assist in achieving converged accurate solutions. Symptoms of common numerical difficulties are described together with their possible cures. Illustrative test/theory comparisons are given with suggestions as to the causes for discrepancies.

Viable computational results cannot be achieved in significant transonic flows without incorporating the viscous effects into the calculations. The state of development of the viscous phase of the problem understandably lags that of the inviscid phase. Chapter 4 begins with a brief description of the important viscous interactions arising in the transonic flow over wings and briefly describes a selective aspect of recent investigations where both planar and three-dimensional integral boundary layer methods were used. Here the integral methods have been selected since they have yielded reasonable results, even for separated cases, when coupled to the inviscid codes without significantly adding to the computer time.

Chapter 5 reviews the recent efforts in the application of computer codes to configuration design. Applications of hodograph, fictitious gas and inverse codes are given as well as examples of aerodynamic design by means of numerical optimization. The chapter is concluded with a discussion of the possibilities and limitations of the various approaches.

Chapter 6 summarizes important advanced concepts in development to extend the capabilities of the codes, not only in their ability to handle more realistic configurations, but also to reduce the computing times. Topics include general mesh generation schemes to fit complex configurations and convergence speed-up techniques such as approximate factorization methods, extrapolation procedures, and the use of multigrid techniques. A short discussion of the algorithm development for vector computers is also included.

Finally Chapter 7 concludes the AGARDOGRAPH with a brief discussion which puts computational transonic aerodynamics, including future prospects, in a more general perspective.

2. GENERAL THEORY

2.1 Governing equations and boundary conditions

Viscous compressible flow of a perfect gas, in general, is described by the set of conservation laws known as the time-dependent Navier-Stokes equations¹. If we are interested in steady compressible adiabatic flow at high Reynolds number only, the flow, to lowest order, is described by the (reduced) set of conservation laws for inviscid compressible flow known as the (steady) Euler equations, while the thin viscous layers, to first order, are described by the boundary layer equations.

A detailed description of the various forms of (approximations to) the boundary layer equations and in particular of the various approaches to the turbulence closure problem is considered to be outside the scope of this AGARDograph; the reader is referred to reference 2 for a recent survey. The problem of describing the interaction between the thin viscous layers and the outer inviscid flow is addressed in chapter 4. In this chapter we will consider the equations that describe inviscid (transonic) flow.

2.1.1 Inviscid rotational flow; Euler's equations

Neglecting body forces, steady adiabatic inviscid compressible flow is, in Cartesian coordinates, described by the following conservation laws:
conservation of mass:

$$\frac{\partial}{\partial x}(\rho u) + \frac{\partial}{\partial y}(\rho v) + \frac{\partial}{\partial z}(\rho w) = 0 \quad (2.1)$$

conservation of momentum (Euler's equations):

$$\left. \begin{aligned} \frac{\partial}{\partial x}(\rho u^2 + p) + \frac{\partial}{\partial y}(\rho uv) + \frac{\partial}{\partial z}(\rho uw) &= 0 \\ \frac{\partial}{\partial x}(\rho vu) + \frac{\partial}{\partial y}(\rho v^2 + p) + \frac{\partial}{\partial z}(\rho vw) &= 0 \\ \frac{\partial}{\partial x}(\rho wu) + \frac{\partial}{\partial y}(\rho wv) + \frac{\partial}{\partial z}(\rho w^2 + p) &= 0 \end{aligned} \right\} \quad (2.2)$$

conservation of energy:

$$\frac{\partial}{\partial x}(\rho u h_0) + \frac{\partial}{\partial y}(\rho v h_0) + \frac{\partial}{\partial z}(\rho w h_0) = 0 \quad (2.3)$$

In equations (2.1) to (2.3) u, v, w represent the x, y and z components of the velocity vector, respectively; q is the total velocity and p and ρ are the pressure and density, respectively. h_0 is the total enthalpy given by

$$h_0 = e + \frac{p}{\rho} + \frac{1}{2} q^2 \quad (2.4)$$

e is the specific internal energy given by the caloric equation of state

$$e = c_v T \quad (2.5)$$

T representing the total temperature and c_v the specific heat at constant volume.

The system (2.1) to (2.3/4) for the six unknowns u, v, w, p, ρ and e is completed by the thermal equation of state for a perfect gas

$$p = \rho RT \quad (2.6)$$

$R = c_p - c_v$ being the specific gas constant. Note that the temperature T is readily eliminated by substituting (2.6) into (2.5). The expression (2.4) for the total enthalpy can then be rewritten as

$$h_0 = \frac{\gamma}{\gamma-1} \frac{p}{\rho} + \frac{1}{2} q^2 \quad (2.7)$$

$\gamma = c_p/c_v$ being the ratio of specific heats.

In computational transonic aerodynamics the system of equations given above (or simplifications thereof) are solved for the following boundary conditions¹:

1. Zero normal velocity at the surface $S(x, y, z)$ of a configuration

$$\bar{q} \cdot \bar{n} = 0 \quad \text{on} \quad S(x, y, z) \quad (2.8)$$

\bar{n} being the unit normal to S .

2. The Kutta condition of smooth flow at the trailing edges of the wing and other lifting parts of a configuration. It requires the presence of a surface with a discontinuity in tangential velocity across it that extends from the trailing edge to downstream infinity. The surface of discontinuity or vortex sheet S_v is aligned with the flow and carries zero pressure jump,

$$\text{i.e.} \quad \bar{q} \cdot \bar{n} = 0 \quad \text{on} \quad S_v^+ \text{ and } S_v^- \quad (2.9)$$

$$[p] = p^+ - p^- = 0 \quad \text{on} \quad S_v \quad (2.10)$$

The shape of the vortex sheet is to be determined as part of the solution.

3. Asymptotically vanishing flow perturbation at infinity

$$\left. \begin{aligned} \bar{q} &\rightarrow \bar{q}_\infty \\ p &\rightarrow p_\infty \\ \rho &\rightarrow \rho_\infty \end{aligned} \right\} \quad \text{for} \quad x^2 + y^2 + z^2 \rightarrow \infty \quad (2.11)$$

except in the Trefftz plane at downstream infinity where a two-dimensional cross-flow exists around the vortex sheet.

In most, if not all, practical applications the conditions on the vortex sheet are simplified and approximated by assuming a fixed shape. On this fixed vortex sheet the simplified conditions are imposed of zero jump in normal velocity and zero jump in the velocity component that is parallel to certain prescribed, approximately streamwise directions (preferably coordinate lines) in the sheet, i.e.

$$[\bar{q} \cdot \bar{n}] = 0 \quad \text{on } S_w \quad (2.12)$$

and

$$[\bar{q} \cdot \bar{t}] = 0 \quad \text{along prescribed direction } \bar{t} \text{ on } S_w \quad (2.13)$$

The latter condition implies that the trailing vorticity is constant along lines parallel to \bar{t} . The simplified conditions just described are consistent with the assumption of small perturbations. Note also that flows with leading edge or other extensive boundary layer separations are excluded.

For completeness it is mentioned that some interesting consequences of the Kutta condition for 3-D flows and 2-D flows with shock waves are discussed in references 4, 5 respectively. The implication of this, being that the flow leaves the trailing-edge tangent to either the lower or the upper surface, is not recognized in the current computational methods for transonic flow.

Prior to proceeding to simpler and more approximate systems of equations describing transonic flow it is useful to consider some characteristic features of the Euler equations.

First of all it is important to realize that equations (2.1) to (2.3) are obtained from the Navier-Stokes equations by setting viscosity and heat conduction equal to zero. An important consequence of this is that we have removed the dissipative mechanism that prevents the entropy of a fluid particle from decreasing during its course through the flowfield. For this reason the Euler equations (2.1) to (2.5) must be supplemented with the additional condition that the second law of thermodynamics must be satisfied, i.e. the entropy may not decrease along a streamline. The entropy condition has no implications for continuous flows, for which the conservation laws for mass, momentum and energy can be shown¹ to imply conservation of entropy. However, satisfying the entropy condition is particularly important for discontinuous flows, i.e. for transonic (and supersonic) flows with shock waves. Without enforcing the entropy condition there is, in general, no unique solution, both compression and expansion shocks being possible. As shown by Lax², the entropy or an equivalent additional condition must be enforced to guarantee a unique and indeed the physically relevant solution, i.e. the one with compression shocks only. Moreover, in order to obtain the correct shock jumps, it is essential that the flow equations are cast in conservation form³. We will return to this subject later, in section 2.2. The shock jumps pertaining to the system of conservation laws (2.1) to (2.3) are described by the Rankine-Hugoniot relations¹. In terms of normal Mach number the jump relation is depicted in figure 2.1.

It is further noted that the conservation laws (2.1) to (2.3) can be recombined to yield various auxiliary relations. A particularly useful example which, however, does hold in regions of continuous flow only, is the generalized Crocco relation¹

$$T \text{grad } S + \bar{q} \times \text{curl } \bar{q} = \text{grad } h_0 \quad (2.14)$$

In most aerodynamic applications we have uniform flow at upstream infinity. It then follows from the mass and energy conservation equations (2.1) and (2.3) that, even for flows with shocks,

$$\text{grad } h_0 = 0 \quad (2.15)$$

Hence, (2.14) reduces to

$$T \text{grad } S + \bar{q} \times \text{curl } \bar{q} = 0 \quad (2.16)$$

Equations (2.15) and (2.16) imply that flows that are uniform at upstream infinity have constant total enthalpy throughout and, when continuous, are also homentropic (i.e. have also constant entropy throughout) and irrotational. On the other hand, if the flow is not continuous through the presence of shock waves, it is no longer homentropic in regions downstream of the shocks and rotation is generated in view of (2.16).

In spite of the fact that the Euler equations offer the most complete description of inviscid, compressible flow, they do not form the basis of the current well-established methods for transonic flow computations. The reason for this seems to be that the Euler equations are significantly more complex and require a significantly larger computational effort than the more approximate flow equations, to be described hereafter, on which the majority of the currently available computational methods for transonic flow is based.

Surprisingly, in retrospect, the first technically successful attempt by Magnus, Gallaheer and Yoshihara⁴ to numerically solve the problem of transonic flow with shock waves was based on the Euler equations, albeit that the energy equation was dropped and replaced by a relation expressing conservation of entropy. The properties of this isentropic, rotational flow model have been described at some length by Van der Vooren and Slooff⁵.

Magnus et al, in their approach, obtain the steady state solution in the limit for $t \rightarrow \infty$ of a time-dependent process which is started, at $t = 0$, from a uniform flow by impulsively activating the boundary conditions on the airfoil. Results obtained with this method have been quite satisfactory. However, the method did not meet wide application due to the fact that the computational effort involved is prohibitively large for practical purposes.

In recent years, renewed activities can be noticed in the field of developing (more efficient) numerical methods based on the Euler equations^{6,7}. Such activities are motivated in particular by the requirement to model the strong shock waves and vortex sheets occurring with combat aircraft. However, these developments have, as yet, not led to large-scale application in transonic aerodynamic analysis and design.

2.1.2 Irrotational, isentropic flow; the full potential equation

A significant reduction in the number of dependent variables is obtained if the flow is assumed to be irrotational. It is then possible to introduce a velocity potential Φ , related to the velocity itself by:

^{*)} See also proceedings of 1981 AIAA Computational Fluid Dynamics Conference

$$\bar{q} = \text{grad } \phi \quad (2.17)$$

the single dependent variable ϕ replacing the five dependent variables u, v, w, p and ρ of the Euler equations.

The assumption of irrotationality is of no consequence for continuous flows, which, when uniform at upstream infinity, were shown to be isentropic and irrotational throughout. For (transonic) flows with weak shock waves the assumption can be justified by considering the jump $[S]$ in entropy across a shock wave. It follows from the Rankine-Hugoniot relations¹ that

$$[S] = c_v \frac{2\gamma(\gamma-1)}{3(\gamma+1)^2} (M_n^2 - 1)^3 + O(M_n^2 - 1)^4 \quad (2.18)$$

where M_n is the component of the local Mach number normal to the shock and γ is the ratio of specific heats. Hence the jump in entropy is negligible if M_n is sufficiently close to 1. It then follows from the Crocco relation (2.16) that also the rotation behind the shock is negligible.

An important property of irrotational isentropic flows, that is immediately obvious from the generalized Crocco relation (2.14), is that of constant total enthalpy (Eq. (2.15)). Hence the energy conservation equation (2.3) is automatically satisfied, provided that the mass conservation equation (2.1) is satisfied. In addition it can be shown¹, that, in regions with continuous flow, also the momentum equations are satisfied. In other words continuous, isentropic, irrotational flow is completely described by substituting (2.17) into the mass conservation equation (2.1), leading to the full potential equation in conservation form

$$\frac{\partial}{\partial x} (\rho \phi_x) + \frac{\partial}{\partial y} (\rho \phi_y) + \frac{\partial}{\partial z} (\rho \phi_z) = 0 \quad (2.19)$$

In (2.19), the density ρ is given by the algebraic relation¹

$$\rho = \left\{ 1 - \frac{\gamma-1}{2} M_\infty^2 (\phi_x^2 + \phi_y^2 + \phi_z^2 - 1) \right\}^{\frac{1}{\gamma-1}} \quad (2.20)$$

Note that the velocity (potential) in (2.20) has been scaled by the free stream velocity.

When the solution for ϕ is known, the pressure can be obtained from the expression for the pressure coefficient in isentropic flow¹

$$C_p = \frac{1}{\frac{\gamma}{2} M_\infty^2} \left[\left\{ 1 - \frac{\gamma-1}{2} M_\infty^2 (\phi_x^2 + \phi_y^2 + \phi_z^2 - 1) \right\}^{\frac{\gamma}{\gamma-1}} - 1 \right] \quad (2.21)$$

Discontinuous flows that satisfy the mass conservation equations (2.19) and (2.20) also satisfy the energy conservation equation but do not conserve normal momentum across the discontinuities. As indicated by Steger and Baldwin¹⁰ this implies a wave drag mechanism in the form of a loss of normal momentum across shock waves.

The shock jump relations of (2.19), in terms of Mach number normal to the shock, are also depicted in figure 2.1. It appears that the error is less than 8% if the upstream normal Mach number is < 1.3 .

The requirement that M_n (when > 1) must be sufficiently close to 1 sets certain limitations to the class of flows that can be treated. Expecting normal shocks to occur in any case on bodies and near the root of wings (see also section 2.2) we may generalize this requirement by

$$M^2 \leq 1 + \epsilon, \quad \epsilon \ll 1 \quad (2.22)$$

or, with¹

$$M^2 = \frac{M_\infty^2 q^2}{1 + \frac{\gamma-1}{2} M_\infty^2 (1-q^2)} \quad (2.23)$$

$$\text{by} \quad M_\infty^2 q^2 \leq \left\{ 1 + \frac{\gamma-1}{2} M_\infty^2 (1-q^2) \right\} (1 + \epsilon) \quad (2.24)$$

This can be rearranged to

$$M_\infty^2 q^2 \leq \frac{2}{\gamma+1} + \frac{\gamma-1}{\gamma+1} M_\infty^2 + O[\epsilon] \quad (2.25)$$

or, with $\gamma = 1.4$,

$$M_\infty^2 q^2 \leq 0.83 - 0.17 M_\infty^2 + O[\epsilon] \quad (2.26)$$

For transonic free stream Mach numbers, i.e. $M_\infty = 1-\mu$, $\mu \ll 1$, equation (2.26) reduces to

$$q^2 \leq 1 + O[\epsilon] + O[\mu] \quad (2.27)$$

This illustrates that (full) potential theory is a small perturbation theory for $M_\infty \approx 1$. In practice the requirement (2.22) and its subsequent implications may be somewhat less stringent than suggested upon the assumption of normal shocks. The reason is that due to viscous effects ("viscous wedge" effect, section 4) even "normal" shocks are turned into oblique ones. On swept wings the effect of sweep, at least away from the root and tip, is also to reduce the effective M_n .

Equation (2.19) forms the basis for today's most established procedures for transonic flow calculations.

In most applications it is encountered in a form¹¹ associated with general, non-orthogonal, curvilinear coordinates ξ, η, ζ :

$$\frac{\partial}{\partial \xi} \left(\frac{\rho U}{J} \right) + \frac{\partial}{\partial \eta} \left(\frac{\rho V}{J} \right) + \frac{\partial}{\partial \zeta} \left(\frac{\rho W}{J} \right) = 0 \quad (2.28)$$

where:

$$J = \det. \begin{bmatrix} \xi_x & \xi_y & \xi_z \\ \eta_x & \eta_y & \eta_z \\ \zeta_x & \zeta_y & \zeta_z \end{bmatrix} = \det. [H] = h^{-1} \quad (2.29)$$

h being the Jacobian of the transformation and U , V and W are the contravariant velocity components along the ξ , η and ζ directions, respectively, given by

$$\begin{bmatrix} U \\ V \\ W \end{bmatrix} = [H] \begin{bmatrix} u \\ v \\ w \end{bmatrix} \quad (2.30)$$

or

$$\begin{bmatrix} U \\ V \\ W \end{bmatrix} = [H^T H] \begin{bmatrix} \phi_\xi \\ \phi_\eta \\ \phi_\zeta \end{bmatrix} \quad (2.31)$$

the matrix $H^T H$ being the contravariant metric tensor¹² of the transformation.

Abandoning the strict conservation form, a form called "semi-conservative" by Chattot^{13,14} is obtained if the metric coefficients are written in front of the partial derivatives:

$$\begin{aligned} & A \frac{\partial}{\partial \xi} (\rho \phi_\xi) + B \frac{\partial}{\partial \eta} (\rho \phi_\eta) + C \frac{\partial}{\partial \zeta} (\rho \phi_\zeta) \\ & + D \left\{ \frac{\partial}{\partial \xi} (\rho \phi_\eta) + \frac{\partial}{\partial \eta} (\rho \phi_\xi) \right\} + E \left\{ \frac{\partial}{\partial \xi} (\rho \phi_\zeta) + \frac{\partial}{\partial \zeta} (\rho \phi_\xi) \right\} \\ & + F \left\{ \frac{\partial}{\partial \eta} (\rho \phi_\zeta) + \frac{\partial}{\partial \zeta} (\rho \phi_\eta) \right\} + G = 0 \end{aligned} \quad (2.32)$$

Equation (2.32) has the advantage that the coefficients A , B ... F depend only on the coordinate transformation and, for a given (body fitting) coordinate system, can be calculated once and for all. The function G depends also on the velocity components¹³. Note that the derivation of (2.32) does not require the assumption that the flow is continuous. This would mean that the jump relations of (2.19)/(2.28) are retained, provided that the coordinate transformation is regular.

In several applications of full potential theory an alternative, non-conservative form of the full potential equation, known as the quasi-linear form¹ is encountered:

$$(c^2 - \phi_x^2) \phi_{xx} + (c^2 - \phi_y^2) \phi_{yy} + (c^2 - \phi_z^2) \phi_{zz} - 2 \phi_x \phi_y \phi_{xy} - 2 \phi_y \phi_z \phi_{yz} - 2 \phi_x \phi_z \phi_{xz} = 0 \quad (2.33)$$

The local speed of sound c in equation (2.33) is given by

$$c = c_0 - \frac{\gamma-1}{2} (\phi_x^2 + \phi_y^2 + \phi_z^2) \quad (2.34)$$

c_0 representing the stagnation value.

A convenient form of the non-conservative equation (2.33) that is suitable for application in general curvilinear coordinates ξ , η , ζ is¹⁵ (see also Mangler/Murray¹⁶ and Forsey/Carr¹⁷):

$$c^2 \{ (Uh)_\xi + (Vh)_\eta + (Wh)_\zeta \} - h(UQ_\xi + VQ_\eta + WQ_\zeta) = 0 \quad (2.35)$$

where

$$Q = \frac{1}{2} q^2 = \frac{1}{2} (u^2 + v^2 + w^2) \quad (2.36)$$

U , V and W are again the contravariant components of the velocity vector \bar{q} in the curvilinear coordinate system and h is the Jacobian of the transformation (see (2.29) to (2.31)).

Yet another possibility^{13,18} is to write

$$A \phi_{\xi\xi} + B \phi_{\eta\eta} + C \phi_{\zeta\zeta} + D \phi_{\xi\eta} + E \phi_{\xi\zeta} + F \phi_{\eta\zeta} + G = 0 \quad (2.37)$$

where A , B ... G are now all functions of both the metric coefficients and the velocity components.

The first transonic full potential flow calculations by Steger/Lomax¹⁹ and Garabedian/Korn²⁰ for the 2-D planar case, Jameson²¹ for axisymmetric flow and Jameson^{22,23}, Jameson/Caughey¹⁸ for 3-D wing flow were based on equation (2.37) or variants thereof. Note that, according to Lax⁶, solutions of (2.33/35/37) will in general not exhibit the correct shock jumps.

Finally we give the full potential equation in (non-conservative) perturbation form¹:

$$\begin{aligned} (1-M_\infty^2) \phi_{xx} + \phi_{yy} + \phi_{zz} = & \left\{ (\gamma+1) \phi_x + \frac{\gamma+1}{2} \phi_x^2 + \frac{\gamma-1}{2} (\phi_y^2 + \phi_z^2) \right\} M_\infty^2 \phi_{xx} \\ & + \left\{ (\gamma-1) \phi_x + \frac{\gamma+1}{2} \phi_y^2 + \frac{\gamma-1}{2} (\phi_x^2 + \phi_z^2) \right\} M_\infty^2 \phi_{yy} \\ & + \left\{ (\gamma-1) \phi_x + \frac{\gamma+1}{2} \phi_z^2 + \frac{\gamma-1}{2} (\phi_x^2 + \phi_y^2) \right\} M_\infty^2 \phi_{zz} \\ & + 2 M_\infty^2 (1+\phi_x) \phi_y \phi_{xy} + 2 M_\infty^2 (1+\phi_x) \phi_z \phi_{xz} + 2 M_\infty^2 \phi_y \phi_z \phi_{yz} \end{aligned} \quad (2.38)$$

Equation (2.38) can be obtained from (2.33), (2.34) upon introduction of the perturbation velocity potential ϕ , defined by

$$\phi = x + \varphi \quad (2.39)$$

We shall use (2.38) in the next section in order to arrive at certain small perturbation approximations.

The boundary conditions that go with (2.19) or any of the alternatives are easily derived from (2.8) to (2.13), i.e. we have

- on the surface $S(x,y,z)$ of a wing or body:

$$\text{grad } \phi \cdot \bar{n} = 0 \quad (2.40)$$

- Kutta condition and other boundary conditions on the trailing vortex sheet S_w

$$[\text{grad } \phi \cdot \bar{n}] = 0 \quad (2.41)$$

$$[\phi] = \Gamma(y) \quad (2.42)$$

where $\Gamma(y)$ is the value of $[\phi]$ at the trailing edge.

- at infinity, with the flow at infinity parallel to the x-axis:

$$\phi \rightarrow x \quad \text{for} \quad x^2 + y^2 + z^2 \rightarrow \infty \quad (2.43)$$

except in the Trefftz-plane at downstream infinity where the potential satisfies the Laplace equation for two-dimensional flow around the trailing vortex sheet

$$\phi_{yy} + \phi_{zz} = 0 \quad \text{for} \quad x \rightarrow +\infty \quad (2.44)$$

Note that, in order to avoid the singular behaviour of ϕ at infinity, it may be convenient to introduce a reduced or perturbation potential $\phi = \phi - x$ as the dependent variable. Also, the infinitely large physical domain is usually replaced by a finite computational domain through a convenient coordinate transformation or by simply truncating the physical domain.

2.1.3 Transonic small perturbation theory

General

For wings and airfoils a further and significant simplification of the problem can be obtained if these bodies are assumed to be thin with respect to the local chord and to have only a small inclination relative to the free stream. It is then possible to approximate the boundary conditions by satisfying equation (2.40) in the wing mean plane ($z = 0$) rather than on the actual surface of the wing itself. With the wing surface given by

$$z = F(x, y) = \delta f(x, y), \quad \delta \ll 1 \quad (2.45)$$

and utilizing Taylor series expansion from the plane $z = 0$ for the velocity components, i.e.

$$\phi_x(x, y, z) = \phi_x(x, y, 0) + z \phi_{xz}(x, y, 0) + \frac{1}{2} z^2 \phi_{xzz}(x, y, 0) + \dots \quad (2.46)$$

etc., equation (2.40) can be approximated by

$$\phi_{xx} n_x + \phi_{yy} n_y + \phi_{zz} n_z + z(\phi_{xz} n_x + \phi_{yz} n_y + \phi_{zz} n_z) + \dots = 0 \quad \text{on} \quad S(x, y, 0) \quad (2.47)$$

or, since

$$\left. \begin{aligned} -\frac{n_x}{n_z} &= \frac{\partial F}{\partial x} = \delta f_x \\ -\frac{n_y}{n_z} &= \frac{\partial F}{\partial y} = \delta f_y \end{aligned} \right\} \quad (2.48)$$

and introducing normalized perturbation quantities (2.39), by

$$\phi_z + \delta f \phi_{zz} + \dots = (1 + \phi_x + \dots) \delta f_x + (\phi_y + \dots) \delta f_y \quad \text{on} \quad S(x, y, 0) \quad (2.49)$$

It is easily verified that, if the lowest order approximation, in terms of δ , to (2.49) is to be non-trivial, ϕ_z must be $O[\delta]$.

An important consequence of and indeed the main motivation for the small perturbation assumption is that the approximate planar boundary condition allows easy numerical implementation in simple Cartesian mesh systems. Hence the complexity of setting-up and utilizing a boundary-conforming mesh and curvilinear coordinate system or of cumbersome interpolations in non-boundary-conforming Cartesian grids is avoided. This, however, at the cost of a less accurate flow model. The latter is particularly true at the leading edge of blunt-nosed wings (or bodies) where $f_x, f_y \rightarrow \infty$, irrespective of δ .

An additional but less significant advantage of the small perturbation assumption is that the governing equation for potential flow can be simplified accordingly, thereby reducing, to some extent, the amount of algebra involved with satisfying the discretized form of the flow equation. In the literature on the subject several alternative forms of transonic small perturbation (TSP) equation may be found. They can be categorized according to several different criteria. One way is to distinguish between formulations derived from the conservation form (2.19) of the full potential equation and formulations derived from the non-conservative form (2.33/38). Another is to distinguish between various possible assumptions concerning the asymptotic structure of the flow field (as $\delta \rightarrow 0$), with their related classes of geometry, and more heuristically guided choices of terms in the TSP partial differential equation. In the following discussion we will concentrate on TSP equations that exhibit the preferred proper conservation form and that can be derived on the basis of consistent asymptotic reasoning. Other formulations will be mentioned more briefly.

Equations

As pointed out by Van der Vooren et al.²⁴, proper transonic small perturbation approximations to the full potential equation in conservation form can be obtained by substituting a properly truncated series expansion of the expression (2.20) for the density ρ into equation (2.19). In terms of perturbation velocity potential this leads to

$$\left. \begin{aligned} [\rho \phi_x]_x &= [\rho(1 + \phi_x)]_x = \left[1 + (1 - M_\infty^2) \phi_x - \frac{3 - (2 - \gamma) M_\infty^2}{2} M_\infty^2 \phi_x^2 - \frac{1}{2} M_\infty^2 \phi_y^2 - \frac{1}{2} M_\infty^2 \phi_z^2 + \dots \right]_x \\ [\rho \phi_y]_y &= [\rho \phi_y]_y = [\phi_y - M_\infty^2 \phi_x \phi_y + \dots]_y \\ [\rho \phi_z]_z &= [\rho \phi_z]_z = [\phi_z - M_\infty^2 \phi_x \phi_z + \dots]_z \end{aligned} \right\} \quad (2.50)$$

From this point one may proceed in several ways, depending on additional assumptions with respect to the asymptotic behaviour of the geometry and Mach number of the problem which determine where the series (2.50) may be terminated. The number of possibilities is limited by the requirement that the assumptions should not lead to trivialities or contradictions.

One non-trivial formulation is obtained by introducing the stretched coordinates

$$\left. \begin{aligned} \tilde{y} &= \delta^{1/3} y \\ \tilde{z} &= \delta^{1/3} z \end{aligned} \right\} \quad (2.51)$$

and assuming $1-M_\infty^2$ to be of $\mathcal{O}[\delta^{2/3}]$. Because φ_z is $\mathcal{O}[\delta]$, it follows that φ is $\mathcal{O}[\delta^{2/3}]$. The lowest order approximation to (2.19) is then

$$\left[(1-M_\infty^2)\varphi_{xx} - \frac{3-(2-\gamma)M_\infty^2}{2} M_\infty^2 \varphi_x^2 \right]_x + [\varphi_y]_y + [\varphi_z]_z = 0 + \mathcal{O}[\delta^2] \quad (2.52)$$

in which all terms are asymptotically of equal magnitude $\mathcal{O}[\delta^{4/3}]$. Note that the stretching (2.51) implies that, asymptotically, the wing planform is described by $S(x, \delta^{-1/3}y) = 0$. Hence, equation (2.52) is valid for wings of vanishing thickness $\delta \rightarrow 0$, with sweep angle vanishing like $\delta^{1/3}$ and aspect ratio tending to infinity like $\delta^{-1/3}$ at Mach numbers approaching 1 like $1+\delta^{2/3}$. It can also be derived for bodies of vanishing fineness ratio δ . Equation (2.52) is the correct conservative counterpart of the classical Guderley-Von Karman TSP equation (see, e.g. Spreiter²⁵)

$$(1-M_\infty^2)\varphi_{xx} - (\gamma+1)M_\infty^2\varphi_x\varphi_{xx} + \varphi_{yy} + \varphi_{zz} = 0 \quad (2.53)$$

The latter is obtained when the scaling (2.51) and the assumption $1-M_\infty^2 = \mathcal{O}[\delta^{2/3}]$ are introduced in the non-conservative form (2.38) of the full potential equation.

The first technically as well as economically successful computations of transonic flows with shock waves by Murman/Cole²⁶ and Murman/Krupp^{27,28} for the 2-D planar case, Krupp/Murman²⁸ and Bailey²⁹ for axisymmetric flow and Bailey/Steger³⁰, Ballhaus/Bailey³¹ and Newman/Klunker³² for the case of 3-D wing flow were based on equation (2.53). Recast in conservation form equation (2.53) was used by Bailey and Ballhaus³⁴.

A different result is obtained if the stretching (2.51) is adopted for the z-coordinate only and $1-M_\infty^2$ is assumed to be of $\mathcal{O}[1]$. This leads to²⁴

$$\left[(1-M_\infty^2)\varphi_{xx} - \frac{1}{2}\{3-(2-\gamma)M_\infty^2\}M_\infty^2\varphi_x^2 - \frac{1}{2}M_\infty^2\varphi_y^2 \right]_x + [\varphi_y - M_\infty^2\varphi_x\varphi_y]_y + [\varphi_z]_z = 0 + \mathcal{O}[\delta^2] \quad (2.54)$$

It should be noted that if equation (2.54) is to represent an asymptotically consistent approximation there must hold

$$[(1-M_\infty^2)\varphi_{xx}]_x + [\varphi_y]_y = \mathcal{O}[\delta^{4/3}] \quad (2.55)$$

while φ_{xx} and φ_{yy} themselves are each $\mathcal{O}[\delta^{2/3}]$. The implication of this becomes clear if it is realized that for a yawed wing of infinite span there holds

$$-\tan^2 \Lambda \varphi_{xx} + \varphi_{yy} = 0 \quad (2.56)$$

where Λ is the angle of sweep. Comparing (2.55) and (2.56) it follows that (2.54) represents an asymptotically consistent approximation only for wings of vanishing thickness, $\delta \rightarrow 0$, the planform of which approaches that of an infinite yawed wing of sweep Λ at (supersonic) free stream Mach numbers approaching the value

$$M_\infty = [1 + \tan^2 \Lambda + \mathcal{O}[\delta^{2/3}]]^{1/2} \quad (2.57)$$

Equation (2.54) is known as the NLR equation²⁴. It has also been advocated by W. Schmidt of Dornier³³.

The jump relations of (2.52/54) in terms of the normal component of the local Mach number are also given in figure 2.1. Note that the accuracy of the TSP approximation deteriorates rapidly for $M_n > 1.15^*$.

A non-conservative counterpart of equation (2.54) is obtained by introducing the relevant assumptions into the non-conservative form (2.38) of the full potential equation:

$$[(1-M_\infty^2) - (\gamma+1)M_\infty^2\varphi_x]\varphi_{xx} + [1-(\gamma-1)M_\infty^2\varphi_x]\varphi_{yy} - 2M_\infty^2\varphi_x\varphi_{xy} + \varphi_{zz} = 0 \quad (2.58)$$

Equation (2.58) was first proposed by Lomax et al³⁴ of NASA Ames and has been used with some minor modifications by Albane et al³⁵ and Ballhaus et al³⁶. The latter authors have also recast equation (2.58) in conservation form.

Further asymptotically consistent approximations to the full potential equation in conservation form can be obtained by avoiding any of the scalings (2.51). The general second order accurate conservation form is³³, with $\varphi = \mathcal{O}[\delta]$:

$$[(1-M_\infty^2)\varphi_{xx} - \frac{1}{2}\{3-(2-\gamma)M_\infty^2\}M_\infty^2\varphi_x^2 - \frac{1}{2}M_\infty^2\varphi_y^2 - \frac{1}{2}M_\infty^2\varphi_z^2]_x + [\varphi_y - M_\infty^2\varphi_x\varphi_y]_y + [\varphi_z - M_\infty^2\varphi_x\varphi_z]_z = 0 + \mathcal{O}[\delta^3] \quad (2.59)$$

*) M_n , in this case, has been related to the "canonical" form

$$(1-M_\infty^2)\varphi_{\xi\xi} + \varphi_{\eta\eta} + \varphi_{zz} = 0$$

of the relevant TSP equation through

$$M_n = M \cos \Lambda',$$

Λ' being the angle between the shock and the principal axis (ξ -direction), leading to

$$[M_n] = M_{n1} - \sqrt{2-M_\infty^2} M_{n1}$$

If $1-M_\infty^2$ is assumed to be of $O[\delta]$, the lowest order approximation to (2.59) is

$$[\varphi_y]_y + [\varphi_z]_z = 0 + O[\delta^2] \quad (2.60)$$

Using (2.60) and abandoning the strict conservation form, equation (2.59) can be reduced to

$$[(1-M_\infty^2)\varphi_x - \frac{1}{2}\{3-(2-\gamma)M_\infty^2\}M_\infty^2\varphi_x^2 - \frac{1}{2}M_\infty^2\varphi_y^2 - \frac{1}{2}M_\infty^2\varphi_z^2]_x + [\varphi_y]_y - M_\infty^2\varphi_y\varphi_{xy} + [\varphi_z]_z - M_\infty^2\varphi_z\varphi_{xz} = 0 \quad (2.61)$$

or

$$[(1-M_\infty^2)\varphi_x - \frac{1}{2}\{3-(2-\gamma)M_\infty^2\}M_\infty^2\varphi_x^2]_x - 2M_\infty^2\varphi_y\varphi_{xy} - 2M_\infty^2\varphi_z\varphi_{xz} + [\varphi_y]_y + [\varphi_z]_z = 0 \quad (2.62)$$

Note that the lowest order approximation (2.60) of (2.61/62) is the equation of slender body theory³⁷. This indicates that equation (2.61/62) represents a consistent second order accurate approximation only for slender bodies and slender wings (i.e. low aspect ratio wings or highly swept wings that are typical of fighter and supersonic aircraft configurations) at Mach numbers approaching unity. Together with the fact that equation (2.61/62) can be derived only by abandoning the strict conservation form this indicates further that, basically, equation (2.61/62) is valid for (subcritical) flows without shock waves only. It is a non-linear equation, however, and as such capable of producing shocks.

A variant of (2.62), that can be obtained by introducing the relevant assumptions into (2.38) has been proposed by Hall and Firmin³⁸ of RAE. However, to the present author's knowledge neither this equation nor (2.61/62) has ever been used in actual calculations. The main reason for this seems to be that the term $\varphi_z\varphi_{xz}$ gives rise to numerical difficulties near blunt leading edges³⁸.

Apart from the TSP equations given above, that can be derived on the basis of asymptotically consistent reasoning, several other forms, based on more heuristic arguments may be found in the literature. For example, Klunker and Newman³⁹ use the non-conservative Guderley-Von Karman equation (2.53) with the third order term $\frac{1}{2}(\gamma+1)\varphi_{xx}^2$ added in order "to better approximate the critical speed where the equation changes type from elliptic to hyperbolic". Similar reasoning has led Boppe⁴⁰ to add the same term to the non-conservative equation (2.58). Still other terms have been suggested by Schmidt^{41,42}. Yet another way of empirically improving the agreement between results of TSP theory and more complete formulations, introduced by Krupp^{27,43} has been to modify the power of the coefficient M_∞^2 of the non-linear terms in equation (2.53)⁴⁴ or equation (2.58)^{35,36}.

It is the present author's opinion that such empirical additions or modifications of the basic TSP equations are unnecessary if the correct conservation form (2.52/2.54) or (2.59) of the perturbation mass flux equation is used^{24,33}. The point is illustrated in figure 2.2 which, assuming infinite yawed wing conditions, i.e.

$$\left. \begin{aligned} \varphi_y &= -\varphi_x \tan \Lambda \\ \varphi_{yy} &= \varphi_{xx} \tan^2 \Lambda \\ \varphi_{xy} &= -\varphi_{xx} \tan \Lambda \end{aligned} \right\} \quad (2.63)$$

gives the critical chordwise perturbation velocity as a function of Mach number for several TSP forms and sweep angles.

In spite of the fact that the asymptotic arguments presented above suggest that each of the equations (2.52/53), (2.54/58), (2.61/62) is valid only in a specific narrow range of transonic (i.e. $M_\infty \approx 1$) or supersonic Mach numbers and wing planform shapes, results obtained by means of TSP theory have been found to be surprisingly accurate for Mach numbers well below 1 and widely varying wing planforms^{34,35,36,38,40,44,45,46}. The reason for this seems to be that all TSP equations incorporate the first order accurate Prandtl-Glauert equation

$$[(1-M_\infty^2)\varphi_x]_x + [\varphi_y]_y + [\varphi_z]_z = 0 \quad (2.64)$$

which is valid for subcritical flow about slender bodies and thin wings of arbitrary planform at arbitrary subsonic (or supersonic) free stream Mach numbers. The meaning of this is that TSP theory can also be considered as an extended form of first order accurate subsonic (or supersonic) small perturbation theory with certain non-linear terms added in order to model shock waves. Which terms exactly are added determines how well shock waves are modelled. As shown by Van der Vooren et al²⁴ (see also section 2.2), equation (2.54) is particularly suitable in this respect. Second order accuracy is obtained only in the special asymptotic conditions mentioned above.

Boundary conditions

Surface boundary conditions to the TSP equations may be derived from those of full potential theory according to two different viewpoints. The conventional way is to start out from the velocity boundary condition (2.40) leading to (2.49). With the stretching (2.51) this gives

$$\begin{aligned} \varphi_z &= \delta f_x + \varphi_x \delta f_x + O[\delta^{7/3}] \quad \text{on } S(x,y,0) \\ [\delta] \quad [\delta] \quad [\delta^{5/3}] \end{aligned} \quad (2.65)$$

which is a correct wing boundary condition to the Guderley-Von Karman (2.53) and the related TSP equation (2.52).

The corresponding boundary condition for a slender body can be written as

$$\begin{aligned} n_x + \varphi_x n_x + \varphi_y n_y + \varphi_z n_z &= 0 \quad \text{on } S(x,y,z) \\ [\delta] \quad [\delta^{5/3}] \quad [\delta] \quad [\delta] \end{aligned} \quad (2.66)$$

which is, of course, identical with the exact boundary condition for bodies.

Since all terms in (2.52/53) are $O[\delta^{4/3}]$, it can also be argued that the lowest order approximations

$$\varphi_z = \delta f_x \quad \text{on } S(x,y,0) \quad (2.67)$$

for wings and

$$n_x + \varphi n_y + \varphi_z n_z = 0 + O[\delta^{5/3}] \quad \text{on} \quad S(x,y,z) \quad (2.68)$$

for slender bodies are sufficient. The latter is also true if TSP theory is viewed as an extended form of first order subsonic small disturbance theory.

Adopting the stretching (2.51) for the z coordinate only, (2.49) takes the form

$$\varphi_z = \delta f_x + \varphi_x \delta f_x + \varphi_y \delta f_y + O[\delta^{7/3}] \quad S(x,y,0) \quad (2.69)$$

$$[\delta] \quad [\delta] \quad [\delta^{5/3}] \quad [\delta^{5/3}]$$

which represents a boundary condition to the NASA Ames (2.58) and NLR (2.54) equations. However, here also it can be argued that the simpler form (2.67) is sufficient.

The wing surface boundary condition corresponding to the general second order accurate conservation form (2.59) is

$$\varphi_z + \delta f_{zz} = \delta f_x + \varphi_x \delta f_x + \varphi_y \delta f_y + O[\delta^3] \quad \text{on} \quad S(x,y,0) \quad (2.70)$$

$$[\delta] \quad [\delta^2] \quad [\delta] \quad [\delta^2] \quad [\delta^2]$$

Note that the RAE equation (2.61/62) would also require this boundary condition, which then, because of (2.60), could be reduced to

$$\varphi_z = \delta f_x + \varphi_x \delta f_x + (\varphi_y \delta f)_y + O[\delta^3] \quad (2.71)$$

The viewpoint can be taken (Brune and Rubbert⁴⁷, W. Schmidt³³) that it is the normal component of the mass flux vector ρq rather than the normal component of the velocity vector that should vanish at the surface. The two formulations are completely equivalent in full potential theory but not in small perturbation theory. The point may be illustrated by substituting the series expansion (2.50) for the mass flux vector components into the mass flux form

$$\overline{\rho q} \cdot \bar{n} = 0 \quad \text{on} \quad S(x,y,z) \quad (2.72)$$

of the wing surface boundary condition, which leads to

$$\left[1 + (1-M_\infty^2)\varphi_x - \frac{3-(2-\gamma)M_\infty^2}{2} M_\infty^2 \varphi_x^2 - \frac{1}{2} M_\infty^2 \varphi_y^2 - \frac{1}{2} M_\infty^2 \varphi_z^2 + \dots \right] n_x +$$

$$+ [\varphi_y - M_\infty^2 \varphi_x \varphi_y + \dots] n_y + [\varphi_z - M_\infty^2 \varphi_x \varphi_z + \dots] n_z = 0 \quad \text{on} \quad S(x,y,0) \quad (2.73)$$

In constructing further approximations to (2.73) Schmidt³³ does not make use of the argument that in small perturbation theory n_x and n_y are $O[\delta]$ on wings; n_z being $O[1]$. If we do use this knowledge, equation (2.73) can, with the stretching (2.51) and the assumption that $1-M_\infty^2 = O[\delta^{2/3}]$, and using (2.48), be reduced to

$$\varphi_z - M_\infty^2 \varphi_x \varphi_z = \delta f_x + O[\delta^{7/3}] \quad \text{on} \quad S(x,y,0) \quad (2.74)$$

$$[\delta] \quad [\delta^{5/3}] \quad [\delta]$$

The corresponding boundary condition for a (slender) body is:

$$n_x + (1-M_\infty^2)\varphi_x n_y + (1-M_\infty^2)\varphi_x n_z = O[\delta^{7/3}] \quad \text{on} \quad S(x,y,z) \quad (2.75)$$

$$[\delta] \quad [\delta] + [\delta^{5/3}] \quad [\delta] + [\delta^{5/3}]$$

Equation (2.74) is to be compared with (2.65). Note that they are identical to $O[\delta]$ but that the terms of $O[\delta^{5/3}]$ differ. As boundary conditions to (2.52) equations (2.74/75) are to be preferred over (2.65/66) because they are consistent with a (mass) conservative formulation. However, it can, again, be argued that the simple forms (2.67/68) are sufficient.

From equation (2.73) the corresponding (wing) boundary condition to the NLR and NASA Ames equation (2.54), (2.58) is found as

$$(1-M_\infty^2)\varphi_z = \delta f_x + (1-M_\infty^2)\varphi_x \delta f_x + \varphi_y \delta f_y + O[\delta^{7/3}] \quad \text{on} \quad S(x,y,0) \quad (2.76)$$

$$[\delta] + [\delta^{5/3}] \quad [\delta] \quad [\delta^{5/3}] \quad [\delta^{5/3}]$$

which is to be compared with (2.69). Recalling that equation (2.54) can be derived only for conditions approaching those of an infinite yawed wing, i.e.

$$\varphi_y = -\varphi_x \tan \Lambda + O[\delta^{4/3}] \quad (2.77)$$

and

$$f_y = -f_x \tan \Lambda + O[\delta^{2/3}] \quad (2.78)$$

at free stream Mach numbers satisfying

$$1-M_\infty^2 + \tan^2 \Lambda = O[\delta^{2/3}] \quad (2.79)$$

(see (2.57)), we have

$$(1-M_\infty^2)\varphi_x \delta f_x + \varphi_y \delta f_y = -\tan^2 \Lambda \varphi_x \delta f_x + \tan^2 \Lambda \varphi_x \delta f_x + O[\delta^{7/3}] = 0 + O[\delta^{7/3}] \quad (2.80)$$

Hence, (2.76) reduces to the same form (2.74) (or (2.67) if the lowest order approximation is adopted) as the boundary condition to the Guderley-Von Karman type equation. Using similar arguments it is also possible to derive the "mass flux" equivalent forms of the boundary conditions (2.70) and (2.71) to the general second order and RAE equations.

The main limitation of TSP theory, i.e. the singular behaviour of the solution at blunt leading edges is readily apparent from, e.g., equation (2.67) or (2.73); at the leading edge for $x \rightarrow x_{le}$ we have $f_x \rightarrow \infty$ and hence $\varphi_z \rightarrow \infty$, violating the small perturbation assumption. Note that this is not a typical transonic problem; it is also present in subsonic thin airfoil theory.

Several ways are mentioned in the literature to reduce the problem in actual numerical calculations. Amongst these are:

- longitudinal positioning of the leading-edge between mesh points⁴⁰
- vertical positioning of the wing mean plane ($z = 0$) in between mesh planes while determining φ in $z = 0$ through extrapolation from the first mesh lines above and below $z = 0$ ^{28,43,41,44}
- empirical "tuning" of mesh spacing near the leading edge⁵²
- empirical modification of section leading edge geometry^{53,54}.

However, none of these "recipes" seems fully satisfactory.

With (2.39) the boundary conditions in the plane $z = 0$ representing the trailing vortex sheet and the Kutta condition are rapidly found from (2.41/42), i.e.

$$[\varphi_z] = 0 \quad \text{on} \quad S_w(x, y, 0) \quad (2.81)$$

$$[\varphi] = [\varphi]_{te} = \Gamma(y) \quad \text{on} \quad S_w(x, y, 0) \quad (2.82)$$

At infinity we have

$$\varphi \rightarrow 0 \quad \text{for} \quad x^2 + y^2 + z^2 \rightarrow 0 \quad (2.83)$$

except in the Trefftz-plane where φ must satisfy the Laplace equation for two-dimensional flow around the trailing vortex sheet

$$\varphi_{yy} + \varphi_{zz} = 0 \quad \text{for} \quad x \rightarrow +\infty \quad (2.84)$$

In the literature two alternative approaches to the problem of satisfying the boundary conditions at infinity may be found. One is to reduce the infinitely large physical space to a finite computational domain by means of relatively simple coordinate stretchings^{35,40,46}. The other is to position the outer boundary of the computational domain at a large, but finite distance from the wing or body in the physical space and apply so-called far field boundary conditions at this outer boundary^{36,39,41}. These far field boundary conditions, derived from subsonic theory, can be either analytic or numerical. Analytical expressions for the potential in the far field at an asymptotically large distance from the configuration have been given by Klunker⁴⁸. Chen et al⁴⁹ use a numerical (panel) method to solve a reduced, linear equation (Prandtl-Glauert) in the far field.

Pressure formulae

The conventional way of obtaining "consistent" formulae for the pressure is to expand the expression (2.21) for the pressure coefficient into a power series which is then truncated appropriately. With the stretching (2.51) and $1-M_\infty^2 = O[\delta^{2/3}]$ this leads to

$$C_p = -2 \varphi_x + O[\delta^2] \quad (2.85)$$

as a pressure formula to the Guderley-Von Karman type equations (2.52/53). For the NLR/NASA Ames type equations (2.54/58), with z -stretching only and $1-M_\infty^2 = O[1]$ it leads to

$$C_p = -2 \varphi_x - (1-M_\infty^2) \varphi_x^2 + \varphi_y^2 + O[\delta^2] \quad (2.86)$$

$[\delta^{2/3}] \quad [\delta^{4/3}] \quad [\delta^{4/3}]$

which, because of (2.77), (2.79) also reduces to (2.85).

The corresponding expression to the general second order accurate equation (2.59) is

$$C_p = -2 \varphi_x - (1-M_\infty^2) \varphi_x^2 - \varphi_y^2 - \varphi_z^2 + O[\delta^3] \quad (2.87)$$

$[\delta] \quad [\delta^2] \quad [\delta^2] \quad [\delta^2]$

For $1-M_\infty^2 = O[\delta]$, (RAE equation (2.61/62)), this reduces to

$$C_p = -2 \varphi_x - \varphi_x^2 - \varphi_y^2 + O[\delta^3] \quad (2.88)$$

Schmidt³³ has proposed that the pressure (coefficient) be computed by substituting the approximation (2.50) for the mass flux into a (non-conservative) form of the momentum equation. This procedure leads to additional higher order terms in the expression for C_p , that, however, cannot be justified on the basis of asymptotic arguments.

2.2 The representations of shock waves

A most important aspect of computational models for transonic flow is the ability (or inability) to model shock waves adequately. In this respect it is useful, when considering a computational model for transonic flow, to distinguish between the following questions:

- i) what type of shock waves (normal, oblique, weak, strong) must be represented by the model partial differential equation (PDE)?
- ii) how well are shock waves represented?

The answer to the first question is determined primarily by the type of flow problem that must be solved. The answer to the second question is determined by the type of equation solved (TSP, FP, Euler) and also by numerical aspects.

2.2.1 Shock systems on wings in transonic flow; jump relations

The systems of shock waves that may occur on wings in transonic flow have been described by, e.g., Rogers et al⁵⁰ and Haines⁵¹. Figure 2.3 shows, schematically, the shock system that occurs most frequently on transonic wings. Three types of shock wave may be distinguished.

- i) outboard shock; a "strong" (supersonic \rightarrow subsonic) shock of the type that occurs on an infinite yawned wing
- ii) forward shock; a "weak" (supersonic \rightarrow supersonic) shock, with, approximately, infinite yawned wing

- conditions upstream and flow parallel to the plane of symmetry (or body side) downstream
 iii) rear shock; a "strong", normal shock that is also approximately normal to the free stream direction (a special case of i).

The suitability of the various model PDE's, mentioned in the preceding section, in representing these types of shock waves can be judged by considering the various jump relations. Since each of the model PDE's can be written in the general conservation form

$$[F_1]_x + [F_2]_y + [F_3]_z = 0 \quad (2.89)$$

the jump relations can be covered by the general expression

$$[F_1]n_x + [F_2]n_y + [F_3]n_z = 0 \quad (2.90)$$

where n_x , n_y and n_z are the components of the unit normal to the shock. $F_{1,2,3}$ can be related to the conservation form of the various equations. The jump relations, in terms of the chordwise perturbation velocity, according to several model PDE's, for the three types of shocks, are compared in figure 2.4. For this purpose the essentially non-conservative Guderley-Von Karman, Bailey/Ballhaus³⁶, RAE^{35,45} and Boppe⁴⁰ TSP equations were recast in conservation form. In all cases the shock has been assumed vertical, i.e. $n_z = 0$, and ϕ_z has also been assumed zero. Figure 2.4 (see also Van der Vooren et al²⁴) illustrates that for the modeling of swept shock waves, and in particular "forward" shocks, by means of TSP theory, it is essential to include the $\phi_x\phi_{xy}$ - and $\phi_x\phi_{yy}$ - terms in the partial differential equation. It is also apparent that the use of the correct perturbation mass flux conservation form, such as equation (2.54) should be preferred.

2.2.2 Artificial viscosity and asymptotic shock layer structure

It was mentioned in section 2.1.1 that the problem of inviscid transonic flow does, in general, not have a unique solution and that, according to Lax^{6,7}, the entropy or an equivalent additional condition must be enforced to guarantee a unique and indeed the physically relevant solution, i.e. the one with compression shocks only.

One well-proven way to guarantee a unique solution is the introduction of "artificial viscosity". The artificial viscosity may either be implicit, i.e. be the result of the spatial discretization scheme chosen (Murmán/Cole²⁶ and related work) or explicit, i.e. be in the form of additional terms to the governing partial differential equation (Jameson⁵ and related work, Chattot¹³). Depending on the precise form of the artificial viscosity terms the explicit and implicit formulations may be equivalent. For example, Murman's^{26,27} upwind difference scheme is equivalent to adding a term of the type

$$-\Delta x \frac{\partial}{\partial x} [(1-M_\infty^2 - (\gamma+1)M_\infty^2\phi_x)\phi_{xx}] \quad (2.91)$$

to equation (2.53) and Jameson's²² "rotated" difference scheme is equivalent to adding a term of the type

$$-h(c^2-q^2)\phi_{ss} \quad (2.92)$$

to the full potential equation (2.33). In the last expression s is measured along streamlines and h is a small parameter that is identical with or proportional to the mesh size. The derivatives $\frac{\partial}{\partial x}$, $\frac{\partial}{\partial s}$, respectively, are usually, but not necessarily (Chattot¹³), approximated by means of upwind differences. The effect of adding artificial viscosity to the partial differential equation is not limited to eliminating expansion shocks from the solutions. It also changes the type of the PDE from mixed elliptic/hyperbolic to parabolic-like²⁷. As a result shock waves are represented by (thin) layers with high velocity and pressure gradients rather than discontinuities.

Considerable insight in the relation between artificial viscosity and shock layer characteristics can be obtained by means of asymptotic analysis, yielding analytical solutions for the velocity profile inside the shock layers for vanishing mesh width^{57,58}. Figure 2.5 presents normalized asymptotic shock layer solutions for a normal shock and a 45° weak oblique shock according to the Murman/Jameson type of artificial viscosity. A remarkable feature of this type of artificial viscosity is that for supersonic + subsonic shocks the asymptotic shock layer solution does not exist downstream of the shock. It suggests that this type of artificial viscosity must be switched off in the subsonic part of the flow field, which is exactly what is being done in the current finite difference methods. Note also that, in case of the normal shock, 90 % of the shock jump is "smeared" over about 3 meshes while, in agreement with finite difference experience²⁷, the swept shock takes 10 or more meshes. As a consequence (weak) oblique shocks, as such, are difficult to recognize in results of the current computational methods for transonic flow.

As will be discussed in more detail in chapter 6, variants of the artificial viscosity concept as applied to the conservation form of the full potential equation, known as artificial density or artificial compressibility methods, have been developed in recent years. From a computational point of view the artificial density methods have certain advantages. However, the shock layer characteristics are essentially the same as those of the Murman/Jameson type of artificial viscosity. For an excellent treatise of the subject the reader is referred to Hafez et al⁵⁹.

2.2.3 Conservative versus non-conservative formulations

As mentioned already in section 2.1.1, Lax⁶ has shown that (hyperbolic) partial differential equations must be discretized in conservation form in order to obtain the correct shock jump in the case of vanishing discretization error. For transonic flow computations, in which artificial viscosity is added in the supersonic part of the flow field only, this means that both the basic partial differential equation and the added artificial viscosity terms must be discretized in conservation, i.e. divergence form (Jameson^{21,55,56,60}). For example, one should add a term of the type

$$-\frac{\partial}{\partial s} [u h(c^2-q^2)\phi_{ss}] \quad (2.93)$$

rather than (2.92), where u is a switching parameter having the value 1 in the supersonic part of the flow field and 0 in the subsonic part.

When applied in finite difference approximations such a scheme can be shown to lead to difference operators that are equivalent with Murman's¹¹ parabolic and shock-point operators at the sonic line (2D) or sonic surface (3D) where u switches from 0 to 1 or vice-versa.

In the literature one can also find formulations in which the artificial viscosity is added in divergence form but the basic partial differential equation is discretized in a non-conservative form, such as the quasi-linear form (Bauer et al.⁶², Caughey and Jameson^{15,63}). It can be shown⁶³, that the jump relations implied by such formulations are not unique (even for vanishing mesh width) but depend on the precise location of the finite difference mesh relative to the shock position. However, as illustrated by figure 2.6 for a one-dimensional full potential flow model, the possible discrepancy with respect to the correct, fully conservative result is small, in particular for $M \leq 1.3$.

The mesh-dependence of the shock jump relation is rather dramatic when neither the basic PDE nor the artificial viscosity are discretized in conservation form. As illustrated by figure 2.6 the numerical (finite difference) solution may then range anywhere between sonic velocity just downstream of the shock and the correct value, depending on the precise position of the shock relative to the finite difference mesh. The situation is a result of the fact that mass is not conserved across shock waves, leading to spurious sources along the shock. A similar situation can be shown to exist for non-conservative TSP formulations. Although such mesh dependence is clearly very unsatisfactory if not unacceptable from a computational fluid dynamicist's point of view, the situation, for the applied aerodynamicist, is somewhat confusing because of the fortuitous circumstance that in practice the results of non-conservative inviscid flow computations are generally in better agreement with experimental results than those of quasi- or fully conservative schemes. The reason is that both the spurious sources introduced by the non-conservative schemes as well as viscous (shock-boundary layer) interactions tend to reduce the shock strength relative to the correct inviscid flow value^{44,64}. However, the mechanisms are totally different. As discussed in more detail in chapter 4, improvement of results due to (proper) addition of viscous effects (displacement thickness) via the airfoil or wing and wake boundary conditions may be expected for conservative schemes only.

With the objective of obtaining shock velocity and pressure jumps that are in better agreement with the Rankine-Hugoniot relations yet another formulation has been devised by Collyer and Lock⁶⁵. In their "partially conservative" scheme Collyer and Lock take a weighted average of the non-conservative and the quasi-conservative difference operators at the shock. Although the mesh dependence of the solution has been reduced as compared with the non-conservative scheme (Fig. 2.6) the scheme can still be criticized for not converging to a unique solution in the limit of vanishing mesh size.

2.3 Drag

While the capabilities of computational methods for transonic flow with respect to the prediction of lift and pitching moment are seldom questioned a controversial subject in (approximate) transonic flow calculations has been the subject of drag^{66,10,5}. Because the prediction of drag is an important item of airplane design and analysis it seems appropriate to pay some attention to the (potential) capabilities of the current computational models for transonic flow.

In inviscid flow, the drag of a body consists of induced (or vortex) drag and wave drag only, both constituents being felt in the form of (normal) pressure drag (see also Fig. 2.8). This pressure drag can be determined, in principle, by integrating the streamwise component of the normal pressure force around the body, a feature contained by most computational methods for transonic flow. However, this procedure has a number of shortcomings. First of all it is generally difficult to perform the integration with sufficient accuracy, unless a very large number of mesh points is used^{10,67}. Secondly, by evaluation of the pressure integral only, it is impossible to distinguish between wave drag and induced (vortex) drag, which is highly desirable from an applied aerodynamicist's point of view.

Separate evaluation of the pressure drag contributions is possible by applying the momentum conservation theorem to contours of the type sketched in figure 2.7^{10,5,67}. For the x-component of momentum this leads to

$$\oint_S [p n_x + (\bar{\rho} \bar{q} \cdot \bar{n}) u] dS = 0 \quad (2.94)$$

or, since, in inviscid flow,

$$\oint_{S_B} [p n_x + (\bar{\rho} \bar{q} \cdot \bar{n}) u] dS_B = D \quad (2.95)$$

to

$$D = - \int_{S_{\text{shock}}} [p_{n_1} + (\bar{\rho} \bar{q} \cdot \bar{n}_1) u]_2^1 dS_{\text{shock}} - \int_{S_{\text{wake}}} [p_{n_1} + (\bar{\rho} \bar{q} \cdot \bar{n}_1) u]_2^1 dS_{\text{wake}} + \oint_{S_{(\infty)}} [p n_x + (\bar{\rho} \bar{q} \cdot \bar{n}) u] dS_{(\infty)} \quad (2.96)$$

Note that these expressions are equally valid for full inviscid (Euler), full potential or transonic small perturbation theory. In the former two we have

$$\bar{\rho} \bar{q} \cdot \bar{n} = 0 \quad \text{on } S_B \quad (2.97)$$

because of the boundary condition, so that only the pressure integral contributes to D. In the TSP case with planar boundary conditions we have

$$\text{and } \left. \begin{array}{l} n_x = 0 \\ \bar{\rho} \bar{q} \cdot \bar{n} = -\delta f_x \end{array} \right\} \text{ on } z = \pm 0 \quad (2.98)$$

where \bar{n} is now the (inward) normal to the plane $z = 0$.

In inviscid flow (without boundary layer modeling) the 2nd integral in (2.96) is always zero. The first integral is zero in the case of the exact equations of inviscid motion (Euler equations, conservation of momentum) but it constitutes the wave drag in potential flow^{10,5}. If required it can be rewritten

in terms involving only the direction cosine and flow quantities just upstream of the shock⁵.

The third integral in (2.96) is most easily interpreted in the limit that the contour of integration $S_{(\infty)}$ is at an infinitely large distance from the body. In that case, for subsonic free stream Mach numbers, only the part of $S_{(\infty)}$ at $x = +\infty$ (Trefftz plane) contributes to the integral (if the latter is expressed in terms of differential quantities, relative to the free stream). I.e.

$$-\oint_{S_{(\infty)}} [\rho n_x + (\rho q \cdot \vec{n})u] dS_{(\infty)} = - \iint_{x=+\infty} [(p-p_\infty) + (\rho u^2 - p_\infty u_\infty^2)] dy dz \quad (2.99)$$

In potential flow, with or without shock waves, this integral contains only the induced or vortex drag and can, upon certain approximating assumptions, be reduced to^{3,67}

$$\int_{S_{(\infty)}} = - \int_{S_{\text{wake}}} [\phi] \cdot \vec{n} dy = D_i \quad (2.100)$$

When shock waves are present in inviscid rotational flow (Euler equations) the integral over $S_{(\infty)}$ also contains the wave drag associated with the loss in total pressure and increase in entropy across the shock wave(s). The wave drag can also be expressed in terms of an integral over the shock surface involving the jump in entropy across the shock¹⁰ or flow quantities just upstream of the shock only⁵. In practice, evaluation of the (approximate) vortex drag integral (2.100) does not pose large difficulties. More problematic is the determination of wave drag through integration along the shock surface, in particular in situations with complex shock patterns involving weak supersonic \rightarrow supersonic shocks⁶⁷. The difficulties involve shock detection as well as the determination of the jumps, both being hampered by the fact that, due to the artificial viscosity, the shocks are smeared over several mesh widths.

Given the situation just sketched, the most convenient way to distinguish the inviscid pressure drag between vortex and wave drag is to determine the vortex drag by means of Trefftz-plane integration and the total inviscid drag by means of body contour integration. Provided the latter can be performed with sufficient accuracy, this procedure should, through subtraction of the vortex drag, provide a reasonable estimate of the wave drag.

It should be mentioned that the analysis given above holds only for fully conservative formulations. The spurious mass sources at the shock surfaces in non-conservative formulations affect the first as well as the third integral in (2.96). Because mass is not conserved across shocks, ρq , in the first integral, jumps in a non-conservative formulation, whereas it is continuous in a conservative formulation. The third integral, over $S_{(\infty)}$ contains a contribution, associated with the fact that

$$\oint_{S_{(\infty)}} \vec{\rho p} \cdot \vec{n} dS_{(\infty)} \neq 0 \quad (2.101)$$

in a non-conservative formulation, whereas it is zero in a properly conservative formulation.

Bauer et al.^{61,68} state that, in a non-conservative formulation, the drag as obtained by means of body surface pressure integration should be corrected for the mass generated at the shock by a term of the type (2.101). This statement is hardly relevant for two reasons. Firstly, because their conclusion is based on consideration of a path of integration that does not exclude the shock wave (as it should because of the discontinuities at the shock). Secondly because in a non-conservative formulation the shock jump (and hence the apparent mass production at the shock) depends on the precise position of the shock relative to the mesh-points. As a result the wave drag in a non-conservative formulation is also non-unique and mesh-dependent.

When the effect of the boundary layer is modelled (chapter 4) the drag integrals (2.95/96) contain additional contributions. Considering first the body integral (2.95) we now have the situation that, with the effect of the boundary layer represented, e.g. through "surface transpiration", we have⁶⁹

$$\vec{\rho q} \cdot \vec{n} = - \frac{d}{ds} (\rho_e U_e \delta^*) \text{ in 2-d flow } \neq 0 \text{ on } S_B \quad (2.102)$$

Hence, the second part of the body drag integral (2.95) is now different from zero and indeed negative, illustrating the fact that viscous drag cannot be modelled in potential flow. Note, however, that it can be related to the friction drag by applying the momentum theorem (for viscous flow) to the boundary layer. The friction drag itself can, of course, be determined by integrating the friction forces from the boundary layer calculations. The pressure part of the body integral now also contains the "viscous" pressure drag, as well as the vortex drag and wave drag (Fig. 2.8).

Turning to the control surface integral (2.96) we have the situation that, with boundary layers, the second integral is now different from zero, because, due to the displacement thickness of the wake, $[\rho q \cdot \vec{n}]_{\text{wake}} \neq 0$. The third integral of (2.96) also contains an additional contribution because, for non-zero displacement thickness at infinity downstream, (2.101) holds.

Because the viscous pressure drag (pressure part of the drag due to boundary layers) cannot be related simply to one of the integrals of (2.96) it is seldom evaluated explicitly. Nevertheless it is often instructive in drag analysis to distinguish this part of drag from the other components. This can be done by determining the total viscous drag through boundary layer and (viscous) wake momentum deficit considerations (Squire and Young and related methods) and subtracting the friction drag. Note that the determination along these lines of the viscous pressure drag is a prerequisite if the wave drag is to be determined without integration of the jump in momentum (or entropy) along the shock surfaces. The wave drag can then be obtained by subtracting both the vortex drag and the viscous pressure drag from the total pressure drag.

For completeness a chart of the various drag components is given in figure 2.8. Because of the uncertainties and inaccuracies involved with determining the various drag components it is advisable to use as many different ways as possible. Cross-checking of results obtained along different lines provides a means for obtaining an impression of the accuracy.

The general experience in computational drag determination seems to be that the pressure drag integration is seldom performed with sufficient accuracy. This is particularly true for swept wings, where the net pressure drag is the result of a large pressure drag at the root and a thrust at the tip⁷⁰. For the reasons just mentioned computational determination of the absolute drag level is beyond the present state-of-the-art in computational fluid dynamics. However, the determination of drag increments due to (small?) changes in flow conditions and/or configuration would seem to be possible with sufficient accuracy.

2.4 References

1. Liepmann, H.W., and Roshko, A., Elements of gas dynamics, John Wiley & Sons, Inc., N.Y., 1966.
2. Kordulla, Wilhelm, Calculation of 3-D transonic flows-survey of recent developments including viscous flows, VKI Lecture series 1980-6, March 1980.
3. Ashley, H., and Landahl, M.T., Aerodynamics of wings and bodies, Addison-Wesley Publishing Company, Inc., Reading, Mass., 1965.
4. Mangler, K.W., and Smith, J.H.B., Behaviour of the vortex sheet at the trailing edge of a lifting wing, RAE TR 69049, 1969.
5. Van der Vooren, J., and Slooff, J.W., On isentropic flow models used for finite difference calculations of two-dimensional transonic flows with embedded shocks around airfoils, NLR MP 73024 U, 1973.
6. Lax, P., Weak solutions of non-linear hyperbolic equations and their numerical calculation, Comm. P. and Appl. Math., Vol. VII, 1954.
7. Lax, P., and Wendroff, B., Systems of conservation laws, Comm. P. and Appl. Math. Vol. XIII, 1960, pp. 217-237.
8. Magnus, R., Gallaher, W., and Yoshihara, H., Inviscid supercritical airfoil theory, AGARD CP No.55, 1968.
9. Rizzi, A., editor, GAMM-Workshop on numerical methods for the computation of inviscid transonic flow with shock waves, Stockholm, Sept. 1979. Proceedings to appear in series Notes on numerical fluid dynamics, Vieweg Verlag, Braunschweig.
10. Steger, Joseph L., and Baldwin, Barrett S., Shock waves and drag in the numerical calculation of isentropic transonic flow, NASA TN D-6997, 1972.
11. Viviani, Henri, Formes conservatives des equations de la dynamique des gaz, La Recherche Aérospatiale, 1974-1, p. 65-68.
12. Avis, Rutherford, Vectors, tensors, and the basic equations of fluid mechanics, Prentice-Hall, Inc., N.J. 1962.
13. Chattot, J.J., Coulombeix, C., and da Silva Tomé, C., Calculs d'écoulements transsonique autours d'ailes, La Rech. Aerosp., 1978-4, p. 143-159.
14. Chattot, J.J., and Coulombeix, C., Relaxation method for the full potential equation, ONERA T.P. No.1979-154.
15. Caughey, D.A., and Jameson, A., Numerical calculation of transonic potential flow about wing-body combinations, AIAA Paper 77-677, 1977, AIAA J., Vol. 17, No.2, 1979, pp. 175-181.
16. Mangler, K.W., and Murray, J.C., Systems of coordinates suitable for the numerical calculation of three-dimensional flow fields, RAE TR 73074, 1973.
17. Forsey, C.R., and Carr, M.P., The calculation of transonic flow over three-dimensional swept wings using the exact potential equation. Paper presented at DGLR/GARTEUR 6 Symposium on "Transonic configurations", Bad Harzburg, West Germany, 1978. ARA Memo No.207.
18. Jameson, A., and Caughey, D.A., Numerical calculation of the flow past a swept wing, N.Y. Univ. ERDA Report COO-3077-140, 1977.
19. Steger, J.L., and Lomax, H., Transonic flow about two-dimensional airfoils by relaxation procedures, AIAA Paper 71-569, 1971.
20. Garabedian, P.R., and Korn, D.G., Analysis of transonic airfoils, Comm. P. & Appl. Math., Vol. 24, pp. 841-851, 1971.
21. Jameson, Antony, Transonic flow calculations for airfoils and bodies of revolution, Grumman Aerodynamics Report 391-71-1, 1971.
22. Jameson, Antony, Iterative solution of transonic flows over airfoils and wings, including flows at Mach 1, Comm. P. & Appl. Math., Vol. 27 (1974), pp. 283-309.
23. Jameson, Antony, Transonic flow calculations, VKI Lecture series No.87, 1976.
24. Van der Vooren, J., Slooff, J.W., Huizing, G.H., and van Essen, A., Remarks on the suitability of various transonic small perturbation equations to describe three-dimensional transonic flow-examples of computations using a fully conservative rotated difference scheme, In: Symposium transonicum II (1975), Springer-Verlag, 1976.
25. Spreiter, John R., On the application of transonic similarity rules to wings of finite span, NACA Report 1153, 1953.
26. Murman, E.M., and Cole, J.D., Calculation of plane steady transonic flows, AIAA Paper 70-188, AIAA Journal, Vol. 9, No.1, 1971, pp. 114-121.
27. Murman, E.M., and Krupp, J.A., Solution of the transonic potential equation using a mixed finite difference system, 2nd Int. Symp. Num. Math. Fl. Dyn., Sept. 70, Berkeley. In: Lecture Notes in Physics, Vol. 8, Springer-Verlag, 1971, pp. 199-206.
28. Krupp, J.A., and Murman, E.M., The numerical calculation of steady transonic flows past thin lifting airfoils and slender bodies, AIAA Paper 71-566, 1971, AIAA J. 10,7, pp. 880-886, 1972.
29. Bailey, F.R., Numerical calculation of transonic flow about slender bodies of revolution, NASA TN D-6582, 1971.
30. Bailey, F.R., and Steger, J.L., Relaxation techniques for three-dimensional transonic flow about wings, AIAA Paper 72-189, 1972.
31. Ballhaus, W.F., and Bailey, F.R., Numerical calculations of transonic flow about swept wings, AIAA Paper 72-677, 1972.
32. Newman, P.A., and Klunker, F.B., Computation of transonic flow about finite lifting wings, AIAA Journal, Vol. 10, No.7, 1972, pp. 971-973.
33. Schmidt, W., A self-consistent formulation of the transonic small disturbance theory. In: Recent developments in theoretical and experimental fluid mechanics, Springer Verlag, 1979.
34. Lomax, H., Bailey, F.R., and Ballhaus, W.F., On the numerical simulation of three-dimensional transonic flow with application to the C-141 wing, NASA TN D-6933, 1973.
35. Albone, C.M., Hall, M.G., Joyce, G., Numerical solution of flows past wing-body combinations. In: Symposium transonicum II (Göttingen, 1975), Springer-Verlag, 1976.
36. Ballhaus, W.F., Bailey, F.R., and Frick, J., Improved computational treatment of transonic flow about swept wings. In: Advances in engineering science, Vol. 4, NASA CP-2001, 1976.
37. Ward, G.N., Linearized theory of steady high-speed flow, Cambridge University Press, 1955.
38. Hall, M.G., and Firmin, M.C.P., Recent developments in methods for calculating transonic flows over wings, ICAS Paper 74-18, 1974.
39. Klunker, E.B., and Newman, P.A., Computation of transonic flow about lifting wing-cylinder combinations, J. Aircraft, Vol. II, 1974, pp. 254-256.

40. Boppe, Charles W., Calculations of transonic wing flows by grid embedding, AIAA Paper 77-207, 1977.
41. Schmidt, W., and Vanino, R., The analysis of arbitrary wing-body combinations in transonic flow using a relaxation method. In: Symposium transonicum II (Göttingen 1975), Springer-Verlag 1976.
42. Schmidt, W., and Hedman, S., Recent explorations in relaxation methods for three-dimensional transonic potential flow, ICAS Paper 76-22, 1976.
43. Krupp, J.A., The numerical calculation of plane steady transonic flows past lifting aerofoils, Boeing Sc. Res. Lab. Report D 180-12958-1, 1971.
44. Bailey, F.R., and Ballhaus, W.F., Comparison of computed and experimental pressures for transonic flows about isolated wings and wing-fuselage configuration, NASA SP-347, 1975.
45. Lock, R.C., Research in the UK on finite difference methods for computing steady transonic flows. In: Symposium transonicum II (Göttingen 1975), Springer-Verlag, 1976.
46. Van der Vooren, J., Huizing, G.H., and Van Essen, A., A finite difference method for the calculation of transonic flow about a wing based on small-perturbation theory, NLR TR 81031 U, 1981.
47. Brune, Guenter W., and Rubbert, Paul E., Boundary-value problem of configurations with compressible free vortex flow, AIAA Journal, Vol. 15, No. 10, pp. 1521-1523, October 1977.
48. Klunker, E.B., Contribution to methods for calculating the flow about thin lifting wings at transonic speeds-analytical expression for the far field, NASA TN D-6530, 1971.
49. Chen, A.W., Dickson, L.J., and Rubbert, P.E., A far-field matching method for transonic computations, AIAA Paper 77-208, 1977.
50. Berry, C.J., Rogers, E.W.E., and Townsend, J.E.G., A study of the effects of leading-edge modifications on the flow over a 55° swept back wing at transonic speeds, ARC 21.987, 1960.
51. Haines, A.B., Recent research into some aerodynamic design problems of subsonic transport aircraft, ICAS Paper 68-10, 1968.
52. Yoshihara, H., Fixes to the 3D transonic small disturbance theory, Convair Rept. CASED-ERR-75-012, 1976.
53. Albone, C.M., Further improvements in the solution of the small-perturbation equation for flow past a lifting aerofoil, RAE TR 75101, 1975.
54. Yoshihara, H., Interplay of empiricism with computations, Notebook AIAA Applied computational aerodynamics study seminar, Albuquerque, 1977.
55. Jameson, Antony, Transonic potential flow calculations using conservation form, Proceedings 2nd AIAA Conference on Computational fluid dynamics, Hartford, 1975, pp. 148-161.
56. Jameson, Antony, Transonic relaxation methods, Notebook AIAA Applied computational aerodynamics study seminar, Albuquerque, 1977.
57. Piers, W.J., and Slooff, J.W., Calculation of transonic flow by means of a shock-capturing field panel method, Proc. 4th AIAA Conf. on Computational fluid dynamics, Williamsburg, 1979, paper 79-1459.
58. Piers, W.J., NLR unpublished, 1978.
59. Hafez, M., South, J., and Murman, E.M., Artificial compressibility methods for numerical solutions of transonic full potential equation, AIAA Journal, Vol. 17, No. 8, 1979, pp. 838-844.
60. Jameson, Antony, Numerical computation of transonic flows with shock waves. In: Symposium transonicum II, (Göttingen, 1975), Springer-Verlag, 1976.
61. Murman, Earl M., Analysis of embedded shock waves calculated by relaxation methods. In: Proceedings AIAA Conf. on Computational fluid dynamics, Palm Springs, 1973, pp. 27-40.
62. Bauer, F., Garabedian, P.R., Korn, D.G., and Jameson, A., Supercritical wing sections II, Springer Verlag, N.Y., 1975.
63. Caughey, D.A., and Jameson, A., Recent progress in finite volume calculations for wing-fuselage combinations, AIAA Paper 79-1513, 1979.
64. Ballhaus, W.F., Some recent progress in transonic flow computations, VKI Lecture series 87, 1976.
65. Collyer, M.R., and Lock, R.C., Improvements to the Viscous Garabedian and Korn (VGK) method for calculating transonic flow past an aerofoil, TAE TR 78039, 1978.
66. Yoshihara, H., A survey of computational methods for 2D and 3D transonic flows with shocks, VKI Lecture series 55-6, 1973.
67. Murman, E.M., and Cole, J.D., Inviscid drag at transonic speeds, AIAA Paper 74-540, 1974.
68. Bauer, F., Garabedian, P.R., and Korn, D.G., Supercritical wing sections III, Springer Verlag, N.Y., 1977.
69. Lighthill, M.J., On displacement thickness, J. Fl. Mech. 4, p. 383, 1958.
70. Küchemann, D., The aerodynamic design of aircraft, Pergamon Press, 1978.

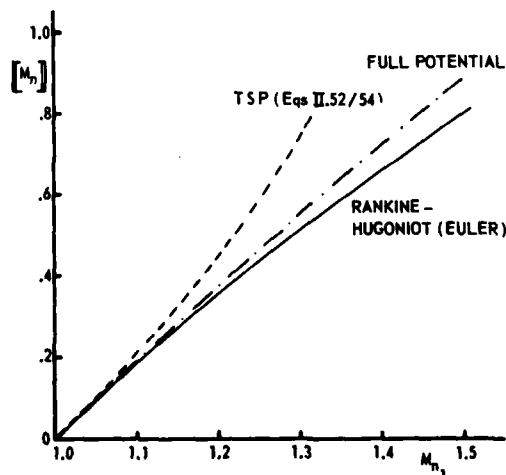


Fig. 2.1 Shock jump relations in terms of normal Mach number

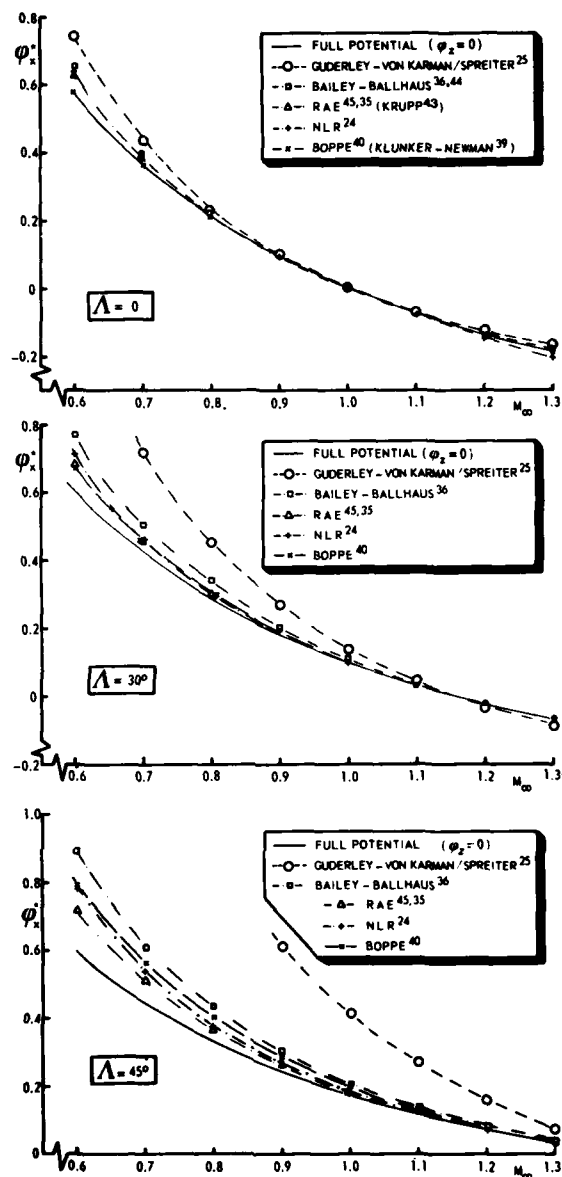


Fig. 2.2 Critical chordwise perturbation velocity on (infinite) swept wing as a function of Mach number for various TSP forms

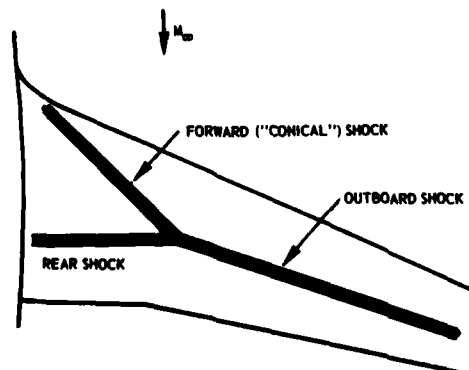


Fig. 2.3 Typical shock pattern on transonic wing

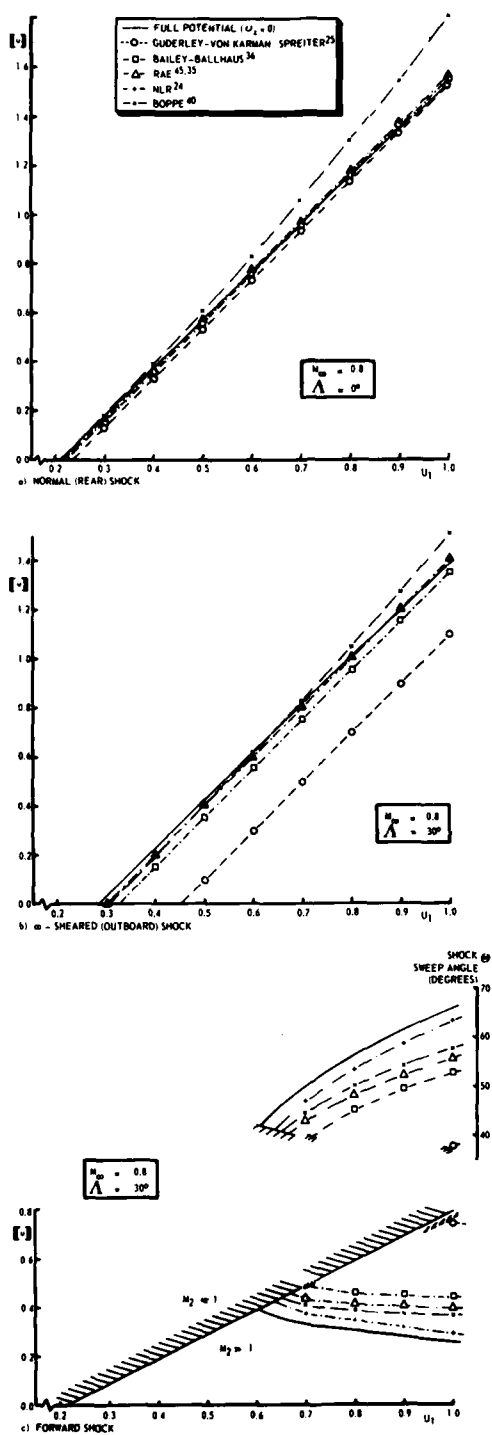


Fig. 2.4 Jump relations for shock system on a swept wing ($M_\infty = 0.8$, sweep 30°)

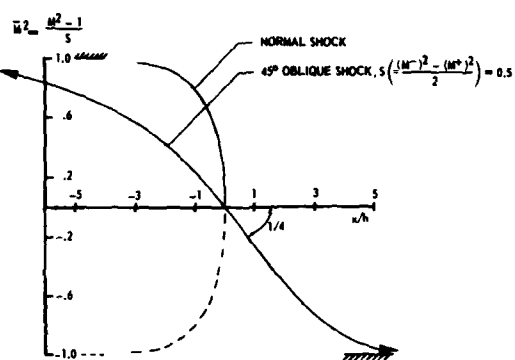


Fig. 2.5 Asymptotic shock layer solutions for Murman/Jameson type of artificial viscosity

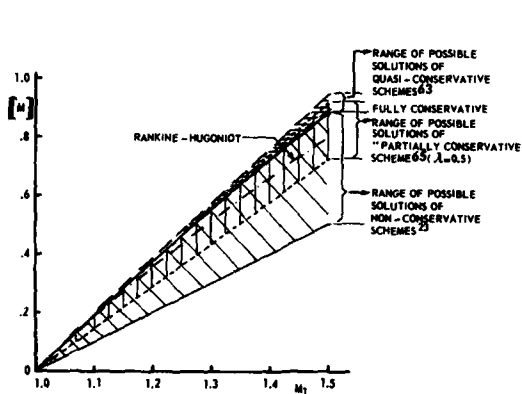


Fig. 2.6 Shock jump conditions for one-dimensional full potential flow according to conservative and non-conservative schemes

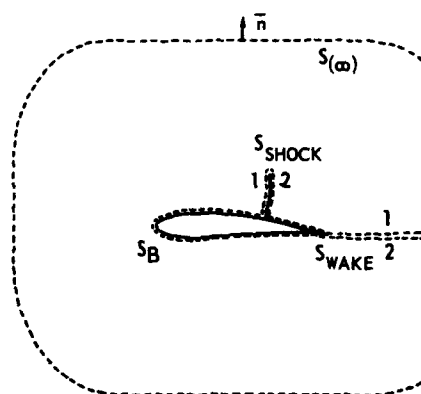


Fig. 2.7 Control surfaces for drag determination

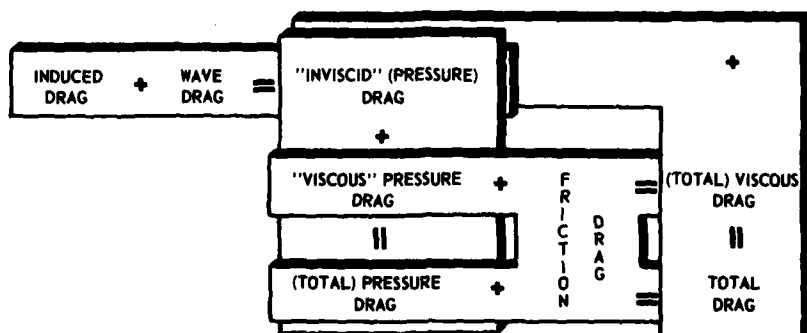


Fig. 2.8. Summary of drag components

3. EXISTING COMPUTATIONAL TRANSONIC AERODYNAMIC (CTA) METHODS

In this chapter a review of existing CTA computer codes is presented. The main emphasis is on codes which have been used extensively by many users for a wide range of applications. Therefore, codes which have been introduced recently are not discussed. Applications involving the TSP and full potential formulations (both conservative and nonconservative form) are presented. Two- and three-dimensional applications are discussed, although the emphasis will be on three dimensions. General aspects associated with transonic relaxation algorithms, including both spatial differencing and iteration scheme characteristics will be briefly outlined first. Because the vast majority of established application codes use successive-line overrelaxation (SLOR), this will be the only iteration scheme reviewed in this chapter. For more advanced solution schemes, that should see widespread use in applications in the next 3-5 years, see chapter 6 (Advanced Concepts). Additional review papers emphasizing existing computational aerodynamic methods are Hall [1], Gessow and Morris [2], da Costa [3], and Slooff [4]. For a general review of computational fluid dynamics see Chapman [5,6].

3.1 The typical transonic solution procedure

The spatial differencing schemes in existing CTA application codes typically use an idea introduced by Murman and Cole [7] for the TSP potential equation and later advanced by Steger and Lomax [8], Garabedian and Korn [9], Bailey and Steger [10], and Ballhaus and Bailey [11] for a variety of additional formulations in both two and three dimensions. The basic idea is as follows: First, determine the local flow type at each grid point, either elliptic ($M < 1$) or hyperbolic ($M > 1$), by central differencing the velocity potential. Then, at subsonic points use a standard central-difference approximation (second-order accurate). At supersonic points use an upwind-biased difference approximation (usually first-order accurate). The second-order accuracy in subsonic regions and first-order accuracy in supersonic regions are typical characteristics of most transonic difference schemes based on potential formulations. This yields an overall differencing scheme in which the computational domain of dependence simulates the physical domain of dependence. The supersonic upwind differencing scheme is usually constructed to model the original second-order-accurate central difference approximation plus an upwind-differenced artificial viscosity term. As discussed in sections 2.1.1 and 2.2.2 this artificial viscosity term is the mechanism that excludes physically incorrect expansion shocks.

For the general nonorthogonal curvilinear coordinate systems involved in airfoil and wing computations, the upwind direction may not be aligned with a particular coordinate direction or may change from one coordinate direction to another. For this situation simple schemes that upwind along only a single coordinate direction are often inadequate, especially for cases with large regions of supersonic flow. Jameson [12] first resolved this problem by introducing the concept of "rotated differencing" to solve the nonconservative full potential equation for transonic flows about swept wing geometries. This concept utilizes the ideas just discussed, namely, second-order-accurate central differencing for subsonic flow and first-order-accurate upwind differencing for supersonic flow. However, to remove the directional difficulties associated with simple supersonic differencing schemes, a coordinate invariant difference scheme was introduced. The full potential equation was transformed into a local stream and stream-normal coordinate system. At elliptic grid points ($M < 1$), standard central difference formulas were used for all derivatives. At hyperbolic grid points ($M > 1$), central difference formulas were used for all contributions to the normal coordinate derivatives and upwind difference formulas were used for all contributions to the stream coordinate derivatives. Thus, regardless of the velocity vector orientation, an upwind influence is guaranteed in supersonic regions. Use of the rotated differencing scheme greatly enhances algorithm reliability. However, several disadvantages are introduced: The rotated difference scheme, because of increased complication, is somewhat slower in convergence. The increased size of the computational module can increase shock smearing. In addition, this differencing scheme, when implemented as in reference 12, must be swept in the flow direction, a minor but often annoying problem for some applications using general curvilinear meshes.

The standard relaxation scheme used in most of the widely accepted application codes is SLOR. This iteration scheme, coupled with an appropriate spatial differencing scheme, has proved to be generally reliable in a wide variety of applications for both two- and three-dimensional transonic flows. The SLOR iteration scheme is so named because it is implicit along one coordinate direction or line (usually the direction normal to the flow direction), and explicit in the other directions. A standard SLOR scheme applied to Laplace's equation in two dimensions

$$\phi_{xx} + \phi_{yy} = 0 \quad (3.1)$$

is given by

$$\frac{\phi_{i+1,j}^n - 2\phi_{i,j}^{n+1} + \phi_{i-1,j}^{n+1}}{\Delta x^2} + \frac{\phi_{i,j+1}^{n+1} - 2\phi_{i,j}^{n+1} + \phi_{i,j-1}^{n+1}}{\Delta y^2} = 0 \quad (3.2)$$

where the i, j subscripts denote position in the finite-difference mesh and the n superscript denotes the iteration number. The $n+1$ superscript is an intermediate iteration level used to obtain the $n+1$ level by

$$\phi_{i,j}^{n+1} = \omega \phi_{i,j}^{n+1} + (1-\omega) \phi_{i,j}^n \quad (3.3)$$

where ω is a "relaxation factor". To obtain all the $n+1$ values for each $i = \text{constant}$ line requires a tridiagonal matrix inversion. Because the points along the $i-1 = \text{constant}$ line were previously computed the superscript on $\phi_{i-1,j}$ is $n+1$. For stability, ω must be between zero and two. Optimum convergence rates are achieved for values of ω near two in subsonic regions and near one in supersonic regions. Theoretically, $\omega = 2$ is optimum for subsonic regions of flow only as the mesh spacing approaches zero. Values of ω near 1.6 to 1.8 are generally used in existing application codes for subsonic regions of flow.

Successful transonic relaxation procedures generally have one additional important feature: temporal damping in the supersonic region. As shown in reference 12, explicit addition of the quantity

$$\epsilon \left(\frac{\Delta t}{\Delta x} \frac{u}{q} \phi_{xt} + \frac{v}{q} \phi_{yt} \right) \quad (3.4)$$

in supersonic regions provides a stabilizing influence to the relaxation process. The quantities, q , u and

v are the speed of the fluid, and the velocity components in the x and y directions, respectively. The time-like derivative is obtained by considering the iteration scheme to be an iteration in pseudo-time, for example,

$$\phi_{xt} \approx (\phi_{i,j}^{n+1} - \phi_{i,j}^n - \phi_{i-1,j}^{n+1} + \phi_{i-1,j}^n) \quad (3.5)$$

The parameter ϵ in expression (3.4) is a user-specified constant chosen by experience to be large enough to maintain stability but not so large as to excessively slow convergence.

A serious problem associated with the SLOR iteration scheme and often cited by active users, is slow convergence, particularly during the final stages of convergence. Because of the elliptic nature of transonic flows, each grid point must be influenced by every other grid point during convergence. With a line relaxation scheme, disturbances travel rapidly along the implicit direction but very slowly in other directions. Convergence of three dimensional solutions may take several hundred iterations and many minutes or hours of cpu time on even the fastest computers. This level of expense places, in some cases, severe restrictions on the amount such computer codes can be used. The solution to this problem is twofold: Faster, more cost effective computers and faster more efficient iteration algorithms. Various aspects of these two subjects are discussed in Chapter 6.

3.2 Existing CTA methods (two dimensions)

Many computer codes designed to solve the two-dimensional flow about airfoils or axisymmetric geometries have been developed and are currently in wide use. Some of these codes are tabulated along with important characteristics in tables 3.1 and 3.2. Table 3.1 presents a review of widely-used, two-dimensional transonic codes applied to airfoils and cascade geometries. Table 3.2 presents a review of widely-used, axisymmetric transonic codes applied to inlets and bodies. Specific references are included to allow the interested reader to easily explore more detailed aspects of each code. The transonic small perturbation (TSP) formulation and the full potential (FP) formulation in both conservative (C) and nonconservative (NC) form are all represented. Detailed discussion on the derivation of these formulations including limitations is presented in Chapter 2. These codes have been and still are used in a host of different applications including cases with viscous corrections, for supersonic free streams, with wind tunnel walls and in a variety of design or inverse modes. (For more information about design applications in transonic flow see Chapter 5.)

An indication of the type of grid generation scheme used for each code is also provided in each table. Conformal or sheared-conformal mapping procedures are most often used, followed by stretched Cartesian and numerical mapping procedures. The grid topologies are categorized (if appropriate) into one of three standard classes: O mesh, C mesh or H mesh. A sketch showing the basic features of each of these topologies for a typical airfoil geometry is shown in figure 3.1 (For more information about grid generation schemes see Sect. 6.2.)

The most common iteration scheme used by the codes presented in tables 3.1 and 3.2 is SLOR. However, some of the more advanced approximate factorization (AF), multigrid (MG), and extrapolation (EXT) schemes are also represented. (See Chapter 6 for a discussion of these more advanced algorithms.) This is to be expected, since new algorithms are often developed within two-dimensional "test-bed" codes before implementation in the more difficult three-dimensional mode.

Mesh sizes used in typical applications range from code-to-code and from case-to-case. A typical mesh consists of several thousand points with a hundred or more points to define the aerodynamic surface of interest. Computer times required by these codes to reach nominal levels of convergence (relative to the CDC 7600 computer), range from several minutes to several seconds and hence are not expensive to run.

A series of two-dimensional calculations taken from reference 37 is shown in figures 3.2 and 3.3. The nonconservative full potential code of reference 13 which includes a simple boundary layer correction, was used for these calculations (a version modified by Douglas Aircraft). The results shown in figure 3.2 are for a series of three different free stream Mach numbers ($M_\infty = 0.499, 0.690$ and 0.732). Results at the largest Mach number are presented in figure 3.3 for three different lift coefficients ($C_L = 0.898, 0.645$ and 0.499). Inviscid results at the largest Mach number are also presented in figure 3.2 for calculations in which the experimental values of the angle of attack and the lift have been matched. All other results include the boundary layer correction and have the level of lift set to the experimental value. The airfoil used is a typical supercritical section as indicated by the large aft loading. Note the large discrepancies between the inviscid computations and the experimental results. The calculated results with viscous effects modeled are in good agreement with experiment for every case.

The matched experimental lift requirement is caused by deficiencies in mathematical modeling as well as experimental and numerical errors. The experimental pressure distribution and therefore the resulting lift can be easily measured but the angle of attack cannot. This is primarily due to wind tunnel wall interference, model distortion, and flow angularity effects. The numerical simulation has none of these difficulties but does have several numerical sources of error arising from mesh effects and formulation approximations. The largest error usually is associated with the simulation of viscous effects, primarily those associated with flow separation, trailing-edge and (near)-wake flow. Therefore, to obtain good numerical/experimental pressure distribution correlation, the best procedure is to match the experimental lift in the numerical calculation. This, however, is not always sufficient for good drag correlation (Chapter 4).

The primary way in which two-dimensional transonic codes are used in the aircraft industry is to determine initial estimates for new wing designs. By using simple sweep theory and two-dimensional analysis or design codes, a suitable starting geometry for a 3-D wing design can be constructed span station by span station. However, transonic wing/fuselage flow fields tend to be rather three dimensional in nature (especially when the wing aspect ratio is not large and the free stream Mach number is near one) and are very sensitive to relatively small changes in the geometry (especially the more efficient supercritical wing designs). Therefore, the final numerical design modifications are best made with codes that consider all three dimensions. Existing three-dimensional CTA procedures are discussed next.

3.3 Existing CTA methods (three dimensions)

3.3.1 Introduction

Several computer codes designed to solve the three-dimensional transonic flow over wing and wing/body configurations have been developed and are currently in wide use in the aircraft industry. A few of these codes are listed in tables 3.3 and 3.4 along with specific references describing the details of each code. Table 3.3 lists codes which use some form of TSP formulation. Different variants of the TSP formulation are discussed in reference 60. Table 3.4 lists codes which use the full potential formulation. Note that both the conservative and nonconservative versions are represented. Fundamentals of these formulations are given in Chapter 2, for example, see Section 2.1.2 for a discussion of the full potential equation and Section 2.1.3 for a discussion of the various TSP equations.

The iteration scheme used by the codes listed in tables 3.3 and 3.4 is almost exclusively SLOR. The newer approximate factorization or multigrid schemes are not yet generally used in production codes. This produces very slow convergence making these codes expensive to run. One feature generally employed with SLOR iteration schemes is the use of grid refinement. Converged results from a coarse mesh are interpolated onto a medium mesh, then reconverted, and finally interpolated to a final fine mesh. Thus a good initial solution is provided for the fine mesh calculation. The grid sequence philosophy generally provides a factor of two or three increase in convergence speed (for loose levels of convergence). Most of the codes listed in tables 3.3 and 3.4 use this technique.

The amount of computer time required to run a complete transonic wing solution depends on several factors: (1) the level of convergence desired, (2) the number of grid points used, (3) the type of formulation chosen, and (4) the distribution of grid points (i.e., grid smoothness). The amount of computer time reported by two different users from the same computer code can be substantially different simply due to the first two factors. Computer time comparisons which address most of these aspects are given in table 3.5 (taken from Ref. 61). Note that all codes compared have about the same number of wing surface grid points, although the total number of field points is quite different. The Bailey-Ballhaus code uses a concept called grid embedding (first introduced by Boppe [46] to more adequately cluster grid points at the wing surface. This concept uses a coarse mesh to cover the entire flow field from the far field boundary to the wing surface and only a localized fine mesh to resolve detail near the wing surface. This concept is very attractive because the mesh topology is much more efficient, thus reducing the number of grid points, the computer time per iteration, and the number of iterations required for a typical solution. When the interface between the coarse outer and fine embedded grids is placed sufficiently far from the aerodynamic surfaces, no deterioration in the solution (to plottable accuracy) can be detected at these surfaces. The reason grid embedding has not been used with the full potential formulation is due to the resulting mapping complications. In addition, full potential meshes are generally more efficient than TSP meshes (that is, TSP meshes without grid embedding), and therefore, grid embedding would not be as useful in this type of formulation.

All three results shown in table 3.5 were obtained for the same transonic wing at identical test conditions. All three codes used a coarse-medium-fine mesh sequence. Convergence was monitored by examining the pressure distribution histories at two span locations. The Bailey-Ballhaus code converged in approximately 200 iterations, the FLO22 code in 50-100 iterations and the FLO27 code in about 200 iterations. For these conditions the FLO27 code solution time is approximately twice that of the FLO22 code and about five times that of the Bailey-Ballhaus code. (The convergence characteristics are essentially the same for both the conservative and nonconservative options available in the Bailey-Ballhaus code.) For more information about this set of comparisons see reference 61. A more detailed comparison of various transonic computer codes including both accuracy and convergence speed comparison can be found in Van der Koik and Slooff [62].

3.3.2 Specific code characteristics

The fine inner grid used in the Bailey-Ballhaus, Boppe, RAE, and NLR 3D TSP computer codes is sheared Cartesian, whereby the planform is mapped to a rectangle (see Fig. 3.4). Thus, each spanwise station has the same number of grid points along the chord. The wing leading edge is positioned to lie between two grid lines. Thus the infinite slope problem at the leading edge of a blunt-nosed wing does not cause any difficulties in applying the boundary condition. However, the invalidity of the small disturbance assumption near the leading edge stagnation line, generally results in a poor representation of the flow field in this region.

The Dornier TSP code, in its original form, uses an unsheared Cartesian mesh. The mesh is adjusted to have a uniform spanwise placement of the wing leading edge between chordwise mesh points. This simplifies the TSP equation because the cross-derivative terms introduced by the shearing transformation are eliminated. However, this strictly Cartesian coordinate system can lead to inefficient treatment of highly swept, tapered wing geometries. As with other TSP codes, the Dornier TSP code solution accuracy suffers near the leading edge due to invalidity of the small disturbance assumption in this region.

All the three-dimensional TSP codes mentioned above have been used extensively in the past several years in many types of applications, both commercial and military. For example, the RAE 3D TSP code can be used to model many specific features including [63]: (1) wing/fuselage junction fillets, (2) boundary layer effects, (3) static aeroelastic distortion, (4) up to three interfering bodies of nacelle or store type, and (5) an improved method of treating supersonic to supersonic shock waves. The fuselage and store geometries are implemented by applying appropriate boundary conditions on rectangular "boxes" of infinite streamwise extent. Finite length effects can be simulated with a special treatment applied near the nose and tail regions of the appropriate interfering body. The position of these interfering bodies is quite arbitrary and, for example, can be above or below the wing or even at the wing tip. To date, no modeling of nacelle or store pylons has been included in this code.

In the NLR code [64], the effect of (finite) bodies and wing-body fillets is simulated by prescribing normal velocities, obtained from a panel method, in a vertical plane at the wing root.

The Jameson-Cauchey nonconservative full potential computer code (FLO22) uses a sheared parabolic coordinate system defined by (see Ref. 48)

$$\begin{aligned} x_1 + iy_1 &= [x - x_0(z) + i(y - y_0(z))]^{\frac{1}{2}} \\ z_1 &= z \end{aligned} \quad (3.6)$$

where z is the spanwise coordinate, and x_0 and y_0 define a singular line of the coordinate system located just inside the leading edge. The effect of this transformation is to unwrap the wing to form a shallow bump (see Fig. 3.5)

$$y_1 = s(x_1, y_1) \quad (3.7)$$

Next, a shearing transformation is used

$$\xi = x, \quad \eta = y_1 - s(x_1, y_1), \quad \zeta = z \quad (3.8)$$

to map the wing surface to a coordinate surface. Finally, the ξ , η and ζ coordinates are stretched by using an appropriate stretching formula which stretches the infinite physical domain into a finite computational domain. A revealing diagram of the overall wing grid system shown in the physical domain is reproduced from reference 65 in figure 3.6.

An interesting aspect of the FLO22 algorithm, created by the grid topology, is the orientation of the tridiagonal matrix inversions used in the SLOR iteration scheme. This aspect is illustrated in figure 3.7, which has been taken from reference 48. This diagram shows the computational domain in a spanwise cross-sectional plane; note the orientation of the streamlines. The purpose of sweeping through the mesh in the fashion shown is to always avoid sweeping in an upwind direction in the supersonic region. If this procedure is not followed, unstable operation could result.

The Jameson-Caughey FLO27 computer code is capable of treating the flow about isolated swept wings or wings mounted on an infinite cylinder. The FLO28 and FLO30 codes are closely related derivatives of FLO27, but they allow more sophisticated treatment of the fuselage. A comparative study of these FLO codes is made by Verhoff and O'Neil [66]. In this study wing/fuselage simulation capabilities are discussed (see Fig. 3.8), and a new technique for extending capabilities, called the equivalent simple body (ESB) technique, is outlined.

A finite volume spatial difference scheme is used in the FLO27, FLO28 and FLO30 codes to model the conservative full potential equation. This scheme uses a numerical evaluation of the metric coefficients, and therefore, theoretically could be used for flow calculations in any type of physical domain for which the grid point Cartesian coordinates are known. This generality produces a decrease in computational efficiency relative to FLO22. This is due to the numerical evaluation of the transformation metrics which are recomputed each iteration (or stored permanently on disk and accessed iteratively during the solution process). The actual transformation used for most FLO27 and FLO28 wing calculations is very similar to the transformation described for the FLO22 computer code and will not be discussed further. The transformation used in the FLO30 code is somewhat more sophisticated and is described in detail in reference 54.

The ONERA transonic full potential code due to Chattot, Coulombeix, and da Silva Tome [57] is capable of treating the flow about isolated wing geometries. The mapping used is again very similar to the previous descriptions and will not be discussed further. This code, like the more recent FLO codes, uses numerical evaluations of the metric quantities and therefore could support mesh generation routines of varying type provided they all used the same general topology.

Most full potential codes are designed for either conservative or nonconservative form. However, the ONERA code includes spatial differencing options for both forms. This allows direct comparison of the two forms in a format which is unencumbered by different iteration algorithms, grid topologies, or programming styles. Such a comparison is shown in figure 3.9 for a rectangular planform, nonlifting NACA 0012 wing at a free stream Mach number of 0.85. The conservative result produces a shock that is too strong and about 10-15 % downstream of the experimental shock position. The nonconservative shock location is incorrect in just the opposite direction; it is too weak and too far forward. This type of disagreement between conservative and nonconservative forms (for either the TSP or the full potential equations) is characteristic. The CTA code user should be aware of which formulation is being used and how the resulting solutions should be interpreted.

The ARA full potential wing/body code, of Forsey and Carr [58], is capable of solving the nonconservative full potential equation about isolated wings and wing/body combinations. Bodies must be circular in cross-section although the body radius may vary axially. This has the effect of providing a relatively good wing/body interference simulation but does not produce good finite-length body effects.

The mapping procedure used in the ARA code is implemented in two phases. First, the body is transformed via conformal mapping into a slit that corresponds to a portion of the symmetry plane. Because each body cross section is constrained to be circular, this mapping is analytic. Next, the wing leading and trailing edges are extended to infinity to produce a "flat-plate wing" outboard of the tip. Each flat-plate wing cross section is mapped to the interior of a circle using an analytic conformal mapping, and each finite-thickness wing cross section is mapped using a numerical conformal mapping. Thus, the total effect of this transformation is to map the surface of the wing (including the flat-plate wing extension) to the inside surface of a circular cylinder and the free stream outer boundary to the circular cylinder center. Unlike the FLO full potential codes (FLO22, FLO27, FLO28, and FLO30), which use a "C" mesh topology about each wing span station, the ARA code uses an "O" mesh topology. This produces a somewhat more efficient mesh for the ARA code, that is, for the same number of total grid points, the ARA code mesh puts about 30 to 40 % more points on the wing surface than a typical FLO code mesh.

3.3.3 Selected results obtained with existing methods

The next item of importance is accuracy, that is, how well do these codes actually predict transonic wing flow fields? Figure 3.10 shows a pressure coefficient distribution comparison between FLO22 (the nonconservative full potential computer code) and experiment taken from reference 67. This frequently used test case (ONERA M-6 wing at a free stream Mach number of 0.84 and an angle of attack of 3.06 deg) represents a difficult test for a transonic flow calculation procedure because of the existence of a double shock. This feature is evident in the first three pressure coefficient distributions. In the final pressure distribution at 95 % of the semi-span there is only a single shock. Generally speaking, except for a slight smearing of the shocks, these results are in excellent agreement. For this case no boundary layer correction was applied which suggests that the nonconservative differencing across the shock modeled the shock/boundary layer interaction so far as the pressure distribution is concerned. In addition, no corrections to the angle of attack or the free stream Mach number were required to achieve good agreement. This situation, as we shall soon see, is a somewhat rare occurrence.

The next two comparisons shown in figures 3.11 and 3.12 were taken from reference 68. Both results were obtained for the same wing geometry which consisted of NACA 64, 212 normal airfoil sections,

an aspect ratio of six, a streamwise thickness ratio of 0.098, and a quarter chord sweep angle of 35.18 deg. The results shown in figure 3.11 are for a free stream Mach number of 0.6, that is, a subcritical case. Both the FLO22 and the Boppe TSP results are compared with experiment. As expected the TSP results suffer in the leading edge region. This is probably due in part to the poor leading edge treatment associated with the TSP formulation. In contrast, the results produced by the FLO22 code are in excellent agreement with the experiment. For this subcritical calculation no differences between the nonconservative and conservative full potential formulations should exist.

The results shown in figure 3.12 are for a free stream Mach number of 0.85, that is, a transonic case. The TSP formulation was in the nonconservative mode. Both numerical results agree reasonably well with the experimental results. Thus, the constraint that practical TSP calculations must be run for transonic conditions is reinforced.

This behaviour results from an effective cancellation of errors between the leading-edge singularity error and the small-disturbance boundary condition error that seems to exist only for transonic calculations. The mesh spacing in the vicinity of the leading edge plays an important role in this error cancellation. Theoretically, the TSP equation is equally valid (or equally invalid) for subcritical cases, but the results in this speed regime are generally inferior to the transonic regime results. For more discussion on this point see Section 3.4.2.

Three additional sets of comparisons are shown in figures 3.13, 3.14, and 3.15. The first two are from reference 69 and show comparisons for a rather difficult case (F-16 wing-alone configuration at $M_\infty = 0.9$, $C_L = 0.6$, and with no viscous effects included). These results are plotted at 58 % of the semi-span. Figure 3.13 shows results from the FLO27 and the Bailey/Ballhaus (conservative form) transonic codes compared with experiment and a linear panel code result. The linear panel code produces no shock waves and therefore is inappropriate for this calculation. Both conservative transonic codes produce shocks which are too strong, as expected, without the inclusion of viscous effects, especially the shock/boundary layer interaction. The Bailey/Ballhaus result underpredicts the leading edge expansion. Since these calculations have been made at a constant lift coefficient, the resulting leading edge loss of lift is made up by an aft shift in the shock position.

Figure 3.14 shows a similar set of comparisons for results which are all nonconservative: Bailey/Ballhaus (nonconservative form), Boppe, and FLO22. For this set of comparisons much better agreement at the shock is obtained. The leading edge expansion underprediction by the Bailey/Ballhaus code is not as severe although a significant discrepancy still exists in this region. The discrepancy between the numerical and experimental values of pressure at the trailing edge is probably due to trailing edge viscous effects which are not modeled numerically. The correct pressure level between the two shocks is best predicted by the Bailey/Ballhaus code. All results, both conservative (Fig. 3.13) and nonconservative (Fig. 3.14), seem to slightly mispredict the forward shock position. This error and the TSP leading edge expansion error, to an extent, are caused by local leading edge errors introduced by an angle of attack change away from the experimental value required to produce the proper level of lift. The inclusion of proper viscous corrections should reduce this effect substantially.

Figure 3.15 (taken from Ref. 57) shows a series of results for the ONERA M-6 wing which was previously discussed in figure 3.10. Three numerical results, Jameson (conservative), Bailey/Ballhaus (conservative), and ONERA (nonconservative) are compared with experiment at a semi-span station of about 20 %. The free stream Mach number was 0.841, the angle of attack was 3 deg, and no viscous effects were included. The double shock configuration is predicted by all three results with some variation in the second shock position. The conservative results predict a somewhat stronger second shock slightly downstream of the nonconservative shock. In this case a good leading edge expansion is predicted by the TSP code probably because the leading edge grid was properly selected and the experimental angle of attack, instead of the experimental lift, was matched.

An experimental/numerical correlation involving an extremely sophisticated configuration for transonic flow analysis is shown in figure 3.16. In this particular example the Boeing KC-135 aircraft (including the wing, fuselage, all four pylons and nacelles, and both wing-tip-mounted winglets) is modeled via the TSP technique of Boppe [47]. In this calculation the winglets were mounted at a 90 deg angle with respect to the wing surface while in the experiment the winglets were canted outboard 15 deg. Strong shock waves are not present in this calculation which was for cruise conditions. Agreement between experimental and numerical results is excellent.

Results from the ARA full potential code (taken from Ref. 70) are presented in figures 3.17 and 3.18. The wing/body configuration used in this calculation is shown in figure 3.17. The body was a circular cylinder of constant radius, and the mid-mounted wing had the following characteristics: AR = 6, TR = 1, sweep = 25 deg. The wing had a constant supercritical airfoil section and was used without twist. Viscous effects were simulated by the addition of a displacement thickness obtained from a two-dimensional transonic viscous code [71].

Computed results for a free stream Mach number of 0.86 and an angle of attack of 4.2 deg are compared in figure 3.18 with experimental results for the same Mach number at two different angles of attack, 4.6 and 3.7 deg. The calculation was performed with the usual grid sequence involving 300, 100, and 160 iterations on the coarse, medium, and fine meshes, respectively. The finest mesh for this case consisted of $160 \times 20 \times 24 = 76,800$ grid points. The computational time required for this calculation was equivalent to about 25 min of CPU time on the CDC 7600 computer. Results are shown for three span stations, $y = 0.37$, 0.55, and 0.73, and are generally in excellent agreement with experiment. Note the unusually sharp shock capture displayed in figures 3.18(b) and (c). This is a result of the efficient mesh topology used in the ARA full potential code in conjunction with a relatively fine mesh.

Results from the RAE 3D TSP code (taken from Ref. 72) are presented in figures 3.19-3.22. The wing/fuselage configuration used in the first calculation is shown in figure 3.19. It consists of a low-mounted wing on a fuselage of circular cross section. The wind tunnel test model was constructed with a fillet between the wing upper surface and the body starting at the wing crest and extending downstream. Figure 3.20 shows a pressure coefficient comparison between numerical results (with and without the fillet model) and experiment. The experimental results are plotted at a wing station of $y = 0.31$ and the numerical results are plotted at $y = 0.268$. Note the improved agreement when the fillet is modeled.

The second RAE 3D TSP configuration is shown in figure 3.21. It consists of a wing/fuselage/nacelle geometry with several options available for the nacelle stream tube. The nacelle stream tube surfaces are treated as solid boundaries in the numerical calculations. The effect of the nacelle stream tube geometry on the lift distribution is displayed in figure 3.22. This type of simulation is very difficult to obtain experimentally but is relatively easy to model numerically.

The last result presented in this section is from a computer code developed by Yu [73]. This

code is basically a modified version of the Jameson-Caughey finite-volume code. The primary improvement utilized in the Yu code is a new efficient and flexible grid generation method based on the body-fitted coordinate method of Thompson, et al. [74,75]. In this approach a set of linear elliptic equations are solved numerically to determine the three-dimensional grid. The interior grid distributions are controlled by the boundary grid distributions in a manner developed by Middlecoff and Thomas [76]. For more information about this grid generation technique see Section 6.2.2.

Results from the Yu code (taken from Ref. 77) are presented in figures 3.23 and 3.24. The wing/fuselage configuration is shown in figure 3.23. In this calculation procedure the restriction to simplified fuselage geometries is not required; reasonably complex geometries can be accurately simulated. In this case the flow field about the Boeing 747-200 wing/fuselage geometry is computed for a free stream Mach number of 0.84 and an angle of attack of 2.8 deg. The section pressure coefficient distributions are compared with experiment at three span stations in figure 3.24. The agreement at each station is excellent.

An interesting trend, which is now taking place in CTA, is the advancement of nonlinear codes to include more sophisticated geometrical modeling. Only when all geometrical aspects of a configuration are included in a flow-field simulation can proper answers result. This is particularly important in the transonic regime because of nonlinear interference effects. Examples of more complete geometrical modeling are given by: Rizk [78] in which the propeller slipstream/wing interaction was considered, Mercer and Murman [55] in which wind tunnel walls were simulated, Yeh [79] in which nacelle/pylon combinations were included into wing/fuselage calculations, and Wai and Yoshihara [80] in which wing/fuselage/pylon/nacelle combinations with powered jet exhausts were simulated. The prospects for reasonably general simulation of complete aircraft in the transonic regime is quite likely to become a reality in the next few years.

3.3.4 Conservative versus nonconservative formulations

At this point a general observation can be made concerning conservative versus nonconservative form. Better agreement with experimental results is achieved with a nonconservative inviscid code than with a conservative inviscid code. This is due to the well-known effective mass source introduced at shocks when nonconservative differencing is used [81]. This numerically generated "error", fortuitously models the reduced shock pressure rise caused by the shock/boundary layer interaction, and therefore, in most cases, produces better agreement with the experimental pressure distribution than a conservative result.

For cases with viscous corrections added the conservative versus nonconservative situation is more difficult to assess. The addition of viscous corrections is indeed important for conservative CTA schemes because of the large discrepancies that exist without such corrections. Likewise, it is generally accepted that adding viscous corrections to nonconservative codes, especially to model shape change and decambering effects, is important to obtain good accuracy over a wide range of cases. If the viscous effects are accurately determined, the nonconservative formulations will still produce results with the undesirable effective mass source at shock waves and therefore introduce errors in the solution. However, under these circumstances, the conservative formulation should produce the correct physical answer, providing the isentropic shock approximation is not violated. This last constraint generally holds for cases in which the maximum local, normal-shock Mach number does not exceed 1.3.

The nonconservative CTA scheme will of course continue as an engineering tool for many applications, where the proper shock/boundary layer interaction cannot be incorporated. However, the ultimately correct formulation must be based on the mathematically sound conservative form. Most recent inviscid algorithm research has been on conservative formulations and will receive the main emphasis in Chapter 6 (Advanced Concepts).

3.4 Problems and limitations with existing techniques

3.4.1 Introduction

The use of CTA techniques for the design and analysis of new aircraft is rapidly becoming widely accepted. Their use can substantially reduce development time and cost, as for example, in the case of the Airbus A-310 wing design [82]. New transonic computational methods were used to improve the cruise characteristics of the A-310 wing relative to the A-300 wing. The resulting improvement in aerodynamic efficiency could save billions of dollars in fuel costs over the lifetime of a fleet of such aircraft.

However, many problems with the implementation of CTA methods still exist. Some of these include: (1) errors generated by the improper usage of CTA methods, (2) lack of sophistication in modeling proper geometrical aspects, (3) errors in the numerical calculation procedure, and (4) errors in the experimental results, which in turn are used to verify the numerical results. A good summary of some of these difficulties is given by Hicks [83] in a recent paper which discusses the successes and failures of CTA codes applied to the transonic wing design problem.

A complete description of user guidelines applicable to CTA computer codes is difficult to formulate, primarily because of the extremely diverse nature of these codes. Many times certain difficulties are case dependent which further complicates the formulation of user guidelines. Differences in the governing equation formulation, grid topologies and grid generation techniques, the nature of viscous corrections, boundary condition application, etc., are just a few areas where significant differences can exist. Nevertheless, the following section is devoted to the discussion of code characteristics with special emphasis on problems or limitations. In addition, some of the fixes used to successfully overcome these prominent difficulties are also presented and discussed.

The first, and perhaps most general comment concerns not a specific computer code but rather the user. Generally speaking, before an engineer is trusted with the responsibility of conducting a wind tunnel test for the purpose of designing a new aircraft or aircraft component, many years of experience are required. Much the same philosophy should be applied to the utilization of CTA methods for the design or modification of an aircraft. Perhaps not years, but at least months of experience for a single code/user interface should be obtained before realistic results can be expected.

Geometry input and checkout as well as the related mesh generation process can be a very complex task. Specification of relaxation factors, acceleration parameters, and damping coefficients required to optimize convergence or prevent divergence is another difficult task. Being able to properly interpret the resulting solution is the most difficult task. The CTA code user must constantly be concerned about (1) level of convergence, (2) coarse mesh effects, (3) viscous effects, and (4) the validity of the potential formulation to accurately model each case. These questions can be answered systematically and effectively

with the proper level of experience.

Experience with subsonic panel methods does not fully prepare the user for transonic code applications. This is primarily due to the increased complexity of transonic flow fields (shocks and shock/boundary layer interactions), the increased sensitivity of transonic flow to surface coordinate specification, and the fact that panel grids are only two-dimensional while transonic grids are three-dimensional. To gain experience with transonic codes, simple problems should be attempted first. Two-dimensional airfoil calculations or simple three-dimensional solutions (for example, wings with little or no sweep, taper or twist at low Mach numbers and angles of attack) are good examples. Then as experience is obtained, more complex configurations at higher Mach numbers and angles of attack can be tried. With this philosophy a good understanding of code limitations can be obtained in terms of accuracy, convergence reliability, and range of application.

The most complex aspect of transonic code operation, which requires the most experience, involves code modification. Because of the rather limited number of geometry options offered by most CTA codes, modification for new geometries is often required. This, of course, is best completed by the code author or someone with extensive experience with the internal algorithm, grid generation, and geometry specification logic.

In summary, if the proper amount of time is devoted to learning and understanding the various aspects associated with CTA methods, then these methods can be a valuable asset for the design of modern transonic aircraft. General problems and suggested fixes associated with various formulations are discussed next, followed by more specific problems associated with individual codes.

3.4.2 TSP equation leading edge limitation

Several significant limitations exist within the TSP equation formulation (as already mentioned in Sect. 2.1.3). The first is that significant errors arise in the vicinity of blunt leading edges (near stagnation points or lines). This error is caused by a breakdown of the small disturbance assumption near the leading edge stagnation region. Implementation of the small disturbance boundary condition to achieve flow tangency at the airfoil or wing surface is difficult because the body surface slopes become large in this region. Poor resolution of the stagnation region is a result of this problem but is not the greatest point of concern. Poor representation of the leading edge expansion as previously shown in figures 3.13 and 3.14 is a much more serious problem.

This TSP leading edge singularity is basically inherent. No completely-effective, easy-to-implement solutions for this problem have yet been devised. (For one specific attempt to improve the TSP leading edge situation see Ref. 84.) The basic symptom of this problem is the existence of solution non-uniformness in the leading edge region, that is, as the leading edge mesh is refined, different leading edge solutions will result. As the mesh becomes very fine stability problems may develop. To eliminate or reduce this instability a common fix is to modify the leading edge slope by using

$$\left(\frac{dy}{dx}\right)_{\text{modified}} = \left(\frac{dy}{dx}\right)_{\text{actual}} / \sqrt{1 + \left(\frac{dy}{dx}\right)_{\text{actual}}^2} \quad (3.9)$$

where dy/dx is the slope of the airfoil surface (see Ref. 85 for more discussion on this point). With this modification the leading edge difficulties are moderated. However, the original geometrical configuration has been modified which alters the resulting final solution.

Another problem associated with the TSP formulation for highly swept and tapered configurations occurs when the standard embedded grid approach is used (see Sect. 3.3.1 for a more complete description of the TSP embedded grid approach). This instability is the so-called "wing tip shock wave instability" and can be identified by diverging values of the maximum correction at the wing tip. For cases in which the problem is acute, propagation of this divergence inward toward the root can be observed [86]. This instability is caused by large differences in mesh resolution at the tip between the fine embedded wing grid and the coarse global crude grid. It occurs only when strong shock waves exist at the wing tip. A simple code modification suggested by Boppe [86] to relieve this problem basically consists of reducing the chord-wise mesh density associated with the fine embedded wing grid so as to make it more compatible with the global crude grid. This fixup has the effect of reducing solution accuracy and therefore should not be used when it is not needed. However, if the wing tip shock wave instability does exist, this modification quite likely will remove it.

3.4.3 Slow convergence

Another problem associated with all three-dimensional transonic formulations is the excessive amount of computer time required to obtain a single solution. Depending on the formulation, typical CPU times (CDC 7600 computer) range from about 5-20 min for the TSP formulation to about 30-60 min for the conservative full potential formulation (see Sect. 3.3.1 for more discussion on this point). These times can be considerably larger for other, slower computers. The most alarming aspect about these run times is that typically, the convergence criteria and grid dimension sizes are selected to minimize computational cost (that is, CPU time) often without sufficient regard for solution accuracy. Frequently, final results are obtained after a fixed number of iterations regardless of the solution convergence level. Significant errors in the shock position and strength and level of lift can result. This error seems to be worse for high aspect ratio wings where the lift development can be quite slow.

Grid size also plays a very important role in code efficiency and accuracy. Accurate results require far more grid points than most design/analysis engineers realize. For example, the asymptotic behaviour of a typical transonic airfoil solution on a sequence of successively refined grids was reported in reference 87. A grid consisting of 64×16 points underpredicted the lift (relative to the asymptotic value) by approximately 18 %, and a grid of 128×32 points, which is fine compared to most wing cross sectional grids, underpredicted the lift by about 10 %. The problem in three dimensions is more severe than this simple two-dimensional study indicates. Supersonic-to-supersonic shocks, which often appear in swept wing calculations, are much more difficult to capture without excessive smearing because of their entirely first-order-accurate nature. This suggests that most three dimensional codes, with typical mesh dimensions (for example, 80 to 100 points on the wing surface at each span station), produce results with 10 to 15 % of error in lift just due to mesh coarseness. To improve this situation, schemes with higher accuracy should be sought. A promising approach was presented in reference 87 for an entirely second-order-accurate scheme. Although significant improvements in accuracy were obtained, the convergence efficiency was somewhat

reduced. More discussion concerning schemes with higher-order accuracy is presented in Section 6.1.1.

The ultimate solution to the problems of accuracy and computational efficiency is two fold. First, faster, more cost effective computers with enhanced performance from vector architectures will allow finer and therefore more accurate meshes to be used in a routine and efficient fashion. Second, an improved generation of transonic relaxation algorithms will help to improve both the computational efficiency of the iteration process and the accuracy associated with the spatial differencing scheme. Details associated with both of these aspects are discussed in Chapter 6 (Advanced Concepts).

3.4.4 Viscous corrections

A common problem associated with poor numerical/experimental correlation is the lack of proper viscous corrections. This is an extremely complex subject involving four major effects: (1) shock/boundary layer interaction effects, (2) the decambering and thickness effects due to the addition of a simple displacement thickness, (3) trailing-edge effects, and (4) near-wake effects. Viscous corrections for most transonic flow conditions are significant and must be modeled to obtain good correlation with experimental results. More extensive discussion of this subject with special emphasis on the implementation of corrections for viscous effects is given in Chapter 4.

3.4.5 Problems due to the inadequate treatment of geometry

Some of the discrepancies between numerical and experimental results are due to the inadequate geometrical treatment associated with the numerical simulation. For instance, trying to model a wing/fuselage experiment with a wing-alone code can produce large errors. Interesting examples presented in reference 83 address this problem and are briefly discussed here. The wing/fuselage geometry used in this set of comparisons is shown in figure 3.25 along with pertinent geometrical characteristics. Figures 3.26 and 3.27 show the numerical/experimental pressure coefficient comparisons obtained at a free stream Mach number of 0.8. The numerical results of figure 3.26 are from FLO22, which is strictly speaking a wing-alone code. The numerical results of figure 3.27 are from FLO30 which simulates the entire wing/fuselage model. The FLO22 code is nonconservative and in this case was not coupled with a boundary layer code. The FLO30 code is conservative and was coupled with a boundary layer code. In both cases the numerical and experimental angles of attack were matched. The wing/fuselage numerical results (FLO30) are in much better agreement with the experiment near the wing root than the wing-alone numerical results (FLO22). The amount of discrepancy between the two codes decreases outboard toward the wing tip. This is, generally speaking, an expected result because of the more complete geometrical modeling provided by the wing/fuselage code.

However, as pointed out in reference 83 the use of a wing/fuselage code to model a wing/fuselage experiment does not necessarily guarantee good experimental/numerical correlation. Two examples in which poor numerical/experimental comparisons were obtained for a wing/fuselage configuration are discussed in reference 83. The code used in these calculations was FLO28. Reasons for disagreement can come from many sources and are difficult to formulate. Hicks [83] suggests four primary contributors to poor numerical/experimental correlation: model errors, viscous effects, tunnel effects, and code limitations. Hicks suggests two procedures to help minimize the numerical error associated with a particular code. The first is to compute each solution on a sequence of meshes, each new mesh slightly finer than the previous mesh. Interpolation of the previous coarse mesh solution onto the next finer mesh could be used to reduce computer time. The final solution is approached asymptotically as the mesh is refined. This allows an assessment of the solution truncation error. If a large difference exists between two successive solutions, then this indicates a large amount of truncation error and the need for further mesh refinement.

The second procedure to help minimize error is to iterate on each grid, not a fixed number of iterations, but until the solution stops changing by a fixed amount. Because these two suggestions could increase computer time drastically, they may not be practical until faster computers and/or iteration schemes are routinely used. However, an approach along this line, to reduce errors associated with poor mesh resolution and lack of solution convergence, must ultimately be adopted before CTA codes obtain the reliability and level of accuracy required for routine production usage.

As mentioned above, a common cause for poor numerical/experimental correlation is due to experimental errors. Wind tunnel wall interference is a particularly important cause for discrepancy especially as free stream Mach numbers approach one. One method to help eliminate this problem is to include the wind tunnel walls as part of the numerical simulation. Examples are provided in [14,20,88] for two dimensions and in [54] for three dimensions. Although modeling of the proper ventilated wall boundary conditions is difficult, significant improvements in estimating the wall effects can be obtained by this approach.

Wind tunnel results can also be inaccurate because of flow angularities or model distortion. Frequently these problems, as well as some numerical inaccuracies, are overcome by first "calibrating" a particular code to an existing facility for a given model configuration. This is accomplished by applying "corrections" to the angle of attack, free stream Mach number, and/or wing twist distribution until a good numerical/experimental correlation is achieved. In addition, inadequate geometry modeling (for example, using a wing code to model a wing/fuselage experiment) can be partially overcome by this procedure.

Numerical/experimental comparisons using this philosophy are shown in figures 3.28 and 3.29 for a high aspect ratio ($AR = 10.3$) supercritical wing tested by NASA Langley (taken from Ref. 67). The wing is swept 27° at the quarter chord line, and has streamwise section thickness ratios of 14.9% at the fuselage junction, 12% at the trailing-edge break, and 10.6% at the tip. Viscous effects were modeled by a two-dimensional integral boundary-layer method applied in streamwise strips. The calculation angles of attack were determined by matching the experimental lift coefficients.

Figure 3.28 presents results from FLO22 which does not model the fuselage used in the experiment. In an attempt to account for the fuselage interference effect this calculation was run at a free stream Mach number of 0.80 while the experiment was run at 0.79. Agreement is excellent everywhere except near the inboard stations, where details of the fuselage interference are probably important.

Figure 3.29 presents results from FLO27. For this case the fuselage is modeled as an infinite cylinder with a radius equal to the maximum radius of the fuselage on which the wing was mounted in the experiment. The low-mounted position of the test wing was also simulated in the numerical calculation. For this case, the aeroelastic deformation of the model was estimated by introducing 0.36° of wash out (negative twist) at the tip. This aeroelastic twist was added linearly from the trailing-edge break to the tip; it was not included in the FLO22 calculation of figure 3.28. The Mach number correction used for the

FL027 result was 0.007 and was applied to account for the effect of the finite fuselage used in the experiment. It is clear from figure 3.29 that representation of the effect of a finite fuselage by a simple Mach number shift is an oversimplification. Results in figure 3.29 are in better agreement with experiment near the root station than the results of figure 3.28, but in poorer agreement outboard near the tip. Nevertheless reasonable agreement is obtained in both cases by making these ad hoc adjustments or calibrations.

A fairly simple, but adequate and therefore convenient way to introduce finite body and wing-body fillet effects into the FL022 code has been developed by Van der Vooren et al. [89]. Similar as in [64], normal, i.e. spanwise velocities are prescribed in a vertical plane at the wing root. These velocity components are obtained from a panel method calculation for the complete wing-body configuration. As indicated by the example of figure 3.30 a substantial improvement in the capabilities of the FL022 code is realized in this way.

In design applications the general procedure in using CTA methods is that, after the results are calibrated, geometry perturbations are sought either by trial-and-error or by using a suitable design approach to force desirable characteristics into the solution, for example, reduction in shock strength at constant lift or a reduction in the isentropic pressure gradient also at constant lift to avoid separation. With this kind of approach the use of numerical methods is most attractive. (For a more detailed discussion on design methods see Chapter 5.) A large number of geometry perturbations can be examined quickly and efficiently. Once the optimal configuration is found numerically it can then be verified experimentally. As a result of this type of approach, much larger design spaces can be explored in the time available to the designer. This ultimately translates into more efficient aircraft designs obtained more cost effectively.

3.5 References

1. Hall, M.G., Computational fluid dynamics - A revolutionary force in aerodynamics, Proceedings of the fifth AIAA Computational Fluid Dynamics Conference, Palo Alto, Calif., June 1981.
2. Gessow, A., and Morris, D.J., A survey of computational aerodynamics in the United States, NASA SP-394, 1977.
3. da Costa, L.A., Application of computational aerodynamics methods to the design and analysis of transport aircraft, Proceedings XI ICAS Congress, Vol. 1, 1978.
4. Slooff, J.W., Requirements and developments shaping the next generation of integral methods, Presented at the IMA Conference on numerical methods in aeronautical fluid dynamics, Reading, U.K., March-April, 1981.
5. Chapman, D.R., Computational aerodynamics: Review and Outlook, 1979 Dryden Research Lecture presented at the 17th AIAA Aerospace Sciences Meeting, New Orleans, La., January 1979. Also, AIAA J., Vol. 17, December 1979, pp. 1293-1313.
6. Chapman, D.R., Trends and pacing items in computational aerodynamics, Presented at the seventh International Conference on Numerical Methods in Fluid Dynamics, Stanford University and NASA Ames Research Center, Calif., June 1980.
7. Murman, E.M., and Cole, J.D., Calculation of plane steady transonic flows, AIAA J., Vol. 9, No. 1, January 1971, pp. 114-121.
8. Steger, J.L., and Lomax, H., Numerical calculation of transonic flow about two-dimensional airfoils by relaxation procedures, AIAA J., Vol. 10, No. 1, January 1972, pp. 49-54.
9. Garabedian, P.R., and Korn, D., Analysis of transonic airfoils, Comm. on Pure and Applied Math., Vol. 24, 1971, pp. 841-851.
10. Bailey, F.R., and Steger, J.L., Relaxation techniques for three-dimensional transonic flow about wings, AIAA Paper No. 72-189, January 1972.
11. Ballhaus, W.F., and Bailey, F.R., Numerical calculation of transonic flow about swept wings, AIAA Paper No. 72-677, June 1972.
12. Jameson, A., Iterative solution of transonic flows over airfoils and wings, including flows at Mach 1, Comm. on Pure and Applied Math., Vol. 27, 1974, pp. 283-309.
13. Bauer, F., Garabedian, P., Korn, D., and Jameson, A., Supercritical wing sections II, Lecture Notes in Economics and Mathematical Systems, Vol. 108, Springer-Verlag 1975.
14. Murman, E.M., Bailey, F.R., and Johnson, M.L., TSFOIL - A computer code for two-dimensional transonic calculations, including wind tunnel wall effects and wave-drag evaluation, NASA SP-347, March 1975, pp. 769-788.
15. Carlson, L.A., Transonic airfoil analysis and design using Cartesian coordinates, Proceedings of the second AIAA Computational Fluid Dynamics Conference, Hartford, Conn., June 1975, pp. 175-183.
16. Carlson, L.A., Inverse transonic airfoil design including viscous interactions, NASA CP-2001, November 1976, pp. 1387-1395.
17. Jameson, A., Transonic potential flow calculation using conservative form, Proceedings of the second AIAA Computational Fluid Dynamics Conference, Hartford, Conn., June 1975, pp. 148-155.
18. Melnik, R.E., Wake curvature and trailing edge interaction effects in viscous flow over airfoils, NASA CP-2045, March 1978, pp. 255-270.
19. Albane, C.M., Catherall, D., Hall, M.G., and Joyce, G., An improved numerical method for solving the transonic small-disturbance equation for the flow past a lifting airfoil, RAE Technical Report 74056, 1974.
20. Catherall, D., The computation of transonic flows past aerofoils in solid, porous or slotted wind tunnels, AGARD CP-174, Paper No. 19, 1975.
21. Eberle, A., A finite element method for calculating transonic potential flow around profiles, MBB UFE1325(0), 1977.
22. Holst, T.L., An implicit algorithm for the conservative, transonic full potential equation using an arbitrary mesh, AIAA Paper No. 78-1113, July 1978. (Also, AIAA J., Vol. 17, October 1979, pp. 1038-1045.)
23. Dougherty, F.C., Holst, T.L., Gundy, K.L., and Thomas, S.D., TAIR - A transonic airfoil analysis computer code, NASA TM-81296, May 1981.
24. Chattot, J.J., and Coulombeix, C., Relaxation method for the full-potential equation, ONERA T.P. No. 1979-154, 1979.
25. Jameson, A., Acceleration of transonic potential flow calculations on arbitrary meshes by the multiple grid method, Proceedings of the fourth AIAA Computational Fluid Dynamics Conference, Williamsburg, Va., July 1979, pp. 122-146.

26. Deconinck, H., and Hirsch, C., Subsonic and transonic computation of cascade flows, Proceedings of the fourth IRIA International Symposium on Computing Methods in Applied Sciences and Engr., North-Holland Publishing Co., 1980.
27. Baker, T.J., Potential flow calculations by the approximate factorisation method, J. of Comp. Phys., Vol. 42, 1981, pp. 1-19.
28. South, J.C., and Jameson, A., Relaxation solutions for inviscid axisymmetric transonic flow over blunt or pointed bodies, Proceedings of the AIAA Computational Fluid Dynamics Conference, Palm Springs, Calif., July 1973.
29. Keller, J.D., and South, J.C., RAXBOD: A Fortran program for inviscid transonic flow over axisymmetric bodies, NASA TM X-72831, February 1976.
30. Arlinger, B.G., Calculation of transonic flow around axisymmetric inlets, AIAA J., Vol. 13, No. 12, December 1975, pp. 1614-1621.
31. Arlinger, B.G., Axisymmetric transonic flow computations using a multigrid method, Presented at the seventh International Conference on Numerical Methods in Fluid Dynamics, Stanford University and NASA Ames Research Center, Calif., June 1980.
32. Baker, T.J., A numerical method to compute inviscid transonic flow around axisymmetric ducted bodies, IUTAM Symposium Transsonicum II, Göttingen, September 1975.
33. Caughey, D.A., and Jameson, A., Accelerated iterative calculation of transonic nacelle flow fields, AIAA J., Vol. 15, No. 10, October 1977, pp. 1474-1480.
34. Reyhner, T.A., Cartesian mesh solution for axisymmetric transonic potential flow around inlets, AIAA J., Vol. 15, No. 5, May 1977, pp. 624-631.
35. Eberle, A., Transonic potential flow computations by finite elements: Airfoil and wing analysis, airfoil optimization, Lecture held at the DGLR/GARTEur 6 Symposium, Transonic Configurations, Bad Harzburg, June 1978.
36. Chen, L.T., and Caughey, D.A., Calculation of transonic inlet flow fields using generalized coordinates, J. of Aircraft, Vol. 17, No. 3, March 1980, pp. 167-174.
37. Henne, P.A., Applied computational transonics - capabilities and limitations, Presented at the Transonic Perspective Symposium, held at NASA Ames Research Center, Moffett Field, Calif., February 1981.
38. Bailey, F.R., and Ballhaus, W.F., Comparisons of computed and experimental pressures for transonic flows about isolated wings and wing-fuselage configurations, NASA SP-347, Aerodynamic Analysis Requiring Advanced Computers, March 1975.
39. Mason, W., Mackenzie, D.A., Stern, M.A., and Johnson, J.K., A numerical three-dimensional viscous transonic wing-body analysis and design tool, AIAA Paper No.78-101, January 1978.
40. Rohlf, S., and Vanino, R., A steady relaxation method for two- and three-dimensional transonic flows, Presented at Euromech 40, Transonic Aerodynamics, Saltsjobaden, Sweden, September 1973.
41. Schmidt, W., and Hedman, S., Recent explorations in relaxation methods for three-dimensional transonic potential flow, ICAS Paper No.76-22, October 1976.
42. Albone, C.M., Hall, M.G., and Joyce, G., Numerical solutions for transonic flows past wing-body configurations, Symposium Transonicum II, Göttingen, September 1975, Springer-Verlag 1976.
43. Firman, M.C.P., Calculations of transonic flow over wing/body combinations with an allowance for viscous effects, AGARD CP-291, Paper No.8, 1981.
44. Rae, W.J., Calculation of three-dimensional transonic compressor flow fields by a relaxation method, Journal of Energy, Vol. 1, No.5, September-October 1977, pp. 284-296.
45. Rae, W.J., and Lordi, J.A., A study of inlet conditions for three-dimensional transonic compressor flows, Calspan Report No.XE-6129-A-4, June 1978.
46. Boppe, C.W. Calculation of transonic wing flows by grid embedding, AIAA Paper No.77-207, January 1977.
47. Boppe, C.W., and Stern, M.A., Simulated transonic flows for aircraft with nacelles, pylons, and winglets, AIAA Paper No.80-130, January 1980.
48. Jameson, A., Caughey, D.A., Newman, P.A., and Davis, R.M., A brief description of the Jameson-Caughey NYU transonic swept-wing computer program FLO-22, NASA TM X-73996, 1976.
49. Newman, P.A., Carter, J.E., and Davis, R.M., Interaction of a two-dimensional strip boundary layer with a three-dimensional transonic swept-wing code, NASA TM-78640, March 1978.
50. Reyhner, T.A., Transonic potential flow around axisymmetric inlets and bodies at angle of attack, AIAA J., Vol. 15, 1977, pp. 1299-1306.
51. McCarthy, D.R., and Reyhner, T.A., A multi-grid code for three-dimensional transonic potential flow about axisymmetric inlets at angle of attack, AIAA Paper No.80-1365, July 1980.
52. Jameson, A., and Caughey, D.A., A finite-volume method for transonic potential flow calculations, Proceedings of the third AIAA Computational Fluid Dynamics Conference, June 1977, pp. 35-54.
53. Caughey, D.A., and Jameson, A., Numerical calculation of transonic potential flow about wing-body combinations, AIAA J., Vol. 17, No. 2, February 1979, pp. 175-181.
54. Caughey, D.A., and Jameson, A., Progress in finite-volume calculations for wing-fuselage combinations, AIAA J., Vol. 18, No.11, November 1980, pp. 1281-1288.
55. Mercer, J.E., and Murman, E.M., Application of transonic potential calculations to aircraft and wind tunnel configurations, AGARD CP-285, May 1980.
56. Heckmann, G., Etude par la methode des elements finis des interactions voilure-fuselage-nacelle d'un avion du type Falcon a Mach = 0,79, AGARD CP-285, May 1980.
57. Chattot, J.J., Coulombeix, C., and da Silva Tome, C., Calculs d'écoulements transsoniques autour d'ailes, La Recherche Aerospaciale, No.4, 1978, pp. 143-159.
58. Forsey, C.R., and Carr, M.P., The calculation of transonic flow over three-dimensional swept wings using the exact potential equation, ARA Memo No.207, 1978. (Also, Proceedings of the DGLR/GARTEur 6 Symposium, Transonic Configurations, Bad Harzburg, West Germany, June 1978.)
59. Chen, L.T., and Caughey, D.A., Higher-order, finite-difference scheme for three-dimensional transonic flow fields about axisymmetric bodies, J. of Aircraft, Vol. 17, No.9, September 1980, pp. 668-676.
60. van der Vooren, J., Slooff, J.W., Huizing, G.H., and van Essen, A., Remarks on the suitability of various transonic small perturbation equations to describe three-dimensional transonic flow; Examples of computations using a fully-conservative rotated difference scheme, IUTAM Symposium Transsonicum II, Göttingen, September 1975, Springer-Verlag, 1976.

61. Hinson, B.L., and Burdges, K.P., Acquisition and application of transonic wing and far-field test data for three-dimensional computational method evaluation, Air Force Report No.AFOSR-TR-80-0421, March, 1980.
62. van der Kolk, J.T., and Slooff, J.W., A comparison of computational results for transonic flow around the ONERA M6 wing, To be published as an NLR Report, 1982.
63. Albone, C.M., Private communication, 1980.
64. Van der Vooren, J., Huizing, G.H., and Van Essen, A., A finite difference method for the calculation of transonic flow about a wing, based on small perturbation theory, NLR TR 81031 L, 1981.
65. Henne, P.A., and Hicks, R.M., Wing analysis using a transonic potential flow computational method, NASA TM-78464, July 1978.
66. Verhoff, A., and O'Neil, P.J., Extension of FLO codes to transonic flow prediction for fighter configurations, Presented at Transonic Perspective - A critique of transonic flow research, Workshop held at NASA Ames Research Center, February 1981. (Also, MCAIR Report No.81-004, 1981.)
67. Caughey, D.A., Newman, P.A., and Jameson, A., Recent experiences with three-dimensional transonic potential flow calculations, NASA TM-78733, July 1978.
68. Henne, P.A., and Hicks, R.M., Transonic wing analysis using advanced computational methods, AIAA Paper No.78-105, January 1978.
69. Bateley, I.C., and Cox, R.A., The application of computational methods to transonic wing design, Presented at Transonic Perspective - A critique of transonic flow research, Workshop held at NASA Ames Research Center, Moffett Field, Calif., February 1981.
70. Forsey, C.R., Unpublished data, 1979.
71. Lock, R.C., The prediction of viscous effects on aerofoils in transonic flow, Proceedings of the DGLR/GARTeUR Symposium, Transonic Configuration, Bad Harzburg, West Germany, June 1978.
72. Albone, C.M., Unpublished data, 1980.
73. Yu, N.J., Grid generation and transonic flow calculations for three-dimensional configurations, AIAA Paper No.80-1391, July 1980.
74. Thompson, J.F., Thames, F.C., and Mastin, C.W., Automatic numerical generation of body-fitted curvilinear coordinate system for field containing any number of arbitrary two-dimensional bodies, *J. Comp. Phys.*, Vol. 15, 1974, pp. 299-319.
75. Thompson, J.F., Thames, F.C., Mastin, C.W., and Shanks, S.P., Use of numerically generated body-fitted coordinate systems for solution of the Navier-Stokes equations, Proceedings of the second AIAA Computational Fluid Dynamics Conference, Hartford, Conn., 1975, pp. 68-80.
76. Middlecoff, J.F., and Thomas, P.D., Direct control of the grid point distribution in meshes generated by elliptic equations, Proceedings of the fourth AIAA Computational Fluid Dynamics Conference, Williamsburg, Va., July 1979, pp. 175-179.
77. Yu, N.J., Private communication, 1981.
78. Rizk, M.H., Propeller slipstream/wing interaction in the transonic regime, AIAA Paper No.80-0125, January 1980.
79. Yu, N.J., Transonic flow simulations for complex configurations with surface fitted grids, AIAA Paper No.81-1258, June 1981.
80. Wai, J.C., Yoshihara, H., and Abeyounis, W.K., Transonic perturbation analysis of wing-fuselage-nacelle-pylon configurations with powered jet exhausts, AIAA Paper No.82-0255, January 1982.
81. Newman, P.A., and South, J.C., Conservative versus nonconservative differencing: Transonic streamline shape effects, NASA TM X-72827, February 1976. (Also, *AIAA J.*, Vol. 14, No. 8, August 1976, pp. 1148-1149.)
82. Jupp, J.A., The development of the Airbus wing, *World Airnews*, December 1980.
83. Hicks, R.M., Transonic wing design using potential-flow codes - Successes and failures, SAE Paper No.810565, 1981.
84. Yoshihara, H., Fixes to the 3D transonic small disturbance theory, General Dynamics Report No. CASD-ERR-75-012, 1975.
85. Albone, C.M., Further improvements in the solution of the small-perturbation equation for flow past a lifting aerofoil, RAE TR 75101, 1975.
86. Boppe, C.M., Private communication, 1980.
87. Caughey, D.A., and Jameson, A., Basic advances in the finite-volume method for transonic potential flow calculations, Presented at the Numerical and Physical Aspects of Aerodynamic Flows Symposium, California State University, Long Beach, Calif., January 1981.
88. Kacprzyński, J.J., Transonic flow field past 2-D airfoils between porous wind tunnel walls with nonlinear characteristics, AIAA Paper No.75-81, 1975.
89. Van der Vooren, J., et al., XFLO22 NLR, A modified version of FLO22; Computer code for the calculation of transonic flow about a wing, including body influence, Unpublished NLR Memorandum, 1980.

TABLE 3.1
Some existing transonic potential codes for two-dimensional applications

Code name	Date	Governing equation	Iteration scheme	Grid	Remarks
Garabedian - Korn ⁹	1971	FP(NC)	SLOR	Conformal 0 mesh	Viscous effects option ¹³
TSFOIL ¹⁴	1975	TSP(C or NC)	SLOR	Stretched-Cart.	Wind tunnel wall option. $M_\infty > 1$ option. Detailed documentation
Carlson ¹⁵	1975	FP(NC)	SLOR	Stretched-Cart. nonaligned	Design option. Viscous effects option ¹⁶
FLO6 ¹⁷	1975	FP(C or NC)	SLOR or Hybrid	Conformal 0 mesh	Viscous effects option (GRUMFOIL ¹⁸)
RAE TSP ^{19,20}	1975	TSP(NC)	SLOR	Stretched-Cart.	Wind tunnel wall option
Eberle ²¹	1977	FP(C)	SLOR	Finite element 0 mesh	Wind tunnel wall and cascade flow versions
TAIR ^{22,23}	1978	FP(C)	AF	Numerical 0 mesh	Detailed documentation
Chattot ²⁴	1979	FP(C)	AF	Sheared parabolic C mesh	
FLO36 ²⁵	1979	FP(C)	MG/AF	Conformal 0 mesh	
Deconinck and Hirsch ²⁶	1979	FP(C)	SLOR or AF	Finite element	Cascade and channel flow versions
Baker ²⁷	1980	FP(NC)	AF	Conformal 0 mesh	

TABLE 3.2
Some existing transonic potential codes for axisymmetric applications

Code name	Date	Governing equation	Iteration scheme	Grid	Remarks
RAXBOD ^{28,29}	1973	FP(NC)	SLOR	Body-normal/ sheared- cylindrical	Blunt or pointed axisymmetric bodies, $M_\infty > 1$ capability
Arlinger ^{30,31}	1975	FP(NC)	SLOR and MG/SLOR	Conformal	Axisymmetric inlets and bodies, $M_\infty > 1$ capability
Baker ³²	1975	FP(NC)	SLOR	Patched	Axisymmetric inlets
Caughey and Jameson ³³	1976	FP(NC)	SLOR + EXT	Sheared conformal	Axisymmetric inlets
Reyhner ³⁴	1976	FP(NC)	SLOR + EXT	Stretched-Cart. nonaligned	Axisymmetric inlets with or without center bodies
Eberle ³⁵	1978	FP(C)	SLOR	Finite element	Axisymmetric inlets and bodies
Chen and Caughey ³⁶	1979	FP(C or NC)	SLOR + EXT	Sheared conformal	Axisymmetric inlets with or without center bodies

TABLE 3.3
Some existing three-dimensional codes using the TSP formulation

Name	Date	Type of formulation	Iteration scheme	Grid	Remarks
Bailey - Ballhaus ^{11,38}	1972	C or NC	SLOR	Stretched-sheared Cartesian	Wing and wing/body geometries viscous effects (GACAMES ³⁹), embedded grid option
Dornier ^{40,41}	1973	NC	SLOR	Stretched Cartesian	Wing and wing/body geometries
RAE TSP ⁴²	1974	NC	SLOR	Stretched-sheared Cartesian	Wing, wing/body and wing/body/multiple store geometries including nacelles, Viscous effects option ⁴³
NLR TSP ^{60,64}	1975	C or NC	SLOR	Stretched-sheared Cartesian	Wing, body effects simulated
Rae ^{44,45}	1976	NC	SLOR	Stretched-sheared Cartesian	3-D Cascade geometries
Boppe ^{46,47}	1977	NC	SLOR	Stretched-sheared Cartesian	Wing, wing/body, wing/body/multiple store geometries including nacelles and winglets, embedded grid option

TABLE 3.4
Some existing three-dimensional codes using the full potential formulation

Code name	Date	Type of formulation	Iteration scheme	Grid	Remarks
FLO22 ^{12,48}	1974	NC	SLOR	Sheared conformal C mesh	Isolated wing geometries Viscous option available ⁴⁹
Reyhner ^{50,51}	1976	NC	SLOR or MG/SLOR	Sheared Cartesian (nonaligned)	Axisymmetric inlets at angles of attack with and without center bodies
FLO27, FLO28 FLO30 ^{52,53,54}	1977	C	SLOR	Sheared conformal C mesh	Wing and wing/body combination Wind tunnel wall version ⁵⁵
Dassault ⁵⁶	1977		optimal control conjugate grad.	Finite-element	Wing, wing/body and wing/body/nacelle combinations
ONERA ⁵⁷	1978	C or NC	SLOR or AF	Sheared conformal C mesh	Isolated wings
ARA ⁵⁸	1978	NC	SLOR	Sheared conformal O mesh	Wings and wing/body combinations (bodies must have circular cross-section)
Eberle ⁵⁵	1978	C	SLOR	Finite-element	Isolated wings
Chen and Caughey ⁵⁹	1979	C or NC	SLOR	Sheared conformal	Axisymmetric inlets at angle of attack with and without center bodies

TABLE 3.5

Grid features and computing times for several transonic wing computer codes (data taken from Ref. 61)

Code	Wing chordwise grid points	Wing spanwise grid points	Total Field points	Approximate CPU min. (CDC 7600)	Number of iterations
Bailey- Ballhaus (includes grid embedding)	37	25	41,000	6	200
FLQ-22	61 (Root) 40 (Tip)	21	159,000	15	50-100
FLQ-27	51	21	90,000	30	200

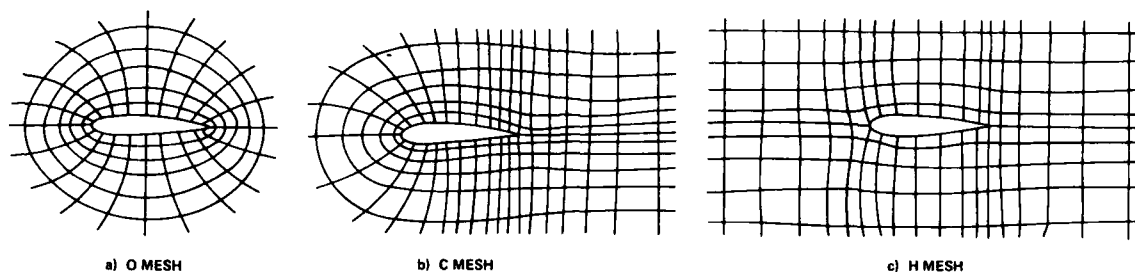


Fig. 3.1 Several surface-fitted airfoil grid topologies

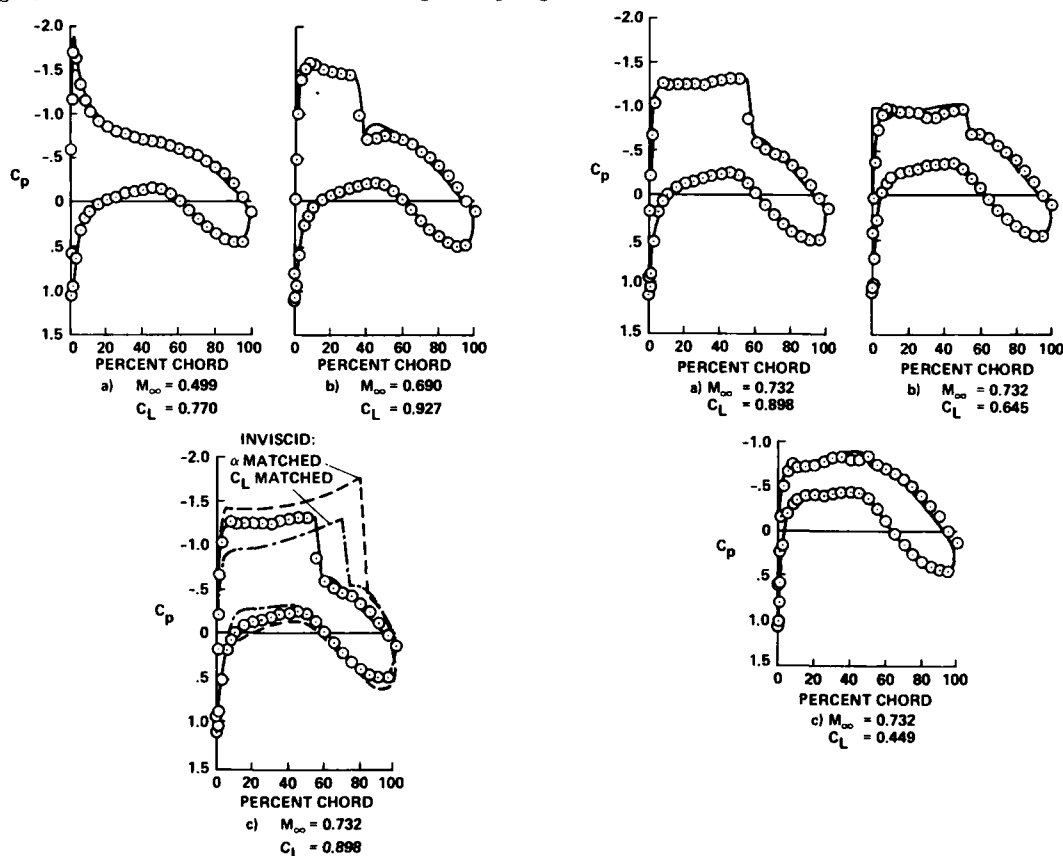


Fig. 3.2 Comparison of calculated and measured pressure coefficient distributions over a range of Mach numbers *or a supercritical airfoil, (Henne [37])

Fig. 3.3 Comparison of calculated and measured pressure coefficient distributions over a range of lift coefficients for a supercritical airfoil, (Henne [37])

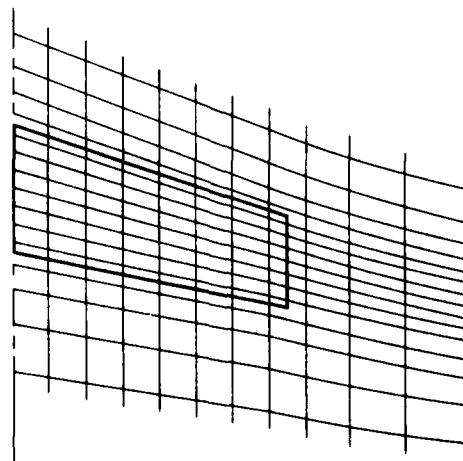


Fig. 3.4 Sketch of a typical sheared Cartesian grid for the TSP formulation, wing planform plane

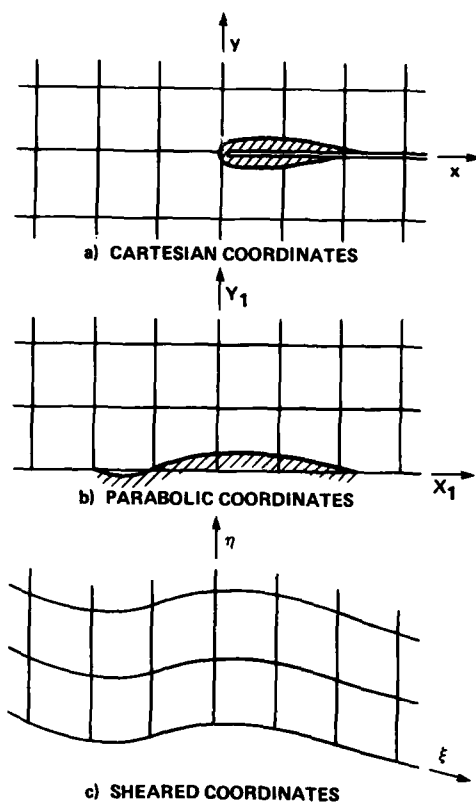


Fig. 3.5 Construction of the sheared parabolic coordinate system used in FLO22, (Jameson, et al. [48])

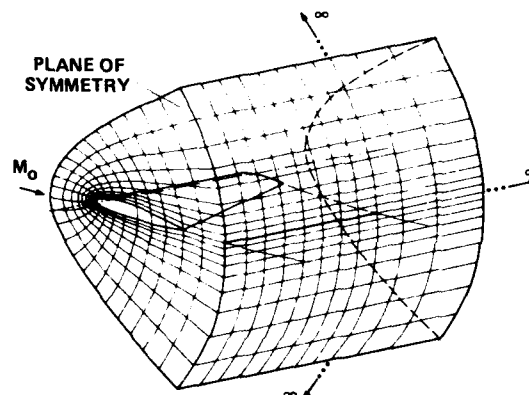


Fig. 3.6 Sheared parabolic coordinate system used in FLO22, (Henne and Hicks [65])

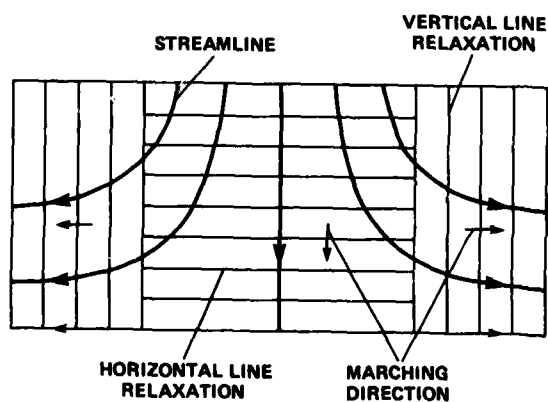


Fig. 3.7 Marching directions of relaxation scheme used in FLO22, (Jameson, et al. [48])

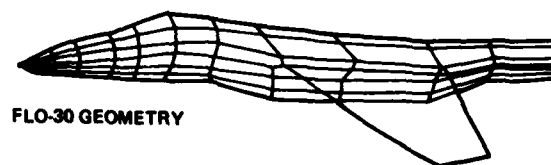
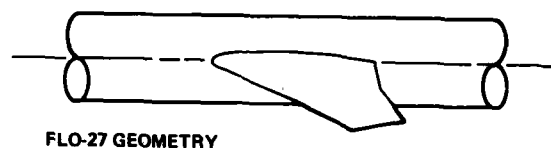


Fig. 3.8 Comparison of the various FLO code geometry modeling capabilities, (Verhoff and O'Neil [66])

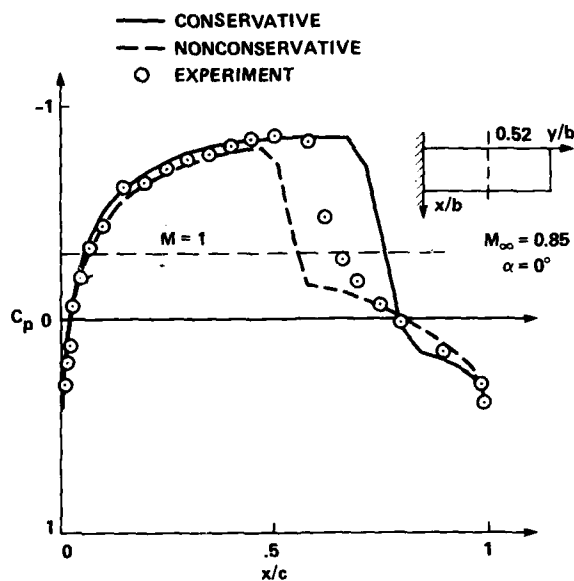


Fig. 3.9 Pressure coefficient comparisons for a rectangular planform NACA 0012 wing, conservative versus nonconservative differencing, (Chattot, et al. [57])

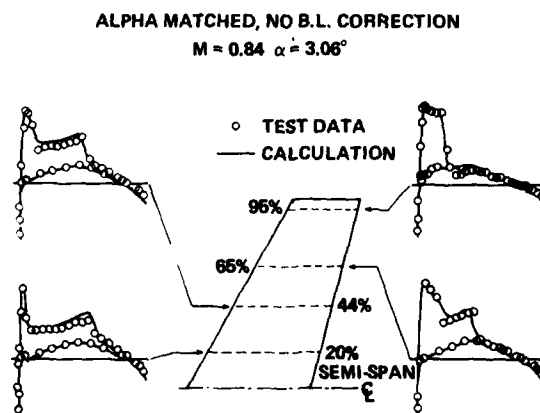


Fig. 3.10 Comparison of FLO22 results with experiment for the ONERA M6 wing, $Re = 18$ million, (Caughey, et al. [67])

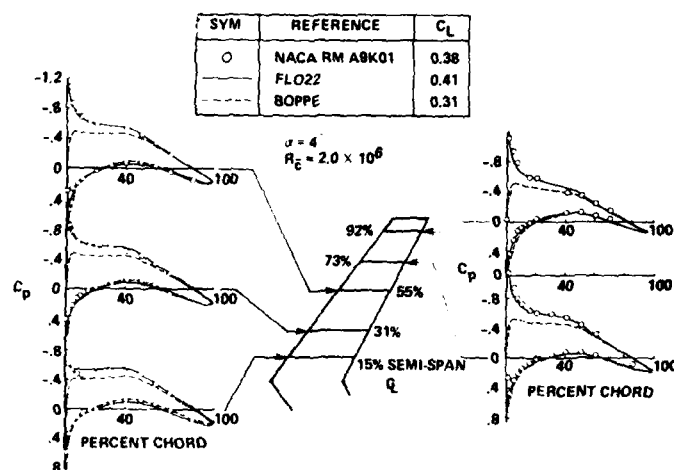


Fig. 3.11 Comparison of calculated and experimental wing pressure coefficient distributions, $M_\infty = 0.6$, $AR = 6$, sweep = 35.18 deg, NACA 64, 212 normal airfoil sections, (Henne and Hicks [68])

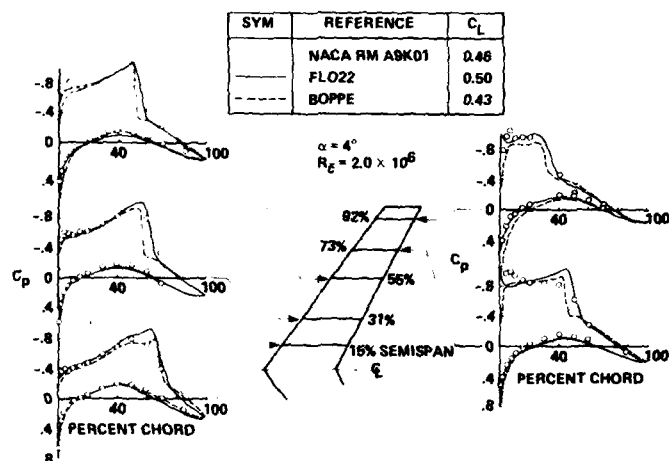


Fig. 3.12 Comparison of calculated and experimental wing pressure coefficient distributions, $M_\infty = 0.85$, $AR = 6$, sweep = 35.18 deg, NACA 64, 212 normal airfoil sections, (Henne and Hicks [68])

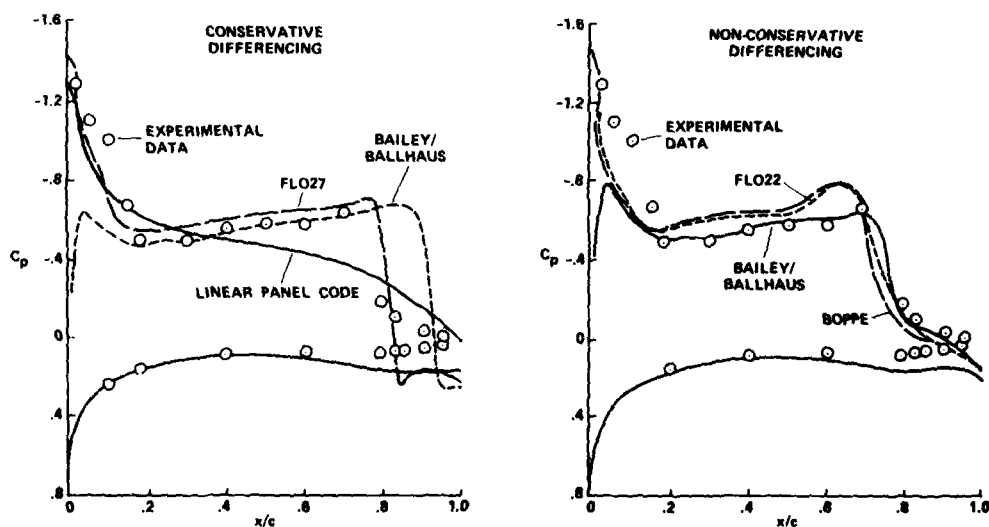


Fig. 3.13 Inviscid pressure coefficient comparisons for an F-16 wing-alone configuration, conservative differencing, $M_\infty = 0.9$, $C_L = 0.6$, 58 % semispan station, (Bhateley and Cox [69])

Fig. 3.14 Inviscid pressure coefficient comparisons for an F-16 wing-alone configuration, nonconservative differencing, $M_\infty = 0.9$, $C_L = 0.6$, 58 % semispan station, (Bhateley and Cox [69])

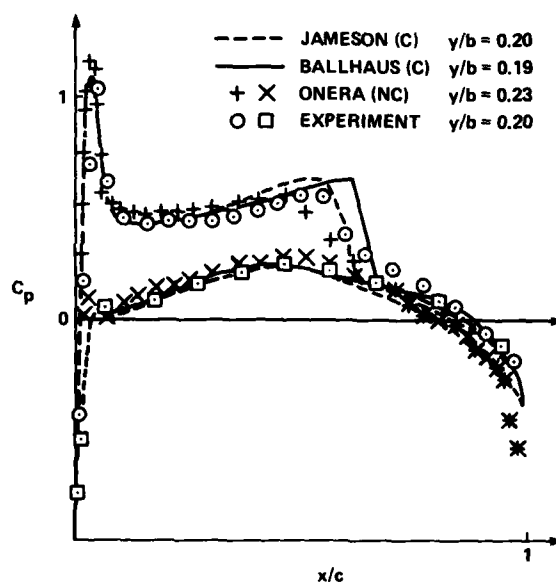


Fig. 3.15 Inviscid pressure coefficient comparisons for the ONERA M6 wing configuration, $M_\infty = 0.841$, $\alpha = 3$ deg, (Chattot, et al. [57])

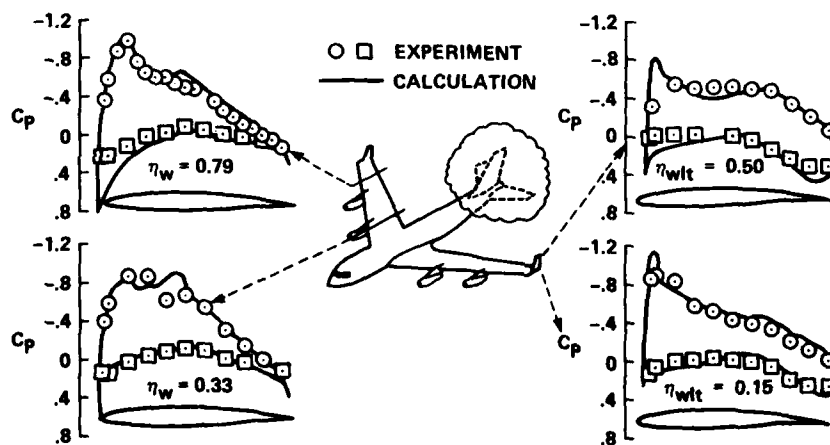


Fig. 3.16 Boeing KC-135 wing and winglet pressure coefficient distribution correlation, $M_\infty = 0.78$ and $\alpha = 2$ deg, (Boppe and Stern [47])

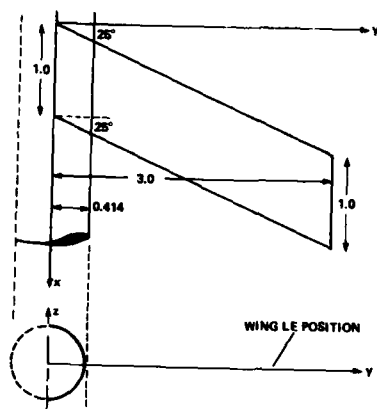


Fig. 3.17 Wing/body configuration details used for the results presented in Fig. 3.18 (Forsey [70])

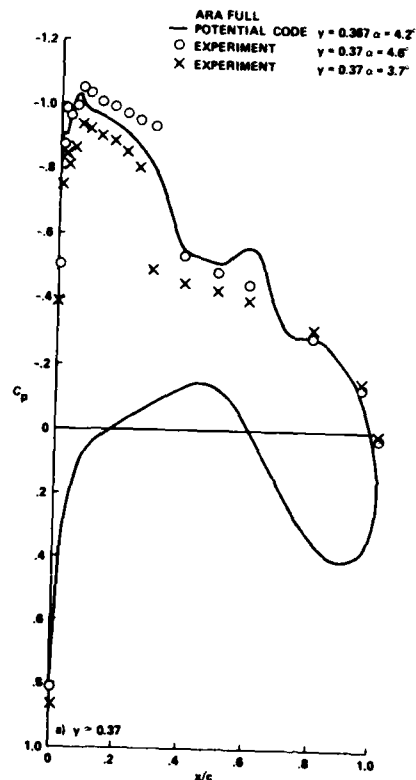


Fig. 3.18a

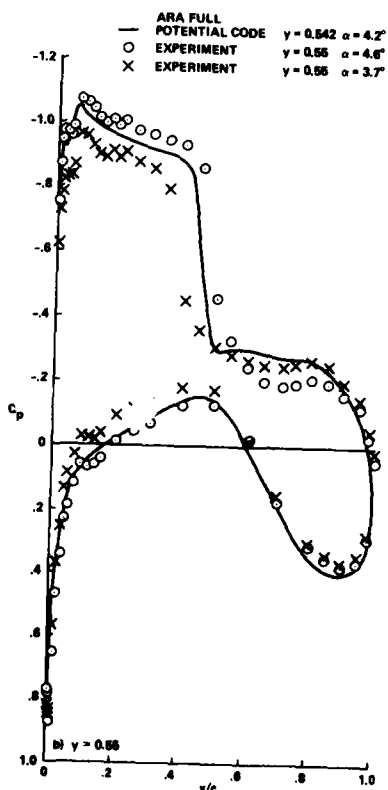


Fig. 3.18b

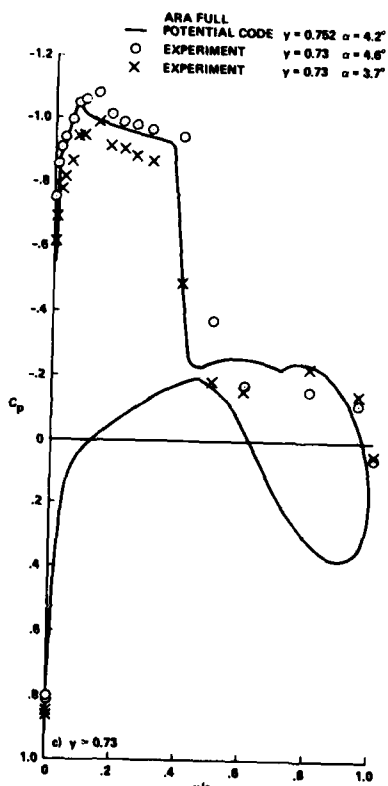


Fig. 3.18c

Fig. 3.18 Pressure coefficient comparison for the configuration of Fig. 3.17, $M_\infty = 0.86$, (Forsey [70])

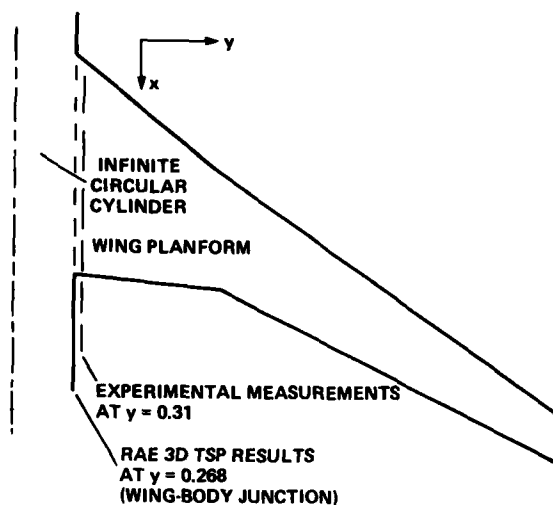


Fig. 3.19 Advanced civil transport wing/fuselage with upper-wing-surface/fuselage fillet used for the results presented in Fig. 3.20, (Albone [72])

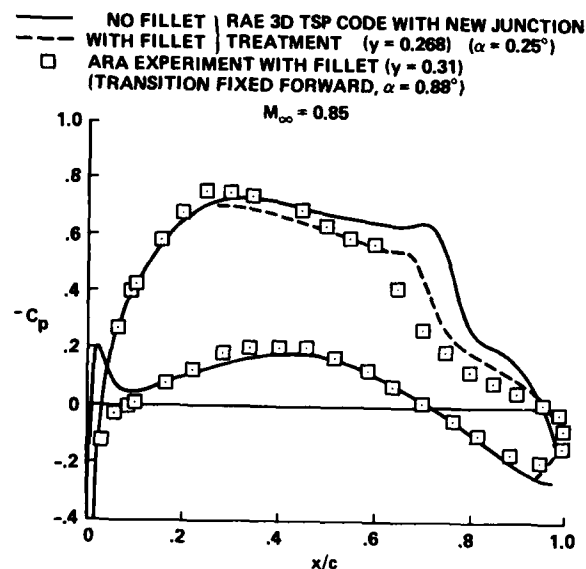


Fig. 3.20 Pressure coefficient comparison for the configuration of Fig. 3.19 (Albone [72])

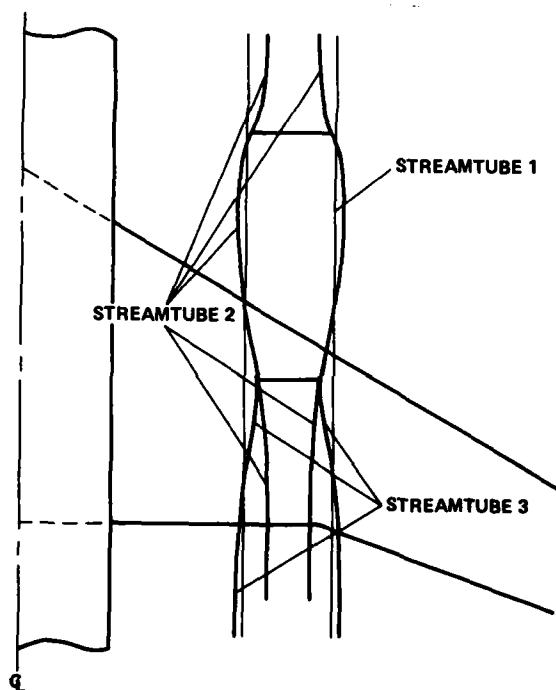


Fig. 3.21 Wing/fuselage/nacelle with three streamtube models, used for the results presented in Fig. 3.22, (Albone [72])

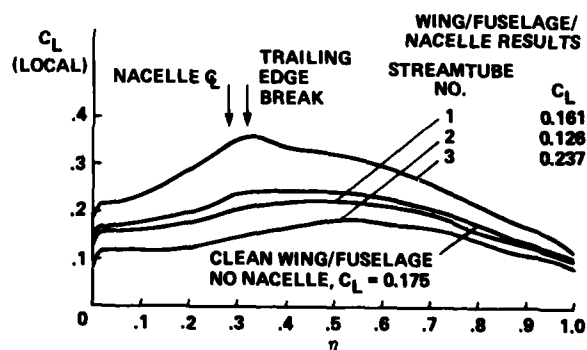


Fig. 3.22 Spanwise variation of lift computed from the RAE 3D TSP computer code for the configuration of Fig. 3.21, $M_\infty = 0.8$, $\alpha = -1.3$ deg, (Albone [72])

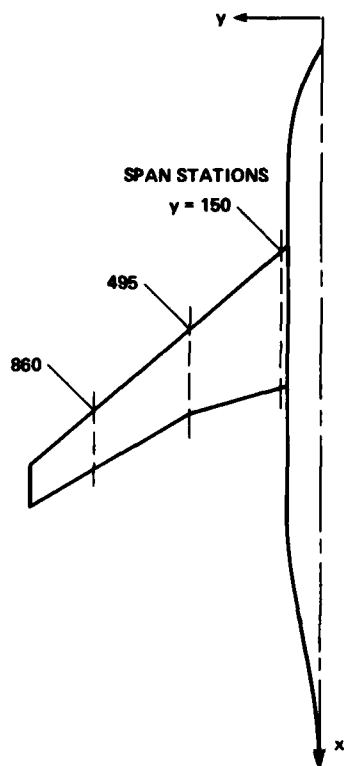


Fig. 3.23 Boeing 747-200 wing/fuselage configuration used to obtain results of Fig. 3.24, (Yu [77])

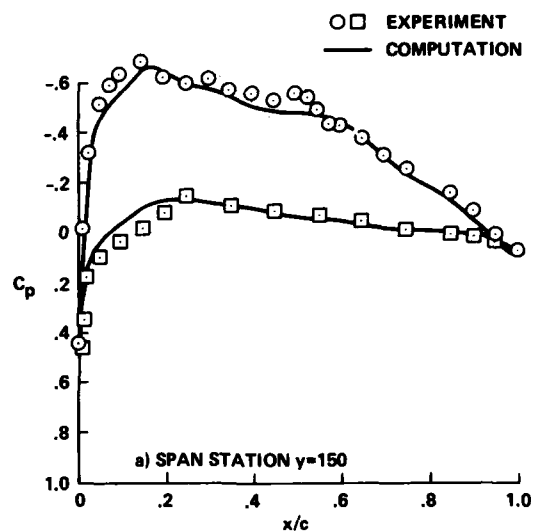


Fig. 3.24a

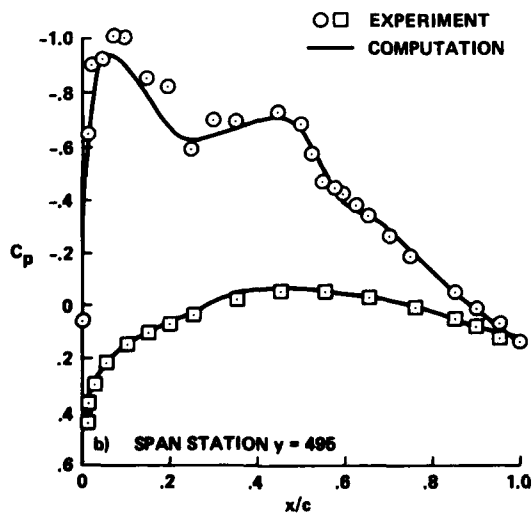


Fig. 3.24b

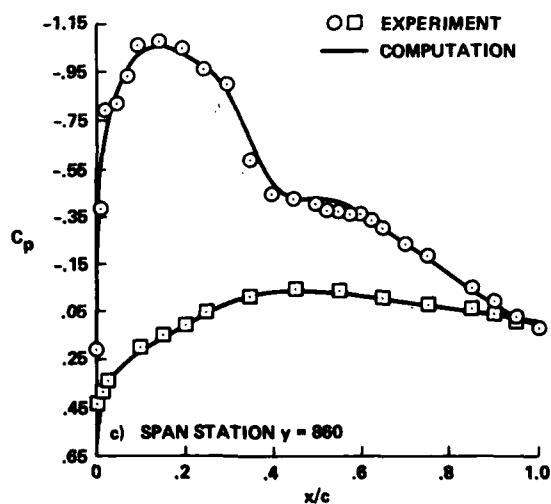


Fig. 3.24c

Fig. 3.24 Pressure coefficient comparisons for the configuration of Fig. 3.23, $M_\infty = 0.84$, $\alpha = 2.8$ deg, with boundary layer, (Yu [77])

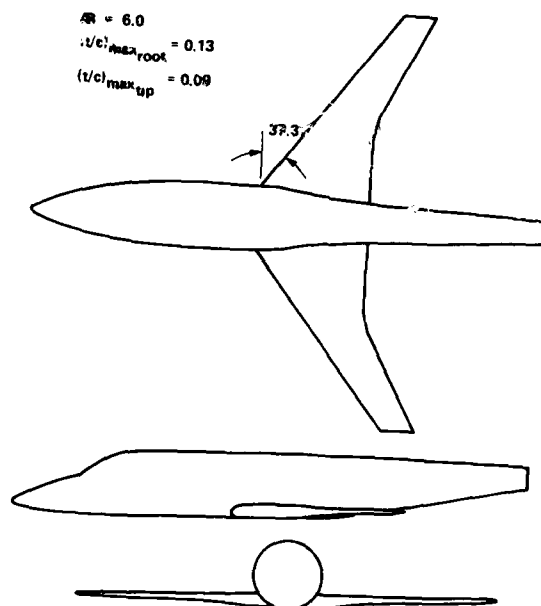


Fig. 3.25 Wing/fuselage configuration used to obtain the results of Figs 3.26 and 3.27, (Hicks [83])

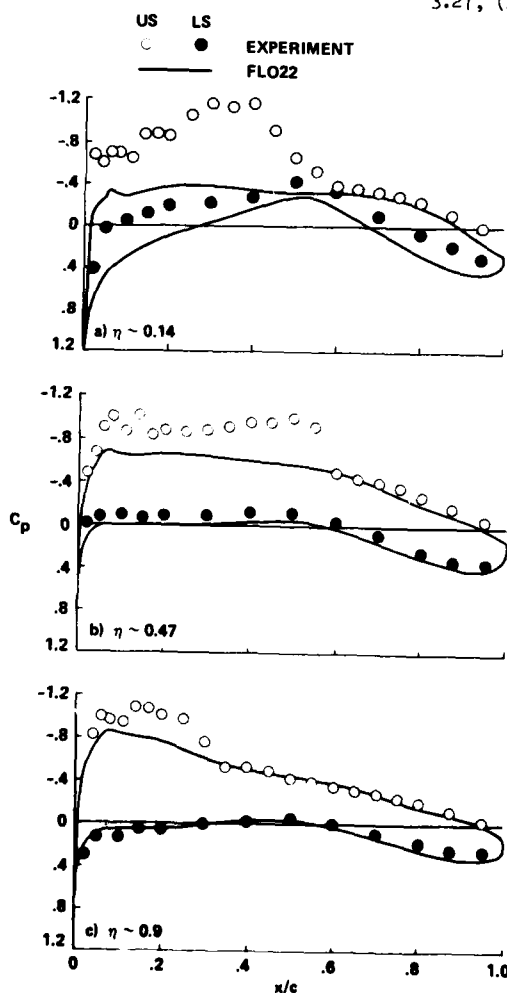


Fig. 3.26 Pressure coefficient comparisons for the configuration of Fig. 3.25, wing-alone code (FLO22) used to simulate a wing/fuselage experiment, $M_\infty = 0.802$, $Re = 2.3$ million, $\alpha = 3.17$ deg, (Hicks [83])

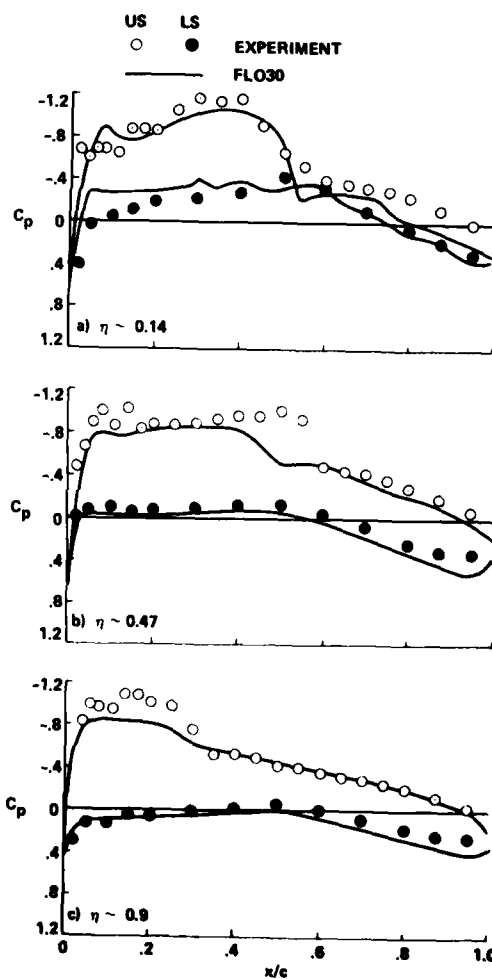


Fig. 3.27 Pressure coefficient comparisons for the configuration of Fig. 3.25, wing/fuselage code (FLO30) used to simulate a wing/fuselage experiment, $M_\infty = 0.802$, $Re = 2.3$ million, $\alpha = 3.17$ deg, (Hicks [83])

LIFT MATCHED, ITERATED 2-D STRIP B. L.

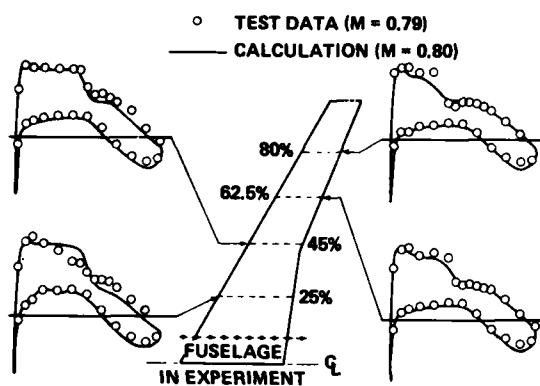


Fig. 3.28 Comparison of FLO22 results with experiment for NASA supercritical wing, $Re = 2.4$ million (Caughey, et al. [67])

LIFT MATCHED, ITERATED 2-D STRIP B. L.

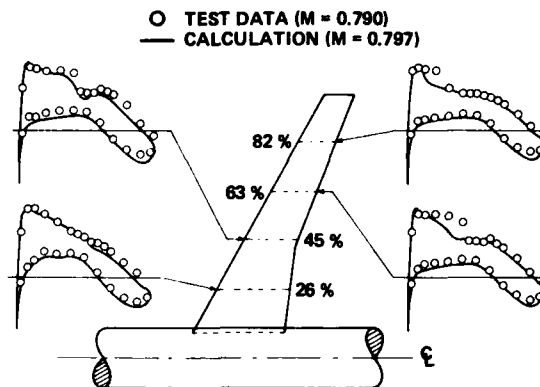


Fig. 3.29 Comparison of FLO27 results with experiment for NASA supercritical wing, $Re = 2.4$ million, (Caughey, et al. [67])

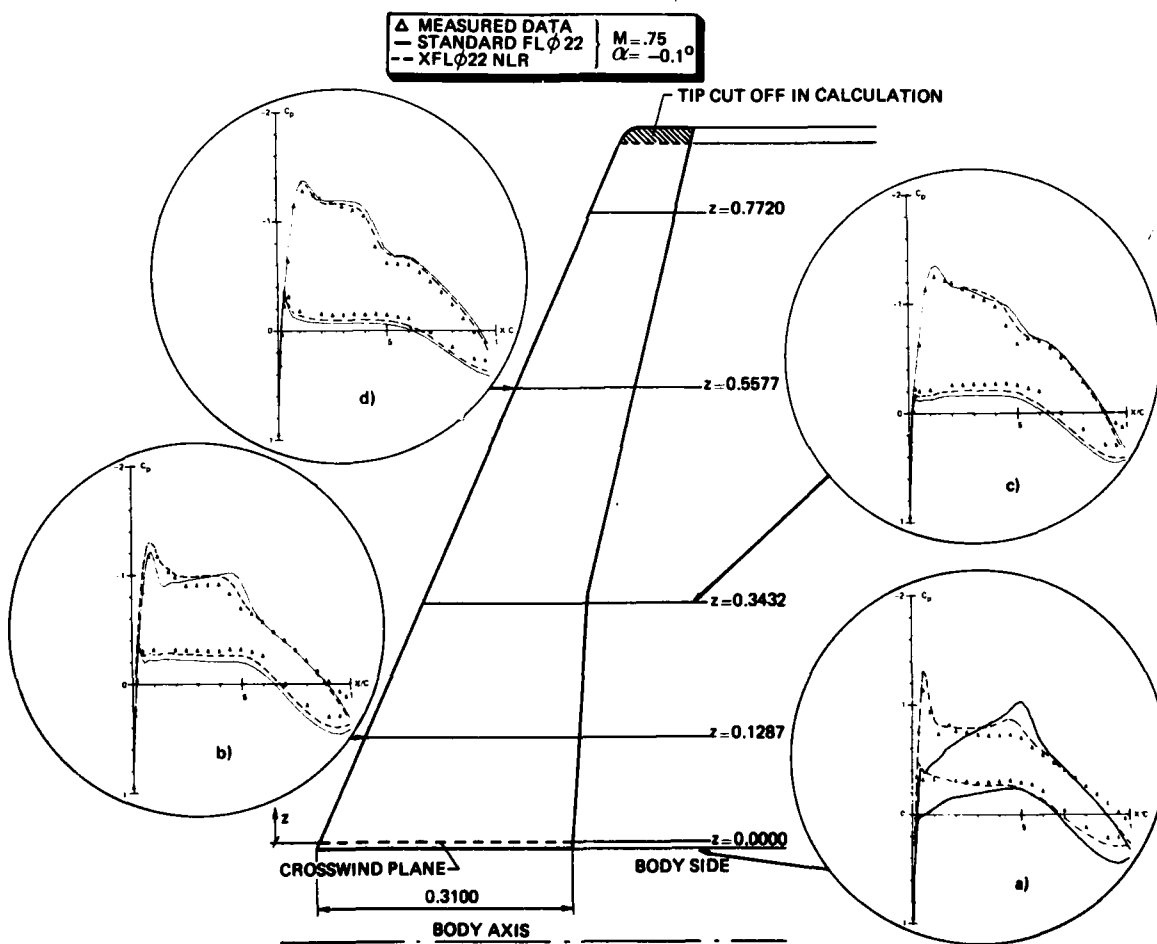


Fig. 3.30 Body plus fillet effect simulation in FLO22 by X-wind from panel method, [89]

4. VISCOUS INTERACTIONS

4.1 Introduction

In transonic flows over airfoils and wings viscous effects play an essential role, greatly affecting the resulting forces and moments. The primary effect is the shock-boundary layer interaction which weakens the shock relative to the inviscid case usually causing a significant upstream displacement of the shock. The difference of the viscous displacement thickness along the aft upper and lower surfaces of the airfoil can alter the loading over the entire airfoil as well as displace the shock. Such aft camber changes have pronounced significance for supercritical airfoils and conventional airfoils at lift with large aft loading. An important viscous interaction can arise at the airfoil trailing edge which modifies the Kutta condition used in inviscid flow to establish the local circulation. Such an interaction is complex, and our understanding of this phenomenon is incomplete presently. Finally the displacement and camber effects of the near-wake can feed upstream to affect the airfoil pressure distribution. These effects are, however, secondary relative to the displacement effects on the airfoil.

For airfoils and wings with small sweep, an adverse chordwise history effect arises when the boundary layer encounters successive adverse pressure gradients such as through a shock and the trailing edge pressure recovery (see Pearcey, Osborn, and Haines, Ref. 1). In this case, the boundary layer thickens, and its velocity profile suffers a loss of fullness after passage through the shock. When the boundary layer then encounters the second adverse gradient in this deteriorated state, it is less able to remain attached, resulting usually in a severe separation and buffet. Such adverse synergism appears primarily in flows over thick airfoils and for conventional airfoils at large lifts where severe aft pressure gradients arise.

In the high subsonic region, leading edge separation is usually not of concern. Here the appearance of severe buffet due to shock-induced and aft separations usually limits the permissible angle of attack to well below that for which leading edge separation occurs.

For wings of larger sweep, an adverse spanwise history effect in the boundary layer arises when a tipward spanwise flow of the low energy air occurs. This progressively thickens and thereby deteriorates the outboard boundary layer: in the tipward direction, promoting premature separation in this region. The consequence is a contribution to a pitch-up instability and a loss of outboard control effectiveness.

Separations on a swept wing can assume the planar bubble type separations where the separated air is confined to the vicinity of the wing surface; but it can also assume the free shear layer type topology unique to 3D flows. Here the separated air, instead of remaining near the wing surface, is swirled into a free vortex which detaches from the surface and trails downstream tied to a streamline. Such free vortex separations can arise in shock-induced separations when the shock is sufficiently swept and sufficiently strong as in the case of the forward shock at high lift. It can also arise together with a bubble type separation occurring only over a portion of the span. Here part-span free separation vortices are shed from each extremity of the bubble. Free separation vortices play a significant role, but unfortunately the boundary layer procedures which we consider are incapable of handling such separations.

During the past several years, there have been important progress in the development of both the planar (2D) and 3D boundary layer methods suitable for transonic applications. It is the primary purpose of the present sections to review selected aspects of these developments. In particular we shall confine our attention to integral boundary layer methods because of their demonstrated ability to yield viable results with significantly less computing time than for example differential equation methods. Procedures to couple the boundary layer and inviscid methods are reviewed, giving examples for both 2D and 3D flows including separated cases.

4.2 Planar viscous interactions

Unquestionably the shock-boundary layer interaction offers the greatest difficulty (see Fig. 1). Here the flow is unsteady due to the interaction of the large scale coherent turbulence with the shock wave. The shock itself penetrates the boundary layer and is non-uniform, weakening and vanishing as it approaches and reaches the sonic line in the lower part of the boundary layer. Through the subsonic path beneath the shock, the shock pressure-rise is attenuated (See laser velocimeter measurements of East, Ref. 2).

Our goal is not the calculation of the complex flow sketched above, but the determination of the time-averaged flow yielding the pressure distribution as measured for example by pressure taps in a wind-tunnel test. For such a flow it is clear that the boundary layer approximations are invalid. Local analytical solutions for the shock-boundary layer interaction have therefore been proposed isolating the boundary layer and solving the resulting flow with an asymptotic form of the Navier-Stokes equations in a triple-deck domain. (See Melnik Ref. 3 for a recent review.) There is, however, a fundamental difficulty in posing the strong interaction problem in this isolated manner. By definition in a strong interaction flow there is an essential coupling between the inviscid and viscous flows precluding any possibility of isolating either of the flows. In isolating the boundary layer flow in the triple deck solution, the difficulty arises in defining the boundary condition to be the prescribed at the outer edge of the boundary layer where the flow is a function, not only of the local flow, but of the global strong interaction flow. It is clear that the normal shock pressure distribution from the inviscid solution used above is inappropriate. More appropriate here might be to prescribe the oblique shock pressure distribution with a near-sonic post-shock pressure measured along the airfoil surface, but here pressure gradients across the boundary layer would degrade such a prescription.

Matched asymptotic solutions were also used for the strong interaction between the inviscid and viscous flows about the trailing edge of the airfoil (Ref. 3). Here also the viscous flow greatly distorts the inviscid solution, so that it will be difficult to formulate the problem for only the viscous portion of strong interaction flow. Here the boundary condition at the outer edge of the boundary layer must reflect to first order the strong interaction effects.

Green's lag entrainment integral boundary layer method (Ref. 4), despite being based upon the boundary layer approximations, has recently yielded reasonable results for complex transonic viscous interactions including those with separations (Ref. 5). It is thus an attractive procedure for use in applications for the near term, and in the present section we shall first briefly review its principal features and describe several procedures coupling it to inviscid methods.

4.2.1 Green's lag entrainment method

This procedure comprises a system of three first order ordinary differential equations, two of which are obtained by integrating the continuity and streamwise momentum equations across the layer, while the third is derived from the Bradshaw-Ferriss turbulent energy equation.

A form of these equations derived by East, Smith, and Merryman (Ref. 5) is convenient to describe important features of the equations. In the direct form one has

$$\delta_x^* = F_1 + F_2 U_{e_x} \quad (4.1)$$

or by rearranging terms, one has the inverse form

$$U_{e_x} = F_2^{-1}(\delta_x^* - F_1) \quad (4.2)$$

Here U_e is the inviscid outer velocity, δ^* is the displacement thickness, x the streamwise coordinate, F_1 and F_2 are functions of the boundary layer variables, and the subscript denotes differentiation. The above equation is supplemented by a sufficient number of the original equations to obtain a fully determined set of equations. The labelling of the above equations is primarily for identification purposes.

The above equations are also applicable for the wake when the skin friction coefficient is set equal to zero, and a dissipation length scale parameter is halved to obtain the proper asymptotic far field wake. The wake is usually treated in an approximate but adequate manner by dividing it into two independent parts. Here each part is considered as half of a symmetric wake which patches onto the upper or lower surface boundary layer in a continuous fashion at the trailing edge.

4.2.2 Inviscid-viscous flow coupling

The problem on hand is complex and involves a transonic inviscid flow boundary value problem in which the boundary layer and wake equations constitute boundary conditions along the airfoil and contact jump conditions along the rear wake. Classically this problem is solved in an iterative fashion treating the inviscid and boundary layer flows as separate problems. The inviscid solution over the airfoil is taken as the first approximation. The resulting pressure distribution is then input into the boundary layer and wake equations, which are solved to yield for example the displacement thickness. The latter is used to define a new effective "shape" of the airfoil, which is then used to upgrade the inviscid solution.

The above procedure can be made to converge even with shocks present so long as the boundary layer is not separated. When separation occurs, the procedure diverges. The cause can be seen in equation (4.1). With separation the absolute magnitude of F_2 assumes very large values. Small errors in the pressure distribution will therefore lead to large changes of the displacement thickness, so that the above iterative process then ceases to converge. As pointed out more recently by East, Smith, and Merryman (Ref. 5), Green's equations in this case must be posed in the inverse form as given by equation (4.2). That is, the viscous problem is to be posed such that the pressure gradient is determined for a given displacement thickness input.

To be complementary, the inviscid problem may also be posed in the inverse or design mode; namely, determine the airfoil slopes given the pressure distribution. The resulting iterative procedure with the boundary layer and inviscid flows posed in the inverse fashion is, however, difficult to carry out. This is due to the difficulty of determining an adequate initial guess for the displacement thickness or the pressure distribution when the shock location is not known to assure a convergent iteration. Procedures to circumvent this difficulty will be described in a latter section.

4.2.3 Weak coupling with exact potential methods

Two recent noteworthy contributions coupling Green's integral viscous equations with the exact potential equation are due to Melnik (Ref. 3) and Collyer and Lock (Ref. 6). These methods have several elements in common, both using the relaxation method of Bauer, Korn, Garabedian, and Jameson for the inviscid flow and the weak interaction iterative procedure described above. They are thus restricted to unseparated flows. The boundary layer displacement here was incorporated as an equivalent source distribution on the base airfoil, thus precluding the need to generate a new mesh after each change of the effective airfoil shape.

Melnik's procedure differed from that of Collyer and Lock by the incorporation of an analytically derived modification of the trailing edge flow using matched asymptotic expansions discussed earlier. A fully conservative shock capture procedure was used by Melnik, but a weighed average of the conservative and non-conservative shock point operators was used by Collyer and Lock to compensate for the potential approximation to the shock jump conditions. The introduction of the non-conservative portion of the shock point operator can lead to some inconsistencies due to the non-telescoping (non self-cancelling) of the shock profile truncation errors. Moreover such compensations are usually unnecessary since viscous interactions usually weaken the shocks sufficiently to permit the potential flow approximation to the shock jump conditions. Both methods include a pressure jump across the wake for the curvature effect of the wake, the latter, however, calculated in the approximate fashion described earlier.

For the unseparated cases considered, both methods yielded results comparing well with experiments when the angle of attack and/or the Mach number were adjusted such that the lift was matched in the comparison. In figure 2 is shown the test-theory agreement for a Whitcomb supercritical airfoil obtained by Melnik. In figure 3 is shown the test-theory comparison for the RAE 2822 airfoil obtained by Collyer and Lock with comparable agreement, not only in the pressure distribution, but also for the boundary layer variables.

The above excellent test/theory agreement obtained both by Melnik and Collyer and Lock is impressive, but the adjusting of the Mach number and/or the angle of attack in the respective calculations to match the measured lift clouds the assessment of the two methods. An evaluation of computational methods must await wind tunnel results for example with the wall interference fully defined.

There is, however, one question that must be resolved in the above procedures. In the calculation of the inviscid flow with a difference algorithm, shock waves are captured with a profile and a thickness that are mesh size dependent being generated by truncation error viscosity. Typically the shock profile is spread over three meshes. Use of such an unphysical pressure gradient would suggest an

unphysical shock-boundary layer interaction. However, calculations with Green's equations in the direct form show that when the boundary layer is attached, for a given pressure rise across the shock, the post-shock values of the boundary layer variables are closely invariant with respect to the thickness of the shock. That is, halving the shock thickness, doubles the pressure gradient but halves the integration interval, resulting in the near-invariant post-shock boundary layer variables. Thus the mesh-dependent shock pressure rise profile will not be of concern, provided of course the above invariant values are meaningful.

4.2.4 Strong coupling with the small disturbance inviscid method

Le Balleur (Ref. 7) and more recently Wai and Yoshihara (Ref. 8) coupled the integral boundary layer method with the small disturbance relaxation method. These methods suffer relative to those described in the previous section in the use of the small disturbance approximation for the inviscid flow. On the other hand an attempt was made in these methods to treat separated flows.

Consider first Le Balleur's semi-direct method for the separated cases. Here an iterative coupling procedure was used where the viscous equations were formulated in the inverse form as appropriate for the separated case. However, to avoid the problem of initiating the iterative procedure in the inverse mode described earlier, the inviscid flow was posed in the direct mode. With an initial guess for the airfoil slopes and the displacement thickness, the inviscid and viscous problems were each solved to yield pressure distributions which in general would not match. By a local linear inviscid analysis, changes of local shape compensating for the above differences of the pressure were determined. These shape changes suitably under-relaxed were then used to upgrade the shape inputs.

Variants of Le Balleur's procedure have also been used for example by Carter (Ref. 9) and Wigton and Holt (Ref. 10). These procedures have yielded reasonable results for attached cases with significantly less success for separated cases. The latter most probably is due to the failure of the linear displacement thickness correction in the non-linear shock region.

In the method of Wai and Yoshihara (Refs 8 and 11), the small disturbance line relaxation method (TSFOIL code) is used for the inviscid flow. Instead of the iterative procedures for the viscous-inviscid coupling of the previous methods, the viscous equations were prescribed directly as a boundary condition for the inviscid flow calculations. With the displacement slopes added, the airfoil tangency condition becomes

$$\varphi_y = f_x + \delta_x^* \quad (4.3)$$

where φ is the perturbation potential, y the transverse coordinate, $y = f(x)$ defines the airfoil, and the subscripts denote differentiations. If one now inserts the displacement slopes from equation (4.1) into equation (4.3), one obtains the required viscous tangency condition for the airfoil given by

$$\varphi_y = f_x + F_1 + F_2 \varphi_{xx} \quad (4.4)$$

Here F_1 and F_2 are functions of the boundary layer variables, which in a given relaxation step, must be evaluated from the previous iteration.

In the above procedure there are no iterations performed between the inviscid and boundary layer flows as in the weak interaction case, so that a distinction between the inverse and direct formulations does not arise. The above procedure may thus be used for both attached and separated cases.

The above procedure was used to calculate the flow over the RAE 2822 airfoil at $M = 0.75$, angle of attack 3.19° degrees, and the chord Reynolds number of 6.2×10^6 (61 cm chord). Experiments (Ref. 12) showed this to be a case with shock-induced separation with reattachment just upstream of the trailing edge.

In figures 4 and 5 the calculated and experimental results are compared. Reasonably good agreement in the pressure distribution is seen here, but the displacement thickness is overpredicted. Calculations furthermore do not predict reattachment undoubtedly due to the overprediction of the displacement thickness. Here the good test/theory agreement of the pressure distribution despite the poor agreement in the post-shock displacement thickness is not inconsistent with the stiff property of Green's equations in separated flow described earlier. In general the test/theory comparison shown here is good, but further refinement of the interaction procedure as well as in the boundary layer equations is needed.

4.3 Three dimensional viscous interactions

Both three dimensional (3D) integral as well as differential equation boundary layer methods have demonstrated their ability to yield viable results with reasonable computing times (for example see Refs 13 and 14). In the following we shall restrict our consideration to the integral methods which have yielded comparable results with less computing times relative to differential equation methods.

4.3.1 Integral boundary layer methods

In the following we shall review the general features of 3D integral methods as typified by those of Smith (Ref. 15) and Stock (Ref. 16) both based on the earlier method of Myring (Ref. 17). The starting point is the set of two momentum equations and the continuity equation, simplified in the boundary layer limit. The velocity components are taken along and normal to the outer inviscid streamlines, while generalized curvilinear coordinates are used for the independent variables. Here the streamwise component of the velocity was selected to carry over the planar experience. The choice of the non-orthogonal coordinate system permits a flexibility to tailor the grid system to the problem on hand.

The final form of the equations are obtained by integrating the set of equations across the layer. The resulting integral terms are then evaluated by postulating profiles for both velocity components and eliminating the density by the Illingsworth-Stewartson transformation where the integration differential element is scaled by the density.

For the entrainment function appearing in the integral continuity equation, both the local and lag models were carried over from the planar case.

The final equations form a set of three first order quasi-linear partial differential equations for five dependent variables, for example, for the streamwise momentum thickness, the compressible form factor (H), the angle β between the outer and limiting surface streamlines, and the two components of the

inviscid velocity at the edge of the boundary layer.

As in the planar case, the above set of boundary layer equations are in principle fully determinate when they are posed as a boundary condition along the wing surface and contact jump conditions along the wake for the transonic inviscid problem. In this form the boundary layer equations of themselves cannot be characterized, for example, with respect to their characteristics, as in a fully determinate set of first order quasilinear partial differential equations.

In the iterative procedure between the inviscid and boundary layer flows, the equations for the latter are made determinate by considering two of the five dependent variables as known inputs. Thus in the direct case, the two components of the outer velocity are considered as inputs. In this case, a fully determinate set of equations results which is found to be fully hyperbolic. Three sets of characteristics arise, two of which conform approximately to the outer and limiting streamlines, while the third lies in between. With the problem fully hyperbolic in the direct case, the formulation and solution of the problem are straightforward. Hence the method of characteristics forms a reliable guide (Ref. 18). Thus initial or starting conditions must be furnished along a space-like line near the wing leading edge where the values of the dependent variables must be prescribed. Additionally boundary conditions must be prescribed along time-like boundaries as along the wing centerline or the tip chord when the range of influence of these boundary points falls onto the planform. Here the number of data to be prescribed equals the number of characteristics pointing into the planform.

Thus in the case of the wing alone, the wing centerline is an outer streamline and hence a characteristic. The other two characteristics, including the limiting streamline, point into the planform, so that two conditions must be prescribed; and these are furnished by the centerline symmetry conditions. The situation for the wing-fuselage configuration is more complex since the fuselage boundary layer, and in particular the wing-fuselage juncture boundary layer, must be taken into account. Because of our present inability to calculate the latter in an expedient fashion, the inboard boundary condition must be approximated. In reference 16, for example, wing-alone centerline symmetry conditions were used. The resulting error, so far as the direct boundary layer problem is concerned, is confined to the narrow range of influence bounded by the wing centerline and the limiting streamline characteristic from the wing apex. So far as the overall solution is concerned, however, the effect of the juncture boundary condition extends further onto the wing through the inviscid flow. Thus, for example, the effects of a shock wave on the wing interacting with the juncture boundary layer can extend well beyond the above range of influence.

A difficulty also arises for the boundary condition at the wing tip. In the lifting case a separation vortex appears when the tip is sufficiently sharp or the lift sufficiently high, necessitating the simultaneous consideration of the boundary layer on both sides of the wing. Moreover, the 3D boundary layer methods in consideration are incapable of treating such a flow. Thus an approximate treatment of the tip flow must be made. The boundary layer calculations can be marched independent of the tip condition to the outer streamline characteristic bounding the range of influence of the tip. In the latter inaccessible region, the boundary layer variables must then be approximated in a benign fashion, for example, by a simple outboard extrapolation. The resulting consequences should not be great, since the region is usually small, and the error should not extend much beyond the narrow range of influence of the tip chord.

For the direct problem formulated above, a reliable numerical procedure is the method of characteristics. Here the characteristic coordinates are constructed in the process of the solution, and their use insures the proper domain of dependence. It is, however, more expedient to carry out a finite difference marching process in a suitably chosen direction. In the references mentioned above an explicit difference scheme was employed, and this should suffice for present applications since the overall computing times are usually relatively insignificant. Significant reductions of computing time can, of course, be achieved by using well-established implicit schemes as the alternating direction methods if future applications necessitate reduction of the computer time.

Difficulties in the marching procedure for the direct problem can be anticipated from the more familiar analogous problem of the planar rotational supersonic inviscid flow. Here the Mach waves correspond to the outer and limiting streamline characteristics. In the supersonic flow, it is well-known that compressive Mach waves of one family can coalesce forming a cusped envelope and an overlapping flow. Flow discontinuities in the form of shock waves and contact (slip) surfaces can also arise as permissible weak solutions. The above Mach wave envelope anomaly is then precluded by the appearance of a shock wave.

In principle, the above solution features can formally arise also for the 3D integral boundary layer equations in the direct form. For example, an envelope of the limiting streamline characteristics is suggested in the calculated results shown in figure 6 from reference 19. Such an envelope in the boundary layer implies a need, not of a shock wave type discontinuity, but more likely of a contact surface. With the correct outer velocity input, this envelope is suggestive of a separation line. In such a case, the "reversed" flow downstream of the separation line must be marched upstream towards the separation line, posing a difficult numerical problem.

To resolve this difficulty, the inverse formulation of the boundary layer equations was suggested (Refs 19 and 20). Here the outer velocity components are now considered as dependent variables, and two of the boundary layer variables are considered as inputs. In the next section a successful example of the indirect procedure for a separated case is given. It is thus clear that in the indirect formulation the nature of the differential equations and the characteristic families must be significantly altered. It would be of interest to derive the resulting characteristics for the indirect equations. Finally it will be of importance to determine the physical significance, if any, of the possible discontinuities of the 3D integral boundary layer equations which must be expressed in the proper conservation form for this purpose. Though straightforward, these significant analyses have not appeared in the published reports.

4.3.2 3D coupling examples

There are but few cases reported for the viscous interactions arising for a wing or a wing/fuselage configuration. One recent example is due to Firmin (Ref. 21) who treated a wing/fuselage configuration and incorporated a wake calculation. Here the inviscid flow was calculated by the RAE small disturbance line relaxation method which did not capture the shock conservatively; and the boundary layer and wake flows were computed with the method of Smith with lag entrainment. The two flows were coupled by the weak interaction procedure.

The sheared coordinate transformation was used for the inviscid flow in which the wing planform is mapped to a rectangle. Essentially the same coordinate system was used for the boundary layer and wake.

For the boundary layer, the initial conditions were prescribed along a line downstream of the leading edge where the prescribed values were calculated assuming an infinite yawed wing boundary layer. Only the wing boundary layer and wake were computed, inputting wing-alone symmetry conditions at the wing-body juncture. The boundary layer and wake were extrapolated to their outboard side edges by one-sided inboard differences. A marching scheme with an explicit difference scheme was used with the boundary layer updated and relaxed after each ten iterations of the inviscid flow. Overall the computing time was found to be approximately doubled by the addition of the viscous effects.

Several cases were calculated by Firmin, and in figure 7 one of the cases is shown where the calculated pressure distributions are seen to compare well with experiments.

Comparable test-theory comparisons were obtained by Stock (Ref. 20) for several wing planforms.

There have been several calculations with the indirect procedure demonstrating its ability to calculate separated flows. These are due to Cousteix and Houdeville (Ref. 19) and Stock (Ref. 20) who treated the case of an infinitely yawed flat plate with 35 degrees yaw at incompressible velocities. This case was tested by Van den Berg and Elsenaar (Ref. 22). The latter measured all of the dependent variables appearing in the 3D integral boundary layer equations. The inverse method was then tested by inputting two of the measured boundary layer variables, and then calculating the remainder of the dependent variables and comparing them to the measured values. (Note that the above calculation was carried out earlier by Elsenaar et al., Ref. 23, by the differential equation method.)

The above two calculations were carried out for different free stream velocities so that they cannot be compared. Both results compared well with experiments. In figure 8 is shown the excellent test-theory agreement obtained by Stock. Compared are the streamwise momentum thickness θ_{11} , the skin friction coefficients, angle between the outer and limiting streamlines β , and the outer velocity vector in polar representation. In the above figures the calculated and measured separation points are shown.

For most of the procedures described above for the direct problem, the cross-flow velocity profile is defined in terms of the streamwise profile as in the frequently used Mager's cross-flow profile. In the case of separated flow such cross-flow profiles would be inappropriate since the cross-flow velocity profile would reverse when a reversal occurred in the streamwise profile. To circumvent this conceptual difficulty, in the above calculation, Stock (Ref. 20) decoupled the streamwise and "transverse" velocity profiles and introduced an empirically based "flat plate" profile in the transverse direction defined by the local isobar.

The above computations did not involve the inviscid flow, serving only as a consistency check for the boundary layer equations and a feasibility test of the indirect procedure. There still remains the task of devising a suitable and expedient procedure to couple the boundary layer and inviscid flows for the separated case.

4.4 Concluding remarks

The above brief review has illustrated some of the recent achievements in computing transonic viscous interactions. Though further development is required for the planar separated cases, the future effort most in need is for the 3D viscous interactions arising in wing-fuselage configurations.

Because of their complexity, 3D transonic turbulent flows must be treated phenomenologically for the near future. Experiments are thus needed to improve the definition of the turbulence including the entrainment phenomena particularly for the separated case; to improve the modelling of the 3D shock-boundary layer interactions; and finally to provide a reliable comparison base to assess the computational methods. In the latter, results free of wall interference are not necessary, so long as the conditions along the walls are measured to be inputted as wall boundary conditions in the computations.

The present review is not intended to be complete. Many excellent investigations are omitted, and these are described and referenced in the more complete reviews of references 3, 7, 14 and 24.

4.5 References

1. Percy, H., Osborn, J., and Haines, B., The interaction between local effects at the shock and rear separations - A source of significant scale effects in wind tunnel tests on aerofoils and wings. AGARD CP No. 35, 1968.
2. East, L.B., The application of a Laser anemometer to the investigation of shock-wave boundary-layer interactions, AGARD CP-193, 1976.
3. Melnik, R., Turbulent interactions on airfoils at transonic speeds-recent developments, AGARD CP 291, 1980.
4. Green, J., Weeks, D., and Brooman, J., Prediction of turbulent boundary layers and wakes in incompressible flow by a lag-entrainment method, RAE R and M 3791, 1973.
5. East, L., Smith, P., and Merryman, P., Prediction of the development of separated turbulent boundary layers by the lag-entrainment method, RAE report 77046, 1977.
6. Collyer, M., and Lock, R., Prediction of viscous effects in steady transonic flow past an airfoil, *Aero Quart.*, 30, p. 485, 1979.
7. Le Balleur, J.C., Calcul des écoulements a forte interaction visqueuse au moyen de methodes de couplage, AGARD CP 291, 1980.
8. Wai, J., and Yoshihara, H., Planar transonic airfoil computations with viscous interactions, Proceedings 7th International Conference on numerical methods in fluid dynamics, Stanford University and NASA-Ames, 1980.
9. Carter, J.E., A new boundary-layer inviscid iteration technique for separated flow, AIAA CFD Conference (Williamsburg), 1979.
10. Wigton, L., and Holt, M., Viscous-inviscid interaction in transonic flow, AIAA Fluid and Plasma Dynamics Meeting (Palo Alto), 1981.
11. Wai, J., and Yoshihara, H., Planar transonic airfoil computations with viscous interactions, AGARD CP 291, 1980.
12. Barche, J. (Editor), Experimental data base for computer program assessment, AGARD AR 138, 1979.
13. Humphreys, D.A., Comparison of boundary layer calculations for a wing: The May 1978 Stockholm Workshop Test Case, FFA TN AE-1522, 1979.
14. Kordulla, Wilhelm, Calculation of 3-D transonic flows - Survey of recent developments including viscous flows, VKI LS 1980-6, March 1980.

15. Smith, P.D., An integral prediction method for three-dimensional compressible turbulent boundary layers, ARC R and M 3739, 1979.
16. Stock, H., Eine Integralmethode zur Berechnung dreidimensionaler, turbulenter inkompressibler Grenzschichten, Dornier Report 77-16, 1977.
17. Myring, D.F., An integral prediction method for three-dimensional turbulent boundary layers in incompressible flow, RAE TR 70147, 1970.
18. Courant, R., and Friedrichs, K., Supersonic flow and shock waves, Interscience Publishers, 1948.
19. Cousteix, J., and Houdeville, R., Analogie des singularités dans les methodes directs de calcul des couches limites tridimensionnelle stationnaire et bidimensionnelle instationnaire-analyse des modes inverses, AGARD CP 291, 1980.
20. Stock, H., Ablöseverhalten von Grenzschichten an dreidimensionalen Flügeln, Dornier Report 79/41 B, 1979.
21. Firmin, M.C.P., Calculations of transonic flow over wing/body combinations with an allowance for viscous effects, AGARD CP 291, 1980.
22. Van den Berg, B., and Elsenaar, A., Measurements in a three-dimensional incompressible turbulent boundary layer in an adverse pressure gradient under infinite swept wing conditions, NLR TR 72092 U, 1972.
23. Elsenaar, A., Van den Berg, B., and Lindhout, J.P.F., Three-dimensional separation of an incompressible turbulent boundary layer on an infinite swept wing, AGARD CP.168, 1975.
24. Lock, R., A review of methods for predicting viscous effects on aerofoils and wings at transonic speeds, AGARD CP 291, 1980.

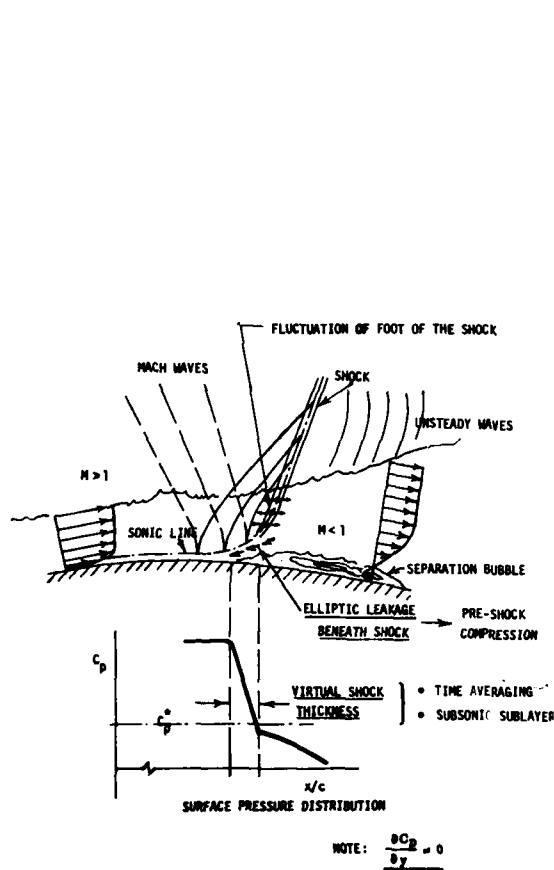


Fig. 4.1 Complexities of the shock-boundary layer interaction

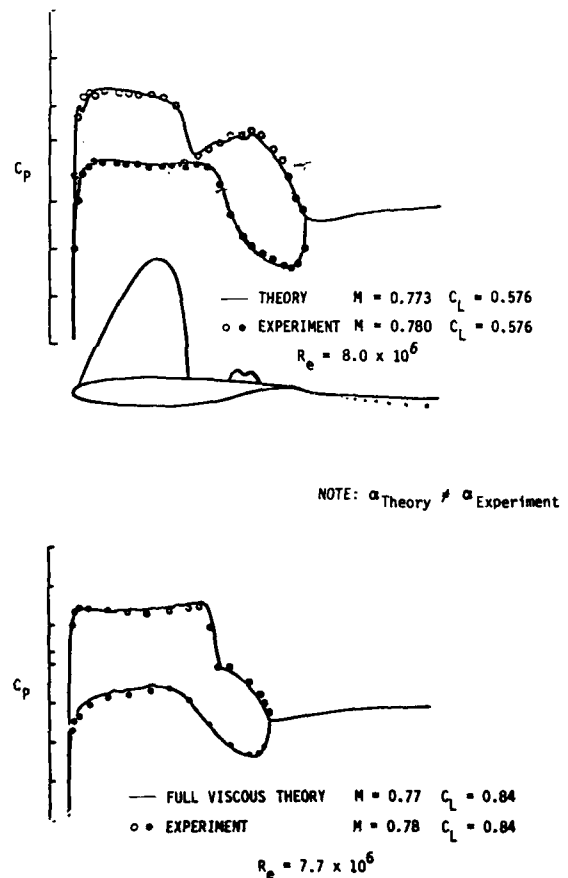


Fig. 4.2 Test-theory comparison - Melnik (Ref. 3)

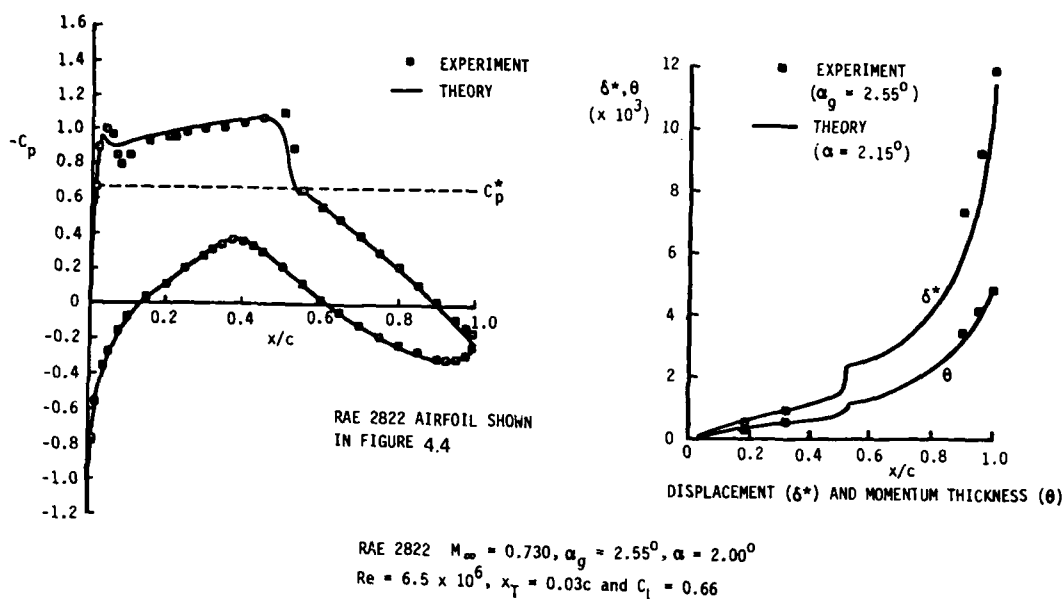


Fig. 4.3 Test-theory comparison - Collyer & Lock (Ref. 6)

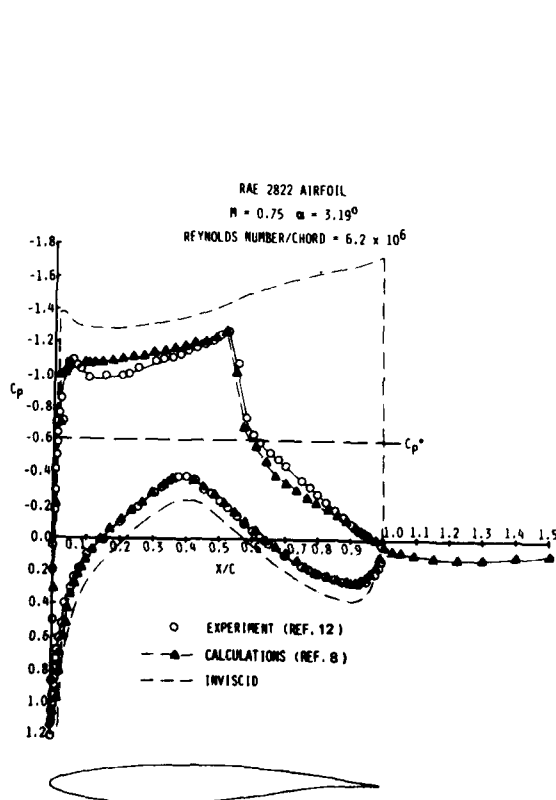


Fig. 4.4 Test-theory comparison RAE 2822 airfoil (pressure distribution)

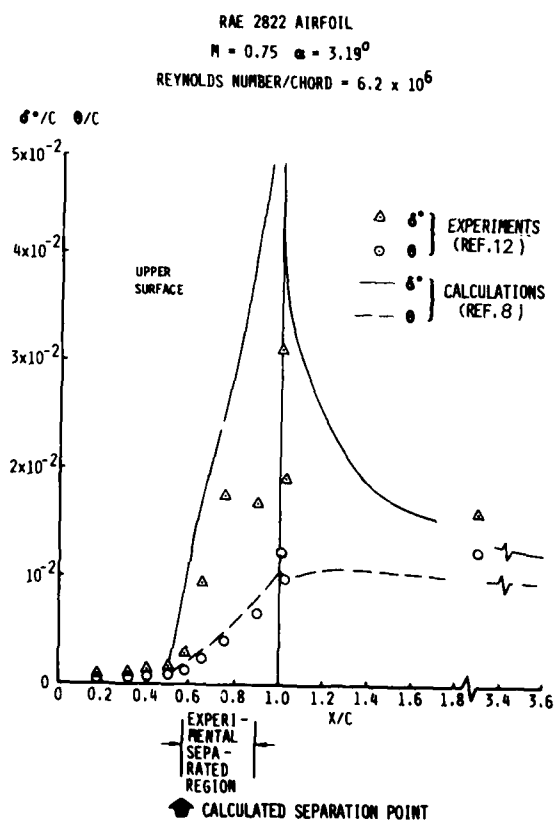


Fig. 4.5 Test-theory comparison RAE 2822 airfoil (boundary layer & wake characteristics)

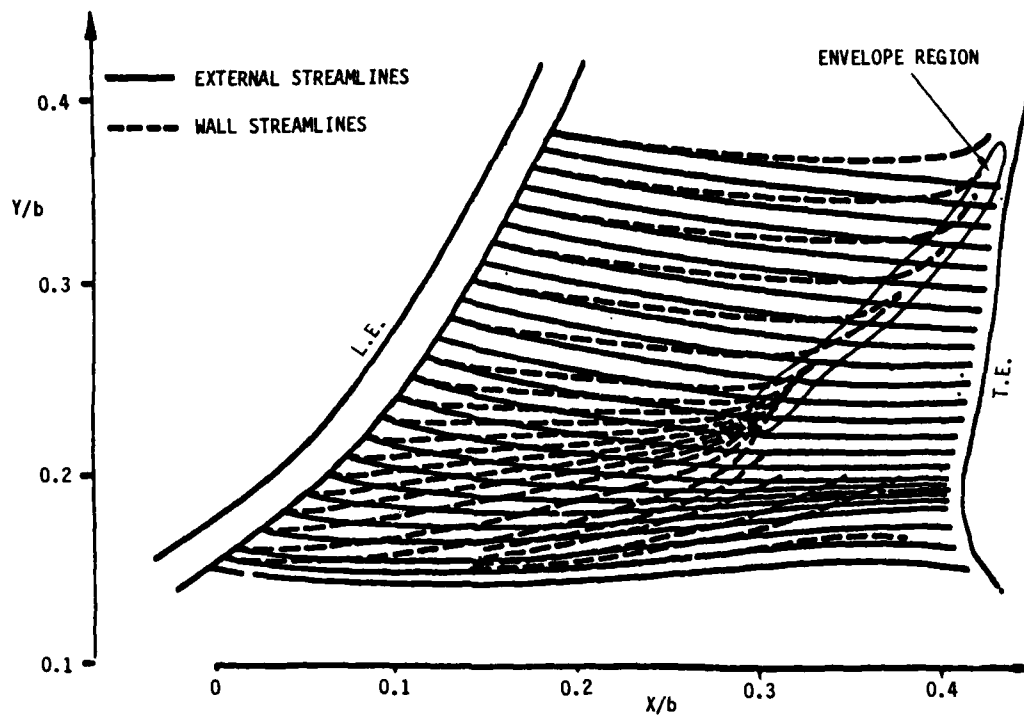


Fig. 4.6 Characteristic envelope in direct problem (Cousteix and Houdeville - Ref. 19)

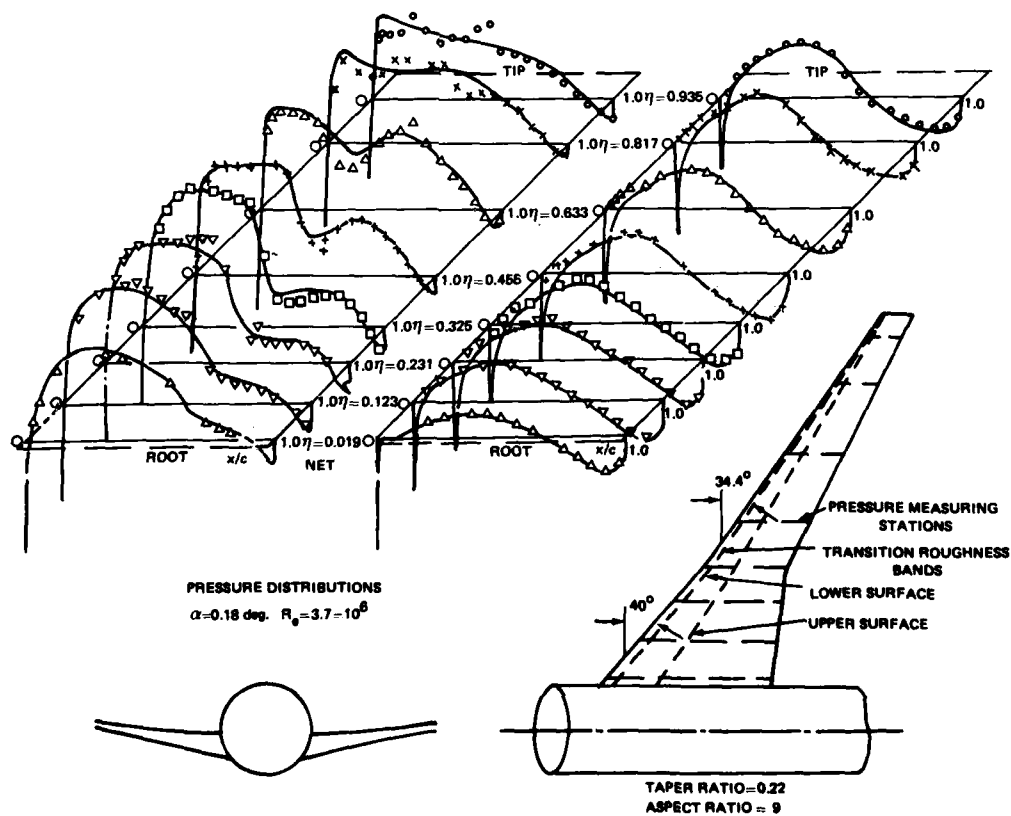
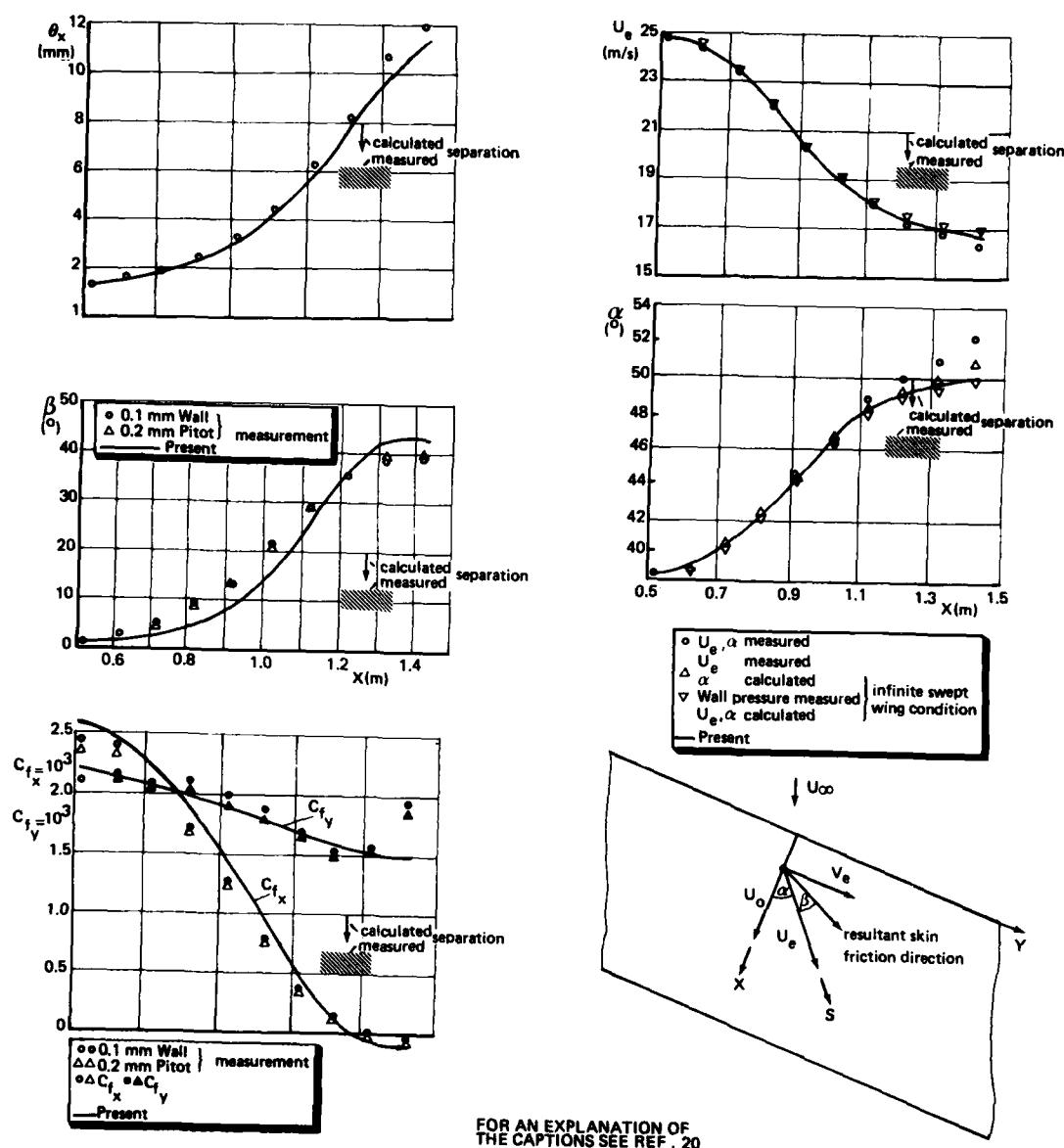


Fig. 4.7 Test-theory comparison - Firmin (Ref. 21)



FOR AN EXPLANATION OF
THE CAPTIONS SEE REF. 20

CALCULATIONS: STOCK (REF. 20)
EXPERIMENTS: VAN DEN BERG AND ELSENAAR (REF. 23)

Fig. 4.8 The indirect procedure for separated flow

5. COMPUTATIONAL PROCEDURES IN TRANSONIC AERODYNAMIC DESIGN

5.1 Introduction

The availability of computational methods for transonic flow has greatly improved the possibilities for the early, but admittedly approximate, aerodynamic analyses of given configurations. The greatest potential of such a capability, when suitably adapted, is probably in the possibility of generating shapes that will perform aerodynamically as required. In this design mode, computational aerodynamic methods are really complementary to wind-tunnel testing¹.

The purpose of this chapter is to review some of the computational procedures for transonic aerodynamic design that can be found in the literature. Since, at least to the author's knowledge, there exist no such methods for arbitrary 3-D bodies, the discussion is necessarily limited to computational procedures in airfoil and wing design. For convenience we will distinguish between three different categories of such procedures, viz.

1. Procedures involving indirect methods. Indirect methods are characterized by the fact that, in principle, the designer has direct control over neither aerodynamic quantities such as lift, pitching moment and pressure distribution nor over the geometry. Rather than specifying such quantities directly, the designer has to manipulate a number of (generally non-physical) parameters and see what comes out of it. The hodograph and fictitious gas methods are in this category.
2. Procedures involving inverse methods. In this category we will consider methods for solving the classical inverse problem of aerodynamics, i.e. determine the shape of an airfoil or wing for a given pressure distribution (and hence given lift, pitching moment, etc.).
3. Design and optimization by means of direct methods. This category is characterized by the use of direct, analysis methods. It ranges from the simple cut and try approach, in which an analysis method is used as a checking tool, to more sophisticated automated procedures in which an optimization algorithm and a direct fluid dynamics solver are linked together to minimize some aerodynamic object function.

After discussing examples from each of the three categories listed above some concluding remarks are made concerning the limitations of the various approaches including suggestions for improving the applicability and efficiency of aerodynamic design methods.

5.2 Indirect methods

5.2.1 Hodograph methods

The first successful computation of transonic potential flow about airfoil-like shapes was performed by Nieuwland², using analytic hodograph theory. Methods based on hodograph theory make use of the fact that, in hodograph (u, v or q, θ) variables the partial differential equations of compressible potential flow are linear, in contrast to the partial differential equations in the physical plane. This feature is used extensively in the sense that solutions are constructed by linear superposition of fundamental solutions of the hodograph equations. Although, in theory, it is possible to model shock waves, this turns out to be very difficult in practice. Hence, hodograph methods are limited to generating shock-free flows, which, of course, is of interest for drag minimization. The advantage of the linearity of the partial differential equations is, at least partly, offset by the fact that the mapping from the hodograph plane to the physical plane must be determined. If the mapping turns out to be singular outside the area occupied by the airfoil in the physical plane, the solution is meaningless from the physical point of view.

For the applied computational aerodynamicist an accessible review of hodograph methods has been given by Boerstoe³. Distinction can be made between incompressible flow transformation methods (Nieuwland⁴, Takanashi⁵) and compressible flow hodograph image transformation methods (Boerstoe-Huizing⁶, Sobieczky⁷, Eberle⁸). The method of Garabedian and Korn^{9,10} carries aspects of both categories.

The incompressible flow transformation methods are characterized by the fact that hodograph solutions for incompressible flow are taken as a starting point. These solutions are transformed to compressible flow by means of a suitable mathematical technique⁴. A flow chart of this design technique, taken from reference 3, is reproduced in figure 5.1a. The input consists of parameters defining the superposition of incompressible flow solutions and the free stream Mach number of the compressible airfoil flow that is being sought. The output is an airfoil shape and corresponding pressure distribution. The major difficulty of the incompressible flow transformation method is that, in order to obtain the degree of freedom required for generating airfoil flows of engineering interest, the basic incompressible flow solution must be described by many parameters. Choosing and tuning of these parameters has turned out to require a major and indeed prohibitive effort of the user-aerodynamicist. In spite of this, the technique has produced several airfoils of engineering interest. In particular since it was found that parts of the contour of shock-free airfoils can be modified to better suit engineering requirements without drag penalty^{11,12}.

Although based on different mathematical techniques the hodograph method of Garabedian and Korn^{9,10} suffers from the same difficulty. In their approach, the problem of constructing solutions to the hodograph equations for compressible flow is formulated as a characteristic initial value problem by extending all real dependent and independent variables of the equations for compressible irrotational flow into the complex domain. This initial value problem is solved along the complex characteristics by means of finite differences.

In the method of Garabedian and Korn it is the choice of the initial data that determines whether flows of engineering interest are obtained. This choice is guided by know-how of incompressible flows about airfoils. The problem of choosing the initial data in the complex characteristics method and that of choosing the incompressible flow parameters in the hodograph transformation methods are of comparable difficulty. For this reason the method has, apparently¹⁴, not met with wide application in industry. However, airfoils produced by the authors of references 9, 10 (see Ref. 10 in particular) contain several examples of engineering interest; some of these have been reproduced in figure 5.2. Note that most of the airfoils of reference 10 exhibit an open trailing edge of finite thickness. This is due to the fact that the method contains a primitive correction for boundary layer effects, the validity of which, however, is doubtful.

The problem of constructing flows of sufficient engineering interest with acceptable effort has been reduced, to some extent, in the second category of hodograph methods, i.e. the compressible flow hodograph image transformation methods⁷. In the latter methods the (estimated) image on the hodograph plane of the desired airfoil is the input of the calculation process (Fig. 5.1b). This image constitutes the

boundary condition in a Tricomi-like boundary value problem for the stream function in the compressible hodograph plane. After solving this boundary value problem the flow in the physical plane is, again, obtained by determining the mapping from the hodograph to the physical plane.

In the method of Boerstoele⁶ the solution is constructed by the linear combination of basic compressible flow solutions. The coefficients in the linear combination are determined so as to, approximately, satisfy the boundary conditions in the Tricomi boundary value problem. Sobieczky⁷ has ingeniously circumvented the Tricomi boundary value problem (and the associated question of well-posedness) by modifying, for $M > 1$, the gas law in such a way that the partial differential equations remain elliptic everywhere in the flow field. In this way the Tricomi boundary value problem can be replaced by a Dirichlet boundary value problem. When the Dirichlet problem has been solved, the part of the solution corresponding to $M > 1$ with incorrect gas law, is replaced by the solution of a Cauchy initial value problem with the correct gas law and with the initial conditions at the sonic line $M = 1$ taken from the solution of the Dirichlet problem.

In [7] Sobieczky utilizes the rheo-electrical analogy for solving the Dirichlet problem. Eberle⁸ has constructed numerical approximate solutions to the Dirichlet problem by converting it into an integral equation problem which is then solved by means of singularity distributions (panel method). The Cauchy initial value problem is solved by a numerical characteristics method.

Although the compressible flow hodograph image transformation methods are more "user-oriented" than the incompressible hodograph transformation methods they still suffer from the fact that appreciable user's experience is required in specifying the hodograph image such that the transonic airfoil flow pursued by the designer is realized. Nevertheless, the technique has produced many airfoils suitable for engineering applications¹³. A summary of airfoils and their corresponding design pressure distributions taken from Boerstoele's^{3,6} and Eberle's⁸ work have been reproduced in figures 5.3 and 5.4, respectively. It can be noted that the hodograph image methods are capable of producing airfoils of considerable variety.

In an effort to make their hodograph method more user-oriented, Bauer, Garabedian and Korn¹⁴ have extended their method so that shock-free airfoils can be obtained with pressure distributions satisfying prescribed data with the smallest possible deviation. Hence the method can also be classified as an approximate inverse method. Note that the prefix approximate is necessary because a solution to the problem of finding an airfoil with transonic shock-free flow that satisfies a given pressure distribution does not necessarily exist. Neither does, of course, the transonic shock-free flow about an airfoil of given geometry (Morawetz¹⁵). We will return to this point in sections 5.3 and 5.5.

In [14] the solution of the non-linear boundary value problem of designing a shock-free airfoil, on which the pressure or speed is assigned as a function of the arc length, is approached iteratively as follows (Fig. 5.1c). First the complex analytic function is determined that maps the unit circle in the complex domain onto the region of flow in the hodograph-plane for the case of an incompressible flow with the prescribed velocity distribution. With the mapping function given, a new, compressible flow is calculated using the method of complex characteristics. From this a relation between the velocity q and arc-length s in compressible flow is calculated and compared with the required relationship. The difference, in turn, leads to an improved approximation of the mapping function through updating of the incompressible flow q - s relationship. The process is repeated until a compressible flow is found that fits the prescribed data adequately.

From the point of view of aerodynamic design, the possibility of designing (approximately) for a given pressure distribution implies clearly a significant advantage over the more classical hodograph methods. Note, however, that solutions may still have to be disregarded when the mapping from the hodograph to the physical plane contains unacceptable singularities (limit lines).

Examples of airfoils designed with the above method (a computer code listing of which is contained in [14]) have been reproduced in figure 5.5. The examples suggest that, provided a physically realistic pressure distribution is asked for, the pressure distribution of the resulting shock-free airfoil can be quite close to the required one. Another example, not conforming to this requirement, is given in Section 5.5.

5.2.2 Fictitious gas method

Perhaps the most severe limitation of hodograph methods is that the concept cannot be extended to three dimensions. This limitation has been overcome in the more recently evolved (semi-)indirect methods based on Sobieczky's fictitious gas concept. The fictitious gas methods are closely related¹⁶ to the Sobieczky-Eberle hodograph methods mentioned in the preceding section. Both are based on the concept of the elliptic continuation of the subsonic part of a mixed subsonic/supersonic flow field into the supersonic zone by modifying the pressure-density (or velocity - density) relation. However, instead of working in the hodograph plane the fictitious gas method¹⁷ utilizes a direct (analysis) transonic potential flow method of the type described in chapter 3 with the pressure (velocity)-density relation modified locally whenever $M_{local} > 1$. The modified analysis code is used to compute the fictitious gas flow about a given base configuration, the transonic wave drag characteristics of which, at given angle of attack and Mach number, have to be improved. When the solution to the fictitious gas flow problem is known, the correct supersonic flow field inside the sonic surfaces is determined by solving an initial value problem with the initial data given on the sonic surface. The new correct flow inside the sonic "umbrella" defines a new stream surface that is tangent to, and has the same curvature as, the stream surface (contour) at the intersection of the sonic surface and the original body. In this way a part of the original body is modified and indeed in such a way that, at the same conditions of Mach number and angle of attack a transonic shock-free flow is obtained. Hence, the fictitious gas method should be considered as a shock-free redesign method¹⁸.

An appealing feature of the fictitious gas method is that, in principle, any available 2-D or 3-D analysis code may be modified, and used to solve the elliptic part of the problem. In 2-D, Sobieczky et al.¹⁷ use Jameson's FL06 code¹⁶, while in another application of the concept, Eberle¹⁹ uses a 2-D version of his finite element method. Applications in 3-D have seen the use^{17,20} of a Bailey-Ballhaus type of transonic small perturbation code as well as the more advanced Jameson-Caughey full potential FL022 and FL027 codes ([18], [21]). As demonstrated in [22] and [23] it is also possible to utilize analysis codes including viscous-inviscid interactions.

In two dimensions^{17,19} the initial value problem in the supersonic part of the flow field may be solved by means of either a characteristics method in a hodograph-like working plane, similar as in the Sobieczky/Eberle⁸ hodograph methods, or by a finite difference marching procedure²¹. In 3-D a marching

procedure is used, going inward from the sonic surface by successive surfaces of constant density for the full potential equation or constant longitudinal flow speed u for the small perturbation equation.

An important point to note is that the (re)design problem as sketched above does not always have a useful solution. This is associated with the character of the initial value problem to be solved in the supersonic part of the flow field. In the 2-D hodograph plane the problem is well posed and the solution is readily found. However, as mentioned earlier, the solution may not be useful because of the appearance of limit lines in the transformation from the hodograph to the physical plane. Limit lines or surfaces may also appear directly when the marching procedure is used^{17,20}. If they appear, a next attempt towards a physically meaningful solution may be made by using a "more elliptic" fictitious gas law. An additional complication in 3-D is that the initial value problem for the supersonic domain seems to be ill-posed^{17,20}; i.e. small changes in the initial data will cause large changes in the solution elsewhere. As a consequence the marching procedure, or, indeed, any numerical method, is unstable in principle. However, the instability appears to be manifest only when spanwise gradients are large, and, apparently, is of little consequence for moderate to high aspect ratio wings²⁰.

It is interesting to note at this point that indications of "ill-posedness" have also been found for the 3-D inverse problem in incompressible flow¹. We will return to this point in Section 5.3.

Some examples of application of the fictitious gas method are reproduced in figures 5.6 and 5.7. Figure 5.6, taken from [17], shows the (inviscid) shock-free redesign of the NACA 64A410 airfoil at a Mach number of 0.72 and 0.4 degrees angle of attack. Note that the modified airfoil is somewhat thinner and has a 10 % lower lift coefficient. An illustrative 3-D example, taken from [22] has been reproduced in figure 5.7. Shown is the result of the shock-free redesign of a 15.7° swept wing built-up from GA(W)-2 type airfoil sections. This type of airfoil is known to have good low speed $C_{L_{max}}$ characteristics, but as indicated by the figure, the high speed characteristics at $M = 0.8$ are poor. Also shown is the result of a shock-free redesign at $M = 0.8$ which has not affected the first 9 % of the airfoil chord. Because of the latter it can be expected that the new wing will also have a good low speed $C_{L_{max}}$.

Examples such as this serve to illustrate the point that the fictitious gas method is a viable tool for the shock-free redesign of a given wing in the final stages of the aerodynamic design process. However, because of the fact that a suitable basic shape is required from the outset, additional tools such as those described in the following section are required if the complete aerodynamic design of a wing or airfoil is the objective.

It seems appropriate at this point to comment on the, apparently, still wide-spread misconception that, from an engineering point of view, shock-free flows are less interesting than other supercritical airfoil flows. This is so, it is argued, because the best L/D for a given Mach number is always obtained with a weak shock present and also because of the large aerodynamic center shifts that would be produced by shocks occurring at slightly off-design conditions.

The correct statement that $(L/D)_{max}$ is obtained when a weak shock is present does not necessarily make "shock-free" designs less attractive. In fact, "shock-free" designs very seldom turn out to be really shock-free in practice. Due to inappropriate boundary layer modelling, wind tunnel wall interference and aeroelastic distortions, most if not all shock-free designs will exhibit weak shock waves at and around the design C_L and Mach number in the wind tunnel or atmospheric flight environment. Shock-free designing must therefore be viewed as one (of several) possible means to design for flows with small or negligible wave drag for a certain range in C_L and Mach number. The reader is referred to the Round Table Discussion contained by [25] for a recent discussion on the issue. The possible problem of rapid shifts with Mach number of the aerodynamic center is not confined to shock-free designs. Such rapid shifts occur on most advanced and many conventional airfoils at significant transonic conditions. Airplane designers have learned to live with it, with Mach trim compensators found on most commercial jet transports.

5.3 Inverse methods

5.3.1 General

While the indirect methods discussed in the preceding section are characterized by the fact that the designer can exercise direct control over neither the aerodynamics nor the geometry^{*}, he does have direct control over the aerodynamics (but not over the geometry) when using inverse methods¹. In the inverse problem of aerodynamics the shape is to be determined of an airfoil or wing with given planform that will, for a given Mach number, produce a given pressure distribution and hence given lift and pitching moment, spanwise lift distribution, etc. In incompressible potential flow, the problem is non-linear in the boundary conditions. In transonic flow it is non-linear in both the boundary conditions and flow equations.

Due to the non-linearity of the boundary conditions, the inverse problem is fundamentally more complicated than the analysis problem. This is already so in the case of 2-D incompressible flow, as pointed out by Lighthill²⁶ and Woods²⁷, and recently by Volpe and Melnik²⁸. In particular it has been demonstrated by Lighthill that a unique and correct solution to the inverse problem of 2-D, incompressible flow does not exist unless the prescribed velocity distribution satisfies certain integral constraints associated with airfoil closure and with the fact that the free stream is given in magnitude and direction. Woods²⁷ pointed out that similar constraints are also required in the mixed design problem in which the pressure distribution is prescribed for some parts of the airfoil and the shape is prescribed for other parts. Volpe and Melnik²⁸ have pointed out that the role of constraints and the question of correct formulation of the inverse problem have never been properly addressed for (2-D) compressible flows and that, as a consequence, most existing inverse codes for transonic flow are based on improper formulations of the inverse problem. For 3-D flows the situation is still more unsatisfactory. To the author's knowledge the question of proper formulation has not been addressed even for incompressible flows. This, however, has not prevented the development of useful transonic inverse procedures.

5.3.2 Methods based on small perturbation theory

The problem of non-linearity in the boundary conditions (and of course that of generating a boundary fitted coordinate system) is avoided when the boundary conditions are satisfied in the wing mean plane, as in TSP theory. The additional conditions to be satisfied for a proper formulation of the inverse

^{*}) This is, of course, not completely true for the fictitious gas methods.

TSP problem are not known. However, we do have some indications about such conditions from the limiting case of incompressible flow, i.e. from the classical thin airfoil and thin wing theories. For a good understanding of the inverse problem it is useful to consider these first.

In thin airfoil theory²⁹, the symmetric (thickness) and antisymmetric (lifting) parts of the incompressible flow are described by the following integral relations

$$u_t(x, \pm 0) = \frac{1}{2\pi} \oint_0^1 \frac{[w(\xi)]_0^{0+}}{x-\xi} d\xi \quad (5.1)$$

$$w_z(x, \pm 0) = -\frac{1}{2\pi} \oint_0^1 \frac{[u(\xi)]_0^{0+}}{x-\xi} d\xi \quad (5.2)$$

In these expressions u_t is the chordwise perturbation velocity due to thickness and w_z is the perturbation velocity normal to the y -axis due to lift. $[w]_0^{0+}$ and $[u]_0^{0+}$ denote the jumps in normal and chordwise velocity across the slit ($0 \leq x \leq 1$, $y = 0$) where the airfoil boundary conditions are satisfied. With the linearized boundary conditions, $[w]_0^{0+}$ and w_z are related to the geometric airfoil quantities as follows

$$[w]_0^{0+} = 2 \frac{dz_t}{dx} \quad (5.3)$$

$$w_z = \frac{dz_c}{dx} - \alpha \quad (5.4)$$

where the subscripts t and c refer to thickness and camber, respectively, and α is the angle of attack.

In the direct problem, with the geometric properties (5.3), (5.4) given, (5.1) must be considered as an integral expression for u_t and (5.2) as an integral equation for $[u]_0^{0+}$. Equation (5.2) is the classical integral equation of lifting surface theory. It is well known that equation (5.2) does not have a unique solution, unless an additional condition is satisfied; the reason being that there exists a non-trivial solution of the homogeneous equation. In thin airfoil theory the Kutta condition

$$[u(x=1)]_0^{0+} = 0 \quad (5.5)$$

is the additional condition that guarantees a unique (and indeed physically relevant) solution.

In the inverse problem the situation is exactly opposite. We then have the situation that equation (5.2) represents an integral expression for determining the camber and incidence from the specified load distribution $[u]$, while (5.1), with (5.3), represents an integral equation for the unknown thickness distribution.

Since the integral equation (5.1) of the inverse thickness problem is the same as that (5.2) of lifting surface theory we must also specify an additional condition to be satisfied in order to have a well-posed problem with a unique solution. The relevant choice to be made for this additional condition is of course the closure condition

$$\int_0^1 [w(\xi)]_0^{0+} d\xi = C \quad (5.6)$$

requiring that the airfoil be closed ($C = 0$) or have a given trailing edge thickness ($C > 0$).

It can be shown that in the mixed boundary value problem, in which the velocity distribution is prescribed over part of the slit and the geometry over the remainder, both a condition fixing the circulation and the closure condition must be enforced in order to obtain a problem with a unique solution. It is emphasized that without satisfying, either explicitly or implicitly, the necessary additional condition(s) any numerical scheme is bound to fail. Corresponding additional conditions must be satisfied in the case of 3-D (thin) wing flow (see e.g. [30]).

Early work on a mixed direct/inverse method for transonic airfoil design based on transonic small perturbation theory and utilizing finite differences has been reported by Steger and Klineberg³¹. These authors have studied the problem of an airfoil in transonic flow with given leading-edge geometry with the pressure distribution specified over the remaining portion of the chord. A perturbation velocity potential formulation was used in the leading-edge region and a first order equation system

$$\frac{\partial F}{\partial x} + \frac{\partial w}{\partial z} = 0 \quad (\text{continuity}) \quad (5.7)$$

$$\frac{\partial u}{\partial z} - \frac{\partial w}{\partial x} = 0 \quad (\text{irrotationality}) \quad (5.8)$$

in the remainder of the flow field (Fig. 5.8). F was chosen according to the Guderley-Von Karman formulation of TSP theory (see Sect. 2.1.3). Steger and Klineberg do not mention and, apparently, do not explicitly satisfy the necessary additional condition (closure) required for uniqueness. However, at the same time, rather than specifying u directly as a boundary condition in the finite difference relaxation process, they utilize an iterative procedure in which, successively,

- i) a complete relaxation sweep is performed with direct (analysis) boundary conditions for an estimate of the required geometry
- ii) an improved estimate for the geometry is obtained from the irrotationality condition (5.8) by, successively;
 - ii.1) replacing $u(z = 0)$, on the slit (Fig. 5.8) in the finite difference expression for $\frac{\partial u}{\partial z}(z = 0)$, by the required surface value of u .
 - ii.2) chordwise integration of $\frac{\partial u}{\partial z}$ to yield

$$\begin{aligned}
 w_{\pm} &= \frac{dz_{\pm}}{dx} = \int_{x_1}^x \frac{\partial w}{\partial x} (\xi, z = \pm 0) d\xi + C_1 \\
 &= \int_{x_1}^x \frac{\partial u}{\partial z} (\xi, z = \pm 0) d\xi + C_1
 \end{aligned} \quad (5.9)$$

and

$$z_{\pm} = \int_{x_1}^x w_{\pm} dx + C_2 \quad (5.10)$$

the constants of integration C_1 and C_2 being used to enforce continuity in z and $\frac{dz}{dx}$ at x_1 , where the new shape is joined to the fixed leading-edge geometry.

Although a convergence proof for the procedure is not given, the process does apparently converge. Not in the least, according to the authors, because they maintained consistency between the numerical formulation of direct and inverse boundary conditions, and presumably also because a Neumann type boundary condition is satisfied in each relaxation sweep. Note, that there is no control over the trailing-edge gap, and that the angle between the free stream and the reference coordinate system is held fixed (Fig. 5.8), implying that the orientation of the given leading-edge geometry with respect to the free stream is also fixed.

While the examples presented by Steger and Klineberg are of a fairly academic nature, Langley³² of ARA, utilizing a similar iterative procedure, but a (non-conservative) Murman and Krupp³³ type perturbation velocity potential formulation through the entire flow field, succeeded in carrying the inverse TSP method to appreciably more practical levels of application. The latter is reflected in the fact that Langley arranged his program to have various options. For example, the upper surface and lower surface, aft of a fixed leading-edge geometry, may be altered simultaneously or separately; alternatively the pressure distribution may be specified over the upper surface and the thickness distribution may be kept constant. The latter option was incorporated in order to avoid problems like negative or too large trailing-edge thickness which, as in the Steger/Klineberg approach, may result from the absence of control over airfoil closure. It is interesting to note that Langley, in [32], reports the failure of attempts to solve the inverse problem directly by enforcing the Dirichlet boundary condition for ϕ

$$\phi(x) = \int_{x_1}^x u(\xi) d\xi + \phi(x_1) \quad (5.11)$$

on the slit (reason why he switched to the "indirect" inverse approach in which successive analysis-type calculations are made with regular updating of the airfoil shape through the irrotationality condition). The additional conditions associated with the inverse problem are not mentioned in reference 32. Hence, it seems likely that the failure was caused by not satisfying the necessary additional conditions, resulting in a wrongly posed problem.

Both Steger and Klineberg³¹ and Langley³² stress that the crux of the design problem is the treatment of the airfoil boundary conditions. In Langley's method the Neumann boundary condition is implemented by substituting the given surface slope $\frac{dz}{dx}$ for ϕ_z in the finite difference expression

$$(\phi_{zz})_{i,j} = \frac{2}{(\Delta z)^2} (\phi_{i,j+1} - \phi_{i,j} - \Delta z (\phi_z)_{i,j}) \quad (5.12)$$

for ϕ_{zz} at the (j^{th}) mesh line coinciding with the slit (Fig. 7). The cross-derivative $\phi_{xz} = \frac{\partial u}{\partial z}$ in the expression (5.9) for the geometry update is approximated by

$$(\phi_{xz})_{i,j} = \frac{1}{2\Delta z} \{-3(\phi_x)_{i,j} + 4(\phi_x)_{i,j+1} - (\phi_x)_{i,j+2}\} \quad (5.13)$$

with $(\phi_x)_{i,j}$ replaced by the required velocity.

It should be noted that the geometry update procedure, equation (5.13) in particular, implies continuity of ϕ_x in the z -direction, but not necessarily in the x -direction. The analysis calculation on the other hand does imply continuity of ϕ_x because of the finite difference approximation for ϕ_{xx} . This numerical inconsistency could, presumably, have a negative effect on the convergence of the iteration process and, apparently, shows up as a local oscillation in the resulting pressure distribution at the point x_1 where the fixed leading edge geometry meets the remaining, new shape (Fig. 5.9).

It is further worth noting that Langley reports that substantial underrelaxation (0.1 to 0.3) is required in updating the surface slopes through the irrotationality condition and that 150-300 fine grid iterations, preceded by a similar amount on two successive coarser grids, are required for convergence.

In a latter effort at ARA by Forsey and Carr briefly reported by Lock³⁴, the problem of not being able to successfully enforce the Dirichlet-type boundary condition was apparently overcome. At the same time the method was extended to 3-D wings. An example of application is given in figure 5.10.

Use of the "indirect" inverse technique (as well as failure of the "Dirichlet technique") has also been mentioned by Schmidt et al.³⁵ and Schmidt and Hedman³⁶. In the latter paper the closure problem is crudely disposed off by rotating the lower surface around the airfoil section leading-edge point.

Inverse methods based on TSP formulation which do utilize Dirichlet boundary conditions (except, again, in the leading-edge region where a fixed shape is assumed), have been studied by Shankar et al.^{37,38}. In [37], a non-conservative, transonic similarity form

$$[K - (\gamma + 1)\phi_x]\phi_{xx} + \phi_{zz} = 0 \quad (5.14)$$

of the 2-D Guderley-Von Karman TSP equation is used. K being a transonic similarity parameter and z representing a stretched coordinate. In the leading-edge region the Neumann boundary condition is implemented as in Langley's method. This leads to the following difference equation being solved at the airfoil grid points where the shape, i.e. ϕ_z is prescribed

$$\left[(K-(\gamma+1)\phi_x)\phi_{xx} \right]_{i,j} + \frac{2\phi_{i,j+1} - 2\phi_{i,j}}{(\Delta z)^2} = \frac{2(\phi_z)_{i,j}}{\Delta z} \quad (5.15)$$

The non-linear term, as usual, is approximated by central differences at elliptic points and by upwind differences in hyperbolic points. At the design-portion of the airfoil grid points, the Dirichlet boundary condition is implemented as

$$\phi_{i,j} = \phi_{i-1,j} + u_{i-1,j}(\phi_{i,j} - \phi_{i-1,j}) \quad (5.16)$$

$u_{i-1,j}$ being the required velocity, specified at half-mesh. Equation (5.16) enforces continuity of ϕ at $x = x_1$. The level of ϕ in the design portion is updated during each relaxation sweep. After the relaxation process has converged, the new airfoil slope is computed from the exact inverse of equation (5.15), i.e.

$$(\phi_z)_{i,j} = \frac{\Delta z}{2} \left[(K-(\gamma+1)\phi_x)\phi_{xx} \right]_{i,j} + \frac{1}{\Delta z} (\phi_{i,j+1} - \phi_{i,j}) \quad (5.17)$$

In this way full consistency between the analysis and design formulations is achieved, thereby avoiding, presumably, local oscillations at the analysis/design junction x_1 of the kind observed in figure 5.9. As mentioned earlier the finite difference procedure, and the difference formula for ϕ_{xx} in particular, implies continuity of ϕ_x at x_1 on both upper and lower surfaces. It is suggested here, that these two, implicit, additional conditions serve to fix the circulation and trailing edge openness and thereby the uniqueness of the solution. As in the Steger and Klineberg³¹ and Langley³² procedures this does not leave room for control over the trailing-edge thickness. However, it would seem possible to, additionally, exercise control over trailing-edge closure by introducing the orientation of the fixed leading-edge geometry with respect to the free stream as an additional free parameter.

A point worth mentioning is the statement in [37] that in case of an open trailing edge the far field boundary condition to be satisfied at the outer edge of the finite computational domain should incorporate the effect of a source term, the strength of which is related to the trailing edge gap. I.e., the far field boundary condition should read

$$\phi_{\text{far field}} = -\frac{\Gamma\theta}{2\pi} + \frac{Q \ln \tilde{r}}{2\pi}, \quad (5.18)$$

rather than containing only the circulation (Γ) term. In equation (5.18) Q is the source strength which is related to the trailing edge thickness. θ and \tilde{r} are given by

$$\theta = \arctan \sqrt{Kz/x} \quad (5.19)$$

and

$$\tilde{r} = \sqrt{x^2 + Kz^2} \quad (5.20)$$

respectively.

Although the statement of Shankar et al. is correct in principle, at least for a mass-conservative formulation, it is not applied correctly in [37] because of the fact that a non-conservative finite difference formulation is used. In case of embedded shock waves this leads to spurious mass sources at the shock (Section 2.2.3), which should be accounted for in the source strength Q .

In [38] Shankar et al. have extended their approach to 3-D wings in the presence of a body. The approach was taken to modify the existing 3-D Bailey-Ballhaus TSP analysis code as extended by Mason et al.³⁹. The 3-D code utilizes fully conservative differencing. The far field source term was not included, however.

The 3-D design examples presented in [38] suffer severely from the absence of control over trailing edge thickness. Several suggestions are given for, fairly crude, remedies for this situation, such as rotating the lower surface about the leading edge. However, the possibility mentioned above, to control closure through introduction of an additional free parameter which represents the orientation of the fixed leading edge geometry with respect to the free stream, is not considered.

In a further paper⁴⁰ Shankar, now considering Dirichlet boundary conditions over the whole of the chord, addresses the closure problem by varying the constant of integration in equation (5.11), or, in other words, by varying the potential at the leading edge. In particular he uses the following procedure:

- (1) Compute the flow field for a given starting geometry with the purpose of providing a first estimate for the potential ϕ_{LE} at the leading edge
- (2) Compute the potential on the wing plane from (5.11), (with $x_1 = x_{LE}$).
- (3) Solve the Dirichlet problem for the difference equations by means of line relaxation.
- (4) Determine the trailing edge gap t_{TE} from equation (5.6) and the derivative $\partial t_{TE} / \partial \phi_{LE}$; determine correction $\Delta \phi_{LE}$ from

$$\Delta \phi_{LE} = t_{TE} / \frac{\partial t_{TE}}{\partial \phi_{LE}} \quad (5.21)$$

- (5) Repeat steps (3) and (4) until closure is achieved.

Note that the determination of the n^2 derivatives $(\partial t_{TE})_j / (\partial \phi_{LE})_m$ (n is the number of span stations) is very costly since each requires another Dirichlet problem to be solved. For this reason a simplified procedure is used involving only a small fraction of the gradient matrix elements $\partial t_{TE} / \partial \phi_{LE}$.

Although the procedure can be made to work, apparently, it also seems to be quite cumbersome. Clearly, there is a need for more efficient procedures that enforce closure.

5.3.3 Methods based on full potential theory

General

As mentioned previously inverse methods based on full potential theory with full boundary conditions require iterative procedures with some form of linearization in the boundary conditions. One possibility is to solve a sequence of Dirichlet boundary value problems with the geometry updated after

each Dirichlet step (Fig. 5.11a). Another possibility is to utilize a residual-correction formulation in which, in each iteration step, the residual, that is the difference between the actual and required pressure distribution, is determined by means of an analysis (Neumann) code and a correction to the geometry, driving the residual to zero, is obtained from some approximate inverse procedure (Fig. 5.11b).

Methods belonging to the first category are those of Tranen⁴¹, Carlson⁴² and Volpe²⁸ for 2-D airfoils and those of Henne⁴³ and Shankar⁴⁴ for 3-D wings. In the second category we have the methods of Davis⁴⁵ and McFadden⁴⁶ for 2-D airfoils. The approach of the latter has also been extended to 3-D wings by Garabedian and McFadden⁴⁷.

Two-dimensional flow

The first reported attempt to solve the full potential transonic lifting 2-D inverse airfoil problem is that of Tranen⁴¹. Broadly speaking Tranen's method can be considered as a version of the Garabedian-Korn^{48,49} analysis method with the Neumann boundary condition on the airfoil surface replaced by a Dirichlet boundary condition. In the Garabedian-Korn method (see also Section 3.2) the quasi-linear form of the full potential equation is solved in polar coordinates ω, r in a computational plane obtained by mapping the region exterior to the airfoil onto the interior of a unit circle. Non-conservative differencing with simple upwind bias in the supersonic zone is used and the resulting non-linear system of equations is solved by means of SLOR.

The distribution of the surface potential required for the Dirichlet boundary condition in Tranen's method is obtained by integration of the target velocity distribution, i.e.

$$\phi = \phi(s=0) + \int_{s=0}^s q(s') ds' \quad (5.22a)$$

Note that since,

$$q^2 = U^2 + V^2 \quad (5.22b)$$

this way of linearization requires that the normal velocity V resulting from the solution of the Dirichlet problem be small with respect to U (and q), or, in the other words, that the estimate of the geometry is close to the required one.

While in the original analysis method the velocity components are calculated by means of central differences at the mesh points themselves, Tranen, in specifying the surface potential in the Dirichlet problem, found it necessary to specify the pressure (velocity) at half-mesh and determine ϕ through integration, using an expression of the type

$$\phi_i = \phi_{i-1} + (Uf)_{i-1/2} \Delta\omega \quad (5.23)$$

f being the mapping modulus. (Note that a similar strategy was followed by Shankar⁴⁰, see Section 5.3.2.) In Tranen's method the constant of integration determining the level of the surface potential can either be fixed or can be used to control closure. In the latter case a correction $\delta\phi_0$ to the surface potential level is applied after each relaxation sweep. The magnitude of this correction is taken to be proportional to the net mass flux Q (transpiration) through the airfoil surface, i.e.

$$\delta\phi_0 = \epsilon Q \quad (5.24)$$

with

$$Q = \int_0^{s_{\max}} \rho V ds \quad (5.25)$$

where V is the velocity component normal to the surface (radial direction). The value of the proportionality constant ϵ has been determined empirically. However, utilizing the fact that the potential of a source (in incompressible flow) equals $Q \ln \bar{r}$ (\bar{r} being the distance to the source in the physical plane) it should also be possible to determine ϵ theoretically.

Tranen's way to control closure is probably more efficient than that of Shankar⁴⁰, described in the preceding section; the reason being that Tranen's procedure does not require the numerical determination, through additional Dirichlet problems, of the derivative $\partial\phi_{TE}/\partial\phi_{LE}$ prior to update of the potential but corrects the potential after each relaxation sweep.

While there is some doubt²⁸ whether the Dirichlet problem in Tranen's method, in particular because of the far-field boundary condition used, is well-posed*) the inverse problem as a whole in Tranen's method is certainly not formulated correctly. The latter is a result of the fact that Tranen, as pointed out by Volpe and Melnik²⁸, does not satisfy Lighthill's²⁶ first constraint or an equivalent additional condition. Requiring the net transpiration mass flux to be zero is a necessary but not sufficient condition for proper closure. In addition, in order to obtain a proper stream surface, we must require the solution to contain a branch point or dividing streamline. This, in general, requires a stagnation point. In other words, the additional condition that the normal velocity $V = 0$ where U is specified to be zero (or an equivalent of this) must be imposed. The implication of this last requirement is that a free parameter such as the magnitude of the free stream²⁸ or a free parameter in the target pressure distribution must be introduced. The fact that Tranen's method is not quite correctly formulated is reflected in the way the new airfoil shape is determined. The latter problem requires two steps:

- i. determination of the normal velocity V from the Dirichlet solution
- ii. determination of the displacement of the stagnation streamline (integration of new surface slopes).

In determining the normal velocity V at the surface mesh points from the Dirichlet solution Tranen utilizes the usual⁴⁸ central difference expression

$$V_{i,j=1} = \frac{1}{f_{i,1}} \cdot \frac{1}{2\Delta r} [\phi_{i,2} - \phi_{i,0}] \quad (5.26)$$

with the potential at the dummy point $(i,0)$, inside the airfoil (outside the unit circle in the computational plane) determined by satisfying the difference form of the flow equations in the surface mesh points. As described in the preceding section a similar procedure was adopted by Shankar⁴⁰ for the TSP

*) The critique of Volpe and Melnik²⁸ in this respect, to some extent, is shared by the present author.

equation. Although, as discussed earlier, such a procedure, to some extent, achieves consistency between the analysis and design formulations, an inconsistency seems to be that the prescribed tangential velocity is considered at half-mesh and the normal velocity at the mesh points themselves. Such inconsistency could, presumably, be avoided if a finite volume type of discretization were used to satisfy the full potential mass conservation equation.

The fact that Tranen does not enforce proper branching of the surface streamline is reflected in particular in the procedure for the determination of the δ -placement of the "stagnation streamline". The displacement δ of the new surface, relative and normal to the old shape is determined by quadrature using the mass conservation expression

$$\delta_i = \frac{1}{\rho_i U_i} \left[\rho_{i-1} U_{i-1} \delta_{i-1} + \frac{\rho_i V_i + \rho_{i-1} V_{i-1}}{2} \Delta s \right] \quad (5.27)$$

U_i , V_i etc. are determined by means of central differences of the type (5.26). However, at the trailing edge \bar{V} is set equal to zero by extrapolation from upstream grid points. At the same time some smoothing procedure is required at the grid points nearest to the "stagnation point" (i.e. the point where U , but not necessarily V , is equal to zero) where the integration is started.

As a result of the improper formulation of the inverse problem and the necessarily required adjustments to the surface displacement Tranen requires a direct (= analysis) calculation to check the resulting pressure distribution. A flow chart of the complete design procedure is reproduced in figure 5.11. Note that the procedure exhibits aspects of a residual-correction type of formulation.

Convergence is considered to be obtained when the pressure distribution output by the analysis program is sufficiently close to the prescribed pressure distribution from the previous inverse case. Although convergence in the proper mathematical sense is not guaranteed in Tranen's procedure, examples such as reproduced in figure 5.13 suggest that engineering requirements can be met in two or three inverse - direct iterations. Finally, it is worth mentioning that an approach similar to Tranen's was followed by Volpe⁵⁰ in an attempt to solve the inverse problem for two-element airfoil systems.

As mentioned before, a more fundamental (but not necessarily more practical) approach to the 2-D inverse problem for the full potential equation has been taken by Volpe and Melnik²⁰. The fundamental difference with Tranen's procedure is that Volpe and Melnik satisfy the compressible analogue of Lighthill's first constraint; their solutions represent proper stream surfaces. They do so by allowing the magnitude q_∞ of the free stream to vary in such a way that, in Tranen's terminology, $V = 0$ where U is specified to be zero. In this way they succeed in solving the "pure" inverse problem by a sequence of Dirichlet problems with no need, at any stage, for a direct solution over the current airfoil contour. However, they do not control closure in the sense that a given trailing edge thickness is designed for.

The formulation and solution of the Dirichlet problem in Volpe's method differs from Tranen's in a number of technical but not insignificant details. The most important of these are:

- the "circle plane" finite difference technique is based on Jameson's^{51,10} (non-conservative) rotated difference scheme and mapping procedure rather than those of the Garabedian-Korn method^{48,9}
- the constant of integration fixing the surface potential is chosen arbitrarily but a source term $\sigma \ln r$ is subtracted from the potential. The source term is also represented in the far-field boundary condition and allows for a net mass flow through the boundary as well as for mass generation at shock waves introduced by the non-conservative differencing.
- After each relaxation sweep both the free stream velocity q_∞ and the source term σ are corrected in order to enforce $V = 0$ at the leading edge stagnation point and at the trailing edge. Hence there is no room for control of closure and whatever trailing edge gap results from the computation is accepted.
- After each Dirichlet problem the perturbation slope

$$\delta \theta_{i,j=1} = \tan^{-1} \frac{V_{i,j=1}}{U_{i,j=1}} \quad (5.28)$$

is used to determine the corrections to the mapping modulus that will drive the approximate airfoil surface to become a streamline. Upon convergence the inverse mapping from the unit circle to the converged airfoil shape is carried out using the known mapping modulus and airfoil slopes.

A point of concern with respect to Volpe's method is that substantial underrelaxation must be applied to the changes in airfoil shape in order to ensure convergence of the design process. In spite of this the number of Dirichlet cycles required for convergence is fairly large, being of the order of 15. This should be compared with the 2 to 3 cycles, which, apparently are required in Tranen's approach. We will return to this point shortly.

A remark must be made first with respect to the treatment of the trailing edge. It is recalled that the target surface pressures (velocities) are specified at half-mesh and the circulation fixed by integration. At the same time, after satisfying the difference equations, the velocity components are calculated at the mesh points themselves by means of central differences. As a result, U at the trailing edge is not necessarily zero. Hence there is no complete consistency with the direct solution where the circulation is fixed by requiring U to be zero at the trailing edge. In the inverse method a small correction to the circulation of $O(h^2)$, h being the mesh width, will in general be sufficient to drive U exactly to zero at the trailing edge.

Having noticed that in general, $U \neq 0$ at the trailing edge one may conclude that $\delta \theta$ (equation (5.28)) will also in general remain bounded. Hence the question arises whether the source term σ should be used to drive $V \rightarrow 0$ at the trailing edge. An interesting alternative would seem to be to use σ for control over the trailing edge gap instead. Some control, if necessary at all, over the boundedness of $\delta \theta$ at the trailing edge could be exercised through a (small) correction of $O(h^2)$ to the circulation. There is reason to believe that the use of the source term σ to control closure might also improve the convergence characteristics. The reason is that the value of σ is completely determined by the total integrated net mass flux through the surface and depends only very weakly on the normal velocity in one particular (the trailing edge) point.

A distinctly different approach to transonic flow computations (both analysis and design) has been taken by Carlson⁵². Instead of using a body conforming finite difference mesh in the circle plane, Carlson uses (stretched) Cartesian coordinates in the physical plane. As a consequence special complicated difference formulae must be used to satisfy the airfoil boundary conditions in both the analysis and design mode.

From the design point of view Carlson's method, while based on full potential theory (non-conservative), is very similar to the small perturbation formulation of Shankar³⁸. In both methods a mixed boundary value problem is solved with the leading edge shape or a greater portion of the airfoil fixed and the pressure prescribed over the remaining portion ($x/c > .06$). As in Shankar's method the orientation of the given leading edge shape with respect to the free stream is fixed and there is no actual control over airfoil closure. Closure can be obtained only by adopting a sharper or blunter nose shape.

From the numerical point of view the analysis and design formulations of Carlson are not completely equivalent. As a result there is no perfect agreement between direct and inverse calculations.

A further point worth mentioning is that, rather than determining the new geometry after convergence of the mixed boundary value problem, the geometry is updated after every ten relaxation sweeps. In combination with successive grid refinement Carlson found this to be the most economic procedure.

A simple, but apparently effective residual-correction type of approach towards the inverse airfoil problem has been described by Davis⁴⁵. In this method the FL06 analysis code^{52,14} is utilized to determine the actual pressure distribution for the latest geometry. The residual δC_p is the driver for a simple, perturbation type of surface modification (inverse) routine. For the latter Davis has taken transonic wavy-wall formulae. These relate the required change in pressure to a change in surface curvature when the local Mach number is < 1 and to a change in surface slope when $M_{loc} > 1$. The perturbation slopes and curvatures are then integrated to yield ordinate modifications.

Due to the local perturbation character of the wavy-wall formula the method can be used only for local modifications to the pressure distribution of an existing airfoil. Reference 45 presents results for upper surface contour modifications only, with no control over the trailing edge gap. About 20 iterative cycles are needed for convergence.

While, from the design point of view, the possibilities of Davis' method are limited to local modifications, an advantage of his approach is that only modest development efforts are needed to obtain a working code; the reason being that the (complicated) analysis code is retained in its original form and only the (simple) geometry correction package must be developed.

Another possibility for solving the inverse problem through the use of an analysis method, has been studied by McFadden⁴⁶. In [46] a modified version of the Bauer-Garabedian-Korn-Jameson (BGKJ) circle plane relaxation program¹⁰ with non-conservative rotated difference scheme, and a functional relationship involving the mapping and the velocity distribution along the airfoil surface in the physical and computational planes are used in an iterative sequence. In each iteration a functional relationship of the type

$$\frac{ds}{d\omega}^{(n+1)} = \frac{1}{q(s(\omega))} \frac{\partial \phi}{\partial \omega}^{(n)} (\omega, r = 1) \quad (5.29)$$

is used to obtain a better approximation to the mapping function of the required airfoil. In (5.29) s is the arc length along the airfoil and ω the angular coordinate in the circle plane; the mapping is essentially determined by $\frac{ds}{d\omega}$. $q(s)$ is the required velocity distribution and $\phi^{(n)}$ is the potential on the airfoil surface as obtained from the preceding BGKJ relaxation solution.

Note that, upon convergence, equation (5.29) leads to the identity

$$q(s) = \frac{\partial \phi}{\partial s} = \frac{\partial \phi}{\partial \omega} (\omega, r = 1) \cdot \frac{d\omega}{ds} \quad (5.30)$$

Note also that the procedure bears some resemblance to the "indirect" inverse TSP formulations discussed in Section 5.3.2. In the latter, the irrotationality condition (5.8) plays the same role as equations (5.29)/(5.30) in McFadden's approach.

Further noteworthy features of McFadden's method are that

- the (iterative) relaxation process and the outer iterations for the geometry are intermingled.
- on fine meshes an additional artificial viscosity term that suppresses the formation of shock waves is required for convergence (which takes 200-700 relaxation cycles). As discussed in [46] the undesirable effects of this limitation can be overcome largely by a suitable design strategy.
- in order to avoid singular behaviour of (5.29) at the stagnation point ($q = 0$) a special treatment, implying modification of $\phi^{(n)}$, is incorporated.
- while the analysis routine requires M_∞ and q_∞ to be given (the latter is set equal to unity) the critical velocity c^* must be chosen in the design program. M_∞ is determined from the isentropic relation

$$\frac{1}{2} \left(\frac{c^*}{q_\infty} \right)^2 \frac{\gamma+1}{\gamma-1} = \frac{1}{2} + \frac{1}{(\gamma-1)M_\infty^2} \quad (5.31)$$

- instead of setting q_∞ equal to unity, the free stream velocity, as in Volpe's²⁸ method, comes out as a result of the design calculations. However, rather than using q_∞ to eliminate the stagnation point singularity, q_∞ in McFadden's approach, is used to minimize the functional

$$I = \int_0^{2\pi} \left[\left(\phi_s^{(n)} \right)^2 - \left(\frac{q(s)}{q_\infty} \right)^2 \right] d\omega \quad (5.32)$$

While a motive for this particular choice is not given, the result seems to be that the overall thickness of the new airfoil is approximately the same as that of the starting airfoil.

- there is no control over closure. The trailing edge gap must be accepted as it is or must be manipulated through changes in the target pressure distribution. An alternative possibility would seem to be to use q_∞ to control the trailing edge gap rather than to minimize (5.32).

An example of application of McFadden's method has been reproduced in figure 5.14. The example is interesting in that it illustrates the fact that a smooth surface pressure distribution does not necessarily lead to a shock-free flow or even a flow with low wave drag; the shape of the sonic line as well as the figure for wave drag (40 counts) indicate the presence of a shock wave in the flow field that weakens and vanishes as it approaches the airfoil. Note that reference 46 contains several useful guidelines for the choice of "target" pressure distributions in relation to low wave drag.

Three-dimensional flow

As mentioned earlier the question of well-posedness of the inverse problem in three dimensions does not seem to have been addressed properly even for incompressible flow. One aspect is that the 3-D equivalents of Lighthill's²⁶ constraints have not been formulated. Apart from this there are strong indications that the 3-D inverse problem is ill-posed, [1], [53], in the sense that small differences in specified pressure distribution may lead to large differences in geometry.

Other aspects of the 3-D inverse problem, in particular when formulated in terms of a sequence of Dirichlet problems with geometry corrections based on calculated normal velocity distributions, are the following:

The conversion of specified pressure or velocity distribution into specified velocity potential is fundamentally more complicated than in 2-D flow. Assuming the normal velocity to be sufficiently small the conversion is described by the equation

$$\phi_{\xi}^2 + \phi_{\eta}^2 = q^2(\xi, \eta) \quad (5.33)$$

ξ, η being orthogonal curvi-linear coordinates on the (approximation to the) wing surface. The problem of finding ϕ is similar to one in three-dimensional boundary layer computations⁵⁴ in which the boundary conditions at the edge of the boundary layer require the knowledge of the velocity components of the outer inviscid flow while only the pressure distribution is given. It leads to an initial value problem with either the potential or both velocity components at the leading edge given as initial conditions. Because of the hyperbolic nature of this initial value problem, the characteristics of which are the streamlines, the solution may contain discontinuities manifesting themselves in e.g. "intersecting streamlines", unless the prescribed pressure distribution and/or the initial conditions satisfy additional requirements. Clearly such discontinuities are not acceptable in the inverse problem⁵⁵. However, it is not quite clear how they should be avoided. Presumably one should either avoid to linearize the full non-linear problem in such a way that the solution of initial value problems is required at intermediate steps or one should choose the initial conditions (ϕ or direction of q at the leading edge) such that discontinuities are avoided.

The problem of correcting the geometry when the normal velocity (W) is known from the solution of the Dirichlet problem is closely related to the problem of computing the displacement thickness of a 3-D boundary layer. It follows from the discussion by Lighthill⁵⁵ that, assuming the displacement δ to be small, δ is determined by a quasi-linear first order equation of the type

$$\frac{\partial}{\partial \xi} (\rho U \delta h_{\eta}) + \frac{\partial}{\partial \eta} (\rho V \delta h_{\xi}) = \rho W h_{\xi} h_{\eta} \quad (5.34)$$

In (5.34) ξ, η are orthogonal curvilinear coordinates and h_{ξ}, h_{η} metric coefficients. Note that the streamlines are also the characteristics of (5.34). Hence the remarks given above with respect to the determination of ϕ from (5.33) are also relevant for the determination of δ from (5.34).

Questions like those mentioned above are either ignored or circumvented in the few 3-D transonic (as well as subsonic) inverse methods that can be found in the literature. This is, for instance, the case with the method described by Henne⁴³. Henne's method can be considered as the 3-D equivalent of Tranen's approach for 2-D. The Jameson-Caughey FLQ22 code (Section 3.3.2) has been modified to accept Dirichlet boundary conditions. Figure 5.15 presents a simplified scheme of the procedure. The point is stressed in [43] that the scheme requires the assumption of small changes. While the surface value for the potential in the Dirichlet problem is obtained by "streamwise integration of the velocity at constant span stations" the problem of determining the velocity components is not mentioned. Details about the determination of the surface displacement from the normal velocities are not given either. Nor is mention made of any additional conditions enforcing proper branching of the stream surface. On the other hand, the spanwise variation of the surface potential is reported to be used as a parameter for trailing edge closure control.

As in Tranen's⁴¹ case direct analysis computations are required to check whether the design goal has been achieved. Similarly it is doubtful whether the scheme will converge in the proper mathematical sense. However, the examples of application presented in [43], one of which is reproduced in figure 5.16, indicate that convergence in an engineering sense can be obtained in 2 to 6 inverse cycles.

A somewhat unusual scheme for linearizing the non-linear boundary conditions of the inverse problem to a Dirichlet-type boundary condition is utilized by Shankar⁴⁴ in an attempt to modify the FLQ30 finite volume analysis code (Section 3.3.2) into a design code. Starting out from the analysis solution for a suitable estimate of the required geometry Shankar applies a correction to the surface value of the potential in each relaxation sweep. This correction is determined from the isentropic relation for the density

$$\rho = \left[1 - \frac{\gamma-1}{2} M_{\infty}^2 (q^2 - 1) \right]^{-\frac{1}{\gamma-1}} \quad (5.35)$$

This is linearized to read

$$d\rho = -\rho^{2-\gamma} M_{\infty}^2 |q| d|q| \quad (5.36)$$

or

$$\rho^{(n+1)} - \rho^{(n)} = -\rho^{2-\gamma} M_{\infty}^2 |q^{(n)}| (|q^{(n+1)}| - |q^{(n)}|) \quad (5.37)$$

Utilizing the isentropic relation

$$\rho = \left\{ C_p \frac{\gamma}{2} M_{\infty}^2 + 1 \right\}^{1/\gamma} \quad (5.38)$$

equation (5.37) can, in general curvilinear coordinates, be rewritten as

⁵⁵ In the boundary layer case the discontinuity may be indicative for a separation line, with the discontinuity representing the "footprint" of the associated vortex sheet in the outer inviscid flow.

$$\left(U^{(n)} \frac{\partial}{\partial \xi} + V^{(n)} \frac{\partial}{\partial \eta} \right) \delta \phi = \frac{\left(\rho^{(n)} \right)^{\gamma-2}}{M_\infty^2} \left[\rho^{(n)} - \left\{ C_{p_t} \frac{\gamma M_\infty^2}{2} + 1 \right\}^{1/\gamma} \right] \quad (5.39)$$

In (5.39) U and V are the contravariant surface velocity components. C_{p_t} is the "target" C_p -distribution. Equation (5.39), in discretized form, is solved for the correction $\delta \phi$ to the surface potential.

The procedure just described is related but not identical to one in which the direction of the surface velocity is kept fixed but the magnitude updated. Note that in the latter approach, provided a converged analysis solution is taken as the starting point, the problem of discontinuities in the surface streamline pattern would be avoided.

Using the contravariant velocity component W , computed at half a mesh from the wing surface, the geometry is corrected, without control over closure, after each relaxation sweep. The author of [44] is not very clear, however, on the precise procedure and communicates the opinion that a better procedure to update the wing ordinates, including control over closure should be included.

A residual correction type of formulation that can be considered as a generalization to 3 dimensions of McFadden's⁴⁶ approach, is briefly described by Garabedian and McFadden in [47]. The method utilizes a modified version of the FL022 analysis code in combination with some functional relationship between geometry correction and pressure residual. The functional relationship is in the form of a partial differential equation that is solved along with the partial differential equation for the velocity potential. However, the paper is not very clear on the precise form and the motives for the particular choice.

In order "to avoid questions of closure and other complications with the geometry" the pressure, in [47], is assigned only over the part of the geometry that lies outside a given starting geometry. As a result the wing surface is modified only where the local speed is sufficiently large. There, the method may be used e.g., to reduce the strength of shock waves in areas with supersonic flow. Note that this capability is somewhat similar to that of the fictitious gas method described in Section 5.2.2.

Concluding the discussion on 3-D full potential transonic inverse methods, it would seem that we have only just begun to tackle the problem. Considerable efforts will be required before we will arrive at well founded, reliable engineering tools of practical significance.

5.4 Design by means of numerical optimization

In this section we will discuss design procedures involving the use of aerodynamic analysis methods in combination with a numerical optimization algorithm. While applications have seen the use of various aerodynamic codes, only one single feasible directions/gradient optimization algorithm, developed by Vanderplaats⁵⁶, seems to be used almost exclusively.

The approach is fairly recent (1974, Hicks et al.⁵⁷), owing its existence entirely to the availability of large and fast computer systems. Because of the excessively large computational requirements, at least in 3-D, the approach is sometimes referred to as "design by brute force". Nevertheless it holds great potential for the future. A reappraisal of the technique has been given recently by Hicks⁵⁸.

A generalized flow diagram of the design - by - numerical - optimization technique is presented in figure 5.17. Inherent to the numerical optimization approach are the choice of an aerodynamic object function F that is to be minimized, a number of quantities to be constrained G_j and the choice of a set of design variables. The object function can be the drag or any other suitable aerodynamic quantity. The constraints can be of aerodynamic or geometric nature; e.g. C_L and/or t/c greater than a specified value. The design variables are taken to be the coefficients A_i of a number of shape functions

$$Z = Z_0 + \sum_{i=1}^n A_i \cdot f_i \quad (5.42)$$

describing (modifications to) the starting wing geometry.

The process begins by perturbing, in sequence, each of the shape function coefficients A_i . The resulting n shapes are analyzed by means of the aerodynamic program (determination of F and G_j 's) and the derivatives $\frac{\partial F}{\partial A_i}$, $\frac{\partial G_j}{\partial A_i}$, or rather the difference quotients $\frac{\Delta F}{\Delta A_i}$, $\frac{\Delta G_j}{\Delta A_i}$ are determined. The next step is the formation, by the optimization program, of the gradient ∇F and the determination of the direction of steepest descent of F , in the n -dimensional space formed by the basis vectors \hat{A}_i , while satisfying the constraints. The optimization program then executes a number (typically 3) of steps in this direction, with another aerodynamic analysis performed at each step, until either a constraint is met or F attains a minimum. In the first case, or when the minimum of F is lower than the previous minimum, the process is repeated; new gradients are determined, etc.. When the latest minimum of F is equal to or higher than the previous one the process is terminated.

The optimization process described above requires typically 10 complete cycles or, in other words, $10(n+3)$ analysis calculations, [59]. This immediately illustrates the weakest point of the numerical optimization approach. In order to keep the computational effort required within reasonable bounds one has to put severe limitations on the number n of design variables, in particular in 3-D flow. The problem is enhanced by the fact that for acceptable convergence of the optimization process it is necessary to avoid "numerical noise" in the partial derivatives of the object function, [61], [62]. This requires that the relaxation process in each analysis calculation must be continued until the residual has reached a level beyond that which is often customary in "normal" analysis calculations. It also appears to exclude the use of analysis codes with simple boundary layer corrections, [58].

One way to reduce the number of analysis calculations required in 3-D applications is to evolve the design variables in a series of steps, [64]. For example, by first designing the upper surface, section by section, going from root to tip and then the lower surface. Clearly it is also very important to select a starting geometry having aerodynamic characteristics which are already close to the target. This asks for an information systems/data base approach. With previous experience stored in the data base, the latter can be searched for the most suitable starting solution. As described in [59] the data base approach can also be used to speed-up the convergence of numerical optimization by at least a factor two. With the results of all preceding geometry perturbations stored it is possible to construct higher partial derivatives of the object function and utilize higher order gradient methods.

With the severe limitations on n , the choice of the shape functions is of utmost importance. The choice should be directed towards describing a sufficiently wide class of practical solutions. While

simple polynomial expressions were used in early applications [57], [60], of the numerical optimization concept, a more sophisticated class of shape functions describing more local geometry modifications was used in later applications, [61], [62], [63]. However, as discussed in [64], there is a need for still better shape functions with even more localized curvature variations. In fact it can be argued, following arguments similar to those used by Davis⁴⁵ in selecting the geometry correction formulae in his residual-correction type of inverse method, that while curvature based shape functions are suitable for areas with subcritical flow, slope based shape functions might be more appropriate in areas with locally supersonic flow. In general it can be stated that the design variables must be chosen carefully for each individual optimization problem. Not in the least because the choice also affects the convergence of the optimization progress, [59].

While the choice of the design variables is of great practical significance, the choice of the object function, in conjunction with the choice of the aerodynamic and geometric constraints, is of more fundamental interest. In two-dimensional transonic applications, [57], [59], [60], [61], [65] it has been customary to select the wave drag as the quantity to be minimized, subject to constraints on, e.g., airfoil thickness or volume, lift and/or pitching moment. Although it is clear that constraints are necessary in a meaningful drag minimization problem it is by no means clear how exactly the problem should be formulated in order to guarantee a unique solution. The problem is illustrated by figure 5.18, taken from [59]. Shown are the results of two drag minimization runs with identical free stream conditions and identical constraints on lift and airfoil volume. Only the starting solutions differ. As illustrated by the figure the two resulting airfoils are totally different in shape. Clearly the problem, as formulated, has more than one, local minimum and neither of the two necessarily represents the absolute minimum.

Figure 5.18, the airfoil on the right in particular, also illustrates another problem of direct (inviscid) wave drag minimization: In the absence of (direct) control over the pressure distribution the solution may acquire unrealistically high pressure gradients, such as near the upper surface trailing edge.

A strong point of the numerical optimization approach is the possibility of selecting object functions and constraints suitable for multi-point designs. An example of a two-point design problem directed towards the design of airfoils with low drag creep can be found in [61]. It is also entirely possible to consider, e.g. transonic drag minimization and low-speed stall requirements simultaneously.

While the direct minimization of (inviscid) wave drag is feasible in two dimensions, it is not, at present, in the case of three-dimensional wings. Several unsuccessful attempts in this direction can be found in the literature, [62], [63], [64]. The main reason for this failure is the lack of accuracy in the determination of the pressure drag with the currently available 3-D codes and the limited number of mesh points (Section 2.3). Another problem would seem to be that the problem of uniqueness in three dimensions is even more severe than in two dimensions. The accuracy problem might be overcome when more efficient algorithms (Chapter 6) and/or more computer power (vector machines) allow the number of mesh points to be increased. The uniqueness problem would probably require the introduction of more constraints or more sophisticated object functions.

Because of the difficulties just mentioned most 3-D applications [63], [64], of design-through-numerical-optimization have seen the use of the pressure distribution type of object function

$$F = \sum_{i=0}^N \left(\frac{C_p - C_{p_{target}}}{C_p} \right)^2_i \quad (5.43)$$

When used in this mode, design-by-numerical-optimization is an extremely expensive substitute for the inverse approach described in the preceding section. While the latter is absolutely feasible on currently available general main frame computers, the former, requiring an order of magnitude more computer time, is absolutely not, at least in an industrial environment. On the other hand, inverse design through numerical optimization does have the advantage that direct control over the geometry can be exercised through the application of constraints. The latter possibility is absent in the case of the inverse methods discussed in Section 5.3.

Summarizing the discussion on design by numerical optimization, it may be said that the potential possibilities of the approach are enormous with, at present, unique capabilities such as multi-point and constrained design. However, the approach is also unique in terms of required computer resources. Substantial improvements in both flow optimization code algorithms and/or computer efficiency, relative to current general standards, are required before numerical optimization in 3-D wing design can be used on a routine basis.

5.5 Concluding remarks

Having discussed the possibilities and limitations of several approaches in aerodynamic design, the question may be raised which, if any, of the various techniques is to be preferred. As usual with such questions a general and definitive answer cannot be given. The answer will depend on the particular circumstances that apply and will vary from case to case.

If a choice between the various possibilities is to be made table 5.1 may be of some help. The table illustrates the point mentioned before that if a general design method for complete wings is required neither the fictitious gas method nor the local residual-correction type of inverse approach are adequate. In this author's opinion an inverse approach allowing global wing design as well as local design modifications is, at present, the best compromise, numerical optimization being too expensive.

The most serious limitation of the current inverse methods is that no direct control can be exercised over the geometry. Efforts should be directed towards developing transonic inverse codes which do have this capability. (A subsonic inverse code having this capability is described in [30].)

Another problem with inverse methods is that the specification of the target pressure distribution puts a heavy burden on the aerodynamicist; the target pressure distribution must be chosen such that boundary layer separation is avoided and that drag is minimized while obtaining an acceptable geometry. That this, e.g. in relation to wave drag, is not at all a trivial problem has been illustrated by figure 5.14, showing that a suitably looking shock-free surface pressure distribution may not be suitable for the minimization of wave drag. Another example of this kind is presented in figure 5.19 which was taken from [47]. The figure on the right presents the result of an inverse (McFadden's) method; the resulting airfoil carries a wave drag of 38 counts. The figure on the left, on the other hand, presents the nearest shock-free solution (zero wave drag) as obtained with the hodograph method of [14]. Note that the latter result

could also be obtained by means of the fictitious gas method.

It is conjectured that most if not all of the limitations of the (pure) inverse method could be avoided through an approach which we will call inverse numerical optimization. In this conjectural scheme (Fig. 5.20) the design variables are parameters describing the pressure distribution rather than the geometry. The optimization algorithm is used to optimize a target pressure distribution, e.g. with the objective to minimize the drag. Using the latest available estimate of the geometry this can be done relatively cheap through an induced drag routine (Trefftz plane) a boundary layer code and a pressure drag routine. With the target C_p -distribution established the new geometry can be determined by means of an inverse code. The process is repeated when the new geometry differs significantly from the previous one or when a geometry constraint is met. In the latter case (new) constraints will have to be imposed on the values of the parameters describing the pressure distribution. Information from all the previous iterations can be used to determine these new values.

It is the author's opinion that an approach of the type sketched above, is worthy of further investigation, in particular when embedded in an information systems/data base approach, [65].

5.6 References

1. Slooff, J.W., Windtunnel tests and aerodynamic computations; thoughts on their use in aerodynamic design, AGARD CP. No.210, paper 11, 1976
2. Nieuwland, G.Y., The computation by Lighthill's method of transonic potential flow around a family of quasi-elliptical aerofoils, NLR TR T.83, 1964.
3. Boerstoeel, J.W., Review of the application of hodograph theory to transonic aerofoil design and theoretical and experimental analysis of shock-free aerofoils, Proceeding IUTAM Symposium Transonicum II Springer Verlag 1976. Also NLR MP 75033 U, 1975.
4. Nieuwland, G.Y., Transonic potential flow around a family of quasi-elliptical aerofoil sections, NLR TR T.172, 1967.
5. Takanaski, S., A method of obtaining transonic shock-free flow around lifting aerofoils, Trans. Japan Soc. Aerospace Sci. 16, (34), 1973.
6. Boerstoeel, J.W., and Huizing, G.H., Transonic shock-free airfoil design by an analytic hodograph method, AIAA paper 74-539. Also NLR MP 74025 U, 1974.
7. Sobieczky, H., Entwurf überkritischer Profile mit Hilfe der Rheo-Elektrische Analogie, DLR-FB 75-43, 1975.
8. Eberle, A., Eine exakte Hodographenmethode zum Entwurf überkritische Profile, MBB UFE 1168-75 8, 1975. (See also IUTAM Symp. Trans. II.)
9. Bauer, F., Garabedian, P., and Korn, D., Supercritical wing sections, Springer Verlag, 1972.
10. Bauer, F., Garabedian, P., Korn, D., and Jameson, A., Supercritical wing sections II, Springer Verlag, 1975.
11. Loeve, W., and Slooff, J.W., On the use of panel methods for predicting subsonic flow about aerofoils and aircraft configurations, NLR MP 71018 U, 1971.
12. Slooff, J.W., Wortmann, F.X., Duhon, J.M., The development of transonic airfoils for helicopters, NLR MP 75032 U, 1975.
13. NLR, unpublished work.
14. Bauer, F., Garabedian, P., Korn, D., Supercritical wing sections III, Springer Verlag, 1977.
15. Morawetz, C.S., On the non-existence of continuous transonic flows past profiles, Comm. Pure Appl. Math., Vol. 17, pp. 357-367, 1964.
16. Sobieczky, H., Related analytical, analog and numerical methods in transonic airfoil design, AIAA Paper No.79-1556, 1979.
17. Sobieczky, H., Fung, K.Y., Seebass, A.R., A new method for designing shock-free transonic configurations, AIAA Paper No.78-1114, 1978.
18. Yu, N.J., Efficient transonic shock-free wing redesign procedure using a fictitious gas method, AIAA Paper No.79-0075, 1979.
19. Eberle, A., Transonic flow computations by finite elements: Airfoil optimization and analysis, in: Recent developments in theoretical and experimental fluid mechanics, Springer Verlag, 1979.
20. Fung, K.Y., Sobieczky, H., Seebass, R., Shock-free wing design, AIAA Paper No.79-1557, 1979.
21. Rai, P., Miranda, L.R., Seebass, A.R., A cost-effective method for shock-free supercritical wing design, AIAA Paper No.81-0383, 1981.
22. Fung, K.Y., Seebass, A.R., Dickson, L.J., Pearson, C.F., An effective algorithm for shock-free wing design, AIAA Paper No.81-1236, 1981.
23. Nebeck, H.E., Seebass, A.R., Sobieczky, H., Inviscid-viscous interaction in the nearly direct design of shock-free supercritical airfoils, AGARD CP-291, 1980.
24. Sobieczky, H., Die Berechnung lokaler räumlicher Uberschallfelder, ZAMM 58T, 1978.
25. Subsonic/transonic configuration aerodynamics, Round Table Discussion, AGARD CP-285, 1980.
26. Lighthill, M.J., A new method of two-dimensional aerodynamic design, ARC R&M 2112, 1945.
27. Woods, L.C., The design of two-dimensional airfoils with mixed boundary conditions, Quart. Appl. Math. Vol. 13, pp. 139-146, 1955.
28. Volpe, G., and Melnik, R.E., The role of constraints in the inverse design problem for transonic airfoils, AIAA Paper No.81-1233, 1981.
29. Ashley, H., and Landahl, M.T., Aerodynamics of wings and bodies, Addison-Wesley Publ. Company, Inc., Reading, Mass., 1965.
30. Fray, J.M.J., and Slooff, J.W., A constrained inverse method for the aerodynamic design of thick wings with given pressure distribution in subsonic flow, AGARD CP-285, 1980.
31. Steger, J.L., and Klineberg, J.M., A finite difference method for transonic airfoil design, AIAA J., Vol. 11, No.5, pp. 628-635, May 1973.
32. Langley, M.J., Numerical methods for two-dimensional and axisymmetric transonic flow, ARA Memo 143, 1973.
33. Murman, E.M., and Krupp, J.A., The numerical calculation of steady transonic flow past thin lifting aerofoils and slender bodies, AIAA Paper No.71-566, 1971.
34. Lock, R.C., Research in the U.K. on finite difference methods for computing steady transonic flow, in: Symposium transonicum II, Springer Verlag, 1976.
35. Schmidt, W., Rohlf, S., and Vanino, R., Some results using relaxation methods for two- and three-dimensional transonic flows, Lecture Notes in Physics, Vol. 35, pp. 364-372, 1975.

36. Schmidt, W., and Hedman, S., Recent explorations in relaxation methods for three-dimensional transonic potential flow, ICAS Paper 76-22, 1976.
37. Shankar, V., Malmuth, N.D., and Cole, J.D., Computational transonic airfoil design in free air and a wind tunnel, AIAA Paper No.78-103, 1978.
38. Shankar, V., Malmuth, N.D., and Cole, J.D., Computational transonic design procedure for three-dimensional wings and wing-body combinations, AIAA Paper No.79-0344, 1979.
39. Mason, W., McKenzie, D.A., Stern, M.A., and Johnson, J.K., A numerical three-dimensional viscous transonic wing-body analysis and design tool, AIAA Paper No.78-101, 1978.
40. Shankar, V., Computational transonic inverse procedure for wing design with automatic trailing edge closure, AIAA Paper No.80-1390, 1980.
41. Tranen, T.L., A rapid computer aided transonic airfoil design method, AIAA Paper No.74-501, 1974.
42. Carlson, L.A., Transonic airfoil analysis and design using Cartesian coordinates, J. Aircraft, Vol. 13, pp. 369-356, May 1976.
43. Henne, P.A., An inverse transonic wing design method, AIAA Paper No.80-0330, 1980.
44. Shankar, V., A full potential inverse method based on a density linearization scheme for wing design, AIAA Paper No.81-1234, 1981.
45. Davis Jr., W.H., Technique for developing design tools from the analysis methods of computational aerodynamics, AIAA Paper No.79-1529, 1979.
46. McFadden, G.B., An artificial viscosity method for the design of supercritical airfoils, Ph.D. Thesis, N.Y. University, 1979.
47. Garabedian, P., McFadden, G., Design of supercritical swept wings, proceedings of the 1980 Army Numerical Analysis and Computers Conference, ARO Report 80-3, 1980.
48. Garabedian, P.R., and Korn, D.G., Analysis of transonic airfoils, Comm. Pure and Appl. Math., Vol. 24, 1971.
49. Jameson, A., and Caughey, D.A., A finite volume method for transonic potential flow calculations, AIAA Paper No.77-635, 1977.
50. Volpe, G., Two-element airfoil systems design: An inverse method, AIAA Paper No.78-1226, 1978.
51. Jameson, A., Iterative solution of transonic flows over airfoils and wings, including flows at Mach 1, Comm. Pure Appl. Math., 27, pp. 283-309, 1974.
52. Jameson, A., Accelerated iteration schemes for transonic flow calculations using fast Poisson solvers, ERDA R&D Rept. COO-3077-82, Courant Inst. Math. Sci., N.Y. Univ., 1975.
53. Slooff, J.W., and Voogt, N., Aerodynamic design of thick supercritical wings through the concept of equivalent subsonic pressure distribution, NLR MP 78011 U, 1978.
54. Der Jr., K., and Raetz, G.S., Solution of general three-dimensional laminar boundary layer problem by an exact numerical method, IAS Paper No.62-70, 1962.
55. Lighthill, M.J., On displacement thickness, J. Fl. Mech. 4, p. 383, 1958.
56. Vanderplaats, G.N., CONMIN - A FORTRAN program for constrained function minimization, NASA TM X-62, 282, 1973.
57. Hicks, R.M., Murman, E.M., and Vanderplaats, G.N., An assessment of airfoil design by numerical optimization, NASA TM X-3092, 1974.
58. Hicks, R.M., Transonic wing design using potential flow codes - Successes and failures, SAE Paper 810565, 1981.
59. Vanderplaats, G.N., An efficient algorithm for numerical airfoil optimization, AIAA Paper No.79-0079, 1979.
60. Hicks, R.M., Vanderplaats, G.N., Murman, E.M., and King, Rosa T., Airfoil section drag reduction at transonic speeds by numerical optimization, SAE Paper 760477, 1976.
61. Hicks, R.M., and Vanderplaats, G.N., Application of numerical optimization to the design of supercritical airfoils without drag-creep, SAE Paper 770440, 1977.
62. Hicks, R.M., and Henne, P.A., Wing design by numerical optimization, AIAA Paper No.77-1247, 1977.
63. Haney, H.P., Johnson, R.R., and Hicks, R.M., Computational optimization and wind tunnel test of transonic wing designs, AIAA Paper No.79-0080, 1979.
64. Lores, M.E., Smith, P.E., and Large, R.A., Numerical optimization: an assessment of its role in transport aircraft aerodynamic design through a case study, ICAS-80-1.2, 1980.
65. Narramore, J.C., and Yeary, R.D., Airfoil design and analysis using an information system approach, AIAA Paper No.80-1444, 1980.

TABLE 5.1
Possibilities and limitations of various design approaches (3-D)

	local or global (re) design?	direct control over geometry?	direct control over aerodynamics?					multi-point design?	computational effort	other aspects
			C_L, C_D	induced drag	wave drag	viscous drag	C - distr. p			
Indirect (Fictitious gas)	Local	no	no	no	yes	no	no	no	acceptable	ill-posed problem?
Inverse	Global and local	no	yes	yes	no ^{o)}	no ^{o)}	yes	no	acceptable	ill-posed problem?
	Residual/Correction									
Direct numerical optimization	direct drag minimization	yes	yes	insufficient ⁺	no ^{o)}	no ⁺	no	yes	prohibitive	uniqueness problems?
	inverse mode									
Inverse numerical optimization	Global and local	yes	yes	yes	yes	yes	yes	?	acceptable?	CONJECTURED

*) currently, [47], but not necessarily local?

+) current situation, could be improved in future

o) indirect control through pressure distribution

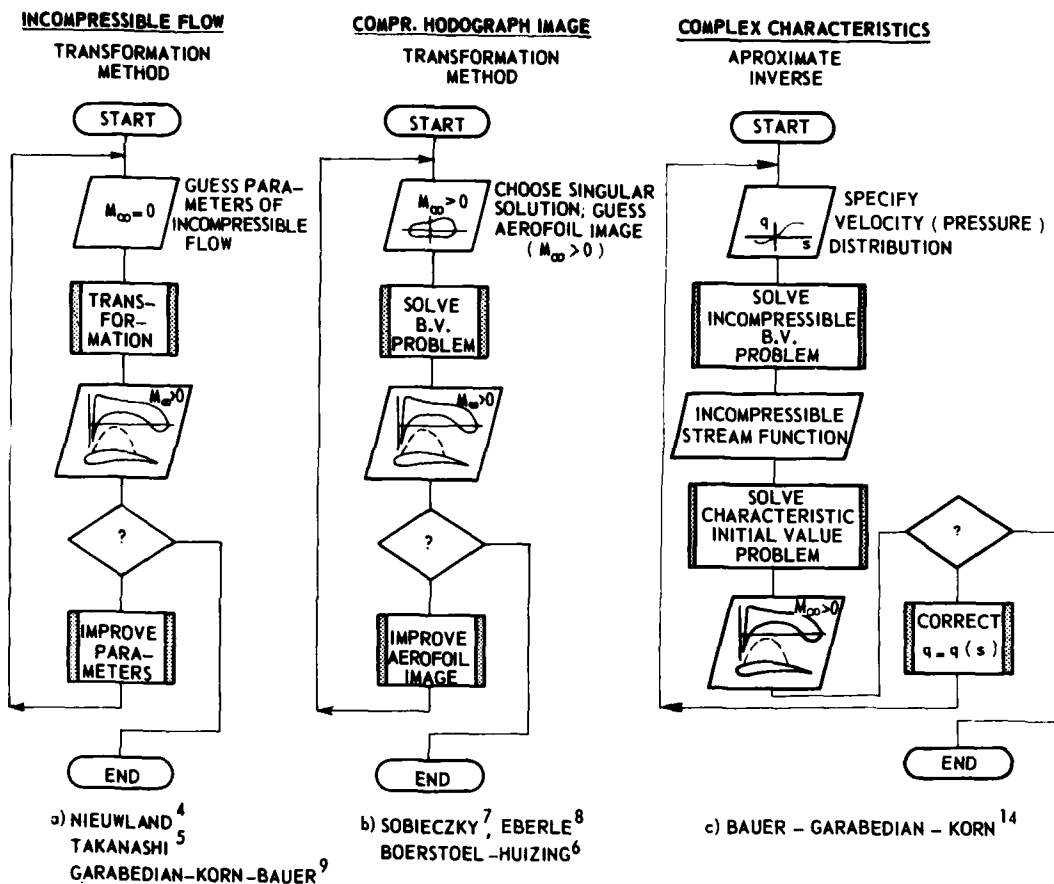
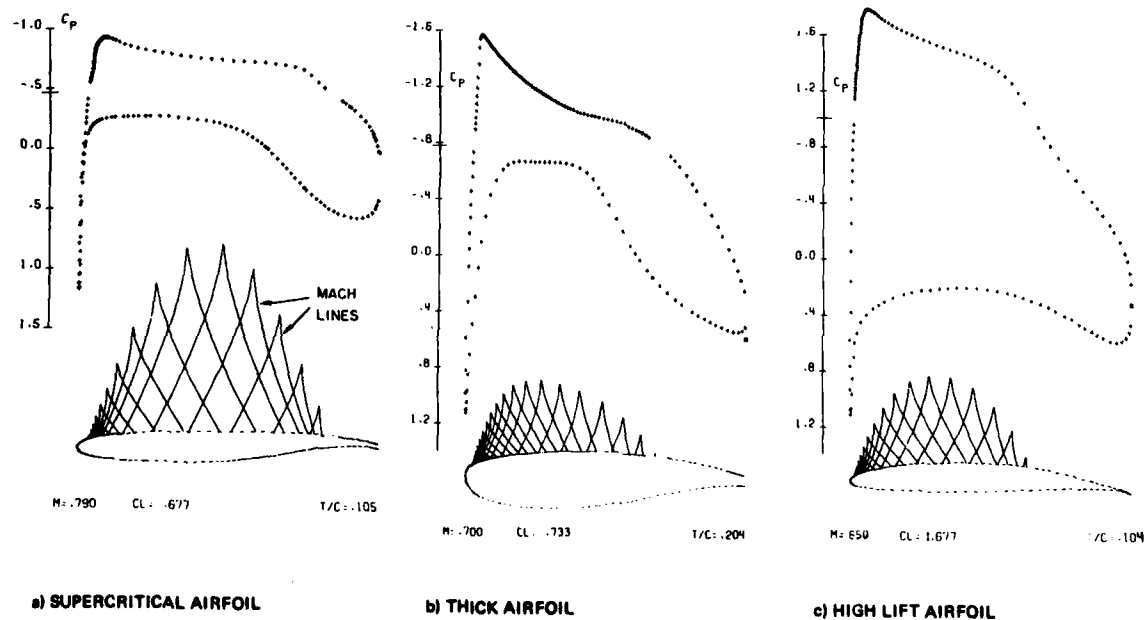


Fig. 5.1 Flow charts of hodograph procedures

Fig. 5.2 Examples of airfoils generated with Garabedian-Korn hodograph method^{9,10}

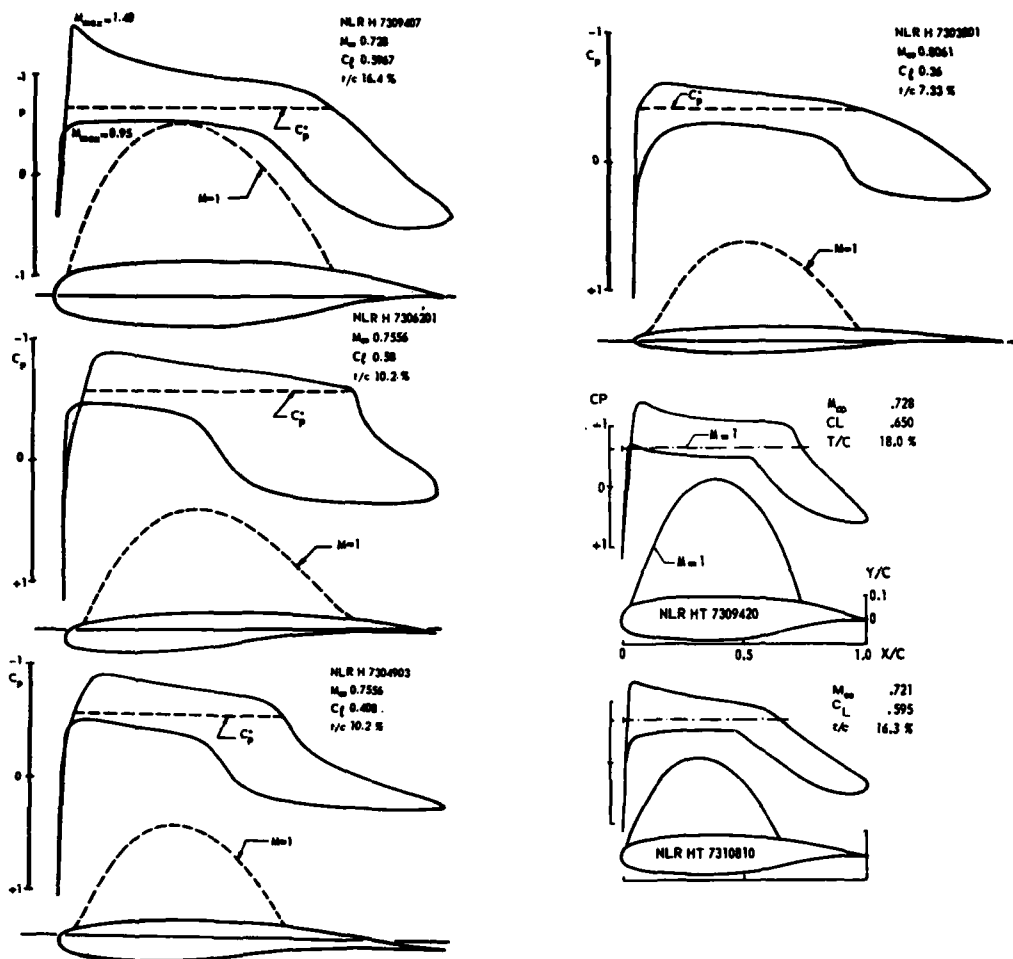


Fig. 5.3 Examples of airfoils generated with Boerstoeel-Huizing^{3,6} hodograph method

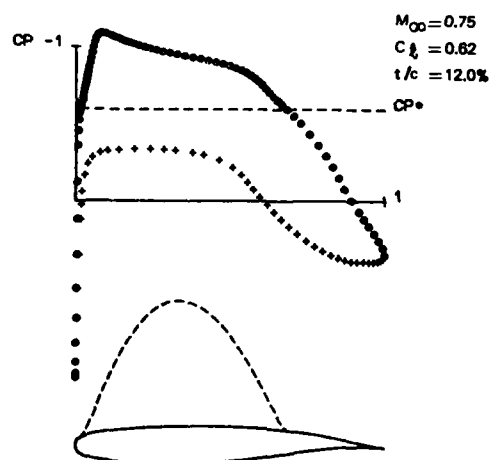


Fig. 5.4 Example of airfoil generated with Sobieczky-Eberle⁸ hodograph method

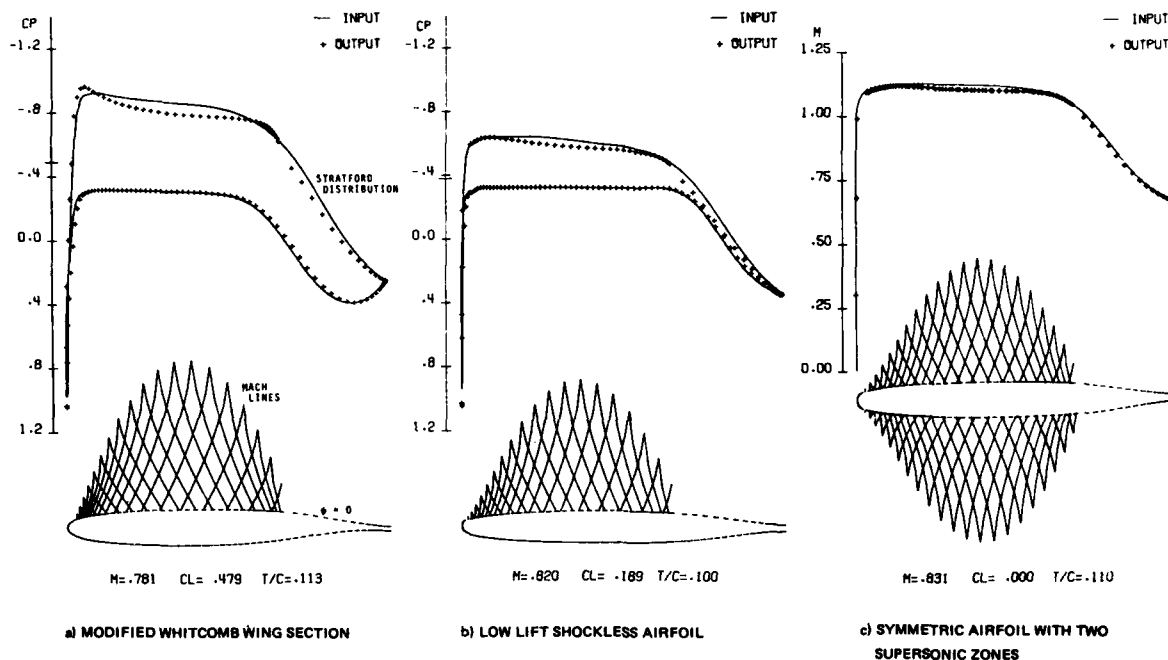


Fig. 5.5 Examples of hodograph airfoils designed for a given pressure distribution¹⁴

COMPARISON OF NUMERICAL ANALYSIS RESULTS FOR ORIGINAL AND SHOCK-FREE AIRFOIL (BASELINE AIRFOIL: NACA 64A410)

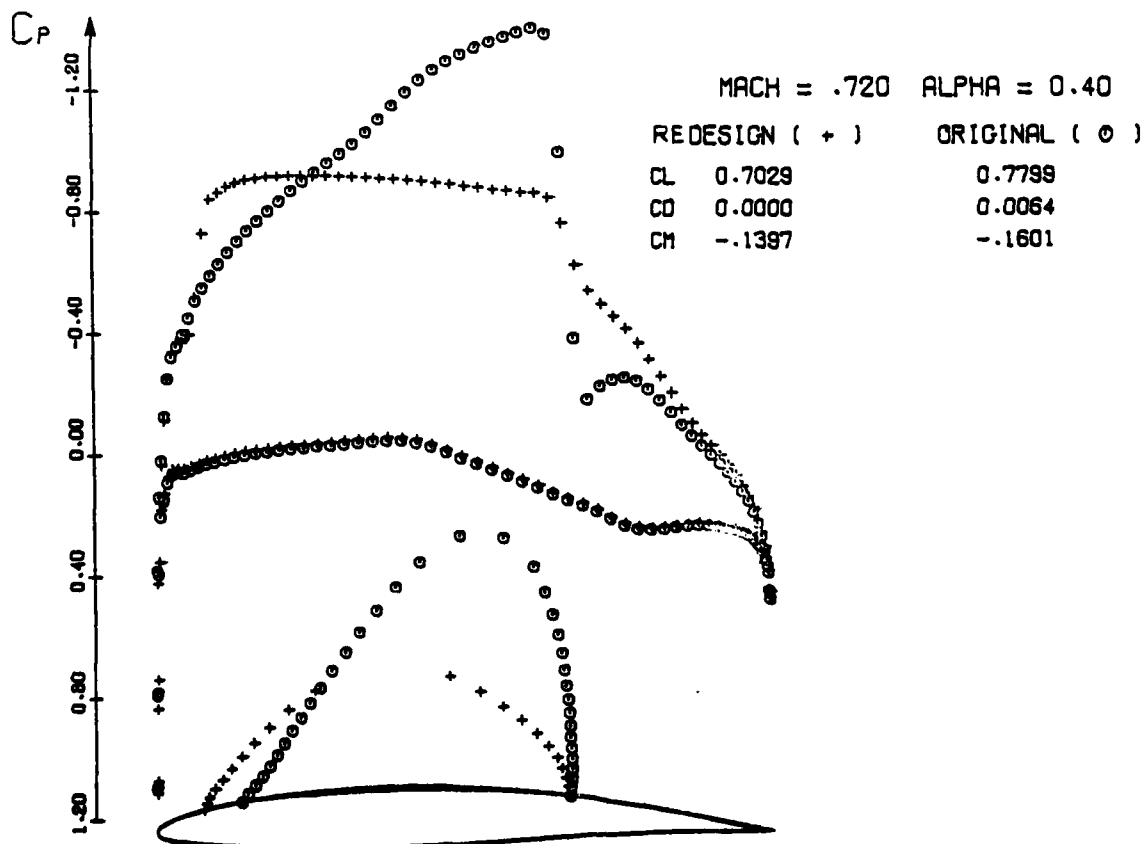


Fig. 5.6 Example of airfoil shock-free redesign by means of fictitious gas method [17]

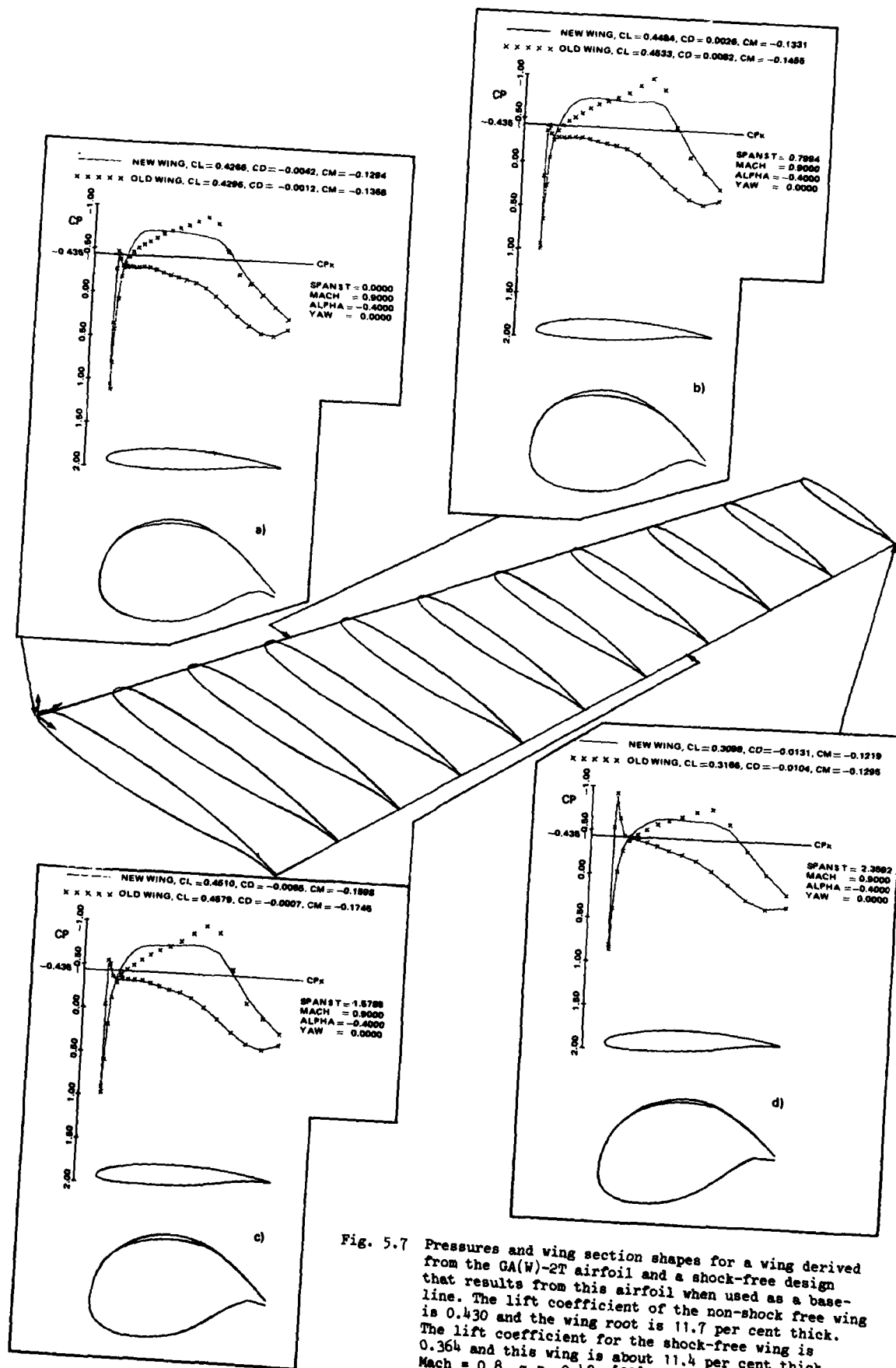


Fig. 5.7 Pressures and wing section shapes for a wing derived from the GA(W)-2T airfoil and a shock-free design that results from this airfoil when used as a baseline. The lift coefficient of the non-shock free wing is 0.430 and the wing root is 11.7 per cent thick. The lift coefficient for the shock-free wing is 0.364 and this wing is about 11.4 per cent thick. Mach = 0.8, $\alpha = -0.4^\circ$, [22]

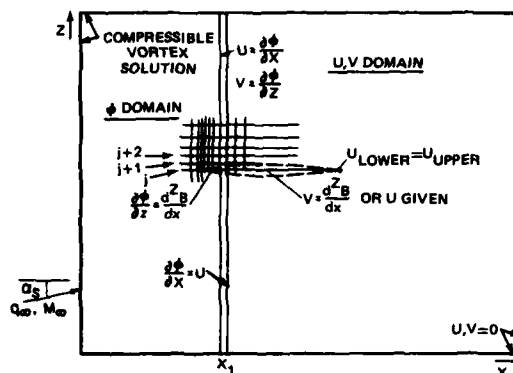


Fig. 5.8 Sketch of field subdivision in Steger/Klineberg³¹ inverse method

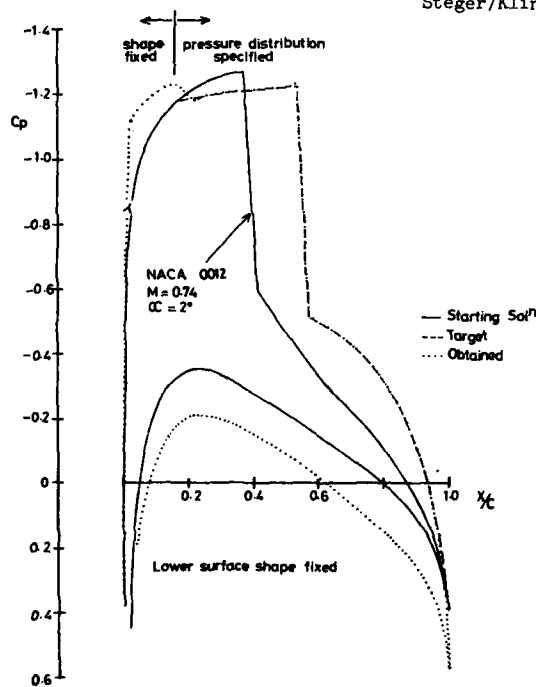


Fig. 5.9 Example of ARA inverse method (2-D)³²

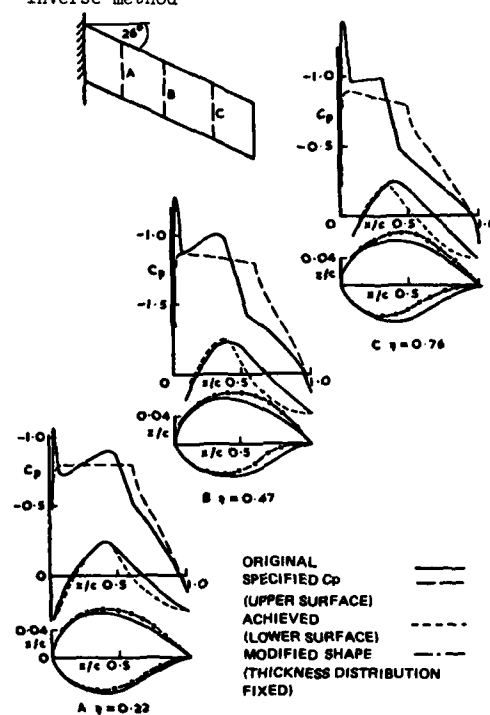


Fig. 5.10 Example of ARA TSP wing design method³⁴

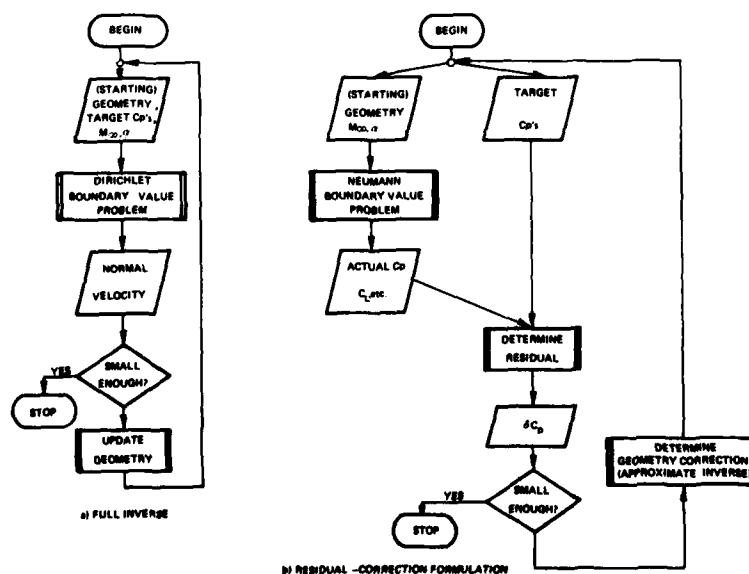
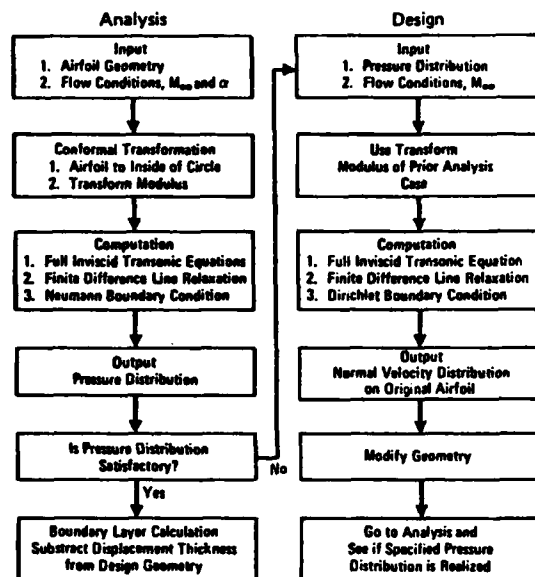
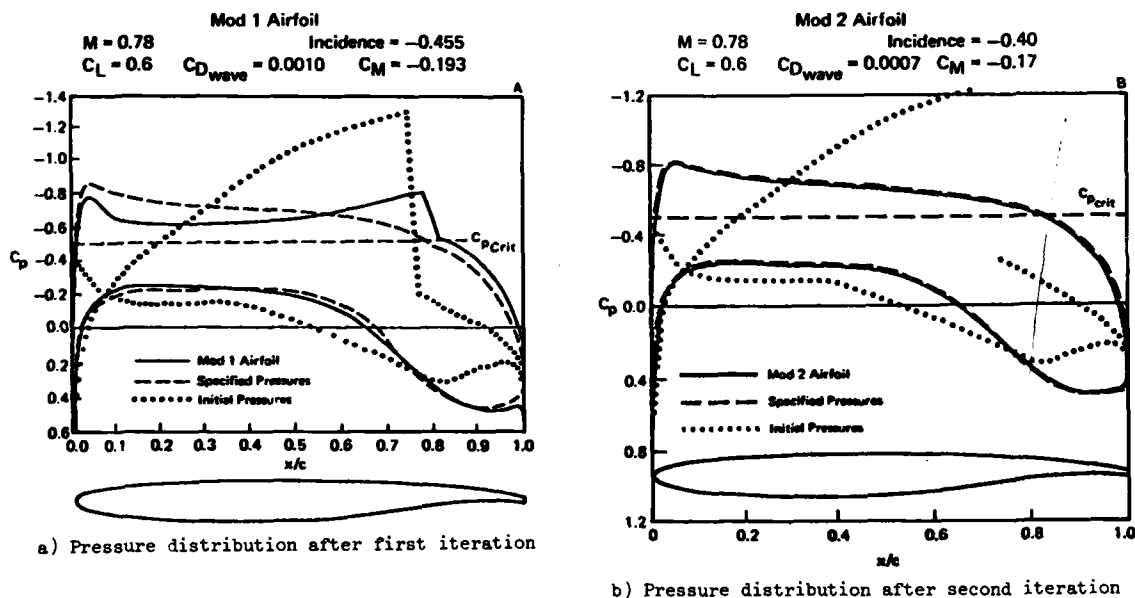
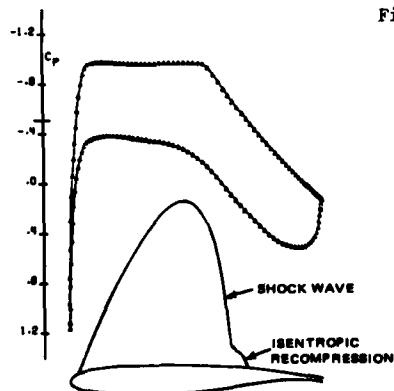
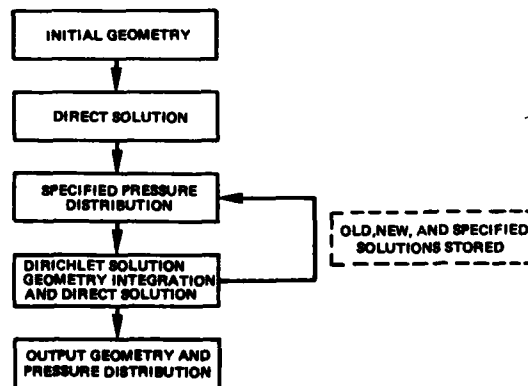


Fig. 5.11 Flow charts of full inverse and residual-correction formulation

Fig. 5.12 Flow chart of Tranen's design procedure⁴¹Fig. 5.13 Example of application of Tranen's⁴¹ design procedure

VISCOUS DESIGN $M_{\infty}=1.00$ $NCV=700$ $EPS1=.000$
 — ART. VISC. $M=0.778$ $ALP=0.00$ $CL=.630$ $CD=.0040$
 Δ INPUT CP $T/C=1.17$ $DG=.38E-02$ $DPH=.88E-04$

Fig. 5.14 Example of shock-free pressure distribution leading to shock wave in flow field with significant wave drag (McFadden's⁴⁶ method)Fig. 5.15 Simplified flow diagram of Henne's method⁴³

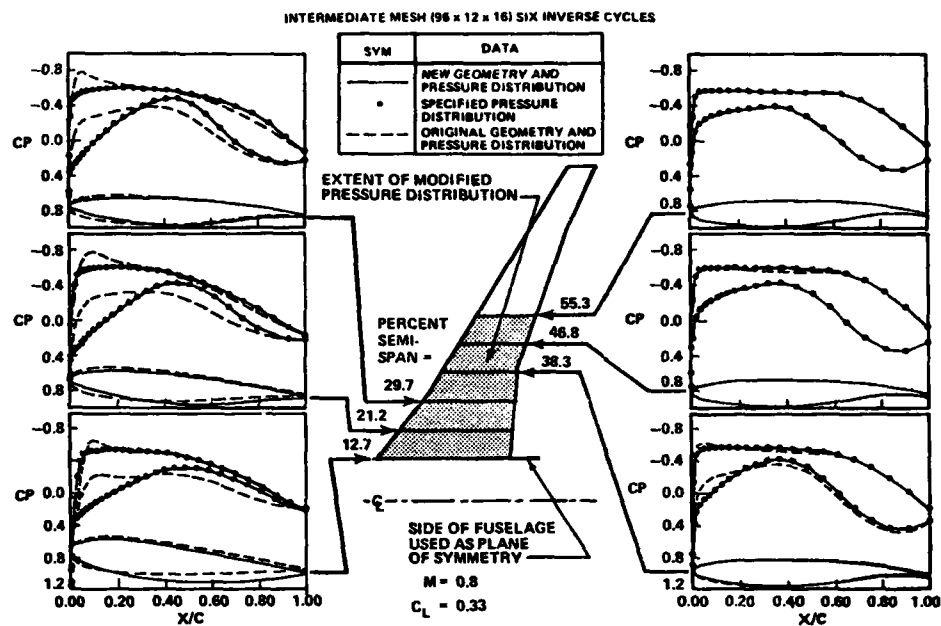


Fig. 5.16 Modification of supercritical swept wing inboard pressure distribution, Henne [43]

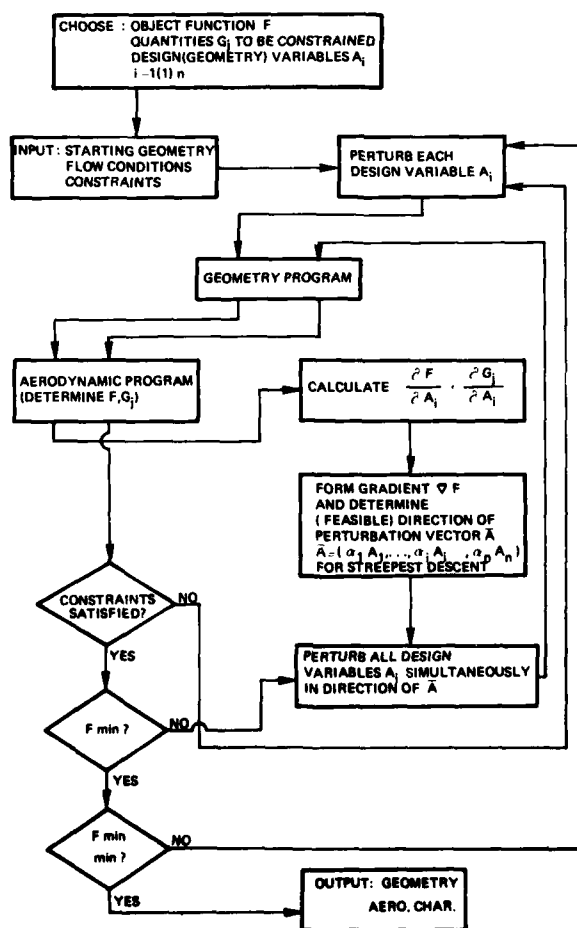


Fig. 5.17 Flow chart of design by numerical optimization

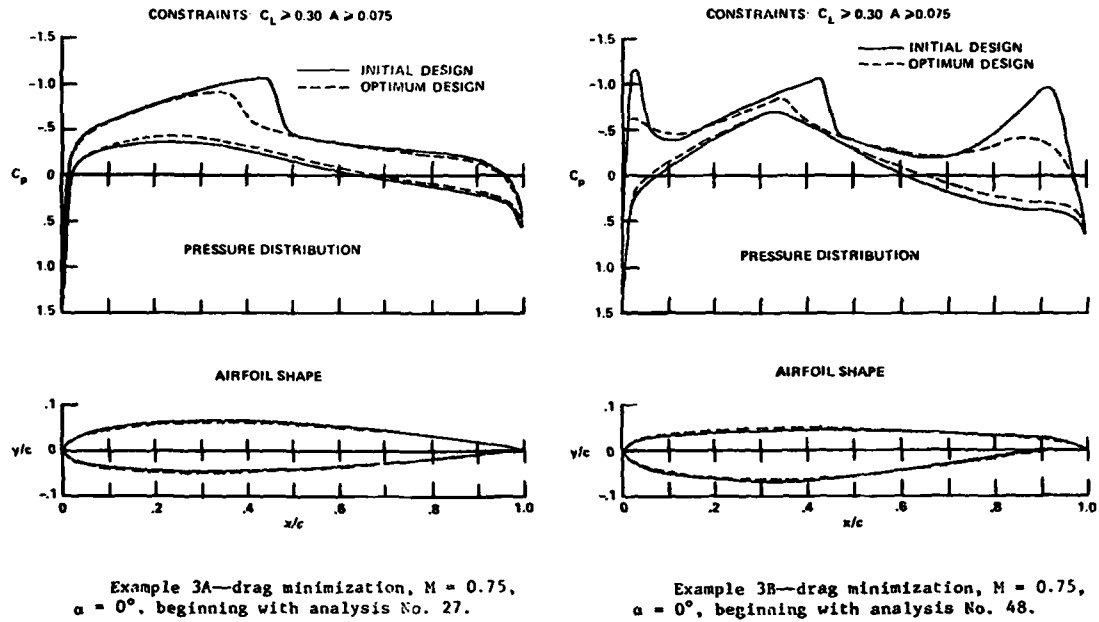


Fig. 5.18 Example of non-uniqueness of wave drag minimization problem [59]

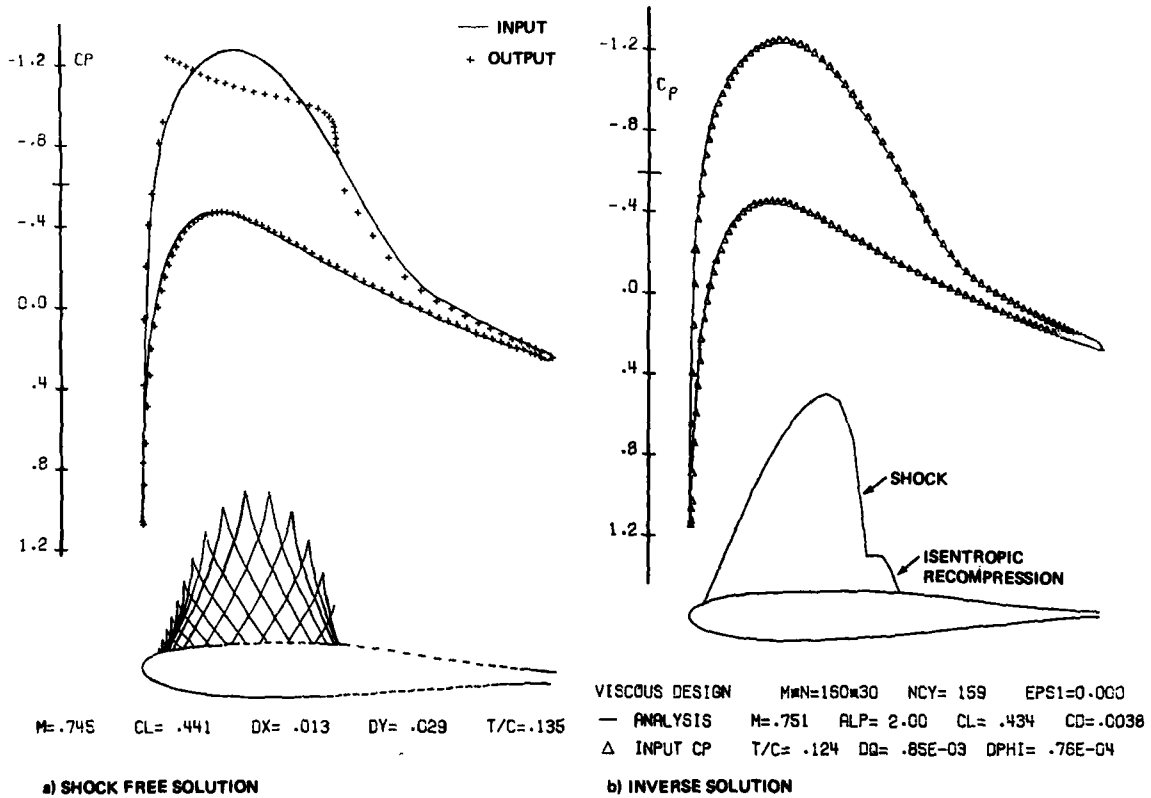


Fig. 5.19 Examples of design-to-pressure [45]

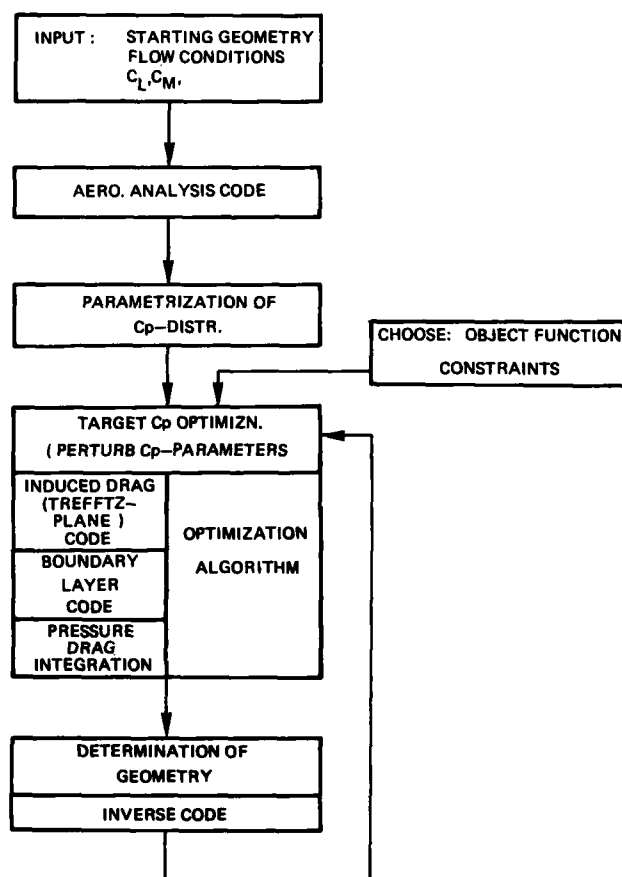


Fig. 5.20 Scheme for inverse numerical optimization (conjectural)

6. ADVANCED CONCEPTS

In the last half decade, new concepts have been developed that have advanced the discipline of computational transonic aerodynamics (CTA) at a remarkable rate. These concepts include new methods for discretizing the governing flow-field equations, accelerated iterative solution procedures, and improved grid generation techniques. These advances, coupled with the anticipated availability of new large-scale scientific computers, indicate the potential for significant near-term improvements in the usefulness of transonic flow-field simulations in aircraft design. Some of the more significant of these advanced concepts are reviewed here. Additional survey papers with emphasis on advanced concepts are given by Kordulla [1] and Baker [2].

6.1 Algorithm development

The two primary aspects associated with CTA algorithm development include spatial discretization schemes and iteration schemes. The spatial discretization scheme controls the order of accuracy of the steady-state solution. Furthermore, properly matching the mixed character of transonic flow with type-dependent discretizations, controls to a large extent algorithm reliability. On the other hand, the iteration scheme controls the rate of convergence, and therefore, is primarily associated with the algorithm execution speed and cost. Other algorithm aspects of importance associated with both the spatial discretization and the iteration scheme include coding ease, storage requirements, algorithm generality, and ease of boundary condition implementation. The discussion begins with a review of advanced spatial discretization schemes.

6.1.1 Spatial discretization schemes

Much of the recent work in transonic potential methods has been devoted to finding better ways of solving the full potential equation in conservation form. Two types of spatial discretizations can be considered at the present time for the numerical solution of this equation; (1) finite-difference schemes and (2) finite-element schemes. The finite-difference schemes have been more widely used than schemes of the finite-element variety, and therefore, will be treated in more detail. Recently, however, the finite-element discretization has been receiving more attention, especially in Europe. Specific discussion comparing various aspects of finite-difference and finite-element techniques will not be presented. For discussion on this topic the interested reader is referred to Hafez, et al. [3,4].

The most interesting aspect of transonic spatial discretization procedures is the manner in which numerical stability is maintained in supersonic regions of flow. This stabilization process is usually achieved by the addition of an artificial viscosity term which biases the discretization scheme in the upwind direction and usually lowers the order of accuracy. This yields a discretization scheme in which the computational domain of dependence correctly models the physical domain of dependence. Addition of the artificial viscosity term is also the mechanism for eliminating expansion shock waves as part of the solution.

Since the initial work making transonic flow calculations feasible (see chapter 3 for a brief review of this work), new approaches have been developed. The first conservative full potential calculations were presented by Jameson [5] in 1975 for airfoil geometries and by Jameson and Caughey [6] and Caughey and Jameson [7] in 1977 for wing and wing/fuselage geometries. An example of this type of discretization applied to the conservative full potential equation (see Eq. (2.19)) is given by

$$L\phi_{i,j} = \left(\delta_{x,i+\frac{1}{2},j} \delta_x + \delta_{y,i,j+\frac{1}{2}} \delta_y \right) \phi_{i,j} \quad (6.1)$$

where L is the residual operator. For convenience of presentation, only two-dimensional Cartesian coordinates are considered. The density at mesh interval midpoints, for example $\rho_{i+\frac{1}{2},j}$, is evaluated using

$$\phi_{x,i+\frac{1}{2},j} \approx \delta_x \phi_{i,j} \quad (6.2a)$$

$$\phi_{y,i+\frac{1}{2},j} \approx \frac{1+E^+}{2} \delta_y \phi_{i,j} \quad (6.2b)$$

and a suitable expression for the density in terms of ϕ_x and ϕ_y (for example, see equation (2.20)). The i and j subscripts indicate position in the finite-difference mesh, that is, $x = i\Delta x$, and $y = j\Delta y$. The operators used in equations (6.1)-(6.2) as well as throughout this chapter are defined by

Backward first difference (first-order accurate)

$$\delta_x^- ()_{i,j} = \frac{()_{i,j} - ()_{i-1,j}}{\Delta x} \quad (6.3a)$$

Forward first difference (first-order accurate)

$$\delta_x^+ ()_{i,j} = \frac{()_{i+1,j} - ()_{i,j}}{\Delta x} \quad (6.3b)$$

Central first difference (second-order accurate)

$$\delta_x ()_{i,j} = \frac{()_{i+1,j} - ()_{i-1,j}}{2\Delta x} \quad (6.3c)$$

Central second difference (second-order accurate)

$$\delta_{xx} ()_{i,j} = \frac{()_{i+1,j} - 2()_{i,j} + ()_{i-1,j}}{(\Delta x)^2} \quad (6.3d)$$

Shift operator

$$E_x^{\pm 1}(\cdot)_{i,j} = (\cdot)_{i \pm 1, j} \quad (6.3e)$$

Additional operators involving other coordinate directions are defined similarly.

Note that the symmetric combination of first-order-accurate difference operators yields a second-order-accurate, central difference operator (for example, $\delta_x \delta_x = \delta_x^2 = \delta_{xx}$). Thus, the differencing procedure given by equations (6.1)-(6.2) is centrally differenced and second-order accurate. As such, it is stable for subsonic flow regions but unstable for supersonic regions of flow.

Jameson [5] stabilized this differencing procedure for transonic calculations by adding the following artificial viscosity term to equation (6.1):

$$-\Delta x (v \phi_{xx})_x - \Delta y (v \phi_{yy})_y \quad (6.4)$$

where v is a switching or transition function defined by

$$v = \max[0, (1 - 1/M^2)] \quad (6.5)$$

and M is the local Mach number. The "max" notation used here causes v to take the maximum value between zero and $1 - 1/M^2$. This artificial viscosity term is differenced with an upwind bias as follows (for $\phi_x > 0$, $\phi_y > 0$):

$$-\Delta x \hat{\delta}_x (v_{i,j} \phi_{x_{i,j}} \hat{\delta}_x \rho_{i+1/2,j}) - \Delta y \hat{\delta}_y (v_{i,j} \phi_{y_{i,j}} \hat{\delta}_y \rho_{i,j+1/2}) \quad (6.6a)$$

and if $\phi_x < 0$, $\phi_y > 0$

$$-\Delta x \hat{\delta}_x (v_{i+1,j} \phi_{x_{i+1,j}} \hat{\delta}_x \rho_{i+1/2,j}) - \Delta y \hat{\delta}_y (v_{i,j} \phi_{y_{i,j}} \hat{\delta}_y \rho_{i,j+1/2}) \quad (6.6b)$$

Similar formulas are required for $\phi_y < 0$. For convenience of presentation, only the first case will be considered hereafter.

Inclusion of the artificial viscosity terms defined by expressions (6.6) does not alter the second-order-accurate central differencing of subsonic regions because for $M < 1$, $v = 0$. In supersonic regions, the differencing is first-order accurate and upwind biased resulting from the addition of artificial viscosity. As the flow becomes increasingly supersonic, the scheme is increasingly retarded in the upwind direction. (Note: Jameson presented a second-order-accurate supersonic spatial differencing scheme in reference 5, which will be discussed subsequently.)

The spatial differencing scheme given by the addition of artificial viscosity to equation (6.1) can be rearranged to give (see Ref. 8)

$$L\phi_{i,j} = (\hat{\delta}_x \tilde{\rho}_i \hat{\delta}_x + \hat{\delta}_y \bar{\rho}_j \hat{\delta}_y) \phi_{i,j} \quad (6.7)$$

where

$$\tilde{\rho}_i = (1 - v_{i,j}) \rho_{i+1/2,j} + v_{i,j} \rho_{i-1/2,j} \quad (6.8a)$$

and

$$\bar{\rho}_j = (1 - v_{i,j}) \rho_{i,j+1/2} + v_{i,j} \rho_{i,j-1/2} \quad (6.8b)$$

Thus, addition of the upwind-biased artificial viscosity term to the original centrally differenced finite-difference scheme is essentially equivalent to retarding the evaluation of the density in the upwind direction.

This scheme can be generalized to arbitrary coordinates [9] and to three dimensions [10]. For instance, the spatial differencing scheme for the two-dimensional, full potential equation written in nonorthogonal curvilinear coordinates is given by [9]

$$L\phi_{i,j} = \hat{\delta}_\xi (\tilde{\rho}_\xi^U \hat{\delta}_\xi)_{i+1/2,j} + \hat{\delta}_\eta (\bar{\rho}_\eta^V \hat{\delta}_\eta)_{i,j+1/2} \quad (6.9)$$

where the contravariant velocity components in the ξ and η directions, U and V , are evaluated using standard second-order-accurate finite-difference formulas. The density coefficients are upwind evaluations of the density and are given by

$$\tilde{\rho}_{i+1/2,j} = ((1-v)\rho)_{i+1/2,j} + v_{i+1/2,j} \rho_{i+r+1/2,j} \quad (6.10a)$$

$$\bar{\rho}_{i,j+1/2} = ((1-v)\rho)_{i,j+1/2} + v_{i,j+1/2} \rho_{i,j+s+1/2} \quad (6.10b)$$

The r and s indices control the upwind directions and are defined by

$$\left. \begin{aligned} r &= +1 & \text{when } U_{i+1/2,j} > 0 \\ s &= +1 & \text{when } V_{i,j+1/2} > 0 \end{aligned} \right\} \quad (6.11)$$

The reliability of this generalized spatial differencing scheme is improved somewhat, especially for strong shock calculations, if the switching parameter definition is changed to

$$v_{i+1/2,j} = \begin{cases} \max[0, (M_{i,j}^2 - 1)C] & \text{for } U_{i+1/2,j} > 0 \\ \max[0, (M_{i+1,j}^2 - 1)C] & \text{for } U_{i+1/2,j} < 0 \end{cases} \quad (6.12)$$

where the original v of equation (6.5) has been multiplied by CM^2 . The parameter C is a user-specified coefficient usually set to between 1.0 and 2.0. Use of this new definition for v increases the amount of upwinding and therefore the amount of artificial viscosity in the differencing scheme.

The differencing scheme given by equations (6.9)-(6.11) maintains an upwind influence for supersonic regions anywhere in the general ξ - η finite-difference mesh for any orientation of the velocity vector. Thus, the effect of "rotated differencing" is closely approximated. This aspect greatly enhances the stability and reliability of this spatial differencing scheme, especially for difficult strong shock-wave cases. For more details about this spatial differencing scheme see reference 9.

Other researchers have used different forms of the artificial viscosity term. A notable example is the one used by Eberle [11-13] for a variety of different applications in both two and three dimensions. In this approach, a typical supersonic point at which an updated value of the velocity potential is desired is denoted as P. Reflecting the fact that P is exclusively influenced by physical data from only the accompanying forward Mach cone, the quantities $\rho\phi_x$ and $\rho\phi_y$ are evaluated at a point H which lies a small distance upstream from P. Mathematically this can be formulated by using the following Taylor series, where only $\rho\phi_x$ is considered

$$(\rho\phi_x)_H \approx (\rho\phi_x)_P + \frac{\partial \rho\phi_x}{\partial s} \Big|_P (s_H - s_P) \quad (6.13)$$

In equation (6.13) s is approximately the arc length along the streamline connecting the points P and H. The quantity $\partial(\rho\phi_x)/\partial s$ is formed as follows:

$$\frac{\partial \rho\phi_x}{\partial s} = \rho q \frac{\partial \phi_x/q}{\partial s} + \frac{\phi_x}{q} \frac{\partial \rho q}{\partial s} \quad (6.14)$$

Since the distance between H and P is small, $\partial(\phi_x/q)/\partial s$ can be neglected. This is equivalent to assuming that the streamline which connects P and H is straight. Since the local density must be computed anyway, it is advisable to change from s to ρ as the independent variable. With these changes and after a little simplification the final expression becomes

$$(\rho\phi_x)_H \approx (\rho\phi_x)_P + \left[\left(1 - \frac{1}{M^2}\right) \phi_x \right]_P (\rho_H - \rho_P) \quad (6.15)$$

This scheme can be generalized to both subsonic and supersonic regions by using the familiar "max" switching function

$$(\rho\phi_x)_H = [\rho_P + \max(0, 1 - \frac{1}{M^2})(\rho_H - \rho_P)] (\phi_x)_P \quad (6.16)$$

For the $\rho\phi_y$ and $\rho\phi_z$ terms it is only necessary to replace ϕ_x with ϕ_y and ϕ_z , respectively.

Another variant of the artificial viscosity term has been presented by Hafez, et al. [14]. In this scheme, which is designed as an artificial compressibility scheme, the following artificial viscosity term is added to the standard subsonic differencing scheme (see equation (6.1)):

$$-(v\phi_x \rho_s \Delta s)_x - (v\phi_y \rho_s \Delta s)_y \quad (6.17)$$

where s is the streamwise coordinate direction and v is the switching function defined by equation (6.5). Addition of this term to the standard subsonic differencing scheme given by equation (6.1) is achieved by evaluating the density as follows:

$$\tilde{\rho}_{i,j} = \rho_{i,j} - v_{i,j} (\rho_s \Delta s)_{i,j} \quad (6.18)$$

where

$$(\rho_s \Delta s)_{i,j} = \left(\frac{\phi_x}{q} \right)_{i,j} \frac{\partial \phi_x}{\partial x} \rho \Delta x + \left(\frac{\phi_y}{q} \right)_{i,j} \frac{\partial \phi_y}{\partial y} \rho \Delta y \quad (6.19)$$

and

$$\frac{\partial \phi_x}{\partial x} \rho \Delta x = \begin{cases} \rho_{i,j} - \rho_{i-1,j} & \text{if } \phi_{x,i,j} > 0 \\ \rho_{i+1,j} - \rho_{i,j} & \text{if } \phi_{x,i,j} < 0 \end{cases} \quad (6.20)$$

A similar definition is used for the $\frac{\partial \phi_y}{\partial y} ()$ term.

Implementation of the supersonic zone stabilization is similar in all the spatial discretization schemes just presented. They all maintain conservative form and all automatically exclude the existence of expansion shocks. This is accomplished by an upwind evaluation of the density in an otherwise centrally differenced subsonic scheme. In other words, this type of supersonic stabilization allows any elliptic discretization scheme with the appropriate density modification to be used in mixed elliptic-hyperbolic calculations. This approach is universal in that it can be applied in finite-difference [8-10,14] or finite-element schemes [11-13]. Its generality is further substantiated by the vast number of applications found in the literature. A few of these include airfoil and cascade calculations [15-16], axisymmetric geometry calculations [17], and unsteady airfoil calculations [18-21]. These spatial discretization schemes have been identified with the terms artificial compressibility, retarded density and artificial density. In the present review this technique of stabilizing supersonic regions is referred to as the artificial density or AD scheme.

One difficulty associated with the AD spatial discretization philosophy is that if the switching function, v and/or the density, ρ are not properly computed, the shock capture process will produce large pre-shock oscillations and poor algorithm reliability. Two guidelines offered by South and Jameson [22] that help eliminate this unacceptable behaviour are: (1) In the calculation of the density coefficient at $i+\frac{1}{2}, j$, that is, $\tilde{\rho}_{i+\frac{1}{2}, j}$, for $\phi_x > 0$, v should be evaluated at i, j , not at $i+\frac{1}{2}, j$ as in some formulations; (2) The density values used in calculating $\tilde{\rho}_{i+\frac{1}{2}, j}$ should be computed at cell centers, that is, at $i+\frac{1}{2}, j+\frac{1}{2}$ and then averaged to obtain $\rho_{i+\frac{1}{2}, j}$ and $\rho_{i, j+\frac{1}{2}}$, for example

$$\rho_{i+\frac{1}{2}, j} = \frac{1}{2} (\rho_{i+\frac{1}{2}, j+\frac{1}{2}} + \rho_{i+\frac{1}{2}, j-\frac{1}{2}}) \quad (6.21)$$

With these guidelines the existence of pre-shock oscillations is greatly diminished. Example calculations

showing the magnitude of these effects are shown in figures 6.1-6.3. Figure 6.1 shows two pressure coefficient distributions from Holst and Albert [23] for an NACA 0012 airfoil at a free stream Mach number of 0.75 and two degrees angle of attack. The two solutions correspond to different values of C (see equation (6.12)). For both of these calculations v is incorrectly evaluated at $i+1, j$ instead of at i, j , and p is computed directly at grid points instead of the preferred cell centers. As a result a pre-shock oscillation exists even for relatively large values of C . Figure 6.2 shows the same comparison with v correctly evaluated at i, j . The pre-shock oscillation has been eliminated even for relatively small values of C , but could still exist for values of v computed from equation (6.5). Figure 6.3 shows a pressure coefficient comparison from South, et al. [24] for a non-lifting NACA 0012 airfoil calculation at a free stream Mach number of 0.85. The two curves correspond to nodal-point and cell-centered evaluation of the density with v correctly evaluated at i, j in both cases and defined by equation (6.5). The cell-centered density evaluation clearly gives the superior result with no oscillations.

Another promising approach for eliminating shock oscillations is provided in the work of Engquist and Osher [25,26]. Finite-difference approximations for the TSP equation are presented, in which sharp, monotone shock wave profiles are guaranteed to result. The new procedure is identical to the Murman-Cole scheme everywhere except at sonic lines and supersonic-subsonic shock waves. Goorjian and Van Buskirk [27] have taken this idea and applied it to unsteady transonic applications using the low-frequency TSP equation. Much larger time-step values can be used with this modification relative to the standard differencing scheme, which produces a considerable improvement in computational efficiency. Extension of this approach to the full potential equation has recently been accomplished by Boerstool [89].

Other interesting spatial difference schemes suitable for transonic flow applications include the field panel method of Piers and Slooff [28], the stream function method of Hafez and Lovell [29] the finite element method of Vigneron, et al. [30], and the penalty function technique described in Bristeau, et al. [31], Periaux [32], and Bristeau et al. [33]. In the last approach a least-square finite-element formulation is used to discretize the full potential equation in conservative form. To exclude expansion shocks the least square functional is modified to include a penalty function. This penalty function takes on large values for solutions containing non-physical expansion shocks, i.e. for solutions with streamwise positive jumps in velocity, and small values for solutions with proper entropy increasing shocks. In a sense this penalty function approach is a dissipative device similar to artificial viscosity that is designed to exclude expansion shocks. A comparison between this finite-element approach and the conservative approach of Jameson is shown in figure 6.4. The solutions are in reasonably good agreement. The finite-element solution exhibits smooth subsonic-supersonic transition and sharp supersonic-subsonic shock waves.

All of the spatial differencing schemes thus far discussed have been "standard schemes", i.e., second-order accurate for subsonic regions of flow and first-order accurate for supersonic regions. Research on higher-order schemes has not received as much emphasis primarily because of the high level of development and satisfactory performance associated with standard schemes. The most important cases in CTA which might require higher-order accuracy are the very sensitive supercritical shock-free solutions, surfaces with large curvature and therefore locally large flow field gradients, and swept wing solutions with supersonic-to-supersonic shocks. The latter case is poorly simulated by present methods because supersonic-to-supersonic shocks are entirely first-order accurate.

Nevertheless, interesting work on higher-order schemes has been presented and is now briefly reviewed. Jameson [5] presented a spatial differencing scheme which was fully second-order accurate for both subsonic and supersonic regions of flow. This scheme produced remarkable improvements in accuracy for supercritical airfoil solutions near their shock-free design points but had stability problems for cases with strong shocks. Caughey and Jameson [34] presented a similar second-order accurate scheme which was more successful in dealing with shocks. The essence of their scheme was to revert back to first-order accuracy in regions of high gradient, including shock waves. Thus, improved accuracy in supersonic regions (although perhaps not everywhere second order) was obtained without greatly affecting the stability at shocks.

Ives and Luitermoza [35] introduced an entirely second-order accurate scheme for the non-conservative full potential equation, and applied it to the solution of transonic cascade flow. Chen and Caughey [36] developed a third-order accurate (first-order accurate in the supersonic region) finite-difference scheme for the full potential equation and applied it to three-dimensional flow about axisymmetric bodies. In this case, the third-order scheme was 25 % more expensive per iteration than a standard scheme, but because of increased accuracy for a given mesh, produced an overall improvement in computational efficiency. Subsequently, Chen [37] presented the same third-order accurate subsonic differencing scheme with a second-order supersonic differencing scheme and made several types of airfoil solution comparisons involving both conservative and nonconservative variations. Deconinck and Hirsch [16] presented results for transonic cascade and airfoil flow fields using a finite-element spatial discretization scheme with various types of higher-order elements. In this study comparisons with several different iteration schemes were made including SLOR, ADI, and Hopscotch.

In all these cases reasonably significant improvements in solution accuracy were judged to exist relative to standard schemes on comparable size meshes. However, many questions about higher-order CTA methods remain unanswered. In some cases decreased robustness, that is, more iterations per solution or lack of stable convergence altogether, coupled with increased computer time per iteration, make the desirability of such schemes questionable. The ability of such schemes to actually improve the accuracy at shock waves without increasing the grid resolution is another unanswered question. More work in the area of higher-order accurate schemes needs to be done before the final level of benefit can be established.

6.1.2 Accelerated iteration schemes

Currently the area of most intensive research in CTA involves the search for solution procedures which are more computationally efficient. This is motivated by the need for more economic computational tools for use in the aircraft industry. The computational efficiency of an algorithm can be analyzed by studying two algorithm properties: (1) the amount of work required for a solution, that is, the number of floating point operations, and (2) how the work is organized. It is the last category which determines the processing rate, that is, the number of operations processed per second of CPU time. This is an important factor in determining the computational efficiency available on vector computers. Review of several algorithms, specifically with respect to vector computational efficiency, will be presented in section 6.1.2.5.

Because transonic flow problems are inherently nonlinear, no direct solution procedures are theoretically known to exist. Therefore, transonic flow solution procedures involve an initial "guess" solution, followed by iteration, and hopefully convergence to the final answer. The amount of computational work required for a solution, therefore, is determined from two categories: (1) the number of iterations per solution and (2) the number of operations per iteration. This situation can be clarified by the following simple example: Suppose we seek the solution to some discrete equation

$$L\phi = 0 \quad (6.22)$$

which approximates a nonlinear differential equation. An iterative solution procedure to solve equation (6.22) can be written

$$NC^n + L\phi^n = 0 \quad (6.23)$$

where $C^n (= \phi^{n+1} - \phi^n)$ is the correction, $L\phi^n$ is the n th iteration residual, and N is an operator determined by the iteration scheme. Let $e^n (= \phi^n - \phi)$ be the error after the n th iteration. Then $C^n = e^{n+1} - e^n$ and equations (6.22) and (6.23) can be combined to give

$$e^{n+1} = Me^n = M^2e^{n-1} = \dots = M^{n+1}e^0 \quad (6.24)$$

where

$$M = I - N^{-1}L \quad (6.25)$$

In equation (6.24) M is assumed to be stationary. For the iteration procedure to converge the magnitude of the largest eigenvalue of M must be less than one. The relationship of the eigenvalues of M with respect to one also controls the convergence rate. If all eigenvalues of M are zero, which is not possible for a nonlinear problem, the initial error is reduced to zero in a single iteration. For more discussion regarding this analysis see Ames [38] and Ballhaus, et al. [39].

A typical convergence history curve for the previously discussed SLOR relaxation scheme is sketched in figure 6.5 (curve A). Because the maximum eigenvalue of the SLOR scheme, λ_{SLOR} , is near unity, convergence for this scheme can be very slow, especially as $\Delta x \rightarrow 0$ where $\lambda_{SLOR} \rightarrow 1$. Several options exist for improving this situation. The first involves improving the initial condition solution, e^0 , for example, by using a grid sequence. The previous convergence history curve modified by using a grid sequence to improve the initial guess is given in figure 6.5 (curve B). Thus, an acceptable convergence tolerance is reached with less work, but the asymptotic convergence rate is essentially unchanged.

Other options available for improving convergence involve improvements associated with M , that is, reducing the number of operations per iteration and/or reducing the magnitude of the maximum eigenvalue of M . This is exemplified by curve C in figure 6.5 where the convergence rate has been improved. These options, of course, mean the implementation of new algorithms.

Specific areas which will now be discussed include: (1) fully implicit approximate factorization (AF) schemes, including alternating direction implicit (ADI) schemes, (2) semi-direct schemes, (3) multi-grid schemes, (4) extrapolation schemes, and (5) methods tailored to vector computers. Both the multi-grid and extrapolation techniques actually represent schemes for accelerating the convergence of other iteration schemes. The implicit AF schemes are reviewed first.

6.1.2.1 Approximate factorization schemes

Several general guidelines for the construction of implicit approximate factorization (AF) schemes can be formulated by considering the two-level iteration procedure

$$NC^n + \omega L\phi^n = 0 \quad (6.26)$$

where C^n is the correction ($\phi^{n+1} - \phi^n$); $L\phi^n$ is the residual, which is a measure of how well the finite-difference equation is satisfied by the n th level velocity-potential solution (ϕ^n); and ω is a relaxation parameter. The iteration scheme given by equation (6.26) can be considered as an iteration in pseudotime, where the n superscript indicates the time-step level of the solution, that is, $(\)^{n+1} - (\)^n \sim \Delta t (\)_t$. The operator N determines the type of iterative procedure, and therefore determines the rate at which the solution procedure converges.

Classical successive over-relaxation (SOR) schemes or SLOR schemes effectively use only a portion of the L operator in forming the N operator. As a consequence, the iteration scheme is relatively simple, but the convergence rate may be very slow. In the AF approach, the philosophy is to choose a representation for N that closely approximates L . This, in theory, will produce a scheme with good convergence characteristics. The procedure for obtaining N consists of two steps: (1) linearize L and (2) factor the linearized result. There are usually two factors for two-dimensional algorithms and three factors for three-dimensional algorithms. The resulting scheme retains the simplicity of requiring only narrow-banded scalar matrix operations. The effects of both the error terms resulting from the factorization and the linearization are removed from the solution simultaneously by means of the iteration scheme. Because each grid point is influenced by every other grid point during each iteration, much faster convergence can be obtained.

Several pertinent early examples of AF schemes can be found in Peaceman and Rachford [40], Douglas [41], Douglas and Gunn [42], and Yanenko [43]. In these pioneering applications different forms of the AF scheme are introduced and applied to purely parabolic or elliptic equations. Additional classical information regarding AF schemes can be found in Mitchell [44]. The first applications of the AF approach to transonic flows governed by potential formulations is the work of Ballhaus and Steger [45], in which numerical solutions of the low-frequency (unsteady) transonic TSP equation were sought. Since this work, many calculations using AF iteration schemes have been used in time accurate transonic applications [19-21, 46-49]. AF algorithms have also been applied in the relaxation mode for solving the steady TSP potential equation in two space dimensions [39] and the full potential equation in both two [8-9, 16, 50-51] and three [10, 52-56] space dimensions.

A particularly successful AF scheme, designated AF2, can be formulated for the two-dimensional full potential equation written in nonorthogonal curvilinear coordinates by choosing the N operator of equation (6.26) as follows [9]:

$$\alpha \text{NC}_{i,j}^n = -(\alpha - \delta_{\eta} A_j)(\alpha \delta_{\eta} - \delta_{\xi} A_i \delta_{\xi}) C_{i,j}^n \quad (6.27a)$$

where

$$A_i = \bar{\rho}_{i-\frac{1}{2},j}^n \left(\frac{A_1}{J} \right)_{i-\frac{1}{2},j} \quad (6.27b)$$

$$A_j = \bar{\rho}_{i,j-\frac{1}{2}}^n \left(\frac{A_2}{J} \right)_{i,j-\frac{1}{2}} \quad (6.27c)$$

The $\bar{\rho}$ and $\bar{\rho}$ coefficients are defined by equation (6.9), and α is an acceleration parameter which may be considered as the inverse of a pseudo-time step, Δt^{-1} . The best approach for choosing α is to use a sequence of values ranging from small to large time steps, that is, large to small values of α . The small time steps are particularly effective for reducing the high-frequency errors and the large time steps are effective for reducing the low-frequency errors. A suitable α sequence with M values is given by [8]

$$\alpha_k = \alpha_H (\alpha_L / \alpha_H)^{\frac{k-1}{M-1}} \quad k = 1, 2, \dots, M \quad (6.28a)$$

The sequence endpoints (α_L, α_H) can be analytically approximated by

$$\alpha_H \sim \frac{1}{\Delta y} \quad \text{and} \quad \alpha_L \sim 1 \quad (6.28b)$$

Refinement of these endpoints by numerical experiment increases the efficiency of the iteration procedure.

Multiplying out the two factors of equation (6.27a) yields an approximation to the L operator defined by equation (6.7) plus two error terms. This approximate L operator does not have the mixed-derivative terms contained by the exact L operator and has been effectively linearized; that is, the coefficients used in equation (6.27a), A_i and A_j , are evaluated at the n th iteration level. In spite of these approximations, rapid convergence is achieved for this iteration scheme.

The AF2 scheme is implemented in two sweeps as follows:

$$\text{sweep 1} \quad (\alpha - \delta_{\eta} A_j) f_{i,j}^n = \omega L \phi_{i,j}^n \quad (6.29a)$$

$$\text{sweep 2} \quad (\alpha \delta_{\eta} - \delta_{\xi} A_i \delta_{\xi}) C_{i,j}^n = f_{i,j}^n \quad (6.29b)$$

where ω is a relaxation factor usually set equal to 1.8, and $f_{i,j}^n$ is an intermediate result array stored at each point in the finite-difference mesh. To maintain stability for transonic calculations, primarily strong shock calculations, the addition of temporal damping is required. This is achieved by adding

$$+ \alpha \beta \delta_{\xi} \quad (6.30)$$

inside the brackets of the second sweep. The parameter β is a user-specified constant which can be adjusted as needed. The double arrow notation on the ξ -difference operator indicates that the difference is always upwind, which depends on the sign of the contravariant velocity component in the ξ direction, U . The sign on the temporal damping term is chosen so as to increase the magnitude of the second sweep diagonal, thus insuring diagonal dominance of the second sweep inversion.

The implicit algorithm just discussed has been coded into a transonic airfoil analysis computer code called TAIR. Computational results produced with TAIR taken from references 57 and 10 are shown in figures 6.6-6.7. The pressure coefficient distribution for a slightly off-design Korn airfoil calculation is compared in figure 6.6a with a result obtained from the GRUMFOIL computer code [58]. The two results are in excellent agreement. The slight disagreement which exists in the supersonic region is caused primarily by differences between the TAIR and GRUMFOIL supersonic spatial difference schemes.

The rms error (E_{rms}) convergence history curves for the Korn airfoil calculation are presented in figure 6.6b. (Using rms error to compare convergence performance is a more quantitatively correct procedure than using the standard maximum residual quantity. See references 8 and 59 for a complete explanation of this point.) The three curves shown in figure 6.6b correspond to the following iteration schemes:

(1) AF2, (2) hybrid, and (3) SLOR. The hybrid scheme is a combination semi-direct/SLOR iteration scheme presented by Jameson [5], which is composed of one semi-direct-solver iteration (see Sect. 6.1.2.2) followed by several SLOR iterations. The purpose of the SLOR iterations is to smooth high frequency errors generated by the direct solver step in regions of supersonic flow. The third scheme (SLOR) is simply the hybrid iteration scheme without benefit of the semi-direct-solver step. For this calculation the AF2 scheme is about five times faster than the hybrid scheme and about ten times faster than SLOR.

As the free stream Mach number approaches unity, interesting airfoil shock-wave patterns develop which represent an extremely difficult reliability test for CTA algorithms. An airfoil solution computed by TAIR [10] which demonstrates this feature is shown in figure 6.7. This example was computed for an NACA 0012 airfoil at $M_{\infty} = 0.95$ and $\alpha = 4$ deg. The Mach number contours clearly illustrate the existence of a so-called "fishtail" shock-wave pattern downstream of the airfoil trailing edge. This difficult calculation demonstrates the convergence reliability associated with the AF2 transonic relaxation procedure.

Another noteworthy AF scheme is the AF3 scheme introduced by Baker [51] for solving the non-conservative full potential equation for transonic flow about airfoils (see equation (2.33) for a description of this equation). The AF3 scheme is given by

$$(-\alpha C_{\delta_y}^2 - A_{\delta_{xx}})(\alpha + \delta_y) C_{i,j}^n = \omega L \phi_{i,j}^n \quad (6.31a)$$

for subsonic regions of flow and by

$$(-\alpha C_{\delta_y}^2 - A_{\delta_{xx}} - A_{\delta_{xx}})(\alpha + \delta_y) C_{i,j}^n = \omega L \phi_{i,j}^n \quad (6.31b)$$

for supersonic regions of flow (when $u > 0$). The difference direction on the third term of the first factor is reversed when $u < 0$. The coefficients A , C , A_c , C_c , and A_u are determined from the nonconserva-

tive full potential equation written in canonical form (stream and stream-normal coordinates, [51]) and are given by

$$\left. \begin{aligned} A_u &= \left(1 - \frac{q^2}{a^2}\right) \frac{u^2}{q^2}, & A_c &= \frac{v^2}{q^2} \\ C_u &= \left(1 - \frac{q^2}{a^2}\right) \frac{v^2}{q^2}, & C_c &= \frac{u^2}{q^2} \\ A &= A_u + A_c, & C &= C_u + C_c \end{aligned} \right\} \quad (6.32)$$

where u and v are the velocity components along the x and y directions, respectively, a is the local speed of sound, and q is the magnitude of the total velocity vector. As in the previous AF2 scheme, ω is a relaxation factor, α an acceleration parameter (cycled over a sequence of values), and $L\phi_{i,j}^n$ is the n th iteration residual defined by

$$L\phi_{i,j}^n = (A\delta_{xx} + B\mu_{xy}\delta_x\delta_y + C\delta_{yy})\phi_{i,j}^n \quad (6.33a)$$

for subsonic regions of flow and by

$$L\phi_{i,j}^n = (A_c\delta_{xx} + A_u\delta_x\delta_x + B_c\mu_{xy}\delta_x\delta_y + B_u\delta_x\delta_y + C_c\delta_{yy} + C_u\delta_y\delta_y)\phi_{i,j}^n \quad (6.33b)$$

for supersonic regions of flow (when $u > 0$ and $v > 0$). The additional coefficients B_u and B_c are given by

$$B_u = 2\left(1 - \frac{q^2}{a^2}\right) \frac{uv}{q}, \quad B_c = -\frac{2uv}{q} \quad (6.33c)$$

The operators $\mu_x(\)$ and $\mu_y(\)$ are central averaging operators defined by (for example)

$$\mu_x(\)_{i,j} = \frac{1}{2}[(\)_{i+1,j} + (\)_{i-1,j}]$$

The AF3 factorization is similar to the AF2 factorization and produces exceptional improvements in computational speed. This fact is illustrated in figure 6.8 (taken from Ref. 2). Figure 6.8a shows the pressure coefficient distribution about an NACA 0012 airfoil at $M_\infty = 0.75$ and $\alpha = 2$ deg for several different levels of convergence. After just 10 AF iterations, which corresponds to about 13 SLOR iterations, the solution is nearly converged. The AF3 convergence history for this case is compared with an SLOR convergence history in figure 6.8b. The SLOR convergence history is enhanced by using the standard grid refinement procedure involving two grids, coarse and fine. For this case the SLOR scheme required over 400 iterations to reach plotable accuracy while the AF3 scheme reached plotable accuracy in about 20 iterations (26 equivalent SLOR iterations).

The two-dimensional AF3 scheme just discussed has been extended to three dimensions by Baker and Forsey [53]. Solutions of the nonconservative full potential equation have been obtained for wing and wing/fuselage combinations with a factor of 4 or 5 increase in computational efficiency relative to standard SLOR schemes. In addition, three-dimensional solutions for wing geometries have been obtained by Sankar, et al. [54] using the strongly implicit procedure of Stone [60], by Benek, et al. [55] using two AF scheme variations called AFZ and AFZ2, and by Holst and Thomas [56] using the standard AF2 scheme. In all cases significant improvements in computational efficiency relative to SLOR were obtained. Additional improvements in computational efficiency for transonic flow calculations from AF procedures appear to be likely. The work of Catherall [61] suggests an improvement by splitting the contributions of the various transformation metrics properly between the factors. In addition, optimal values for the acceleration parameter sequence and the relaxation factor are derived and discussed.

More work needs to be done in obtaining optimal convergence before the ultimate success of the AF scheme is realized. However, with the present level of development, it appears that fully implicit AF schemes might be the next generation of iteration algorithms to replace the existing SLOR scheme for a wide variety of transonic flow applications.

6.1.2.2 Semi-direct iteration schemes

Another type of advanced iteration scheme capable of reducing computational work is the semi-direct scheme. The philosophy of this class of iteration schemes can be discussed by using the N-L operator notation used in the previous section, see equation (6.26). The first step associated with the formulation of a semi-direct iteration scheme involves the construction of an appropriate linearized N operator which closely resembles the L operator. This step is essentially identical to the first step in the construction of an AF iteration scheme. Next, the resulting matrix equation is inverted directly using a suitable direct inversion routine [62-64]. Because transonic flow is inherently nonlinear, this process must be repeated iteratively, thus the name semi-direct. This scheme was first applied to slightly supercritical flows by Martin and Lomax [65] in 1974, and later extended to strongly supercritical cases by Martin [66] in 1976. Both of these studies involved nonlifting airfoil solutions using the TSP equation and in both cases large improvements in computational efficiency over standard SLOR schemes were realized.

In 1975 Jameson [5] presented a hybrid iteration scheme for the full potential equation which used one direct-inversion step followed by several SLOR steps. Other notable works utilizing semi-direct iteration schemes for solving the full potential equation include Martin [67] and Yu and Rubbert [68]. In the latter work, Yu and Rubbert took the hybrid scheme of Jameson [5] and modified the direct inversion step by evaluating the density in the upwind direction according to Hafez, et al. [14], that is, they used a variant of the AD spatial differencing procedure. This modification stabilized the semi-direct iteration scheme for supersonic regions and eliminated the need to periodically smooth the supersonic regions by using SLOR iterations. As a result the computational efficiency of this airfoil calculation procedure was greatly improved.

A more recent example of the semi-direct type of iteration procedure is found in the work of Caspar, et al. [69]. With this approach both subcritical and supercritical shock-free solutions about two-dimensional cascades were obtained. A finite-area spatial discretization for the conservative form of the full potential equation was used. In this procedure an outer nonorthogonal mesh is used to establish the solution globally. In this global grid a blade leading edge singularity exists and can adversely affect the leading edge solution, especially for blunt leading edge calculations. To improve the solution, if necessary, a "local analysis" is performed on an orthogonal body-fitted mesh only in the vicinity of the

blade leading edge such that the effect of the leading edge error is removed. Values of the potential are interpolated from the results of the first analysis (global mesh) and prescribed on the boundaries of the local mesh.

A sample calculation using the technique of Caspar, et al. [69] for the Korn cascade geometry is shown in figure 6.9. The Caspar results are in very good agreement with the original hodograph design solution. Even more impressive is the required computer time, only 15 seconds on an IBM 370/168 computer. For this calculation the global mesh contained 45×11 mesh points and required 11 iterations while the local mesh contained 61×11 mesh points and required 10 iterations.

The technique just discussed is compared in a theoretical sense with SLOR and ADI relaxation schemes by Caspar [70]. In this study the importance of using artificial viscosity and implicit temporal damping for transonic calculations by any of the three schemes is emphasized. The convergence rate for the semi-direct scheme of Caspar, et al. [69] decreased as the Mach number level is increased. Therefore, this scheme, which is very efficient for subcritical cases, may be less efficient than properly formulated SLOR and ADI schemes for transonic calculations, especially on fine meshes.

6.1.2.3 Multigrid iteration schemes

The multigrid iteration scheme is actually a convergence acceleration technique and requires a base iteration scheme, for example, SOR, SLOR, AF, etc. Multigrid schemes have existed for quite some time, having been first introduced by Fedorenko [71] in 1964. Since then several authors have analyzed the technique, including Bakhvalov [72] and more recently Nicolaides [73] and Hackbusch [74]. The most significant result of these analyses is the multigrid convergence rate prediction. For example, the number of operations required for convergence of a standard five-point discretization of Poisson's equation using a multigrid enhanced iteration scheme is of the order of several hundred operations per grid point, and in practice can be much less [75]. This is many times fewer operations than the number required by standard SOR or SLOR schemes.

The multigrid technique produces this fast rate of convergence by using a sequence of grids ranging from very coarse to very fine. Each grid is used to eliminate one small range of errors in the error frequency spectrum, namely the errors of highest frequency supported on each mesh. Many relaxation schemes exist which work very well on high frequency errors, for example point Jacobi, AF (with properly chosen acceleration parameters), etc. One of these relaxation schemes is used on each mesh to remove the high frequency error. The nice aspect of this approach is that the high frequency error on the coarsest mesh is actually the lowest frequency error existing in the problem. Because this usually troublesome low frequency error is efficiently dealt with on a coarse mesh, very little computational work is expended in removing it from the solution. Thus a tremendous convergence rate enhancement is obtained.

Implementation of a typical multigrid scheme is described in general terms as follows: Suppose we desire a solution to

$$L^h \phi = f \quad (6.34)$$

where L^h is a typical linear difference operator which approximates a differential operation L on a mesh associated with the grid spacing h . The quantity f contains the problem boundary conditions. Let

$$\phi = u + v \quad (6.35)$$

where u is an approximation to ϕ and v represents an error. Therefore, as the iteration scheme converges $u \rightarrow \phi$ and $v \rightarrow 0$. The basic multigrid scheme can be expressed by

$$L^{2h} v + I_h^{2h} (L^h u - f) = 0 \quad (6.36)$$

where L^{2h} is a finite-difference operator which approximates L on a mesh associated with the grid spacing $2h$, instead of h , that is, twice as coarse as the original mesh. The operator I_h^{2h} is an interpolation or averaging operator which transfers values of the residual $(L^h u - f)$ from the fine mesh to the coarse mesh. After the coarse mesh corrections, v , are obtained, they are transferred back to the fine mesh by using

$$u^{new} = u + I_{2h}^h v \quad (6.37)$$

where I_{2h}^h is an interpolation operator. The process can continue to coarser meshes so that ultimately just one or maybe several mesh cell widths span the entire domain of interest.

To extend the idea to nonlinear problems a simple modification is helpful. By adding and subtracting $L^{2h} u$ from equation (6.36) the new form becomes

$$L^{2h} \bar{u} = \bar{f} \quad (6.38)$$

where

$$\begin{aligned} \bar{u} &= u + v \\ \bar{f} &= L^{2h} u - I_h^{2h} (L^h u - f) \end{aligned} \quad (6.39)$$

The quantity u represents a new or improved estimate of ϕ which is determined from the coarse mesh. The quantity \bar{f} is a modified right-hand side which essentially represents the difference in residuals between the h and $2h$ meshes. New updated coarse values are transferred back to the fine mesh by using

$$u^{new} = u + I_{2h}^h (\bar{u} - u) \quad (6.40)$$

Thus the error quantity v does not have to be stored as in the original version.

Applications utilizing the multigrid scheme were slow to materialize after its introduction primarily because of difficulties in implementation and general underestimation of the potential of multigrid enhanced schemes. The first work to apply the multigrid scheme numerically was that of Brandt [76] in 1972. Later the multigrid scheme was formulated in general terms by Brandt [75]. In this latter reference a good historical background of the multigrid scheme is presented, including a review of related earlier work.

The first use of the multigrid scheme for transonic calculations was presented by South and Brandt [77]. In this study numerical solutions of the TSP equation for nonlifting airfoils were obtained. The speed of an optimized SLOR scheme was improved by a factor of five on uniform meshes and by a factor of two on stretched meshes. A primary difficulty reported by South and Brandt involved the existence of a variety of limit cycle oscillations between several grids, thus inhibiting convergence. This problem seemed to be the result of insufficient smoothing of the high frequency errors on one grid before passing to the next coarser grid. South and Brandt concluded that the SLOR base algorithm used in the multigrid scheme did not have uniform smoothing properties in both directions, especially for non-uniform, highly stretched meshes. They hypothesized that alternating the SLOR sweep direction or utilizing an ADI iteration scheme as the base algorithm might solve this problem.

Another approach proposed by Arlinger [78] was to refine or coarsen the mesh spacing in only one coordinate direction while doing line relaxation along the opposite direction. This technique produced a convergence rate acceleration but did not take full advantage of the multigrid scheme. To date the most successful application of a multigrid convergence acceleration scheme to a practical transonic problem is the work of Jameson [79].

In this study the full potential equation in conservative form is solved using a multigrid scheme with a specially constructed AF base iteration scheme. This scheme when applied to the following linear model equation

$$A\phi_{xx} + B\phi_{yy} = 0 \quad (6.41)$$

is given by

$$(S - A\delta_x^2)(S - B\delta_y^2)\phi_{i,j}^n = \omega SL\phi_{i,j}^n \quad (6.42)$$

where A and B are constants, ω is the standard relaxation factor, and S and L are operators defined by

$$S = \alpha_0 + \alpha_1\delta_x^- + \alpha_2\delta_y^- \quad (6.43)$$

and

$$L\phi_{i,j}^n = (A\delta_x^2 + B\delta_y^2)\phi_{i,j}^n \quad (6.44)$$

In equation (6.43) α_0 , α_1 , and α_2 are parameters which depend on flow type and user input. The quantities δ_x^- and δ_y^- denote first-order-accurate upwind difference operators in the x and y directions, respectively.

The Jameson scheme uses the recursive approach for implementing the multigrid philosophy, instead of the adaptive approach advocated by Brandt [75]. In the adaptive multigrid approach the decision to proceed to the next mesh, either coarser or finer, is based on a convergence rate criteria. If the solution residual is dropping slowly the iteration process proceeds to coarser meshes. Conversely, if the solution residual is dropping rapidly the iteration proceeds to finer meshes. In the recursive approach of Jameson a single multigrid cycle starts with an AF iteration on the finest mesh, followed by an AF iteration on the second finest mesh, etc. This continues until the coarsest mesh is reached. Then the process is reversed starting with the coarsest mesh and ending with the second finest mesh. Therefore, each multigrid cycle consists of one AF application on the finest mesh and two applications on each of the remaining meshes. If a fine grid AF iteration is defined as a unit of work, then one multigrid cycle, using the recursive approach, requires about 1 2/3 work units plus interpolation operations.

Results produced by the Jameson multigrid scheme are displayed in figures 6.10-6.13. The pressure coefficient distribution for an NACA 64A410 airfoil at a free stream Mach number of 0.72 and an angle of attack of 0 deg is displayed in figure 6.10. A moderate strength shock exists at about 60 % of chord. Notice that the residual has been reduced below 10^{-12} , which is approximately an eight order of magnitude reduction from the initial value, in only 29 multigrid cycles. Convergence histories for this case, which were computed using different numbers of meshes (from one mesh, that is, no multigrid, up to five meshes), are shown in figure 6.11. The convergence rate (CR) which is defined as the mean reduction in the average residual per unit of work, is also displayed for each curve. Increasing the number of meshes or equivalently, increasing the coarseness of the coarsest mesh, greatly improves the convergence rate.

The pressure coefficient distribution and associated convergence history for a relatively strong shock calculation (NACA 0012 airfoil, $M_\infty = 0.75$, and $\alpha = 2$ deg) are shown in figures 6.12 and 6.13, respectively. For this case the multigrid convergence is also very rapid after an initial hesitation. A study of the transient solution showed the formation of a pre-shock overshoot which is absent in the steady-state solution.

Other researchers have been recently turning to the advantages of multigrid; and a few examples are now presented. Arlinger [17] has used multigrid coupled with an SLOR iteration scheme to solve the full potential equation for axisymmetric calculations. McCarthy and Reyhner [80] and Brown [81] have applied the multigrid convergence acceleration scheme to an existing three-dimensional engine inlet computer code. The base algorithm was SLOR and the governing equation was the nonconservative full potential equation. For all of these applications a substantial improvement in convergence rate relative to SLOR was demonstrated. Many other references pertinent to the multigrid scheme with varying types of applications do exist. A few are listed here as follows: Brandt [82,83], Fuchs [84], McCormick [85], Brandt, et al. [86], Deconinck and Hirsch [87], Shmilovich and Caughey [88], and Boerstol [89].

6.1.2.4 Extrapolation techniques

Another class of convergence acceleration techniques designed to improve the convergence of standard relaxation procedures is the extrapolation technique. The basic idea is to obtain improved convergence by extrapolation, using several previous solution iterations which are obtained from the base iteration scheme, for example, SOR or SLOR. The extrapolation process is applied periodically with several (10-50) base relaxation iterations in between each extrapolation. This convergence acceleration procedure can be especially effective for very fine mesh calculations in which the convergence rate of standard relaxation techniques suffers drastically.

Several authors including Martin and Lomax [65], Hafez and Cheng [90], and Caughey and Jameson [91], have experimented with different variations of this approach. In the Caughey-Jameson study,

extrapolation was used to accelerate the convergence of transonic nacelle flow fields (axisymmetric). The nonconservative full potential equation was solved using SLOR as the base iteration scheme. The general reasoning for this type of approach proceeds as follows: In a conventional, stable relaxation scheme, such as SLOR, the relaxation matrix has several distinct eigenvalues, all less than one and ordered such that

$$1 > |\lambda_1| > |\lambda_2| > \dots > |\lambda_N| \quad (6.45)$$

After many iterations the convergence rate is controlled by the largest or dominate eigenvalue, λ_1 , such that

$$C^{n+1} \sim \lambda_1 C^n \quad (6.46)$$

where $C^{n+1} = \phi^{n+1} - \phi^n$ is the correction and n is the iteration index. Usually λ_1 is near unity, especially for fine mesh calculations, and therefore, convergence can become painfully slow. The extrapolation process is used to alleviate this situation as follows: An estimate for the remaining error in the solution at the n th iteration, e^n , in terms of λ_1 , can be obtained and is given by

$$e^n \approx C^{n+1} / (1 - \lambda_1) \quad (6.47)$$

Since $1/(1-\lambda_1)$ can be relatively large (e.g. ~ 100), this represents a rather drastic correction for the solution. Therefore, extrapolation of this type should be performed only when a dominate eigenvalue is recognized. In the Caughey-Jameson approach the ratio of two successive corrections over a sampling of grid points in the flow field was computed. If the standard deviation from the mean ratio of successive corrections was less than some tolerance, then a dominate eigenvalue was judged to exist and an extrapolation step was implemented. Application of this technique to a typical axisymmetric nacelle flow field produced the convergence history shown in figure 6.14. The finite-difference mesh used for this case was 64×16 . The extrapolated scheme converged much faster to small residuals than the line relaxation scheme for all fixed values of the overrelaxation factor.

Another notable application of the extrapolation technique for convergence acceleration is in the work of Yu and Rubbert [68]. In this application an extrapolation technique similar to Hafez and Cheng [90] and Caughey and Jameson [91] is used to accelerate the convergence of a three-dimensional wing calculation. To speed the development of a dominate eigenvalue in the relaxation process, and therefore permit more frequent extrapolation, two modifications to the standard SLOR relaxation scheme were made. The first modification was to reverse the direction of sweep, that is, in the new scheme, the line relaxation process starts at the wing and proceeds towards the far field. With this modification, the wing solution propagates to the interior much faster than in the standard far-field-to-surface method.

The second modification involves the use of a smaller overrelaxation parameter which improves high frequency error reduction while promoting the development of the dominate eigenvalue. Computational experiments using this approach have shown that the dominate eigenvalue can adequately be predicted within ten iterations following the previous extrapolation. Consequently, Yu and Rubbert have adopted the policy of extrapolating every ten iterations once the initial features of the solution have been established. Either the ratio of two successive maximum corrections or the ratio of two successive corrections averaged throughout the entire flow field is used to approximate the dominate eigenvalue, λ . The same value of λ is used in calculating the extrapolated velocity potential at each grid point. Maximum tolerated values of λ equal to 0.95 for the coarse and medium meshes and 0.99 for the fine mesh have been found to be reliable and efficient.

Convergence behaviour for an example calculation using the Yu-Rubbert extrapolation technique applied to the Jameson-Caughey FLO27 finite-volume code is shown in figure 6.15. This wing calculation was performed at a free stream Mach number of 0.8 and an angle of attack of 3.06 deg. The new method offers a significant improvement in convergence speed relative to the original relaxation technique.

Perhaps the most important advantage of extrapolation techniques, in general, is the fact that they are relatively easy to implement in existing computer codes. Therefore, if a dominate eigenvalue is easily identifiable, a reasonable convergence acceleration can be obtained with little additional programming effort.

6.1.2.5 Methods tailored to vector computers

The use of CTA as a relatively fast and inexpensive aircraft design tool is finding increased acceptance in the aircraft industry. The expanded use of these tools in the future requires faster and more cost-effective computers. In this regard vector computers such as the CRAY-1 and the CDC CYBER 205 show considerable promise. These vector machines offer greatly enhanced computing speeds arising from the ability to operate on many calculations simultaneously (parallel machines) and/or in an assembly line fashion (pipeline machines). More discussion regarding vector computer architectures can be found in reference 92.

Because of the nature of the speed enhancement, these machines tend to favour certain classes of algorithms. Algorithms which are basically recursive, such as SLOR, tend to have difficulty obtaining maximum performance on vector computers. An example of this is given in Smith, et al [93]. In this study the FLO-22 transonic wing analysis computer program written by Jameson, et al. [94] was vectorized for the CDC ST/R-100 pipeline vector computer. Although this study did not produce optimal vectorization of the SLOR algorithm contained in FLO22, it does represent the level of efficiency obtainable with a reasonable conversion effort. The resulting vectorized code ran at about the same rate as the scalar code ran on the CDC 7600 computer. This disappointing performance was caused by the inherently recursive nature of the tridiagonal inversion step in the SLOR algorithm. In addition, since the tridiagonal inversions associated with the SLOR algorithm are interdependent, they must be performed one at a time, a situation which further complicates conversion to vector code.

Several researchers have presented new algorithms especially designed for vector computers, including Keller and Jameson [95], Hafez, et al. [14], Redhead, et al. [96], Hotovy and Dickson [97], and South, et al. [24]. The primary motivation for this algorithm research was to improve computational efficiency on vector computers. In references 14, 95, and 97 the researchers generally stressed vector characteristics above all else. As a result, these vector algorithms could process very large numbers of grid points per second but usually required more iterations than standard SLOR to converge.

In South, et al. [24] an algorithm called ZEBRA II, which is highly vectorizable and requires about the same number of iterations to converge as SLOR, is described. The ZEBRA II algorithm is an explicit or point scheme which mimicks a full plane SOR algorithm and is designed to solve the conservative full potential equation. In its simplest form for an unstretched three-dimensional Cartesian mesh, ZEBRA II is given by

$$BC_{i,j,k}^n = \frac{\Delta x^2 R_{i,j,k}^n}{\bar{\rho}_{avg}} + \beta C_{i-1,j,k}^n \quad (6.48)$$

where the i,j,k subscripts represent position in the finite-difference mesh, $C_{i,j,k}^n$ is the correction as previously defined, $R_{i,j,k}^n$ is the residual, and

$$B = \frac{2}{\omega_x} + \beta + \frac{2}{\omega_y} + \frac{2}{\omega_z} \quad (6.49)$$

Upwinding in the residual is achieved by using density coefficients defined by equation (6.18), β is a coefficient controlling the amount of ϕ_{xt} , and ω_x , ω_y , and ω_z are relaxation parameters which typically are less than or equal to two. The ZEBRA II procedure is composed of two different types of sweeps. The first is an explicit sweep which is performed for all $j+k$ odd points. The residual for this sweep is entirely evaluated at the n th time level. (Values of ϕ required in the $i-1$ plane for the first sweep are taken from the $n+1$ time level. This is permitted because the direction of sweep is along increasing values of i .) The second sweep is performed for all $j+k$ even points. The residual for this sweep is evaluated at the n th time level for $j+k$ even points and at the $n+1$ time level for $j+k$ odd points.

The ZEBRA II algorithm has two features advantageous for vector computation. First, most operations can be performed with plane parallelism, thus allowing long vectors and efficient operation on any vector computer. Second, the algorithm sweeps through the solution array (ϕ) in only one direction, thus facilitating contiguous data access. This simplifies the operation of vector computers which require contiguous data access, such as the CDC STAR-100. Implicit algorithms, which sweep through the data base in different directions, require several data transposition steps for each iteration to maintain contiguous access on this type of vector machine.

The ZEBRA II algorithm takes a step in the vector computer direction, but other approaches for vector computation may still be superior. A theoretical study comparing the vector processing attributes of four transonic full potential algorithms (SLOR, ADI, AF2, and ZEBRA II) was performed by Holst [98] utilizing a mathematical model of a pipeline vector computer. This theoretical analysis was based on vector length categorization of floating point operation counts obtained from each of the algorithms. In other words, how many floating point operations are required (per iteration, per grid point); and assuming "perfect" programming, what are the resulting vector lengths. From this information an efficiency or per cent of the maximum processing rate can be computed by using a standard vector computer performance curve.

The efficiency of a particular algorithm is only one of three important considerations needed to determine total execution time for a solution. The other two considerations are the number of operations per iteration and the number of iterations required for a solution. The implicit schemes, for example, AF2 and ADI, are not as efficient relative to the explicit schemes, for example, ZEBRA II, in the first two categories, but overwhelmingly gain in the last category. The results of the reference 98 study indicate that implicit algorithms will still enjoy overall supremacy on vector computers relative to explicit or point iterative techniques when all aspects are taken into consideration.

The type of vector computer modeled in the reference 98 study attained most of its efficiency only with long vectors (consisting of 1000 or more elements). In other words, planar parallelism was essentially required for efficient operation. Other vector computers do exist that attain very efficient operation with much shorter vectors, essentially requiring only line parallelism. Also different computer hardwares provide for different alternatives for data transposition, with some machines having no transpose penalties at all. Because of these features, implicit algorithms may provide even larger savings in overall performance. The exact amount of savings can only be determined when all these factors are considered.

6.2 Grid generation

With the advent of faster, more efficient numerical algorithms and larger, more sophisticated computers, the ability to simulate inviscid transonic flow about complete aircraft is within reach. The major obstacle preventing the achievement of this goal is the difficulty in generating "suitable" grids. The primary attributes associated with a suitable grid are that it must be well-ordered, orthogonal (or nearly orthogonal), relatively smooth in variation, body conforming, and relatively free of strong singularities. In addition, grids obtained for reasonably complicated configurations (for example, full aircraft), must be routinely generatable in such a way that coordinate lines of the same family do not cross. Another desirable feature is that grids should be solution adaptive. That is, the grid should be determined simultaneously with, and therefore, influenced by, the flow solution. Thus, the limited number of grid points available can be clustered in regions where they are needed most, i.e., in regions of large flow gradient. Some work on solution adaptive grids has been conducted and can be found in references 99-103.

Of course, not all of these attributes are at the same level of importance for the different available flow solver schemes. The body conforming aspect is generally desirable for allowing simple and accurate application of boundary conditions. Body conforming grids allow for simple and efficient control of grid point clustering and are especially important for bodies with large curvature or slope singularities, which occur frequently in aerodynamic applications.

A few researchers have used non-body conforming grids and have obtained good results [104-107]. These formulations generally rely on interpolation for boundary condition application, which for some geometries (for example, airfoils) works quite well. However, for applications involving general geometries with high curvature (especially three-dimensional applications), non-body conforming meshes may be difficult to cluster appropriately, especially when such features as wing twist, sweep or dihedral are present. Under these circumstances the mesh may become skew with respect to the body. This may produce inaccuracies at the boundary which is precisely the region of greatest sensitivity. In addition, because the grid system used in a non-boundary conforming application is usually stretched Cartesian, the mesh efficiency can be quite low (that is, the ratio of the number of surface grid points to the local number of grid points is

usually quite low for a stretched Cartesian mesh compared to a boundary-conforming, mapped mesh). The vast majority of researchers in CTA use body conforming grids, and therefore, the remaining discussion will be restricted to this area.

Generally speaking, two approaches are available for generating body-oriented grids: Coordinate transformations and triangularization. The latter approach is usually associated with finite element techniques which are generally based on an integral equation formulation. This places less stringent smoothness requirements on the grid. Also, complex geometrical topologies with large surface curvature or surface slope singularities can more generally be discretized and adequately clustered with randomly distributed triangles than with contiguously ordered quadrilaterals. However, many advantages are associated with the coordinate transformation procedures which are not shared by triangularization techniques.

The major advantage associated with coordinate mapping techniques is the simple grid point ordering which results. This feature greatly simplifies the flow solver algorithm by producing a simple matrix structure. For triangularization procedures the grid points are generally ordered in a semi-random fashion. This produces a flow solver algorithm with a more complicated sparse matrix structure. Therefore, solution algorithms associated with coordinate transformations are simpler, that is, they generally require fewer operations per iteration. This advantage is much more important when considered in the light of vector computers (see Sect. 6.1.2.5). For vectorization to be efficient, contiguous streams of data must be easily identifiable. The inversion of a sparse, unstructured matrix is not well suited for this and could easily nullify any advantages associated with the generalities of triangularization procedures.

Furthermore, the use of region adaptive grids, for example, the composite approach suggested by Eiseman [108], the block approach of Lee and Rubbert [109-110], the embedded grid approach demonstrated by Boppe [111-112], or the grid interfacing procedure presented by Atta [113], could be used to adequately cluster grid points about complex geometrical topologies. In this approach the domain of interest would be divided into several subdomains each with a simple topology and its own coordinate transformation. The well-ordered (highly vectorizable), body-conforming characteristics would be retained in each subdomain. Because additional computational expense would be introduced at the subdomain boundaries, the number of subdomains should be minimized, for example, one subdomain about each major component. An aircraft grid might be composed of three subdomain types, wing/fuselage, pylon/nacelle, and horizontal/vertical tail surfaces. Much research needs to be completed before the ultimate grid generation procedure becomes apparent for truly general transonic flow field computation.

Another possible alternative is to use a coordinate transformation as the basis for triangularization. The simple matrix structure is retained, however, some generality in treating complex geometrical topologies is lost. Some finite element researchers have utilized this approach including Eberle [11-13] and Deconink and Hirsch [16]. Because the vast majority of grid generation research seems to be based on the coordinate transformation approach, only this type of grid generation procedure will be discussed in the following sections. Specific topics include: (1) analytic transformation procedures such as conformal mappings, (2) numerical transformation procedures including techniques based on elliptic and hyperbolic partial differential equations, and (3) algebraic or geometric procedures based on parametric surfaces or interpolation techniques.

6.2.1 Analytical grid mapping procedures

Analytical mapping procedures can be simple, for example, involving only a stretching or shearing of the coordinate system, or they can be more complicated, for example, conformal mappings. The stretching and shearing transformations can be useful for simple geometries, for example, standard blunt bodies, or simple fuselage cross sections, but generally are not sufficient by themselves for more complex airfoil and wing calculations. Conformal mappings do have the generality required for providing good quality, economical grids for reasonably complex two-dimensional geometries. Many researchers have utilized conformal mappings to generate arbitrary, orthogonal meshes (or nearly orthogonal meshes when a sheared conformal mapping procedure is used) for a host of two-dimensional applications. A few examples include Garabedian and Korn [114] for an airfoil; Kacprzyński [115] for an airfoil between wind tunnel walls; Ives [116] for the multi-element airfoil; Caughey and Jameson [91] and Chen and Caughey [117] for the axisymmetric nacelle, with and without center hub; and Ives and Liutermoza [118] for axial-flow turbo-machinery cascade applications.

The theory behind conformal mapping techniques is governed by analytic functions of a single complex variable. This theory is well developed, but fundamentally limited to applications in two space dimensions. Nevertheless, some researchers have found ways to use conformal mapping techniques to assist in generating grids for three-dimensional problems. A few examples are given by Jameson [119] for wings, Jameson and Caughey [6] and Caughey and Jameson [7,120] for wing/body combinations, and Ives and Menor [121] for three-dimensional inlet and inlet center-body configurations. Other examples are provided in references 122-123. The basic approach utilized for three-dimensional problems is to generate a series of two-dimensional grids using conformal or sheared-conformal mappings. Then these two-dimensional grids are "stacked" together in the third dimension to form the final three-dimensional grid. This approach has worked well for geometries with smooth variation in the third dimension but lacks generality. Conformal mapping procedures will continue to be used successfully in a wide variety of applications, however, the anticipated trend for grid generation procedures will be away from such techniques and toward the more general (although presently less well developed) numerical and/or geometric mapping procedures.

6.2.2 Numerical grid mapping procedures

Perhaps the most popular new technique for grid generation is the numerical approach. The central idea associated with this technique is to establish a set of curvilinear coordinates by requiring that they be solutions to specially constructed partial differential equations (PDEs), either elliptic or hyperbolic in type. The properties of these PDEs are such that smooth and regular finite-difference grids (or perhaps finite-element grids) are generated. Coordinate lines of the same family do not cross and coordinate lines of opposite families are orthogonal or nearly orthogonal. Dirichlet boundary conditions are specified such that the body automatically becomes a constant coordinate line in the physical domain. This guarantees a one-to-one mapping in which the mesh is well-ordered and body-fitted. Mechanisms for achieving extremely general mesh control exist through boundary condition specification and through the control of various arbitrary coefficients depending upon exactly which formulation is used. The numerical grid mapping procedure is generally valid for both two- and three-dimensional problems involving either

steady or unsteady flows.

The first step involves the transformation of the flow field governing equations from the physical domain to the computational domain. For a two-dimensional steady airfoil problem this transformation can be expressed in the form

$$\left. \begin{aligned} \xi &= \xi(x, y) \\ \eta &= \eta(x, y) \end{aligned} \right\} \quad (6.50)$$

where x and y represent the physical domain coordinates, for example, Cartesian coordinates, and ξ and η represent the computational domain coordinates (see Fig. 6.16). Using the general transformation of equation (6.50) any PDE in conservation-law form can be transformed from the physical domain to the computational domain with the conservation-law form maintained. This is an important point because most differencing schemes use shock capturing procedures that depend on conservation-law form to provide unique shock wave solutions. For more discussion on conservation-law form see references 124-127.

Many numerical grid generation variations have been developed for a wide variety of applications. Some of the earlier examples, in which Laplace's equation (or a modification of Laplace's equation) was used as the base PDE include: Winslow [128], Chu [129], Amsden and Hirt [130], Godunov and Prokopov [131], and Thompson, et al. [132-134]. The approach formulated by Thompson is perhaps the most widely used numerical grid generation procedure. In this approach Poisson's equation is used to define the transformation and is given by

$$\xi_{xx} + \xi_{yy} = P(\xi, \eta) \quad (6.51a)$$

$$\eta_{xx} + \eta_{yy} = Q(\xi, \eta) \quad (6.51b)$$

The P and Q right-hand-side quantities are defined as a sum of exponential terms each with several free coefficients. These coefficients can be adjusted by the user to provide different types of mesh size and skewness control. Equations (6.51) are transformed to (and solved in) the computational domain, that is, the roles of ξ , η and x , y are interchanged such that ξ , η become the independent variables and x , y are the dependent variables. Thus all numerical computations are performed in the more-convenient, equally-spaced computational domain (see Fig. 6.16b).

The numerical solution of the resulting transformed equations is accomplished by first replacing all derivatives by standard second-order-accurate finite differences. The spatial increments, $\Delta\xi$ and $\Delta\eta$, can arbitrarily be chosen (for example, $\Delta\xi = \Delta\eta = 1.0$) and therefore are simply omitted. Once boundary and initial values of x and y are specified the final interior values can be computed by standard relaxation procedures. For many applications a simple successive overrelaxation (SOR) scheme is used, but other techniques are available. For instance, Holst [9] uses an ADI iteration scheme for generating grids about airfoils, and Camarero and Younis [135] use a multigrid technique for generating grids about two-dimensional cascades. In both of these cases significant improvements in computational efficiency relative to SOR schemes are obtained.

An example grid from Thompson, et al. [134] about a Karman-Trefftz airfoil with flap is shown in figure 6.17. To simplify the presentation only the portion of the grid near the airfoil is shown. The actual outer boundary for this calculation was circular with a radius of ten chord lengths. In this example the P and Q forcing terms have been utilized to attract the $\eta = \text{constant}$ coordinate lines to the airfoil surface, thus providing a good grid point resolution on the concave portion of the airfoil. In other more recent applications, the numerical elliptic-solver approach has been used to develop relatively complex grids about wing/fuselage configurations, Yu [136] and Thomas [137], and about wing/fuselage/pylon/nacelle configurations by Yu [138].

An important aspect associated with these numerical elliptic-solver techniques is that they have a high degree of controllability. The vast number of coefficients contained in the P and Q terms (four for each grid point in the reference 132 formulation) is an indication of the staggering amount of control available to the user. There is an obvious difficulty associated with this flexibility, namely, how can it, in a general and simple way, be made available to the user? This is a problem, which poses a difficulty in two dimensions, and becomes seemingly insurmountable in three dimensions.

Several researchers have experimented with different aspects of this problem including Thomas and Middlecoff [139] and Steger and Sorenson [140-141]. In the latter approach a simplified form of the P and Q terms was adopted and is given by

$$P = P_0(\xi)e^{-a(\eta-\eta_1)} \quad (6.52a)$$

$$Q = Q_0(\xi)e^{-b(\eta-\eta_1)} \quad (6.52b)$$

where η_1 corresponds to the η_{\min} inner boundary (see Fig. 6.16), P_0 and Q_0 are sets of constants which vary in the ξ direction on the η_{\min} boundary, and a and b are constants which control the rate of decay of the P and Q forcing terms into the mesh interior. Thus, application of the forcing terms is restricted only to η_{\min} , which is primarily where the control is desired. Steger and Sorenson recognized that two types of control are desired: (1) control of the spacing between $\eta = \eta_1$, and $\eta = \eta_2$ (that is, the first $\eta = \text{constant}$ line away from the inner boundary) while at the same time maintaining continuity between the lines η_1 , η_2 , η_3 , etc., and (2) control of the angle with which $\xi = \text{constant}$ lines intersect the inner boundary. These two conditions can be expressed mathematically by

$$s_\eta = \left. \frac{ds}{d\eta} \right|_\xi = (x_\eta^2 + y_\eta^2)^{1/2} = \Delta s \quad (6.53)$$

and

$$\nabla\xi \cdot \nabla\eta = x_\xi x_\eta + y_\xi y_\eta = |\nabla\xi||\nabla\eta|\cos\theta \quad (6.54)$$

where s is the arc length along the η lines which intersect the body and θ is the angle of intersection. The condition for orthogonality is $\theta = \pi/2$. Other angle specifications are possible by setting θ to values other than $\pi/2$. By utilizing equations (6.52), (6.53) and (6.54) as well as the Dirichlet boundary conditions in x and y , expressions for P_0 and Q_0 can be derived. With these expressions, values of $P_0(\xi)$ and $Q_0(\xi)$, obtained by specification of $\Delta s(\xi)$ and $\theta(\xi)$, can be determined. Therefore, the simplification introduced in reference 140, is to replace the specification of arbitrary abstract coefficients, $P_0(\xi)$ and

$Q_0(\xi)$, with the specification of simple, understandable quantities, Δs and θ .

An example of this technique used to generate a grid about a highly cambered 12 to 1 ellipse is shown in figures 6.18 and 6.19. Figure 6.18 shows global and trailing edge detail of the Laplacian mesh (that is, no control), while figure 6.19 shows the same views with control ($\theta = \pi/2$ and $\Delta s = 0.005$). Note the poor grid quality for the case with no control, especially in the concave portion of the ellipse. The case with control, however, produces a nearly orthogonal grid at the body with a nearly uniform Δs distribution closely approximating the desired value of 0.005.

Other numerical mapping procedures based on hyperbolic PDEs have been reported in the literature but are less well developed than the elliptic procedures. Examples of this type of grid generation procedure include Starius [142] and Steger and Chaussee [143]. In the latter work the PDEs used to numerically define the transformation of equation (6.50) and therefore the finite-difference mesh are given by

$$\nabla \xi \cdot \nabla \eta = \xi_x \eta_x + \xi_y \eta_y = \phi \quad (6.55)$$

$$\xi_x \eta_y - \xi_y \eta_x = J \quad (6.56)$$

Orthogonality is achieved by simply setting ϕ to zero, and J represents the Jacobian of the transformation (that is, effectively the grid cell area). In this formulation both ϕ and J are user-specified functions. This provides a great deal of controllability which is perhaps more direct and easier to implement than in most elliptic PDE formulations. Direct specification of J produces a well-behaved mesh that does not cross over on itself in all but the most severe cases. Because this system of equations is hyperbolic in η , a solution can simply be obtained by marching away from initial data specified on the inner boundary. Because iteration is not required, computation time for this technique is very small.

A disadvantage of this technique lies in the lack of direct control over the position and distribution of grid points on the outer boundary ($\eta = \eta_{\max}$). However, for external aerodynamic applications this limitation is not severe. Other more fundamental problems lie in the treatment of surface singularities or extension to three-dimensions. Because of the hyperbolic nature of the grid transformation governing equations, any singularities imposed in the $\eta = \eta_{\min}$ initial data, for example, a slope discontinuity in the geometry, will propagate in the η direction and perhaps cause problems in the grid interior. Formulation of a suitable algorithm in three dimensions is more difficult because the orthogonality condition (equation (6.55)) expands to three equations. Thus a system of four independent equations is created where only three can be used, one for each independent spatial coordinate.

Much work needs to be completed before numerical grid generation schemes based on hyperbolic PDEs can be used routinely for three-dimensional calculations. However, in the future this grid generation procedure may become the best for external aerodynamic applications.

6.2.3 Geometric grid mapping procedures

The final set of grid mapping procedures discussed in this chapter utilizes an algebraic or geometric construction approach for generating grids. This technique has recently received much attention and promises to develop into a viable approach. Generally speaking, these procedures are relatively efficient, requiring only small amounts of computer time relative to the elliptic-equation grid generation approach, and have general capabilities regarding coordinate line control. In addition, this type of procedure seems to be general enough for easy extension into three dimensions. Eiseman has presented geometric grid generation techniques for several two-dimensional configurations [144-145], including a cascade geometry application and a three-dimensional wing configuration application [146]. The control available with these schemes is quite extensive and allows specification of the grid point position and angle at both the inner and outer boundaries. Even higher degrees of control are possible including different types of clustering or special types of grid smoothing. These newer more elaborate types of grid control can be applied to local regions of the mesh without affecting other regions. In theory these local controls could be used to smoothly interface two grids with distinctly different characteristics. Thus, the idea of "patched" systems of grids for complex aerodynamic configurations is greatly enhanced. The mathematical aspects of this new geometrical grid generation procedure are developed by Eiseman [147-148]. To date some testing of these theories has been conducted, but little experimentation with flow solver algorithms applied to realistic geometries has been reported. Nevertheless this technique does seem to cope with many of the problems associated with other grid generation types, and therefore, widespread usage in a variety of grid generation applications is anticipated.

Another geometrical grid generation procedure has been presented by McNally [149] refined by Graves [150] and used to solve a variety of hypersonic blunt-body problems by Hamilton and Graves [151]. Completely general specification of body geometry is allowed by this technique. The grid is generated quickly and in a straightforward manner by using a two-step procedure which marches away from the body surface. The first step is used to establish the tangential-coordinate family, and the second step is used to establish the opposite normal-coordinate family. The resulting grid is orthogonal although nonorthogonal versions are also available. In many senses this procedure resembles the hyperbolic schemes discussed in the previous section (Sect. 6.2.2). However, one important difference does exist. The grid resulting from this geometrical approach is constructed such that both the inner and outer boundaries (for the blunt body problem, these boundaries correspond to the body surface and the bow shock wave) can be specified as constant coordinate lines in the computational domain. In the hyperbolic PDE procedure of reference 143 only the inner boundary position could be specified.

Another promising geometrical grid generation procedure is the technique introduced by Erikson [152] and used by Rizzi and Erikson [153] to solve transonic flow fields about wing/body configurations. This procedure, which can be viewed as a generalized spline interpolation technique, generates a finite-difference grid in two or three dimensions by interpolating geometric data from the domain boundaries. The geometric data required includes boundary coordinates and derivatives. In some cases outer domain boundaries can automatically be determined by the geometric transformation procedure and therefore, do not necessarily have to be specified. This procedure is computationally efficient and has good coordinate line control properties. For instance, with proper specification of the derivative boundary conditions nearly orthogonal local regions of the grid can be generated.

The algebraic or geometric grid generation procedure has only recently entered the CTA field and therefore its ultimate role is difficult to predict. However, the general properties of this broad class of grid mapping procedures (for example, flexibility, computational efficiency, and controllability)

suggest a large increase in the usage of this procedure for generating the complicated grids associated with more complete aircraft configurations.

6.3 References

1. Kordulla, W., Calculation of 3-D transonic flows-survey of recent developments including viscous effects, VKI Lecture Series 1980-6, March 1980.
2. Baker, T.J., The computation of transonic potential flow, VKI Lecture Series 1981-5, March 1981.
3. Hafez, M.M., Wellford, L.C., and Murman, E.M., Finite elements and finite differences for transonic flow calculations, Finite elements in fluids, Chapter 12, Vol. 3, Ed. Gallagher, et al., John Wiley, 1978.
4. Hafez, M.M., Wellford, L.C., and Murman, E.M., Numerical computations of transonic flows by finite-element and finite-difference methods, NASA CR 3070, December 1978.
5. Jameson, A., Transonic potential flow calculations using conservative form, Proceedings of the second AIAA Computational Fluid Dynamics Conference, Hartford, Conn., June 1975, pp. 148-155.
6. Jameson, A., and Caughey, D.A., A finite-volume method for transonic potential flow calculations, Proceedings of the third AIAA Computational Fluid Dynamics Conference, June 1977, pp. 35-54.
7. Caughey, D.A., and Jameson, A., Numerical calculation of transonic potential flow about wing-body combinations, AIAA J., Vol. 17, No.2, February 1979, pp. 175-181.
8. Holst, T.L., and Ballhaus, W.F., Fast conservative schemes for the full potential equation applied to transonic flows, NASA TM-78469, 1978. (Also AIAA J., Vol. 17, No.2, February 1979, pp. 145-152.)
9. Holst, T.L., An implicit algorithm for the conservative, transonic full potential equation using an arbitrary mesh, AIAA Paper 78-1113, July 1978. (Also AIAA J., Vol. 17, No.10, October 1979, pp. 1038-1045.)
10. Holst, T.L., A fast, conservative algorithm for solving the transonic full-potential equation, Proceedings of the fourth AIAA computational fluid dynamics conference, Williamsburg, Va., July 1979, pp. 109-121. (Also, AIAA J., Vol. 18, No.12, December 1980, pp. 1431-1439.)
11. Eberle, A., A finite element method for calculating transonic potential flow around profiles, MBB UFE1325 (0), 1977.
12. Eberle, A., A finite volume method for calculation transonic potential flow around wings from the pressure minimum integral, NASA TM-75324, Translated from MBB UFE 1407 (0), February 1978.
13. Eberle, A., Transonic potential flow computations by finite elements: Airfoil and wing analysis, airfoil optimization, Lecture at the DGLR/GARTEur 6 Symposium, Transonic configurations, Bad Harzburg, Germany, June 1978.
14. Hafez, M., South, J., and Murman, E., Artificial compressibility methods for numerical solutions of transonic full potential equation, AIAA Paper No.78-1148, 1978. (Also, AIAA J., Vol.17, No.8, August 1979, pp. 838-844.)
15. Ecer, A., and Akay, H.U., Investigation of transonic flow in a cascade using an adaptive mesh, AIAA Paper No.80-1430, July 1980.
16. Deconinck, H., and Hirsch, C., Transonic flow calculations with higher order finite elements, presented at the seventh International Conference on Numerical Methods in Fluid Dynamics, Stanford University and NASA Ames Research Center, June 1980.
17. Arlinger, B., Axisymmetric transonic flow computations using a multigrid method, presented at the seventh International Conference on Numerical Methods in Fluid Dynamics, Stanford University and NASA Ames Research Center, June 1980.
18. Eberle, A., Finite element methods for the solution of full potential equation in transonic steady and unsteady flow, Third International Conference on Finite elements in flow problems, June 1980.
19. Goorjian, P.M., Implicit computations of unsteady transonic flow governed by the full potential equation in conservative form, AIAA Paper No.80-0150, January 1980.
20. Steger, J.L., and Caradonna, F.X., A conservative implicit finite difference algorithm for the unsteady transonic full potential equation, AIAA Paper No.80-1368, July 1980.
21. Sankar, N.L., and Tassa, Y., An algorithm for unsteady transonic potential flow past airfoils, presented at the seventh International Conference on Numerical Methods in Fluid Dynamics, Stanford University and NASA Ames Research Center, Calif., June 1980.
22. South, J.C., and Jameson, A., Recent advances in computational transonics, Polytechnic Institute of New York, Farmingdale, NY, June 1979, to appear in Computers and Fluids.
23. Holst, T.L., and Albert, J., An implicit algorithm for the conservative, transonic full potential equation with effective rotated differencing, NASA TM-78570, 1979.
24. South, J.C., Keller, J.D., and Hafez, M.M., Vector processor algorithms for transonic flow calculations, Proceedings of the fourth AIAA Computational Fluid Dynamics Conference, July 1979, pp. 247-255.
25. Engquist, B., and Osher, S., Stable and entropy satisfying approximations for transonic flow calculations, Math. Comp., Vol. 34, No.149, January 1980, pp. 45-75.
26. Engquist, B., and Osher, S., One sided difference schemes and transonic flow, Proceedings of the National Academy of Sciences, August 1980.
27. Goorjian, P.M., and Van Buskirk, R., Implicit calculations of transonic flows using monotone methods, AIAA Paper No.81-0331, 1981.
28. Piers, W.J., and Slooff, J.W., Calculation of transonic flow by means of a shock-capturing field panel method, Proceedings of the fourth AIAA Computational Fluid Dynamics Conference, Williamsburg, Va., July 1979.
29. Hafez, M., and Lovell, D., Numerical solution of transonic stream function equation, Proceedings of the fifth Computational Fluid Dynamics Conference, Palo Alto, Ca., June 1981.
30. Vigneron, Y., Brocard, O., Bousquet, J., and Lejal, T., Une methode variationnelle d'elements finis pour la resolution d'ecoulements transoniques tridimensionnels, AGARD CP-285, May 1980.
31. Bristeau, M.O., Glowinski, R., Periaux, J., Perrier, P., Pironneau, O., and Poirier, G., Applications of optimal control and finite element methods to the calculation of transonic flows and incompressible viscous flows, Numerical methods in Applied Fluid Dynamics, B. Hunt (ed.), Acad. Press, London, 1980.
32. Periaux, J., Resolution de quelques problemes non lineaires en aerodynamique par des methodes d'elements finis et de moindres carrés fonctionnels, These de 3eme cycle, Universite Pierre et Marie Curie, June 1979.

AD-A121 012

APPLIED COMPUTATIONAL TRANSONIC AERODYNAMICS(U)
ADVISORY GROUP FOR AEROSPACE RESEARCH AND DEVELOPMENT
NEUILLY-SUR-SEINE (FRANCE) Y L HOLST ET AL. AUG 82
AGARD-AG-206

2/2

UNCLASSIFIED

F/G 20/4

NL

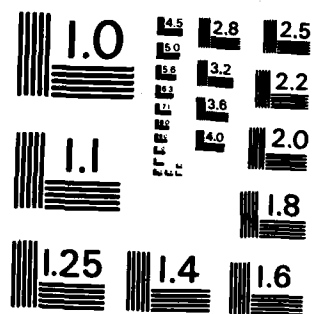
END

DATE

FILED

11 82

DTIC



MICROCOPY RESOLUTION TEST CHART
NATIONAL BUREAU OF STANDARDS-1963-A

33. Bristeau, M.O., Glowinski, R., Periaux, J., Perrier, P., and Pironneau, O., On the numerical solution of nonlinear problems in fluid dynamics by least squares and finite element methods (I) least squares formulations and conjugate gradient solution of the continuous problems, Com. Meth. Appl. Mech. Eng., 17/18, 1979, pp. 619-657.
34. Caughey, D.A., and Jameson, A., Basic advances in the finite-volume method for transonic potential flow calculations, presented at the Numerical and Physical Aspects of Aerodynamic Flows Symposium, California State University, Long Beach, January 1981.
35. Ives, D.C., and Liutermoza, J.F., Second-order-accurate calculation of transonic flow over turbomachinery cascades, AIAA J., Vol. 17, August 1979, pp. 870-876.
36. Chen, L.T., and Caughey, D.A., A higher-order finite-difference scheme for three-dimensional transonic flow fields about axisymmetric bodies, Journal of Aircraft, Vol. 17, No.9, September 1980, pp. 668-676.
37. Chen, L.T., Higher-accuracy finite-difference schemes for transonic airfoil flow field calculations, AIAA Paper No.81-0381, January 1981.
38. Ames, W.F., Numerical methods for partial differential equations, Academic Press, New York, 1977.
39. Ballhaus, W.F., Jameson, A., and Albert, J., Implicit approximate factorization schemes for the efficient solution of steady transonic flow problems, AIAA J., Vol. 16, 1978, pp. 573-579.
40. Peaceman, D.W., and Rachford, Jr., H.H., The numerical solution of parabolic and elliptic differential equations, J. SIAM, Vol. 3, 1955, pp. 28-41.
41. Douglas, J., On the numerical integration of $U_{xx} + U_{yy} = U_t$ by implicit methods, J. Soc. Ind. Appl. Math., Vol. 3, 1955, pp. 42-65.
42. Douglas, J., and Gunn, J.E., A general formulation of alternating direction methods, Part I. Parabolic and hyperbolic problems, Numerische Mathematik, Vol. 6, 1964, pp. 428-453.
43. Yanenko, N.N., The method of fractional steps, Springer-Verlag, 1971.
44. Mitchell, A.R., Computational methods in partial differential equations, John Wiley and Sons, 1969.
45. Ballhaus, W.F., and Steger, J.L., Implicit approximate factorization for the low-frequency transonic equation, NASA TM X-73,082, 1975.
46. Ballhaus, W.F., and Goorjian, P.M., Implicit finite-difference computations of unsteady transonic flows about airfoils, AIAA J., Vol.15, December 1977, pp. 1728-1735.
47. Chipman, R., and Jameson, A., Fully conservative numerical solutions for unsteady irrotational transonic flow about airfoils, AIAA Paper No.79-1555, 1979.
48. Borland, C., Rizzetta, D., and Yoshihara, H., Numerical solution of three-dimensional unsteady transonic flow over swept wings, AIAA Paper No.80-1369, 1980.
49. Sankar, N.L., Malone, J.B., and Tassa, Y., An implicit conservative algorithm for steady and unsteady three-dimensional transonic potential flows, presented at the fifth Computational Fluid Dynamics Conference, Palo Alto, Ca., June 1981.
50. Roach, R.L., and Sankar, N.L., The strongly implicit procedure applied to the flow field of transonic turbine cascades, AIAA Paper No.81-0211, January 1981.
51. Baker, T.J., Potential flow calculation by the approximate factorization method, J. Comp. Phys., Vol. 42, 1981, pp. 1-19.
52. Chattot, J., Coulombeix, C., and da Silva Tome, C., Calculs d'écoulements transsoniques autour d'ailes, La Recherche Aerospatiale, No.4, 1978, pp. 143-159.
53. Baker, T.J., and Forsey, C.R., A fast algorithm for the calculation of transonic flow over wing/body combinations, Presented at the AIAA fifth Computational Fluid Dynamics Conference, Palo Alto, Ca., June 1981.
54. Sankar, N.L., Malone, J., and Tassa, Y., A strongly implicit procedure for steady three-dimensional transonic potential flows, AIAA Paper No.81-0385, January 1981.
55. Benek, J., Steinhoff, J., and Jameson, A., Application of approximate factorization to three-dimensional transonic potential flow calculations, Presented at the AIAA fifth Computational Fluid Dynamics Conference, Palo Alto, Ca., June 1981.
56. Holst, T.L., and Thomas, S.D., Numerical solution of transonic wing flow fields, AIAA Paper No.82-0105, January 1982.
57. Dougherty, F.C., Holst, T.L., Gundy, K.L., and Thomas, S.D., TAIR--A transonic airfoil analysis computer code, NASA TM-81296, May 1980.
58. Melnik, R.E., Wake curvature and trailing edge interaction effects in viscous flow over airfoils. Advanced technology airfoil research, NASA CP-2045, March 1978, pp. 255-270.
59. Ballhaus, W.F., A fast implicit solution procedure for transonic flow, Lecture notes in physics, computing methods in applied sciences and engineering, Springer-Verlag, 1977, pp. 90-102.
60. Stone, H.L., Iterative solution of implicit approximations of multi-dimensional partial differential equations, SIAM Journal of Numerical Analysis, Vol. 5, No.3, 1969.
61. Catherall, D., Optimum approximate-factorization schemes for 2D steady potential flows, Presented at the AIAA fifth Computational Fluid Dynamics Conference, Palo Alto, Ca., June 1981.
62. Buneman, O., A compact non-iterative poisson solver, Report 294, Stanford University Institute for Plasma Research, 1969.
63. Buzbee, B.L., Golub, G.H., and Nielsen, C.W., On direct methods of solving Poisson's equation, SIAM J. Numerical Analysis, Vol. 7, 1970, pp. 627-656.
64. Fischer, D., Golub, G., Hald, O., Leiva, C., and Widlund, O., On Fourier Toeplitz methods for separable elliptic problems, Math. Comp., Vol. 28, 1974, pp. 349-368.
65. Martin, E.D., and Lomax, H., Rapid finite difference computation of subsonic and transonic aerodynamic flows, AIAA Paper No. 74-11, 1974.
66. Martin, E.D., A fast semidirect method for computing transonic aerodynamic flow, AIAA J., Vol. 14, No.7, July 1976, pp. 914-922.
67. Martin, E.D., A split-recoupled-semidirect computational technique applied to transonic flow over lifting airfoils, AIAA Paper No.78-11, January 1978.
68. Yu, N.J., and Rubbert, P.E., Acceleration schemes for transonic potential flow calculations, AIAA Paper No.80-338, January 1980.
69. Casper, J.R., Hobbs, D.E., and Davis, R.L., The calculation of two-dimensional compressible potential flow in cascades using finite area techniques, AIAA Paper No.79-77, January 1979.
70. Casper, J.R., A model problem study of transonic potential flow procedures, AIAA Paper No.80-337, January 1980.
71. Fedorenko, R.P., The speed of convergence of one iterative process, USSR Computational Mathematics and Mathematical Physics, Vol. 4, No.3, 1964, pp. 227-235.

72. Bakhvalov, N.S., On the convergence of a relaxation method with natural constraints on the elliptic operator, USSR Computational Mathematics and Mathematical Physics, Vol. 6, No.5, 1966, pp. 101-135.
73. Nicolaides, R.A., On the L2 convergence of an algorithm for solving finite element system, Math. Comp., Vol. 31, 1977, pp. 892-906.
74. Hackbusch, W., Convergence of multi-grid iterations applied to difference equations, KÖln University Mathematics Institute Report 79-5, April 1979.
75. Brandt, A., Multi-level adaptive solutions to boundary-value problems, Math. Comp., Vol. 31, No.138, April 1977, pp. 333-390.
76. Brandt, A., Multi-Level Adaptive Technique (MLAT) for fast numerical solution to boundary value problems, Proceedings of the third International Conference on Numerical methods in fluid mechanics, Paris, 1972, Lecture notes in Physics 18, pp. 82-89, Springer-Verlag, Berlin and New York, 1973.
77. South, J.C., and Brandt, A., Application of a multi-level grid method to transonic flow calculations, ICASE Report No.76-8, March 1976.
78. Arlinger, B., Multi-grid technique applied to lifting transonic flow using full potential equation, SAAB Report L-0-1 B439, December 1978.
79. Jameson, A., Acceleration of transonic potential flow calculations on arbitrary meshes by the multiple grid method, AIAA Paper No.79-1458, July 1979.
80. McCarthy, D.R., and Reyhner, T.A., A multi-grid code for three-dimensional transonic potential flow about axisymmetric inlets at angle of attack, AIAA Paper No.80-1365, July 1980.
81. Brown, J.J., A multigrid mesh-embedding technique for three-dimensional transonic potential flow analysis, NASA CP-2202, October 1981, pp. 131-149.
82. Brandt, A., Multi-level adaptive computations in fluid dynamics, AIAA Paper No. 79-1455, July 1979.
83. Brandt, A., Multi-Level Adaptive Techniques (MLAT) for partial differential equations: Ideas and software, ICASE report No.77-20, November 1977.
84. Fuchs, L.J., Finite difference methods for plane steady inviscid transonic flows, TRITA-GAD-2, 1977.
85. McCormick, S.F., Multi-grid methods: An alternate viewpoint, UCID report No.18487, October 1979.
86. Brandt, A., Dendy, Jr. J.E., and Ruppel, H., The multi-grid method for semi-implicit hydrodynamics code, J. Comp. Phys., Vol.34, 1980, pp. 348-370.
87. Deconinck, H., and Hirsch, C., A multigrid method for the transonic full potential equation discretized with finite elements on an arbitrary body fitted mesh, NASA CP-2202, October 1981, pp. 61-81.
88. Shmilovich, A., and Caughey, D.A., Application of the multi-grid method to calculations of transonic potential flow about wing-fuselage combinations, NASA CP-2202, October 1981, pp. 101-130.
89. Boerstol, J.W., A multi-grid algorithm for steady transonic potential flows around aerofoils using Newton iteration, NASA CP-2202, October 1981, pp. 151-172.
90. Hafez, M.M., and Cheng, H.K., Convergence acceleration of relaxation solutions for transonic flow computations, AIAA Paper No.75-51, January 1975, (Also AIAA J., Vol. 15, No.3, March 1977, pp. 329-336.)
91. Caughey, D.A., and Jameson, A., Accelerated iterative calculation of transonic nacelle flow fields, AIAA Paper No.76-100, January 1976, (Also AIAA J., Vol. 15, No. 10, October 1977, pp. 1474-1480).
92. Bailey, F.R., A view toward future fluid dynamics computing, AIAA Paper No.78-1112, July 1978.
93. Smith, R.E., Pitts, J.I., and Lambiotte, J.J., A vectorization of the Jameson-Caughey NYU transonic swept-wing computer program FLO-22-VI for the STAR-100 computer, NASA TM-78665, March 1978.
94. Jameson, A., Caughey, D.A., Newman, P.A., and Davis, R.M., A brief description of the Jameson-Caughey transonic swept-wing computer program FLO-22, NASA TM X-73996, December 1976.
95. Keller, J.D., and Jameson, A., Preliminary study of the use of the STAR-100 computer for transonic flow calculations, AIAA Paper No.78-12, January 1978.
96. Redhead, D.D., Chen, A.W., and Hotovy, S.G., New approach to the 3-D transonic flow analysis using the STAR-100 computer, AIAA J., Vol. 17, No.1, January 1979, pp. 98-99.
97. Hotovy, S.G., and Dickson, L.J., Evaluation of a vectorizable 2-D transonic finite difference algorithm, AIAA Paper No.79-276, January 1979.
98. Holst, T.L., An implicit algorithm for solving the transonic, conservative full-potential equation, Proceedings of the 1980 Army Numerical Analysis and Computers Conference, ARO Report 80-3, August 1980, pp. 197-222.
99. Dwyer, H.A., Kee, R.J., and Sanders, B.R., Adaptive grid method for problems in fluid mechanics and heat transfer, AIAA Journal, Vol. 18, No.10, October 1980, pp. 1205-1212.
100. Glowinski, R., On grid optimization for boundary value problems, Stanford University Report No. STAN-CS-79-720, February 1979.
101. Pierson, B.L., and Kutler, P., Optimal nodal point distribution for improved accuracy in computational fluid dynamics, AIAA Journal, Vol.18, No.1, January 1980, pp.49-54.
102. Holst, T.L., and Brown, D., Transonic airfoil calculations using solution-adaptive grids, AIAA Paper No.81-1010, June 1981.
103. Mohan, M., and Anderson, D.A., The use of adaptive grids in conjunction with shock capturing methods, AIAA Paper No.81-1012, June 1981.
104. Carlson, L.A., Transonic airfoil analysis and design using Cartesian coordinates, Presented at the AIAA second CFD conference, Hartford, Conn., June 1975, pp. 175-183.
105. Reyhner, T.A., Cartesian mesh solution for axisymmetric transonic potential flow around inlets, AIAA J., Vol. 15, May 1977, pp. 624-631.
106. Reyhner, T.A., Transonic potential flow around axisymmetric inlets and bodies at angle of attack, AIAA J., Vol. 15, September 1977, pp. 1299-1306.
107. Reyhner, T.A., Transonic potential flow computation about three-dimensional inlets, Ducts and Bodies, AIAA Paper No.80-1364, July 1980.
108. Eisman, P.R., Geometric methods in computational fluid dynamics, ICASE Report No.80-11, April 1980.
109. Lee, K.D., and Rubbert, P.E., Transonic flow computations using grid systems with block structure, Presented at the seventh International Conference on Numerical Methods in Fluid Dynamics, June 1980.
110. Lee, K.D., 3-Dimensional transonic flow computations using grid systems with block structures, AIAA Paper No.81-998, June 1981.
111. Boppe, C.W., Computational transonic flow about realistic aircraft configurations, AIAA Paper No.78-104, January 1978.
112. Boppe, C.W., and Stern, M.A., Simulated transonic flows for aircraft with nacelles, pylons, and winglets, AIAA Paper 80-130, January 1980.

113. Atta, E., Component-adaptive grid interfacing, AIAA Paper No. 81-0382, January 1981.
114. Garabedian, P.R., and Korn, D.G., Analysis of transonic airfoils, Comm. on Pure and Appl. Math., Vol. 24, 1971, pp. 841-851.
115. Kacprzyński, J.J., Transonic flow field past 2-D airfoils between porous wind tunnel walls with nonlinear characteristics, AIAA Paper No.75-81, January 1975.
116. Ives, D.C., A modern look at conformal mapping including multiple connected regions, AIAA J., Vol. 14, No.8, August 1976, pp. 1006-1011.
117. Chen, L.T., and Caughey, D., Calculation of transonic inlet flowfields using generalized coordinates, AIAA Paper No.79-0012, January 1979, (Also, J. of Aircraft, Vol.17, No.3, March 1980, pp. 167-174).
118. Ives, D.C., and Liutermoza, J.F., Analyses of transonic cascade flow using conformal mapping and relaxation techniques, AIAA J., Vol. 25, No.5, May 1977, pp. 647-652.
119. Jameson, A., Iterative solution of transonic flows over airfoils and wings, including flows at Mach 1, Comm. on Pure and Appl. Math., Vol.27, 1974, pp. 283-309.
120. Caughey, D.A., and Jameson, A., Progress in finite-volume calculations for wing-fuselage combinations, AIAA J., Vol.18, No.11, November 1980, pp. 1281-1288.
121. Ives, D.C., and Menor, W.A., Grid generation for inlet and inlet-centerbody configurations using conformal mapping and stretching, Presented at the AIAA fifth Computational Fluid Dynamics Conference, Palo Alto, Ca., June 1981.
122. Moretti, G., Conformal mappings for computations of steady three-dimensional, supersonic flows, Num./Lab. Computer Methods in Fluid Mechanics, December 1976, pp. 13-28.
123. Hall, D.W., Calculation of inviscid supersonic flow over ablated nosetips, AIAA Paper No.79-342, January 1979.
124. Lapidus, A., A detached shock calculation by second-order finite differences, J. Comp. Phys., Vol.2, 1967, pp. 154-177.
125. Viviani, H., Conservative forms of gas dynamic equations, La Recherche Aerospatiale, No.1, January-February 1974, pp. 65-68.
126. Vinokur, M., Conservative equations of gas dynamics in curvilinear coordinate systems, J. Comp. Phys., Vol. 14, February 1974, pp. 105-125.
127. Steger, J.L., Implicit finite difference simulation of flow about arbitrary geometrics with application to airfoils, AIAA Paper No.77-665, June 1977. (See also AIAA Journal, Vol.16, No.7, July 1978, pp. 679-686.)
128. Winslow, A.M., Numerical solution of the quasilinear Poisson equation in a nonuniform triangle mesh, J. Comp. Phys., Vol.1, 1967, pp. 149-172.
129. Chu, W.H., Development of a general finite-difference approximation for a general domain. Part I: Machine transformation, J. Comp. Phys., Vol. 8, 1971, pp. 392-408.
130. Amsden, A.A., and Hirt, C.W., A simple scheme for generating general curvilinear grids, J. Comp. Phys., Vol. 11, 1973, pp. 348-359.
131. Godunov, S.K., and Prokopov, G.P., The use of moving meshes in gas-dynamical computations, USSR Comp. Math. Phys., Vol. 12, 1971, pp. 182.
132. Thompson, J.F., Thames, F.C., and Mastin, C.W., Automatic numerical generation of body-fitted curvilinear coordinate system for field containing any number of arbitrary two-dimensional bodies, J. Comp. Phys., Vol. 15, 1974, pp. 299-319.
133. Thompson, J.F., Thames, F.C., and Mastin, C.W., TOMCAT - A code for numerical generation of boundary-fitted curvilinear coordinate systems on fields containing any number of arbitrary two-dimensional bodies, J. Comp. Phys., Vol. 24, 1977, pp. 274-302.
134. Thompson, J.F., Thames, F.C., and Mastin, C.W., Boundary-fitted curvilinear coordinate systems for solution of partial differential equations on fields containing any number of arbitrary two-dimensional bodies, NASA CR-2729, July 1977.
135. Camarero, R., and Younis, M., Generation of body-fitted coordinates for turbine cascades using multigrid, AIAA Paper No.79-49, April 1979.
136. Yu, N.J., Grid generation and transonic flow calculations for three-dimensional configurations, AIAA Paper No.80-1391, July 1980.
137. Thomas, P.D., Construction of composite three dimensional grids from subregion grids generated by elliptic systems, Presented at the AIAA fifth Computational Fluid Dynamics Conference, Palo Alto, Ca., June 1981.
138. Yu, N.J., Transonic flow simulations for complex configurations with surface fitted grids, AIAA Paper No.81-1258, June 1981.
139. Thomas, P.D., and Middlecoff, J.F., Direct control of the grid point distributions in meshes generated by elliptic equations, AIAA J., Vol. 18, No.6, June 1980, pp. 652-656.
140. Steger, J.L., and Sorenson, R.L., Automatic mesh-point clustering near a boundary in grid generation with elliptic partial differential equations, J. Comp. Phys., Vol. 33, No.3, December 1979, pp. 405-410.
141. Sorenson, R.L., and Steger, J.L., Numerical generation of two-dimensional grids by the use of Poisson equations with grid control at boundaries, Proceedings of the Numerical Grid Generation Techniques Workshop, NASA Langley Research Center, Hampton, Va., NASA CP-2166, October 1980, pp. 449-461.
142. Starius, G., Constructing orthogonal curvilinear meshes by solving initial value problems, Numerische Mathematik, Vol. 28, 1977, pp. 25-48.
143. Steger, J.L., and Chaussee, D.S., Generation of body fitted coordinates using hyperbolic partial differential equations, FSI Report 80-1, January 1980.
144. Eiseman, P.R., A coordinate system for a viscous transonic cascade analysis, J. Comp. Phys., Vol. 26, No.3, March 1978, pp. 307-338.
145. Eiseman, P.R., A multi-surface method of coordinate generation, J. Comp. Phys., Vol. 33, No.1, October 1979, pp. 118-150.
146. Eiseman, P.R., Three-dimensional coordinates about wings, Presented at the AIAA fourth CFD Conference, Williamsburg, Va., July 1979, pp. 166-174.
147. Eiseman, P.R., Coordinate generation with precise controls, ICASE Report No.80-16, June 1980.
148. Eiseman, P.R., Coordinate generation with precise controls over mesh properties, ICASE Report No.80-30, November 1980.
149. McNally, W.D., FORTRAN program for generating a two-dimensional orthogonal mesh between two arbitrary boundaries, NASA TN D-6766, 1972.

150. Graves, Jr. R.A., Application of a numerical orthogonal coordinate generator to axisymmetric blunt bodies, NASA TM 80131, September 1979.
151. Hamilton, II, H.H., and Graves, Jr. R.A., Application of a numerically generated orthogonal coordinate system to the solution of inviscid axisymmetric supersonic flow over blunt bodies, NASA TP 1619, March 1980.
152. Eriksson, L.E., Three-dimensional spline-generated coordinate transformations for grids around wing-body configurations, Proceedings of the Numerical Grid Generation Techniques Workshop, NASA Langley Research Center, Hampton, Va., NASA CP-2166, October 1980, pp. 253-264.
153. Rizzi, A., and Eriksson, L.E., Transfinite mesh generation and damped Euler equation algorithms for transonic flow around wing-body configurations, Presented at the AIAA fifth Computational Fluid Dynamics Conference, Palo Alto, Ca., June 1981.

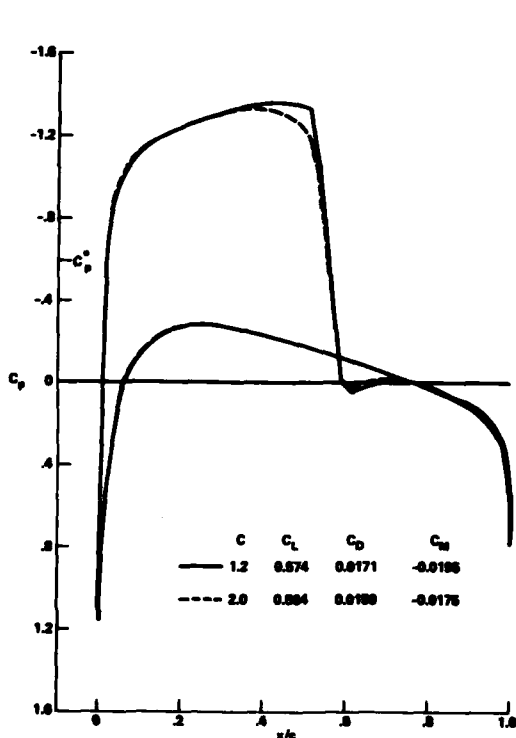


Fig. 6.1 Pressure coefficient distribution for NACA 0012 airfoil at $M_\infty = 0.75$ and $\alpha = 2$ deg, density computed at node points and artificial viscosity parameter (ν) computed at half points, (Holst and Albert [23])

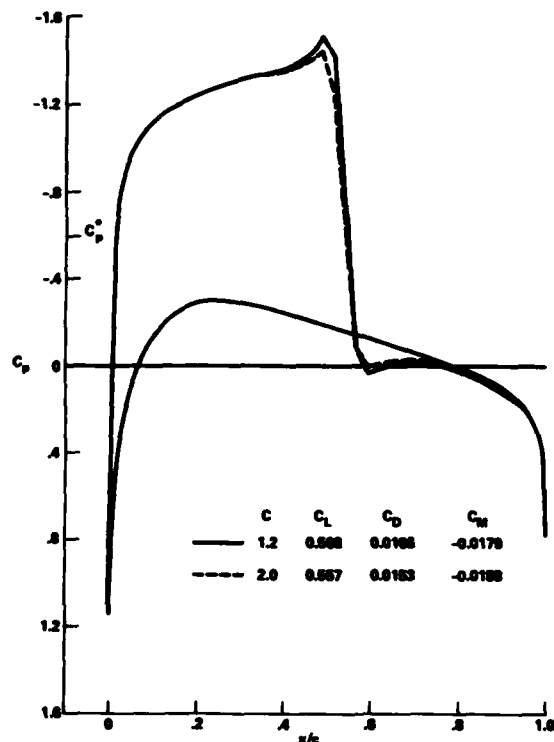


Fig. 6.2 Pressure coefficient distribution for NACA 0012 airfoil at $M_\infty = 0.75$ and $\alpha = 2$ deg, both density and artificial viscosity parameter (ν) computed at node points, (Holst and Albert [23])

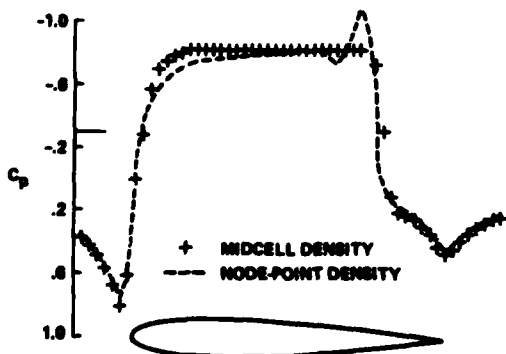


Fig. 6.3 Pressure coefficient distribution for NACA 0012 airfoil at $M_\infty = 0.85$ and $\alpha = 0$ deg, artificial viscosity parameter (ν) computed at node points, (South, et al. [24])

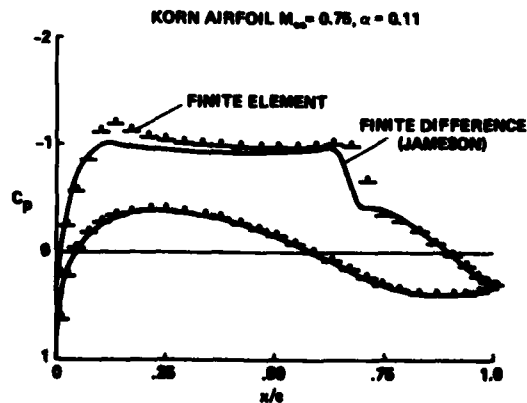


Fig. 6.4 Pressure coefficient comparison, finite element versus finite difference, (Bristeau, et al. [31])

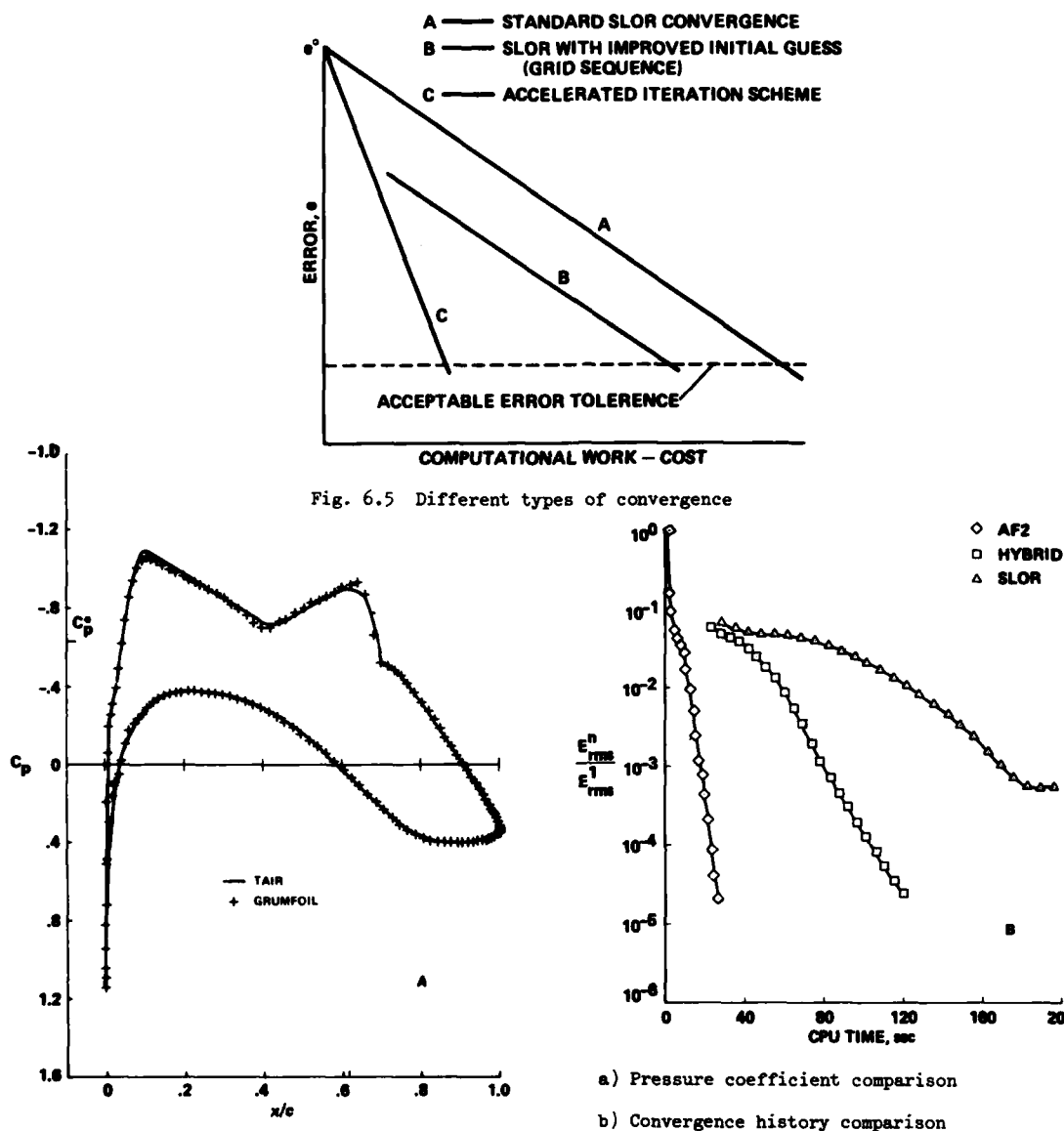


Fig. 6.6 Pressure coefficient and convergence history comparisons, Korn airfoil, $M_\infty = 0.74$, $\alpha = 0^\circ$, (Dougherty, et al. [57])

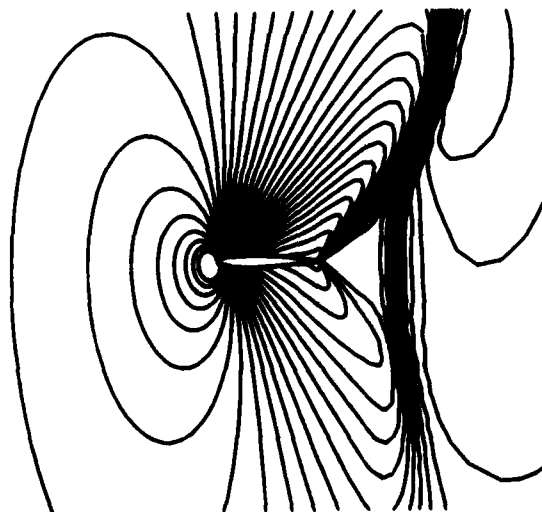


Fig. 6.7 Mach number contours, NACA 0012 airfoil, $M_\infty = 0.95$, $\alpha = 4^\circ$, (Holst [10])

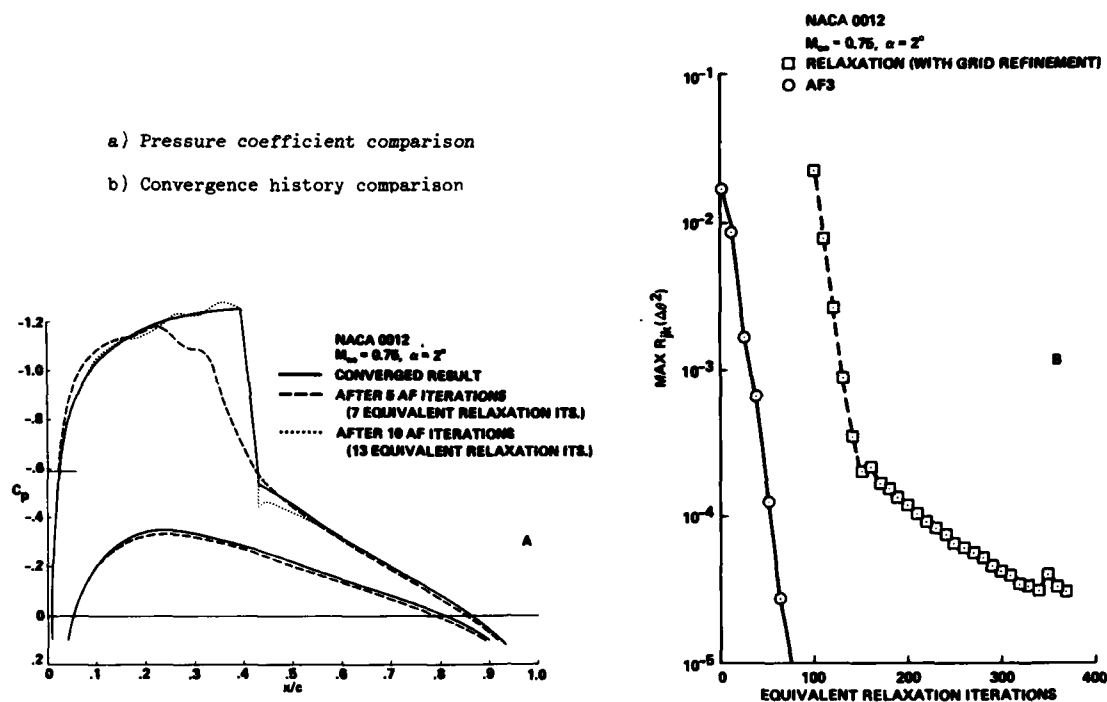


Fig. 6.8 Pressure coefficient and convergence history comparisons, NACA 0012 airfoil, $M_\infty = 0.75$, $\alpha = 2^\circ$, (Baker [2])

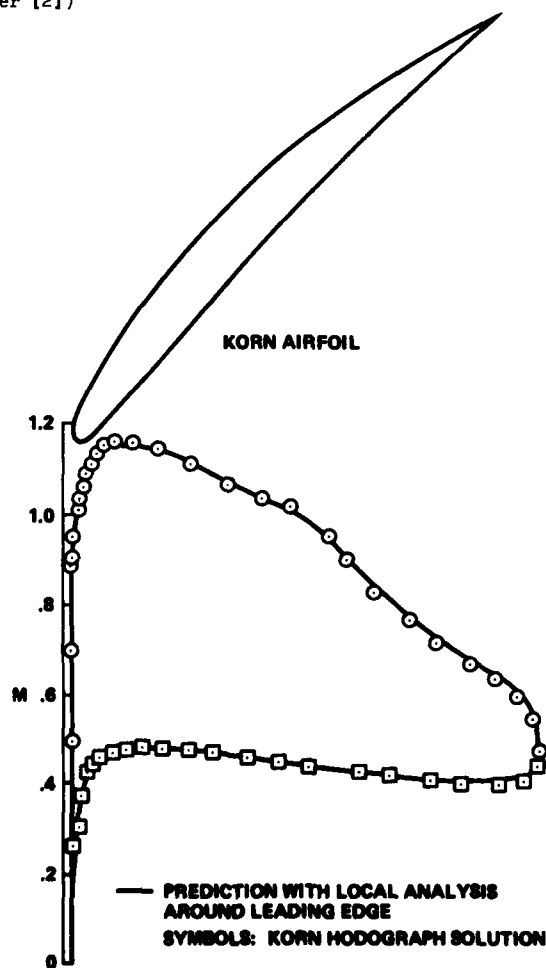


Fig. 6.9 Airfoil surface Mach number distribution for a Korn cascade, (Casper, et al. [69])

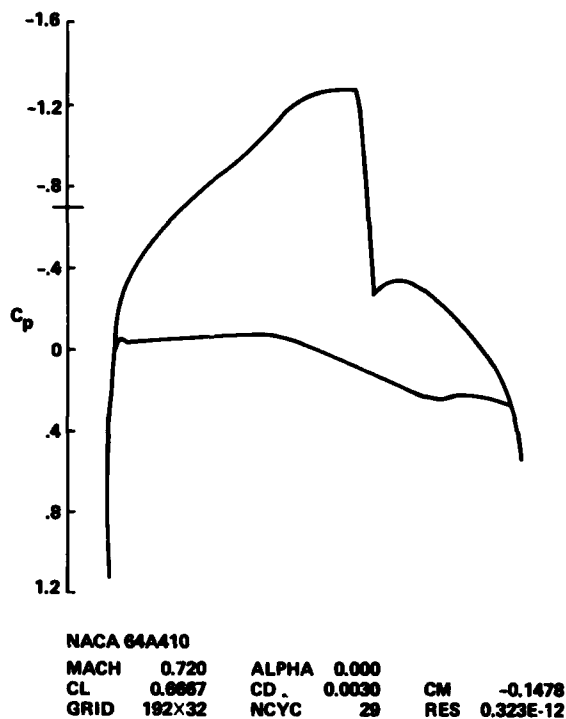


Fig. 6.10 Converged pressure distribution, (Jameson [79])

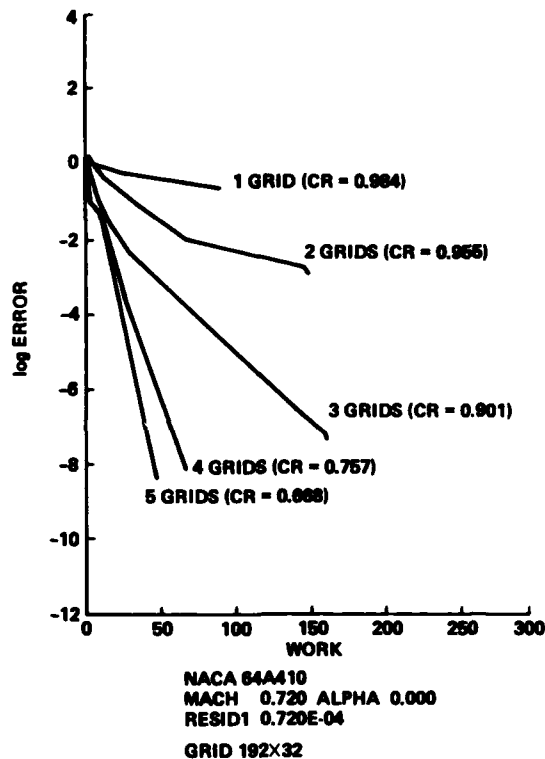


Fig. 6.11 Multi-grid convergence history, (Jameson [79])



Fig. 6.12 Converged pressure distribution (Jameson [79])

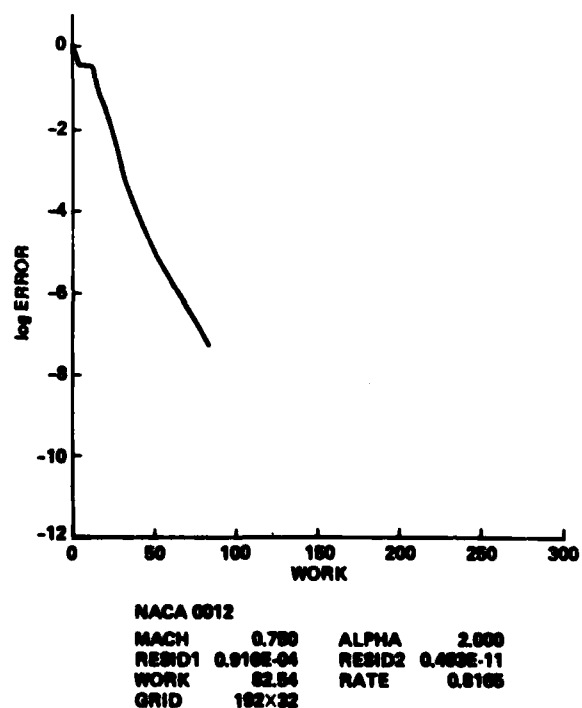


Fig. 6.13 Multi-grid convergence history, five grids, (Jameson [79])

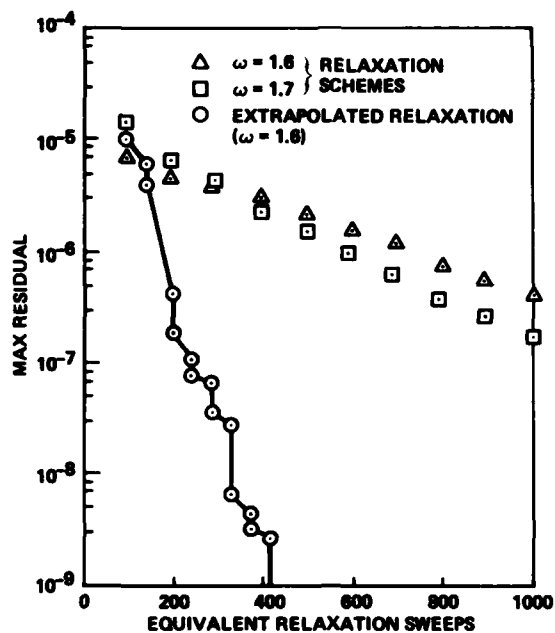


Fig. 6.14 Convergence history showing the effect of extrapolation, (Caughey and Jameson [91])

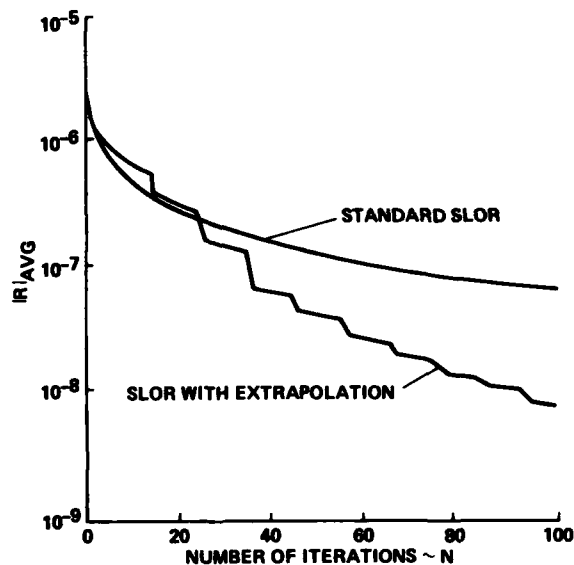


Fig. 6.15 Convergence behaviour for an advanced wing at $M_\infty = 0.8$, and $\alpha = 3.06^\circ$, (Yu and Rubbert [68])

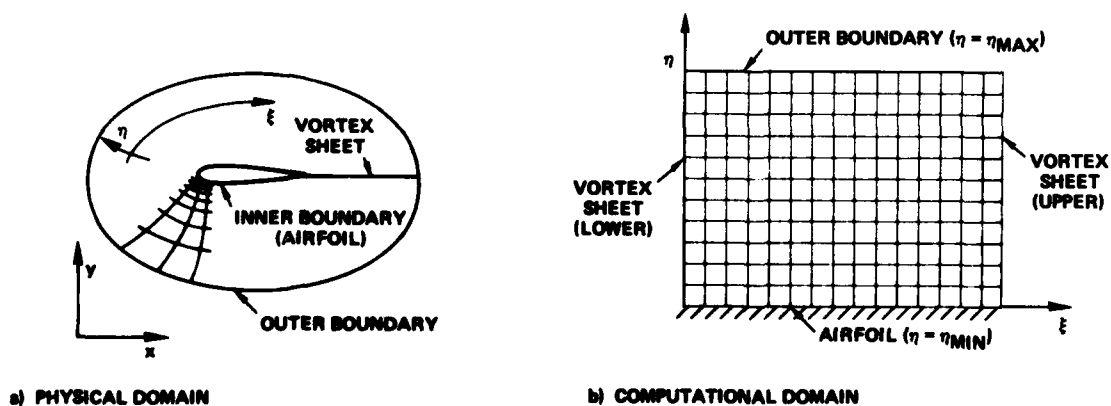


Fig. 6.16 General transformation for an airfoil $(x,y) \leftrightarrow (\xi,\eta)$

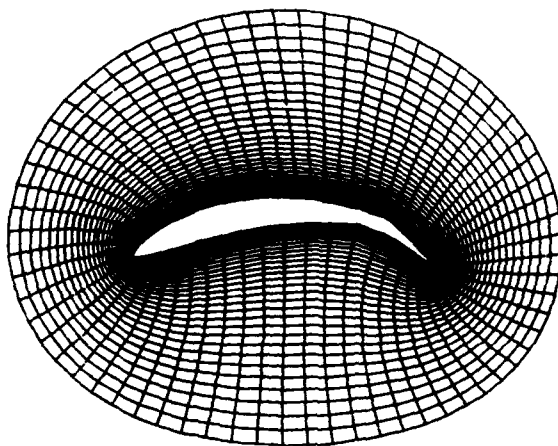


Fig. 6.17 Finite-difference grid about a Karman-Trefftz airfoil with flap, (Thompson, et al. [134])

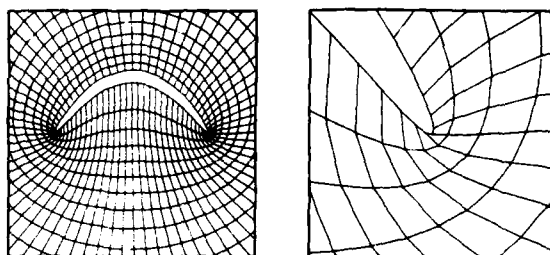


Fig. 6.18 Finite-difference grid about a highly cambered 12:1 ellipse, no control, (Sorenson and Steger [141])

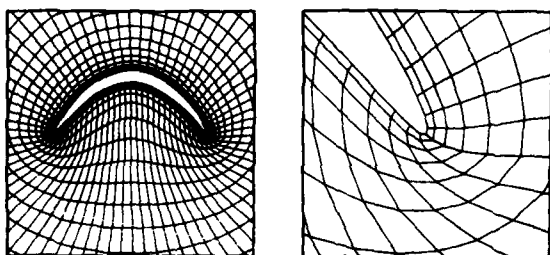


Fig. 6.19 Finite-difference grid about a highly cambered 12:1 ellipse, control terms activated, (Sorenson and Steger [141])

7. CONCLUDING REMARKS AND FUTURE PROSPECTS

Having discussed, to some extent, the problems and solutions, possibilities and limitations, achievements and developments in current computational transonic aerodynamics, it seems appropriate to try to put these in a future perspective. In doing so, figure 7.1, taken from a presentation of P.E. Rubbert is most helpful.

In setting up a time scale for the evolution of transonic computational fluid dynamics Rubbert distinguishes 5 stages. The first two of these represent the glamorous days of innovation, scientific papers and demonstration. The next two stages are those of "sweat, blood and tears"; this is the period of production code development and increasing application in a research/design environment. The last stage is that of general acceptance; the production code has acquired a settled position in the engineering environment and application has become a routine matter.

It would seem that with transonic computational aerodynamics we are about to move from stage II into stage III (at least as far as analysis methods are concerned; design/inverse methods seem to have only just entered the "gee whiz!" phase). However, a prerequisite for entering stage III with full momentum is that the problem of convergence acceleration in the general 3-D case with irregular grids be solved satisfactorily.

At least for transport aircraft applications methods for solving the full potential equation will probably remain to provide the best "value for money". Whether the additional possibilities offered by the Euler equations is worth the added complexity remains to be seen.

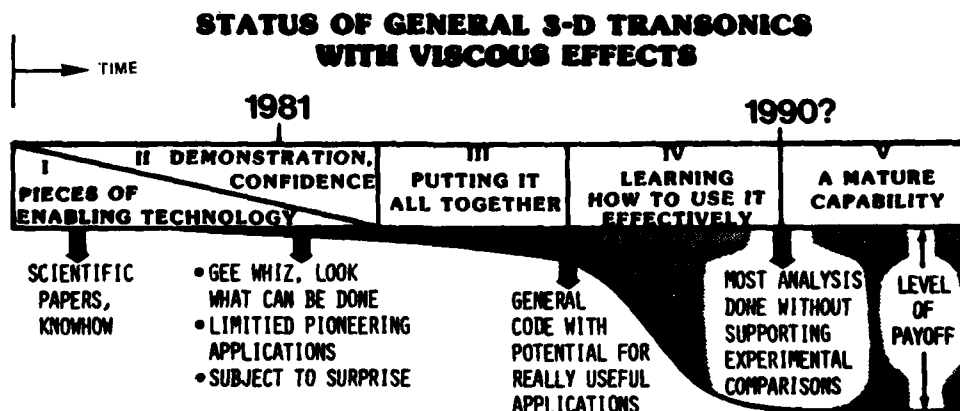
It is expected that the majority of the production codes to be developed will be of the finite volume type with block-structured grids. Generation of grids for the various aircraft components will require a major effort. Another important effort will have to be put into the development of strong viscous interaction algorithms.

A very important point to consider during production code development as well as application is that for optimal functioning computational aerodynamic software systems and aerodynamic analyses/design procedures must be tuned to each other, [2]. This means that the computational fluid dynamicist/code designer must be prepared to look upon his product as a small part of a much bigger information system and tailor his product accordingly. The user/aerodynamicist, on the other hand, must be prepared to adapt his engineering procedures to enable the optimal use of the new possibilities that are being created by the advances in computational aerodynamics.

It is expected, [2], that by 1990, these advances, together with those in computer technology, will have led to a two orders of magnitude increase in computational productivity. Development of the software necessary for controlling and digesting the immense amounts of information that will be generated through aerodynamic computations most likely will become another pacing item in computational aerodynamics. We must expect that the stage of maturity (V in Fig. 7.1) cannot be reached without solving this informatics problem.

7.1 References

1. Rubbert, P.E., Progress in computational aerodynamics, presented at AIAA 5th Computational Fluid Dynamics Conference, Palo Alto, Ca., 1981.
2. Slooff, J.W., Requirements and developments shaping a next generation of integral methods, paper presented at IMA Conference on Numerical Methods in Aeronautical Fluid Dynamics, Reading, U.K. 1981.



TECHNOLOGY PIECES EVOLVING

- COMPLEX GRIDS
- CONVERGENCE ACCELERATION SCHEMES
- STRONG VISCOUS INTERACTION MODELING
- VECTOR COMPUTERS
- EULER EQUATION SOLVERS
- ALTERNATIVES TO SURFACE-FITTED, FINITE VOLUME
- SOFTWARE DEVELOPMENT METHODOLOGY

8. ACKNOWLEDGEMENTS

During the preparation of this AGARDograph, contributions and/or comments were received from many sources. The authors are particularly indebted to the following individuals (alphabetical order):

Dr. C.M. Albone of RAE
Mr. T.J. Baker of ARA
Dr. J.W. Boerstoeel of NLR
Dr. E. Bonner of Rockwell
Mr. C.W. Boppe of Grumman Aerospace
Mr. M.P. Carr of ARA
Dr. J.J. Chattot of ONERA
Dr. A. Eberle of MBB
Mr. M. Firmin of RAE
Mr. C.R. Forsey of ARA
Dr. S. Hedman of FFA
Mr. P.A. Henne of McDonnell-Douglas
Mr. R.M. Hicks of NASA Ames
Dr. W. Kordulla of DFVLR
Dr. P.A. Newmann of NASA Langley
Dr. W. Schmidt of Dornier
Prof. Thiede of VFW
Mr. J. van der Vooren of NLR

Although not all of their contributions could be incorporated, their impact on the AGARDograph has been significant.

REPORT DOCUMENTATION PAGE											
1. Recipient's Reference	2. Originator's Reference AGARD-AG-266	3. Further Reference ISBN 92-835-1431-9	4. Security Classification of Document UNCLASSIFIED								
5. Originator	Advisory Group for Aerospace Research and Development North Atlantic Treaty Organization 7 rue Ancelle, 92200 Neuilly sur Seine, France										
6. Title	APPLIED COMPUTATIONAL TRANSONIC AERODYNAMICS										
7. Presented at											
8. Author(s)/Editor(s) See Flyleaf	9. Date August 1982										
10. Author's/Editor's Address See Flyleaf	11. Pages 108										
12. Distribution Statement	This document is distributed in accordance with AGARD policies and regulations, which are outlined on the Outside Back Covers of all AGARD publications.										
13. Keywords/Descriptors	<table border="0"> <tr> <td>Transonic flow</td> <td>Numerical analysis</td> </tr> <tr> <td>Fluid dynamics</td> <td>Applications of mathematics</td> </tr> <tr> <td>Computation</td> <td>Viscosity</td> </tr> <tr> <td>Computerized simulation</td> <td></td> </tr> </table>			Transonic flow	Numerical analysis	Fluid dynamics	Applications of mathematics	Computation	Viscosity	Computerized simulation	
Transonic flow	Numerical analysis										
Fluid dynamics	Applications of mathematics										
Computation	Viscosity										
Computerized simulation											
14. Abstract	<p>Development of transonic computational fluid dynamics has moved rapidly during the last decade with progress in numerical mathematics and computer technology. This AGARDograph surveys the state of art in the early 1980's, providing a foundation upon which improvements can be based. Chapters on: General Theory; Existing Computational Transonic Aerodynamic (CTA) Methods; Viscous Interactions; Computational Procedures in Transonic Aerodynamic Design; and Advanced Concepts are included.</p> <p>The AGARDograph was commissioned by the Fluid Dynamics Panel of AGARD following several symposia and meetings organized by the panel and referenced in the report.</p> <p style="text-align: center;">102</p>										

<p>AGARDograph No.266 Advisory Group for Aerospace Research and Development, NATO APPLIED COMPUTATIONAL TRANSONIC AERODYNAMICS by T.L.Holst, J.W.Slooff, H.Yoshihara and W.F.Ballhaus Edited by B.M.Spee and Dr H.Yoshihara Published August 1982 108 pages</p> <p>Development of transonic computational fluid dynamics has moved rapidly during the last decade with progress in numerical mathematics and computer technology. This AGARDograph surveys the state of art in the early 1980's, providing a foundation upon which improvements can be based. Chapters on: General Theory;</p> <p>P.T.O.</p>	<p>AGARD-AG-266</p> <p>Transonic flow Fluid dynamics Computation Computerized simulation Numerical analysis Applications of mathematics Viscosity</p>	<p>AGARDograph No.266 Advisory Group for Aerospace Research and Development, NATO APPLIED COMPUTATIONAL TRANSONIC AERODYNAMICS by T.L.Holst, J.W.Slooff, H.Yoshihara and W.F.Ballhaus Edited by B.M.Spee and Dr H.Yoshihara Published August 1982 108 pages</p> <p>Development of transonic computational fluid dynamics has moved rapidly during the last decade with progress in numerical mathematics and computer technology. This AGARDograph surveys the state of art in the early 1980's, providing a foundation upon which improvements can be based. Chapters on: General Theory;</p> <p>P.T.O.</p>	<p>AGARD-AG-266</p> <p>Transonic flow Fluid dynamics Computation Computerized simulation Numerical analysis Applications of mathematics Viscosity</p>
<p>AGARDograph No.266 Advisory Group for Aerospace Research and Development, NATO APPLIED COMPUTATIONAL TRANSONIC AERODYNAMICS by T.L.Holst, J.W.Slooff, H.Yoshihara and W.F.Ballhaus Edited by B.M.Spee and Dr H.Yoshihara Published August 1982 108 pages</p> <p>Development of transonic computational fluid dynamics has moved rapidly during the last decade with progress in numerical mathematics and computer technology. This AGARDograph surveys the state of art in the early 1980's, providing a foundation upon which improvements can be based. Chapters on: General Theory;</p> <p>P.T.O.</p>	<p>AGARD-AG-266</p> <p>Transonic flow Fluid dynamics Computation Computerized simulation Numerical analysis Applications of mathematics Viscosity</p>	<p>AGARDograph No.266 Advisory Group for Aerospace Research and Development, NATO APPLIED COMPUTATIONAL TRANSONIC AERODYNAMICS by T.L.Holst, J.W.Slooff, H.Yoshihara and W.F.Ballhaus Edited by B.M.Spee and Dr H.Yoshihara Published August 1982 108 pages</p> <p>Development of transonic computational fluid dynamics has moved rapidly during the last decade with progress in numerical mathematics and computer technology. This AGARDograph surveys the state of art in the early 1980's, providing a foundation upon which improvements can be based. Chapters on: General Theory;</p> <p>P.T.O.</p>	<p>AGARD-AG-266</p> <p>Transonic flow Fluid dynamics Computation Computerized simulation Numerical analysis Applications of mathematics Viscosity</p>

<p>Existing Computational Transonic Aerodynamic (CTA) Methods; Viscous Interactions; Computational Procedures in Transonic Aerodynamic Design; and Advanced Concepts are included.</p> <p>The AGARDograph was commissioned by the Fluid Dynamics Panel of AGARD following several symposia and meetings organized by the panel and referenced in the report.</p> <p>ISBN 92-835-1431-9</p>	<p>Existing Computational Transonic Aerodynamic (CTA) Methods; Viscous Interactions; Computational Procedures in Transonic Aerodynamic Design; and Advanced Concepts are included.</p> <p>The AGARDograph was commissioned by the Fluid Dynamics Panel of AGARD following several symposia and meetings organized by the panel and referenced in the report.</p> <p>ISBN 92-835-1431-9</p>
<p>Existing Computational Transonic Aerodynamic (CTA) Methods; Viscous Interactions; Computational Procedures in Transonic Aerodynamic Design; and Advanced Concepts are included.</p> <p>The AGARDograph was commissioned by the Fluid Dynamics Panel of AGARD following several symposia and meetings organized by the panel and referenced in the report.</p> <p>ISBN 92-835-1431-9</p>	<p>Existing Computational Transonic Aerodynamic (CTA) Methods; Viscous Interactions; Computational Procedures in Transonic Aerodynamic Design; and Advanced Concepts are included.</p> <p>The AGARDograph was commissioned by the Fluid Dynamics Panel of AGARD following several symposia and meetings organized by the panel and referenced in the report.</p> <p>ISBN 92-835-1431-9</p>

END

DATE
ILME